DESIGN, SYNTHESIS AND STUDY OF NOVEL POLYCYCLIC AROMATIC SYSTEMS

A THESIS SUBMITTED IN PARTIAL FULFILLMENT OF THE REQUIREMENTS FOR THE DEGREE OF DOCTOR OF PHILOSOPHY

LALHRUAIZELA
MZU REGISTRATION NO. : 4459 of 2010-11
PH.D REGISTRATION NO. : MZU/Ph.D/847 of 21.04.2016

DEPARTMENT OF CHEMISTRY
SCHOOL OF PHYSICAL SCIENCES
MAY, 2022

DESIGN, SYNTHESIS AND STUDY OF NOVEL POLYCYCLIC AROMATIC SYSTEMS

BY
LALHRUAIZELA
Department of Chemistry

Under the supervision of
Dr. VED PRAKASH SINGH

Submitted
In partial fulfillment of the requirement of the Degree of Doctor of Philosophy
in Chemistry of Mizoram University, Aizawl.

MIZORAM UNIVERSITY
(A central University under the Act of Parliament)
Department of Industrial Chemistry
School of Physical Sciences

Dr. Ved Prakash Singh
Associate Professor

CERTIFICATE

This is to certify that the thesis entitled "***Design, Synthesis and Study of Novel Polycyclic Aromatic Systems***" submitted by **Lalhruaizela** to Mizoram University, Tanhril, Aizawl, for the award of the degree of ***Doctor of Philosophy*** in Chemistry is a *bona fide* record of the original investigations carried out by him under my supervision. He has been duly registered and the thesis presented is worthy of being considered for the award of the Ph.D. degree. This work has not been submitted for any degree in any other university.

Dated: May 13, 2022

(Dr. VED PRAKASH SINGH)
Supervisor

Declaration of the Candidate

Mizoram University

May, 2022

I, Lalhruaizela, hereby declare that the subject matter of this thesis is the record of work done by me, that the contents of this thesis did not form basis of the award of any previous degree to me or to do the best of my knowledge to anybody else, and that the thesis has not been submitted by me for any research degree in any other University/ Institute.

This is being submitted to the Mizoram University for the degree of Doctor of Philosophy in Chemistry.

(LALHRUAIZELA)
Candidate

(Prof. MUTHUKUMARAN R.)
Head

(Dr. VED PRAKASH SINGH)
Supervisor

ACKNOWLEDGEMENT

First and foremost, I thank Almighty God for blessing me with health, strength and knowledge to accomplish my work. Without his grace and mercy, this work would have perished.

I would like to acknowledge and give my warmest appreciation to my supervisor, ***Dr. Ved Prakash Singh***, *Associate Professor, Department of Industrial Chemistry, Mizoram University*, for his immense dedication, support and motivation in my Ph.D research work. I admire his advise on lab safely rules and good laboratory practices. His scientific knowledge had a great impact for the ease of my research work. I also appreciate his empathy and patience with me during my entire research program.

I extend my gratitude to all the teaching faculty, *Prof. Muthukumuran R., Head, Department of Chemistry, MZU, Prof. Diwakar Tiwari, Dr. N. Mohondas Singh, Dr. Zodinpuia Pachuau, Dr. A. Bimolini Devi* and non-teaching staff, *Mr. Brojendro Singh Shagolsem, Sr. Laboratory Technician, and Mr. John Vanlalhruaia, Technical Assistant, Chemistry Department. MZU,* for their endless help and support throughout my academic career.

I appreciate the good cooperation I have experienced from my fellow research scholar of the department. I would like to give credit to my fellow labmate *Dr. Jayanta Dowarah, Mr. Brilliant N. Marak, Mr. Laldingluaia Khiangte and Mr. Biki Hazarika* for their limitless assistance in my research work. They were my devoted friends and never fail to comfort me during my times of difficulties. Their good deeds would be remembered during my entire life.

I also express my deepest gratitude to an expert crystallographer *Prof. Geeta Hundal* and *Dr. Balkaran Singh Sran, Department of Chemistry, Guru Nanak Dev Univesrsity, Amritsar, Punjab* and *Dr. Ramesh Kataria, Department of Chemistry, Panjab University, Chandigarh* for their collaboration in refining the crystal structure of my compounds.

I also thank Sophisticated Analytical Instrument Facility (SAIF), Gauhati University and Central Drug Research Institute (CDRI), Lucknow; Indian Institute of Chemical Technology (IICT), Hyderbad and Banaras Hindu University, Varanasi for collecting spectroscopic NMR and Mass spectra.

I acknowledge DBT and CSIR New Delhi for their financial support in funding the research work and the fellowship I enjoy during my research period.

It is my pleasure to thank my parents and all of my family members for their prayers, love and support during my tenure for the degree. I also give my heartfelt thanks to my wife for her courage, strength and hard labour she went through for the accomplishment of the degree I sought for.

(LALHRUAIZELA)

CONTENTS

CHAPTER 1

INTRODUCTION

CHAPTER 2

SYNTHESIS AND STUDY OF HETERO-POLYCYCLIC AROMATIC SYSTEMS

CHAPTER 3

SYNTHESIS AND STUDY OF POLYCYCLIC AROMATIC FLEXIMERS

CHAPTER 4

BIOLOGICAL STUDY OF HETERO- POLYCYCLIC/POLYCYCLIC AROMATIC SYSTEMS BY *IN SILICO* ANALYSIS

CHAPTER 5

BIO-DATA

PARTICULARS OF THE CANDIDATE

LIST OF PUBLICATIONS

CONFERENCE AND SEMINAR

LISTS OF TABLES

LISTS OF FIGURES

ABBREVIATIONS

1843U89	(2*S*)-2-[6-[(3-methyl-1-oxo-2*H*-benzo[f]quinazolin-9-yl)methylamino]-3-oxo-1*H*-isoindol-2-yl]pentanedioate
2-D	Two-dimensional
3-D	Three-dimensional
^{13}C NMR	Carbon-13 nuclear magnetic resonance
^{1}H NMR	Proton nuclear magnetic resonance
5-LOX	Arachidonate 5-lipoxygenase
Ach	Acetylcholine protein
ATP	Adenosine triphosphate
CADD	Computer aided drug design
CAFs	cancer-associated fibroblasts
$CDCl_3$	Deuterated chloroform
Chk1	Checkpoint kinase 1
CIF	Crystallographic Information File
COX-2	Cyclooxygenase 2
D…A	Donor…Acceptor
DDQ	2,3-Dichloro-5,6-dicyano-1,4-benzoquinone
D–H	Donor – Hydrogen
D–H...A	Donor–Hydrogen…Acceptor
DMF	Dimethylformamide
DMSO	Dimethyl sulfoxide
DNA	Deoxyribonucleic acid
dUMP	Deoxyuridine monophosphate
Eg5	Kinesin spindle protein
EGFR	Epidermal growth factor receptor
EtOAc	Ethyl acetate
FDA	Food and Drug Administration
FTNMR	Fourier Transform Nuclear Magnetic Resonance
H…A	Hydrogen…Acceptor
HEPES	4-(2-hydroxyethyl)-1-piperazineethanesulfonic acid)

HIV	Human Immunodeficiency Virus
ICMR	Indian Council of Medical Research
IRAP	Insulin-regulated aminopeptidase
IUPAC	International Union of Pure and Applied Chemistry
LY290181	2-amino-4-(3-nitrophenyl)-4H-benzo[h]chromene-3-carbonitrile
M2	Macrophage type 2
MAPK	Mitogen-activated protein kinase
MHz	Megahertz
MS	Mass spectrometry
MX58151	2-Amino-4-(3-bromo-4,5-dimethoxyphenyl)-7-(dimethylamino)-4*H*-chromene-3-carbonitrile
NMR	Nuclear Magnetic Resonance
ORTEP	Oak Ridge Thermal Ellipsoid Plot
PDB	Protein Data Bank
PDE-3	Phosphodiesterase-3
PIM-1	Proviral integration site for Moloney murine leukemia virus-1
PP2A	protein phosphatase 2A
QSAR	Quantitative Structure-Activity Relationship
RB	Round bottom flask
RCSB	Research Collaboratory for Structural Bioinformatics
RNA	Ribonucleic acid
RT	Room temperature
SC-XRD	Single Crystal X-ray Diffraction
TLC	Thin-layer chromatography
TME	Tumor microenvironment
TMS	Tetramethylsilane
UV	Ultraviolet
VDW	van der Waals

CHAPTER 1

INTRODUCTION

1.1. Definition of polycyclic aromatic compounds

In organic chemistry, a polycyclic aromatic compound is a cyclic compound with more than one hydrocarbon loop or ring structure (benzene rings, etc.) (March 1985). The term **“polycyclic aromatic systems”** generally includes all polycyclic aromatic compounds, including the polycyclic aromatic hydrocarbons and the heterocyclic aromatic compounds with multiple rings containing sulfur, nitrogen, oxygen, or another non-carbon atom and substituted derivatives of these compounds.

1.2. Introduction to heterocycles

Heterocyclic chemistry is a branch of chemistry that deals with studying the synthesis, properties, and applications of heterocyclic compounds (Gilchrist, 1998). Heterocyclic chemistry nearly accounts for one-third of modern publications (Katritzky, 2014). Nearly two-thirds of organic compounds known are heterocyclic compounds (Rees, 1992). A carbocyclic compound containing all carbon atoms in ring formation is a cyclic organic compound. If at least one atom other than carbon forms a part of the ring system, it is designated a heterocyclic compound (McNaught et al., 1997). Nitrogen, oxygen and sulfur are the most common heteroatoms, but heterocyclic rings containing other heteroatoms like phosphorus and selenium are also widely known (Abdel-Hafez, 2008; Liu, 2001; Vasu Govardhana Reddy et al., 2004). Heterocyclic compounds generally consist of small **(3- and 4-membered)** and common **(5- to 7- membered)** ring systems. They may have one, two, or more heteroatoms of the same or different kinds as ring constituents.

Heterocyclic compounds are widely distributed in nature and they form the core component of a large number of compounds that are essential for life. The main constituents of Deoxyribonucleic acid (DNA), which contains the genetic instructions for the development and function of all living things, are heterocyclic bases- purines and pyrimidines. In addition, chlorophyll and heme, the oxygen carriers in plants and animals respectively, are also derivatives of the porphyrin ring.

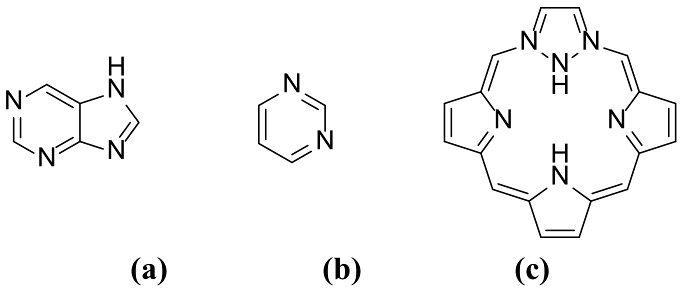

Figure 1.1: (a) Purine, (b) Pyrimidine and (c) Porphyrin

Many heterocyclic compounds, both synthetic and natural, are of biological and pharmaceutical significance. Their importance is mainly attributed to their ability to engage in various intermolecular interactions such as hydrogen bond donor/acceptor capability, π...π stacking interactions, metal coordination bonds, van der Waals and hydrophobic forces. Alkaloids and terpenoids are from an influential group of naturally occurring heterocycles with diverse biological activity. Over 75% of the top 200 branded drugs in the pharmaceutical industry have heterocyclic fragments in their structures (Kaur, 2020). Other heterocyclic moiety drugs are also commonly used as antimicrobial, antiseptics, and anti-inflammatory agents. Some heterocycles exhibit antitumor, antimicrobial, anti-inflammatory, anti-depressant, anti-HIV, anti-diabetic activity, and anti-malarial (Kalaria et al., 2018).

The present work on this thesis includes a convenient and straightforward method of synthesis of polycyclic aromatic compounds containing heteroatoms in their cyclic ring moiety. Analogues of 4H-pyrans and 2-pyridone derivatives were focused on the work, since these heterocyclic compounds are found in many biologically active compounds. The work on this thesis will also focus on a novel synthetic route and synthesize novel polycyclic aromatic compounds. The compounds crystallized as single crystals are studied by X-ray crystallography and Hirshfeld surface analysis to explore the non-covalent interactions in the supramolecular framework. Docking is also performed to study the drug-receptor properties of the compounds with the target molecule.

1.3. Survey of the literature

Non-covalent interactions are weak attractive forces between molecules that do not involve the complete sharing of electrons in the bonding orbitals, but rather involve more dispersed variations of electromagnetic interactions between molecules or within a molecule. Intermolecular forces are non-covalent interactions that occur between different molecules rather than between atoms of the same molecule (Anslyn & Dougherty, 2006). These weak interactions exert strong influences over the properties of molecules in solution and the solid state, where all molecules are continually making contact with those around them. Non-covalent interactions are the core of molecular recognition and supramolecular chemistry (Desiraju, 1995; Daze & Hof, 2016) (chemistry beyond the single-molecule, where assemblies and interactions among polymer chains determine their bulk properties), and all biological processes (where nucleic acids, proteins, lipids, and metabolites participate differently in all living organisms).

All bioprocesses are based on non-covalent interaction, and thus they are extremely important. The major interactions involved in bioprocess are: Ion Pairs, Ion-dipole interaction, Dipole…dipole interaction, Hydrogen bonding, Cation…π interaction, π…π stacking interaction, and Halogen bonding **(Table1.1)**.

Table 1.1: Types and estimated bond energies of non-covalent interactions

Bond type	Bond energy [kJ/mol]	Relative strength
Hydrogen bonding Classical Non-Classical	4-120 40-120 4-40	Weak/medium
Hydrophobic effects	1-3	weak
Ion...ion (1/r)	50-200	strong
Ion...dipole ($1/r^2$)	50-200	weak
Dipole...dipole ($1/r^3$)	10-50	Weak/medium
π...πstacking	0-50	Weak/medium
Dispersion (London) ($1/r^6$) (attractive Vander Waals)	2 <5	weak
Cation...π	5-80	medium
Halogen bonding	10-200	weak

1.3.1. Ion Pairs: An ion pair, in the context of chemistry, consists of a positive ion and a negative ion temporarily bonded together by the electrostatic force of attraction between them. Ion pairs occur in concentrated solutions of electrolytes (substances that conduct electricity when dissolved or molten). Ion pair interactions can be among the strongest non-covalent interactions, with a strong dependence on solvation. For example, gas-phase calculations put simple cation and anion pairs (such as Na+ and Cl−) at >100 kcal mol−1 (Anslyn & Dougherty, 2006). However, it is well known that table salt can be easily dissolved in water, which involves the separation of these two charged ions from each other. Salt bridges are an important example of ion pair interactions in the context of proteins and related recognition **(Figure 1.2)**. Salt bridges are defined as an interaction that involves oppositely charged groups that are also hydrogen bonding to each other. In proteins, electrostatic interactions are often between a negatively charged aspartic acid or glutamic acid and a positively charged arginine, histidine, or lysine.

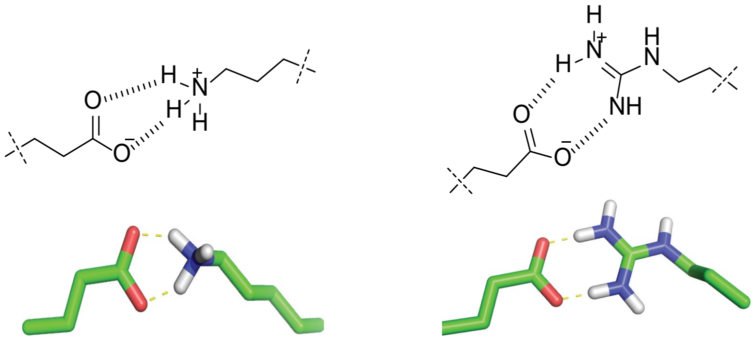

(a) **(b)**

Figure 1.2: (a) and (b) Truncated examples of salt bridge interactions that are often observed in folded proteins and protein-protein interaction interfaces

1.3.2. Ion...dipole interaction: An ion...dipole force consists of an ion and a polar molecule aligning. The positive and negative charges are next to one another, allowing maximum attraction. The solvolysis of ionic compounds in polar solvents is one of the simplest interactions. This kind of ion-dipole interaction is present in both solid-state and solution. Ion...dipole interactions are generally weak, solvent, and orientation-dependent but can be addictive. A simple example is the hydration of ions by water. Water has a dipole due to the significant difference in electronegativities between hydrogen and oxygen atoms and can strongly associate with cations.

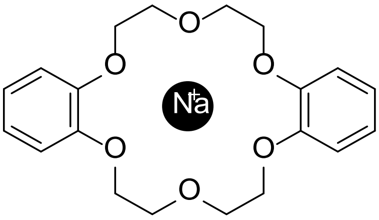

Figure 1.3: The complex between dibenzo-18-crown-6 and Cation through ion...dipole interactions

A classic supramolecular system that employs ion-dipole interactions for molecular recognition is the association complex between cations and crown ethers **(Figure 1.3)**. The same force occurs when crown ether binds with an alkali metal ion. A positive charge on the Cation attracts the oxygen lone pairs making it soluble. 18-crown-6 host-guest complexation with various inorganic cations was explored by molecular dynamics simulation (Dang, 1995).

1.3.3. Dipole...dipole interaction: Different functional groups in an organic molecule generate a dipole moment in the molecule. Usually, dipoles are associated with electronegative atoms, including oxygen, nitrogen, sulfur, and fluorine. Polarization of electrons also occurs due to the electronegativity difference between two directly attached atoms and the polarisable electron. Each molecule acts as a dipole, and alignment of one dipole with another due to attractive interactions takes place **(Figure 1.4)**. It helps in a definite arrangement of the molecules in the solid-state and a solution where these interactions are relatively weak.

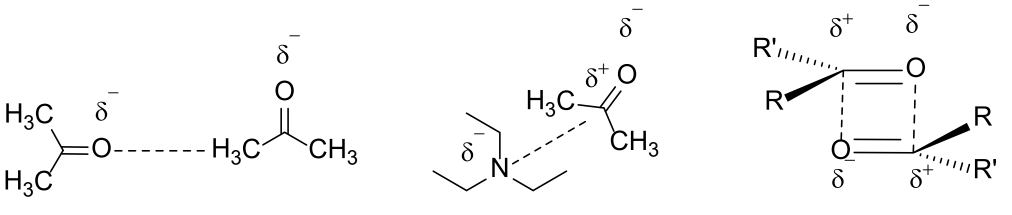

(a) **(b)** **(c)**

Figure 1.4: Dipole...dipole interactions between molecules

The crystal structure of alloxan (pyrimidine-2,4,5,6-tetraone) **(Figure 1.5)**, as an example, features an array of short, almost orthogonal intermolecular C=O...C=O contacts with distances of about 2.8Å and C=O...C angles in the range between

155°and 163°. It is rather than form the hydrogen bonded structure one would expect, given the existence of two acidic NH units per molecule (Bolton, 1964).

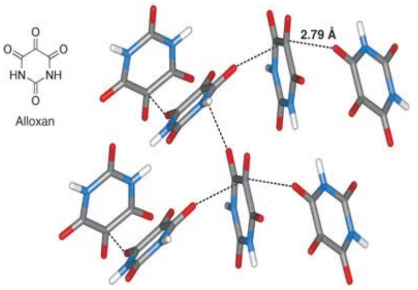

Figure 1.5: Crystal structure of alloxan (CSD-code: ALOXAN) featuring orthogonal intermolecular C=O...C=O contacts

1.3.4. Hydrogen bonding: Hydrogen bonding is a special type of dipole…dipole attraction between molecules, not a covalent bond to a hydrogen atom. It results from the attractive force between a hydrogen atom covalently bonded to a very electronegative atom such as N, O, or F atoms. Hydrogen bonds can exist between atoms in different molecules or parts of the same molecule. The association of water molecules is one of the simplest examples of hydrogen bonds **(Figure 1.6)**. Typically they are depicted as D–H...A. In its most basic form, the hydrogen bond is a simple Coulombic attraction between the H atom, bearing a partial positive charge, and an electron-rich atom bearing a partial negative charge. Due to this, A can be a myriad of different species, including both atoms bearing lone pairs and π-systems. Most commonly, simple hydrogen bonds are depicted as being between N/O–H...N/O, and indeed, this nitrogen- and oxygen-centric hydrogen bond is most common in the chemical literature and Nature.

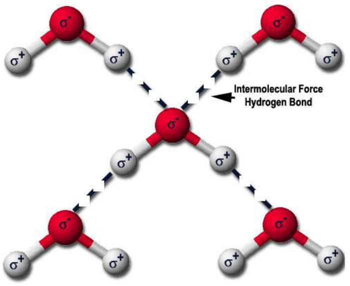

Figure 1.6: Intermolecular hydrogen bonds between water molecules

Hydrogen bonding is relatively strong and highly directional. Some hydrogen bonding groups also show strong directional preferences at the angle of the acceptor atom (Steiner, 2002). The sharing of electrons in overlapping orbitals on the donor and acceptor species must also be a significant part of the attractive force of hydrogen bonding. Hydrogen bonding is extremely important in the arrangement of molecules in solid, liquid, and gaseous states and solutions and the synthesis of biomolecules and laboratory synthesis. The role of hydrogen bonding in the double helix structure of DNA is a well-known example **(Figure 1.7)**, where the DNA double helix is held together by a hydrogen-bond network dictated by the matching of each nucleotide base.

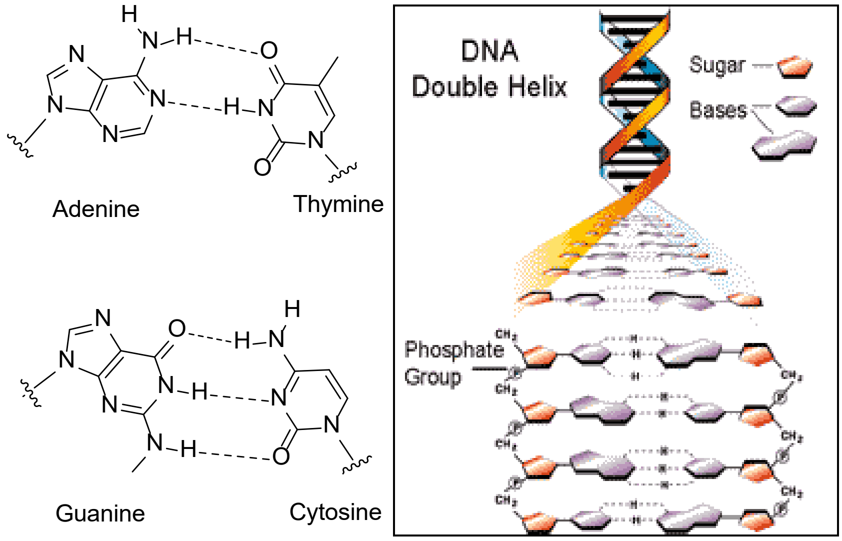

Figure 1.7: Double helix structure of DNA showing Adenine…Thymine and Guanine…Cytosine hydrogen bond network

Hydrogen bonds are important in recognizing biological molecules of all types and the folding of biological molecules into three-dimensionally ordered structures. One prototypical set of hydrogen bonds in biology is the protein secondary structural element, such as the α-helix. These helices are defined by a helical structure of amino acids wherein backbone amides make repeating intramolecular N-H...O=C hydrogen bonds that stabilize the helical backbone conformation while also ensuring that amino acid side chains are projected from the helix in an ordered manner **(Figure 1.8 (a))** (A.-S. Yang & Honig, 1995a; Scholtz & Baldwin, 1992). Another analogous example is the β-sheet secondary structure, in which intramolecular hydrogen bonds between adjacent backbone segments stabilize antiparallel or parallel arrangements of strands within a protein **(Figure 1.8 (b))**.

Again, the secondary structural element is essentially defined by a conserved hydrogen-bonding pattern but retains extensive structural and functional diversity by the projection of varying side chains from the core scaffold; for exemplary work on β-sheets and hydrogen bonding (Deechongkit et al., 2004; A.-S. Yang & Honig, 1995b). These secondary structural elements are built up using hydrogen bonds that obey the requirements of allowed hydrogen-bond angles and distances.

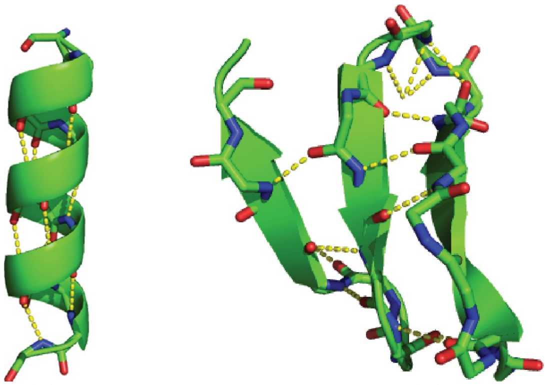

(a) **(b)**

Figure 1.8: Lysozyme (PDB CODE: 1L03) is a protein that contains both (a) and (b) α-helices and β-sheets

Another type of hydrogen bonding interaction that exists between arenes, alkenes, or alkynes with the aliphatic C-H group, known as the **CH...π interaction**, which is the weakest hydrogen bond, plays a significant tool in chemistry and biology (Aliev et al., 2014; Tsuzuki & Fujii, 2008). This non-covalent interaction has been shown to contribute to crystal packing, stereoselectivity, protein stability, and conformation. The CH...π bond also plays a vital role in the molecular recognition of numerous ligand-binding proteins, carbohydrate-binding proteins that affect binding affinity and conformation (Mazik, 2012; Muraki, 2002). The interaction has already been used in drug design to significantly increase a tyrosine phosphatase inhibitor (Nishio et al., 2014; Pace et al., 2012).

For participation in a C-H...π interaction, the hydrogen atom does not need to be positioned directly above the π-plane; it may be slightly offset outside the ring. Earlier reports confirm that heterocyclic compounds are engaged in favorable interactions with one another and with aromatic hydrocarbon units (Tewari & Dubey, 2009). Tsuzuki and co-workers found that for the methane-benzene complex **(Figure**

1.9), the preferred configuration has the methane directly above the center of the benzene with hydrogen pointed at the center of the ring and three directed away.

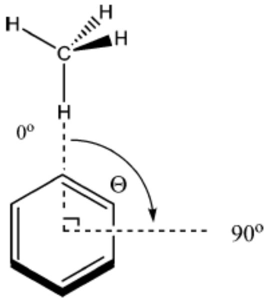

Figure 1.9: Methane-Benzene Complex shows the C-H...π interaction

1.3.5. Cation...π interaction: The Cation...π interaction is the attractive non-covalent force between a cation and π-electrons (Dougherty, 2013; Ma & Dougherty, 1997; Mahadevi & Sastry, 2013). One of the simplest examples of Cation...π attractive interaction is between a benzene ring's face and a sodium cation **(Figure 1.10)**. The range of attractive binding energies determined for Cation...π interactions depends on numerous factors and can be as high as 40 kcal mol−1 and as low as <1 kcal mol−1. Systems that explore the Cation...π interaction have been well studied experimentally (Kearney et al., 1993; Stauffer et al., 1990). Cation...π interactions play an important role in Nature, particularly in protein structure, molecular recognition, and enzyme catalysis. The effect has also been observed and used in synthetic systems (Ma & Dougherty, 1997).

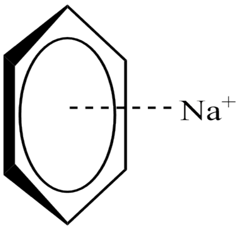

Figure 1.10: Cation...π interaction between the face of benzene and Na^+

The nicotinic acetylcholine receptor is another example of the Cation…π interaction. Its endogenous ligand, acetylcholine (a positively charged molecule), binds via a cation…π interaction to the quaternary ammonium. The Cation...π interaction between a protonated buffer molecule (N-2 hydroxyethylpiperazine-N'-2-ethanesulfonicacid) and Trp in the acetylcholine (ACh) binding site protein **(Figure**

1.11) shows the importance of weak interactions in the function of biomolecules (Brejc et al., 2001).

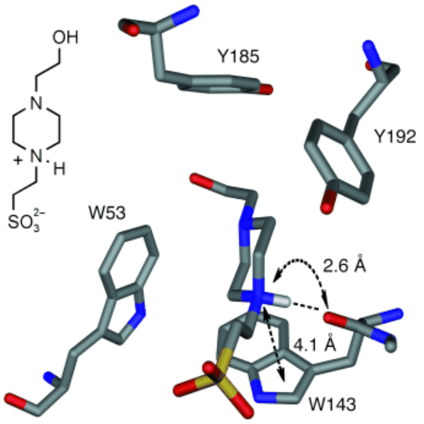

Figure 1.11: Cation...π interactions between a HEPES molecule and Trp143 in the ACh binding site of an ACh-binding protein (PDB CODE: 1I9B)

1.3.6. π...π Stacking interaction: π...π stacking interactions play a weaker but important role in determining the assembly of biological molecules between aromatic rings. The presence of planarity and delocalized electron cloud in aromatic compounds take part in π...π stacking interaction (Sinnokrot et al., 2002). These interactions are caused by intermolecular overlapping of p-orbitals in π-conjugated systems, so they become more robust as the number of π-electrons increases. Because of the many delocalized π electrons, it acts powerfully on flat polycyclic aromatic hydrocarbons such as anthracene, triphenylene, and coronene. This interaction, which is a bit stronger than other van der Waal's interactions, plays an important role in various parts of supramolecular chemistry. Theoretical and experimental studies have provided an understanding of the nature of π...π interactions (Churchill et al., 2010; Hunter & Sanders, 1990). Computational studies have revealed that aromatic rings tend to adopt orientations generally based on edge-to-face and face-to-face geometries (Jennings et al., 2001). There are three geometries of the benzene dimer that have been modeled, parallel-displaced, T-shaped edge-to-face, and eclipsed face-to-face **(Figures 1.12)** at high levels of theory and found to be attractive with a preference for the parallel displaced and T-shaped geometries. Edge-to-face packing appears to have been first noted in single crystals of benzene (Cox et al., 1958). Pioneering work by Burley and Petsko (Burley &

Petsko, 1986; Salonen et al., 2011) established the importance of edge-to-face interactions between aromatic rings in determining the tertiary and quaternary crystalline structure of peptides and proteins.

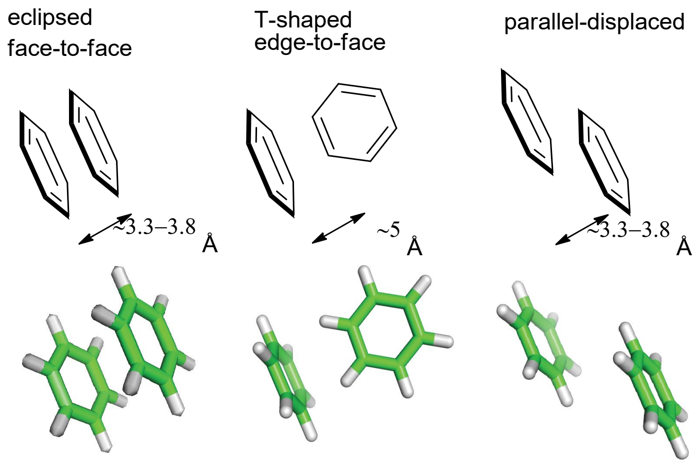

Figure 1.12: π...π stacking interaction between benzene dimer

Recent X-ray crystallographic and NMR evidence indicates that relatively weak intramolecular edge-to-face (Jennings et al., 2001) **(figure 1.13 (a), (b), and (c))** interactions between aromatic rings can affect or determine the conformation of organic molecules in the solid-state and solution (Muraki, 2002; Ringer et al., 2006)(Muraki, 2002; Ringer et al., 2006).

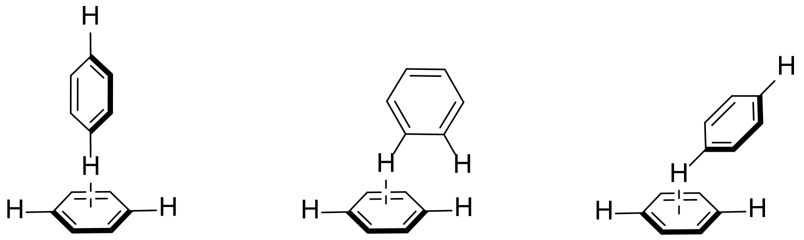

(a) **(b)** **(c)**

Figure 1.13: Edge to face aromatic interaction

Aromatic π…π stacking interactions are abundant between heterocyclic π systems. An excellent example of heterocyclic π...π stacking is provided by the ternary complex of the anticancer drug 1843U89 and dUMP formed at the active site of thymidylate synthase (Weichsel & Montfort, 1995) **(Figure 1.14)**. Moreover, supramolecular architectures, such as helices, have been constructed through stacking interactions (Ringer et al., 2006). The structure of DNA also adopts the π...π stacking interactions and the subsequent aromatic bases, which stabilize the double helix (Mak, 2016) **(Figure 1.15)**.

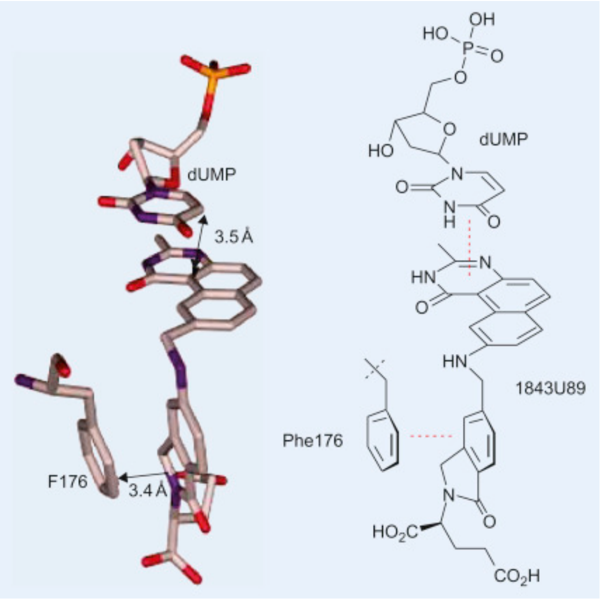

Figure 1.14: Heterocyclic π...π stacking between dUMP and the anticancer drug 1843U89 bound at the active site of thymidylate synthase (PDB CODE: 1TSD)

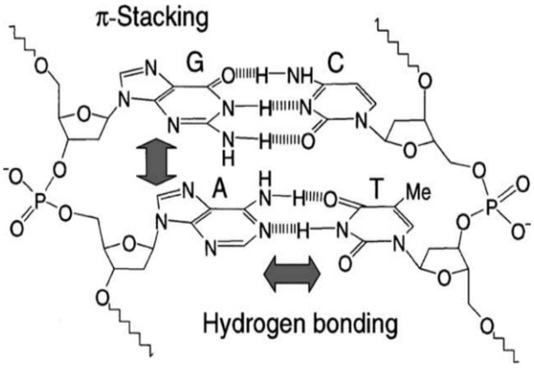

Figure 1.15: π...π stacking interaction between aromatic rings of DNA

1.3.7. Halogen Bonding (XB): Halogen bonds have been known for decades but only recently come under intense investigation for the ability to drive recognition in solution and solid-state. Recently IUPAC defined a halogen bond R–X...Y–Z as "occur[ing] when there is evidence of a net attractive interaction between an electrophilic region on a halogen atom X belonging to a molecule or a molecular fragment R–X (where R can be another atom, including X, or a group of atoms) and a nucleophilic region of a molecule, or molecular fragment, Y–Z” (Desiraju et al., 2013). Other similar definitions are available in the literature (Beale et al., 2013;

Legon, 2010). From this definition, there is a strong analogy between halogen bonding and hydrogen bonding. Per this analogy, the R–X portion is termed the donor and Y–Z as the acceptor. Again, the attractive force between these groups is primarily electrostatic in Nature and arises due to a very electron-poor region of some organic halides called the "σ-hole." A σ-hole is large and significantly positive when a halogen atom is covalently bound to a very electron-withdrawing organic group – the removal of electrons via the sigma C–X bonding orbital produces a strongly electropositive region in the area that would be occupied by the σ* orbital (180° from the σbond itself) (Figure 16) (Beale et al., 2013; Politzer et al., 2007; Sarwar et al., 2010). Halogen bonding has already received much attention from materials scientists and solid-state chemists who have used halogen bonds to engineer various solid and liquid crystalline structures (Caronna et al., 2004; Metrangolo et al., 2008; Nguyen et al., 2004).

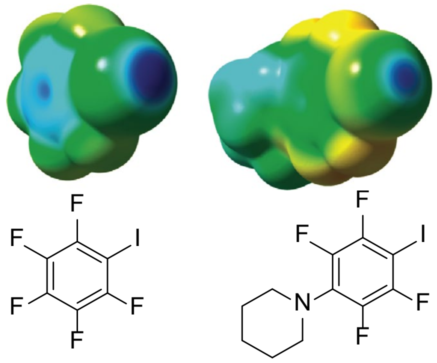

Figure 1.16: Electrostatic potential surfaces of fluorobenzene derivatives

Although organic halides are rare in biomolecules, they are very common in drugs. Diederich and coworkers have conducted a thorough study of halogen bonding in a human Cathepsin L protein-ligand complex (Hardegger et al., 2011). The chemical ligands provide the halogen groups under investigation (Figure 17). A systematic study of this interaction, using inhibitory studies and X-ray crystallography, showed that halogen bonding strength was proportional to the size of the halogen (Cl<Br<I). These interactions were not existent with fluorine (which is not polarisable enough to form a σ-hole). They found a strong dependence on distance and bonding angle, measuring an energetic gain of 2.6 kcal mol−1. Boeckler and coworkers recently used a halogen-biased fragment library to screen for

stabilizing ligands of p53-Y220C mutants (Wilcken et al., 2012). Using a classical fragment-based approach based on a central halogen bond, they could locate a compound that can stabilize p53-Y220C mutants with micromolar affinities. Halogen bonding has received intense interest for its ability to structure complex systems in solution and solid states. Building from these preliminary, simplistic studies, halogen bonding can help guide supramolecular systems that recognize anions and aid in drug design by providing an additional non-covalent interaction between protein and ligand.

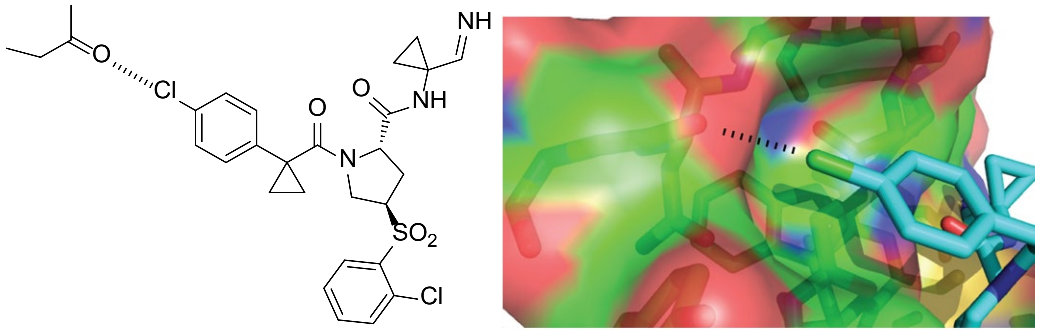

(a) **(b)**

Figure 1.17: (a) and (b) A protein-ligand halogen bond (PDB CODE: 2XU1)

1.4. Molecular recognition

Molecular recognition is a biological phenomenon that refers to the specific interaction at the molecular level in living and chemical systems between two or more molecules through non-covalent bonding such as hydrogen bonding, metal coordination, hydrophobic forces (Breiten et al., 2013), van der Waals forces, π...π interactions, halogen bonding, or resonant interaction (Cosic, 1994) effects. In addition to these direct interactions, solvents can play a dominant indirect role in driving molecular recognition in solution (Baron et al., 2010). The origin of the process lies in the intrinsic capacity of biomolecules to distinguish between other compounds and interact with them based on their molecular complementarities. The essential elements of life occur largely by specific interactions between biological molecules. Thus it is a central topic in biochemistry because it determines whether a compound has beneficial clinical properties.

The concept of molecular recognition was introduced in 1894 by a Dutch chemist Hermann Emil Fischer who proposed the "lock and key" model to explain the high specificity of an enzyme for its substrate. According to this model, the enzyme and the substrate possess a complementary geometric shape that allows them to ideally join one with the other (Fischer, 1894). For the enzyme-substrate interaction, molecular recognition is also the core of other important biological activities such as antigen-antibody binding and DNA duplication and transcription. The modern view of molecular recognition called "induced fit" considers that the interacting molecules are flexible and can change their 3-D structures during recognition (Bosshard, 2001). This induced fit mechanism has been observed experimentally for many protein-ligand interactions(Q. Wang et al., 2013). At a molecular level, the following factors contribute to the complementary between two molecules: i) Shape of the two molecular surfaces, ii) Hydrogen bonding between the molecules, iii) Ion...ion and ion...dipole interactions, iv) Dispersion forces (van der Waals attraction), v) Hydrophobic interaction arising from the unfavorable solvation of nonpolar groups by water.

The different postulated recognition mechanisms allow molecular recognition to classify into two subdivisions; static and dynamic molecular recognition. The static recognition is based on the lock and key model and is established between a single guest molecule and a single host binding site. The dynamic molecular recognition, which reflects the induced fit model, implies the presence of at least two guest molecules. The interaction of the first guest with the first binding site determines conformational change, which promotes the binding of the second guest to the second binding site (Shinkai et al., 2001).

1.5. Supramolecular chemistry

Supramolecular chemistry is an area of chemistry that deals with chemical systems composed of a discrete number of molecules. The molecular recognition phenomenon was extended to the chemical nature of a molecule synthesized in the laboratory, where an organic molecule can hold another molecule or ion with the help of non-covalent interaction. Understanding these binding processes through weak interactive forces made it possible to design and synthesize molecules that can bind other molecules. The term "Supramolecular chemistry" was coined by JeanMarie Lehn in 1969 because molecular chemistry was limited to the chemistry of molecules with stronger bonding forces like covalent bonds. The chemistry beyond the molecules that result from the association of two or more chemical species by intermolecular forces was introduced as "Supramolecular chemistry". Supramolecular chemistry is a part of molecular recognition with particular interactions arising out of the geometry of the single-molecule and non-covalent forces working on binding with another molecule (Schneider, 2009). Such particular interactions have led to some useful supramolecular functions. The designing of new biologically active compounds and therapeutics is carried out considering all these factors, which earlier was based on random preparation and testing of new molecules. Important concepts advanced by supramolecular chemistry include molecular self-assembly, molecular folding, molecular recognition, host-guest chemistry, mechanically-interlocked molecular architectures, and dynamic covalent chemistry (Oshovsky et al., 2007).

1.6. Drug designing

Drug design, also referred to as rational drug design or rational design, is an inventive process of finding new medications based on the knowledge of the biological target (Liljefors et al., 2002). Generally, the biological target is usually a protein or a nucleic acid which is the key molecule involved in a particular metabolic or signaling pathway associated with a specific disease condition. They are not necessarily disease-causing but must be disease-modifying (Dixon & Stockwell, 2009). Tollenaere pointed out that "drug design" to some extent, is a misnomer and uses "ligand design" for a more accurate term, i.e., design of a molecule that will bind tightly to its target (Tollenaere, 1996). The prime aim of rational drug design is to generate an extremely active and selective compound that should bind only to the active site of the malfunctioning enzyme. Moreover, it further prevents the defective enzyme's function and simultaneously inhibits the progression of the disease. The drug is most commonly a small organic molecule that activates or inhibits the function of a biomolecule such as a protein, resulting in a therapeutic benefit to the patient. In the most basic sense, drug design involves the design of small molecules that are complementary in shape and charge to the biomolecular target with which they interact and, therefore, will bind to it. Drug design frequently but not necessarily relies on computer modeling techniques (Merz et al., 2010). This type of modeling is often referred to as computer-aided drug design.

Drug discovery, development, and its introduction into the market are intense and lengthy processes requiring considerable money and labor (DiMasi et al., 2010). The average time to introduce a single drug is around 10-14 years and costs more than a billion dollars (Daina et al., 2017). So it is described as a linear and consecutive process that starts with target and lead discovery, followed by lead optimization and preclinical trials. Nowadays, Computer-Aided Drug Design (CADD) approach plays a vital role in increasing the efficiency of the drug discovery and development process. This method efficiently identifies potential lead compounds from huge compound libraries and helps to develop possible drugs for a wide range of diseases (Baig et al., 2016; Scotti & Scotti, 2015). It has been observed that the CADD can reduce the cost of drug discovery and development by up to 50% (Xiang et al., 2012). In CADD, bioinformatics tools were used to identify the target and analyze their structure for possible binding/active sites, generate candidate molecules, check for their drug-likeness, dock with the target, rank them according to their binding affinities, and further optimize the molecules to improve binding characteristics.

There are two major design approaches through CADD (Merz et al., 2010). They are i) Ligand-based drug design, ii) Structure-based drug design.

1.6.1. Ligand-based drug design: Ligand-based drug design (or **indirect drug design**) relies on knowledge of other molecules that bind to the biological target of interest. These other molecules may be used to derive a pharmacophore model that defines the minimum necessary structural characteristics a molecule must possess to bind to the target (Güner, 2000). In other words, a model of the biological target may be built based on the knowledge of what binds to it, and this model, in turn, may be used to design new molecular entities that interact with the target. Alternatively, a quantitative structure-activity relationship (QSAR), in which a correlation between the calculated properties of molecules and their experimentally determined biological activity, may be derived. These QSAR relationships, in turn, may be used to predict the activity of new analogs (Merz et al., 2010).

1.6.2. Structure-based drug design: Structure-based drug design (or **direct drug design**) relies on knowledge of the 3-D structure of the biological target obtained through methods such as X-ray crystallography or NMR spectroscopy (Jhoti & Leach, 2007). Suppose an experimental structure of a target is not available. In that case, it may be possible to create a homology model of the target based on the experimental structure of a related protein. Using the structure of the biological target, candidate drugs that are predicted to bind with high affinity and selectivity to the target may be designed using interactive graphics and the intuition of a medicinal chemist. Alternatively, various automated computational procedures may suggest new drug candidates (Mauser & Guba, 2008).

Structure-based drug design can be divided roughly into three main categories (Klebe, 2000). The first method is the identification of new ligands for a given receptor by searching large databases of 3-D structures of small molecules to find those fitting the receptor's binding pocket using fast approximate docking programs. This method is known as virtual screening. A second category is the de novo design of new ligands. In this method, ligand molecules are built up within the constraints of the binding pocket by assembling small pieces in a stepwise manner. These pieces can be either individual atoms or molecular fragments. The key advantage of such a method is that novel structures not contained in any database can be suggested (R. Wang et al., 2000). A third method is the optimization of known ligands by evaluating proposed analogs within the binding cavity (Klebe, 2000).

1.7. Method to study non-covalent interactions

X-ray crystallography and Hirschfeld surface analysis tools were to study non-covalent interactions. In a biological system, we have molecular docking simulations to study the interactions of the ligand with the respective target molecule.

1.7.1. X-Ray Crystallography

X-ray Crystallography is a scientific method used to determine the arrangement of atoms of a crystalline solid in 3-D space. This technique uses the interatomic spacing of most crystalline solids as a diffraction gradient for x-ray light, which has wavelengths on the order of 1 angstrom (10^{-8} cm). From the angles and intensities of these diffracted beams, a crystallographer can produce a three-dimensional picture of the density of electrons within the crystal. From this electron density, the mean positions of the atoms in the crystal can be determined, their chemical bonds, their disorder, and various other information.

Crystal symmetry was first investigated experimentally by Nicolas Steno (1669), who showed that the angles between the faces are the same in every exemplar of a particular type of crystal (Steno et al., 1669) and by René Just Haüy (René Just Haüy, 1784) who discovered that every face of a crystal could be described by simple stacking patterns of blocks of the same shape and size. Hence, William Hallowes Miller, in 1839, was able to give each face a unique label of three small integers, the Miller indices, which are still used today for identifying crystal faces. Haüy's study led to the correct idea that crystals are a regular three-dimensional array (a Bravais lattice) of atoms and molecules; a single unit cell is repeated indefinitely along with three principal directions that are not necessarily perpendicular. In the 19th century, a complete catalog of the possible symmetries of a crystal was worked out by Johann Hessel (Hessel, 1830), Auguste Bravais (Bravais, 1850), and Arthur Schönflies and William Barlow (Barlow, 1883). From the available data and physical reasoning, Barlow proposed several crystal structures in the 1880s that were validated later by X-ray crystallography (Barlow, 1883). However, the available data were too scarce in the 1880s to accept his models as conclusive.

X-ray crystallography has led to a better understanding of chemical bonds and non1covalent interactions. The initial studies revealed the typical radii of atoms. They confirmed many theoretical models of chemical bonding, such as the tetrahedral bonding of carbon in the diamond structure and the octahedral bonding of metals observed in ammonium hexachloroplatinate (IV), and the resonance observed in aromatic molecules (Bragg, 1921).

X-ray crystallography is now used routinely by scientists to determine how a pharmaceutical drug interacts with its protein target and what changes might improve it (Scapin, 2006). However, intrinsic membrane proteins remain challenging to crystallize because they require detergents or other means to solubilize them in isolation, and such detergents often interfere with crystallization. Such membrane proteins are a large component of the genome and include many proteins of great physiological importance, such as ion channels and receptors (Lundstrom, 2006).

1.7.2. Hirshfeld surface analysis

The definition of a molecule in a condensed phase is an elusive goal, as many different characterizations exist. However, the extraction of molecular properties from solid-state structures, such as crystalline samples, forces a somewhat arbitrary definition onto the molecules (Stewart, 1979; Hirshfeld, 1991, 1985). Various schemes for partitioning the crystalline electron density distribution into molecular fragments can be adapted. Hirshfeld partitioning is an extension of the Hirshfeld stockholder concept (Hirshfeld, 1977), which divides the electron density into continuous atomic fragments. The concept was generalized to extract continuous molecular fragments from electron density distributions by defining a molecular weight function:

$$w(r) = \frac{\sum_{A\epsilon \mathrm{Molecule}} \rho A\,(r)}{\sum_{A\epsilon \mathrm{Crystal}} \rho A(r)} = \frac{\rho_{\mathrm{promolecule}}(r)}{\rho_{\mathrm{procrystal}}(r)}$$

$\rho A(r)$ are spherically-averaged atomic electron density functions (Clementi & Roetti, 1974) centered on the position of the atoms. The appropriate sums of the electron density of the atoms belonging to molecule and crystal are $\rho_{\mathrm{promolecule}}(r)$ and $\rho_{\mathrm{procrystal}}(r)$, respectively. Molecular properties can be obtained by integration over the weighted electron density, and using this scheme molecular properties have been reported earlier (Moss & Coppens, 1980). A new scheme, molecular Hirshfeld surfaces, is constructed by partitioning space into regions in which the electron density of a sum of spherical atoms of a molecule (the promolecule) dominates the corresponding sum of the crystal (the procrystal) (McKinnon et al., 2004; Spackman & Byrom, 1997).

$$\mathrm{w(r)} = \frac{\rho_{\mathrm{promolecule}}(\mathrm{r})}{\rho_{\mathrm{procrystal}}(\mathrm{r})} = \frac{1}{2}$$

As the molecule is defined by the Hirshfeld partitioning w(r) = ½, this scheme provides a molecular surface, e.g., the Hirshfeld surface. The cut-off value guarantees the maximum proximity of neighboring molecular volumes and minimizes space between adjacent molecules. A larger value of the weight function would result in an overlap of molecules and a smaller value in gaps between adjacent molecules.

The central element is the derivation of the Hirshfeld surface described above, an immediately interpretable visualization of a molecule within its environment. In general, the analyses of small molecule crystal structures are dominated by the description of hydrogen bonding patterns if such are present. However, a crystal structure is determined by a combination of many forces, and hence all of the intermolecular interactions of a structure should be taken into account. Visualization and exploration of intermolecular close contacts of a structure are invaluable, which can be achieved using the Hirshfeld surface. An extensive range of properties can be visualized on the Hirshfeld surface, including the distance of atoms external, de, and internal, di, to the surface. The distance information of the surface can be condensed into a two-dimensional histogram of de and di, a unique identifier for molecules in a crystal structure called a fingerprint plot. This directly accessible 2-D map provides the entire distribution of close contacts (Spackman & McKinnon, 2002). Instead of plotting de and di on the Hirshfeld surface, a normalized contact distance is defined, where r VDW is the van der Waals radius of the appropriate internal or external atom of the surface:

$$d_{\mathrm{norm}} = \frac{d_i - r_i^{vdw}}{r_i^{vdw}} + \frac{d_e - r_e^{vdw}}{r_e^{vdw}}$$

The Hirshfeld surfaces are implemented in the user-friendly program CrystalExplorer (Wolff et al., 2012), which by the use of Crystallographic Information Files (cifs) alone can generate these (Bruno et al., 2002). The program is the basis for rigorous quantitative analysis of molecular properties for comparison with bulk measurement and convenient comparison of molecules in different molecular environments. Analysis of intermolecular interactions using the Hirshfeld surface-based tools represents a major advance in enabling supramolecular chemists and crystal engineers to gain insight into crystal packing behavior. Notably, the technique reveals which atoms are genuinely interacting with each other, as opposed to those that happen to be placed next to each other by coincidence, which is not always possible in other commonly used approaches.

1.8. Scope of the study

The proposed work is to synthesize a new polycyclic aromatic system. It will also contain the development of compounds through new synthetic approach following the principles of green chemistry. Supramolecular architechtures of the synthesized compounds will be studied to understand the importance of non-covalent interactions within the intermolecular as well as intramolecular system. Molecular recognition properties will aslo be conducted by *in-silico* tools to understand nature's interaction of the synthesized molecules with the biological target molecule. The studies may provide a new platform in drug discovery and crystal engineering with some preliminary results.

1.9. Objectives of the work

The objectives of the present research are:

i) The primary objective of the present work is to develop a simple method for the synthesis hetero-polycyclic aromatic system.

ii) In the second objective, the molecular recognition properties of the synthesized molecules will be studied to understand non-covalent interaction within the supramolecular structure of the polycyclic aromatic system.

iii) In the third objective, we will explore the molecular recognition properties of the synthesized compounds with biological target proteins. So our third objective is to study ligand-receptor interactions by in silico analysis.

CHAPTER 2

SYNTHESIS AND STUDY OF HETERO-POLYCYCLIC AROMATIC SYSTEMS

2.1. Introduction

Heterocyclic compounds are cyclic organic compounds that contain at least one heteroatom. The most common heteroatoms are nitrogen, oxygen, and sulfur but heterocyclic rings containing other heteroatoms are also widely known. A carbocyclic compound is a cyclic organic compound containing all carbon atoms in a ring formation. Heterocyclic compounds are considered one of the vital classes of organic compounds, which are used in many biological fields due to their activity in multiple illnesses. Biological molecules such as DNA and RNA, chlorophyll, hemoglobin, vitamins, and many more contain the central skeleton's heterocyclic ring. According to statistics, more than 85% of all biologically-active chemical entities contain a heterocycle (Jampilek, 2019). Medicinal chemistry has become an important field in chemistry because of the joining between chemistry and medical life issues by trying to study the common diseases and how we should solve them. This branch of modern chemistry began when isolating and purifying active materials from plant and animal tissues and taking them from a microorganism. Their fermentation products have become the focus of attention of researchers around the world. Medical chemistry is based on the classical branches of chemistry, especially organic chemistry and biology, and some areas of physics. According to the literature review, heterocyclic compounds are important in medicinal chemistry. Heterocycles are a key structure in medicinal chemistry. Also, they are frequently found in a large percentage of biomolecules such as enzymes, vitamins, natural products, and biologically active compounds, including antifungal, anti-inflammatory, antibacterial, antioxidant, anticonvulsant, antiallergic, enzyme inhibitors, herbicidal activity, anti-HIV, antidiabetic, anticancer activity, insecticidal agents (Jampilek, 2019).

Pyran is an oxygen-containing heterocyclic moiety that exhibits an array of pharmacological properties. Pyran is also one of the important structural subunits found widely in natural products, *e.g.*, coumarins, benzopyrans, sugars, flavonoids, xanthones, *etc.* . Many natural products and drug molecules have the 4H-pyran core (Hatakeyama et al., 1988; Moshtaghi Zonouz et al., 2014; Samir, 2016). These have spurred considerable awareness of the synthetic arena based on their structure, reactivity, synthesis and biological properties (Kumar et al., 2017). Their intriguing pharmacological profile includes antimicrobial (Sangani et al., 2012), antitumor (D.-C. Wang et al., 2014) antibacterial activities (El-Saghier et al., 2007). Their importance is also seen in cosmetics and biodegradable agrochemicals (Adbel Aziz Hafez et al., 1987). Moreover, 4H-pyrans have been used as calcium channel blockers due to their similarity with 1,4-dihydropyridines (Kumar et al., 2017). The synthesis of these molecules has long been an important task in organic chemistry due to their desirable properties. The pyran ring structural moiety is also an important starting scaffold to synthesize other heterocylic aromatic compounds, since they can easily undergo ring opening and rearrangement process (Lalhruaizela et al., 2021).

Benzochromene derivatives are an important class of fused heterocycles, containing pyran ring within its core heterocyclic system and are the important building blocks widely found in many natural products. Such compounds have been identified to have significant pharmaceutical properties such as anti-inflammatory (Chakraborty et al., 2021), antiviral (Decosterd et al., 1993), antifungal (Mirjalili et al., 2017), antimicrobial (Fouda et al., 2020), cholinesterase inhibitors and potent antioxidant, non-Hepatotoxic agents for Alzheimer's disease (Dgachi et al., 2016) and antiproliferative activities (Mata et al., 2017). The search for new heterocyclic compounds and novel synthesis methods is significant in contemporary organic chemistry. Benzochromenes play a unique role in drug discovery programs. Furthermore, benzochromene derivatives are an important class of heterocyclic compounds that show a wide range of potent antitumor activity (Okasha et al., 2017). Other remarkable examples of benzchromenes have emerged in the treatment of human diseases. For instance, 2-amino-4-(3-nitrophenyl)-4H-benzo[h]chromene-3-carbonitrile (LY290181) is a potent antiproliferative agent for a variety of cell types and inhibition of mitosis and microtubules (Panda et al., 1997; Wood et al., 1997).

While 2-amino-5-oxo-4-phenyl-4,5-dihydropyrano[3,2-c]chromene-3-carbonitrile serves as a blood anticoagulant analogue of warfarin (Wiener et al., 1962). Finally, 4-substituted-2-(N-succinimido)-4H-benzo[h]- chromene-3-carbonitriles also display anti-rheumatic activity (Smith et al., 1995) **(Figure 2.1)**.

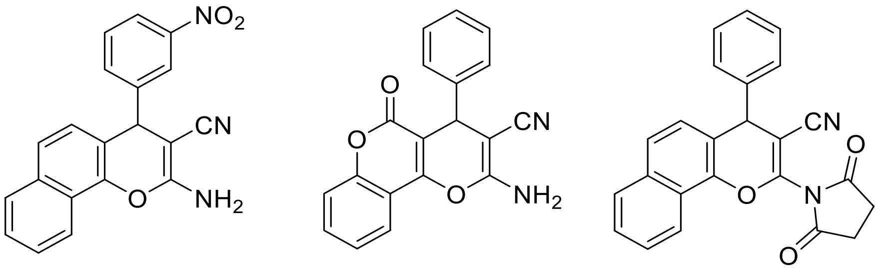

LY290181
antiproliferative agent

Blood anticoagulant

Antirheumatic

Figure 2.1: Potential Benzochromene derivatives

2-Pyridone moiety is present in many natural and synthetic bioactive molecules. 2- Pyridones and their analogues have attracted considerable interest recently because of their antiproliferative, antiviral and anti-inflammatory properties (Bhupathy et al., 1995; Choi et al., 1995). Also, cyanopyridines are important intermediates for synthesizing nicotinamide, nicotinic acid, and isonicotinic acid. 3-Cyano-2-pyridones are one of the biodynamic cyanopyridine derivatives. The significance of 3-cyano-2-pyridone frameworks in the past few decades is undeniable.

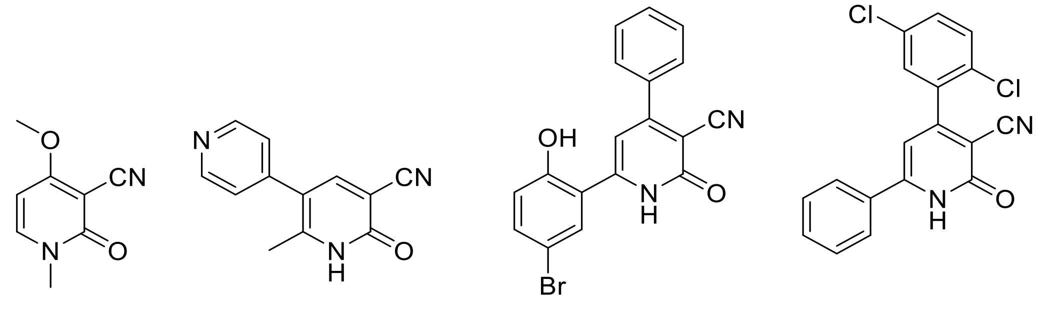

Ricicine

Milrinone

PIM-1 Kinase inhibitor

Survivin inhibitor

Figure 2.2: Biologically active 3-cyano-2-pyridone derivatives

For example, they are the structural basis of the alkaloid ricinine, the first known alkaloid containing a cyano group. Milrinone is a 3-cyano-2-pyridone derivative used to treat congestive heart failure (Baim et al., 1986; Fleming et al., 2010). Another 3-cyano-2-pyridone derivatives has shown anticancer activity which might be due to the interference of the molecule with PDE-3 (Murata et al., 2002), PIM-1 kinase (Cheney et al., 2007) and survivin protein (Aqui& Vonderheide, 2008) **(Figure 2.2)**.

2.2. Present work

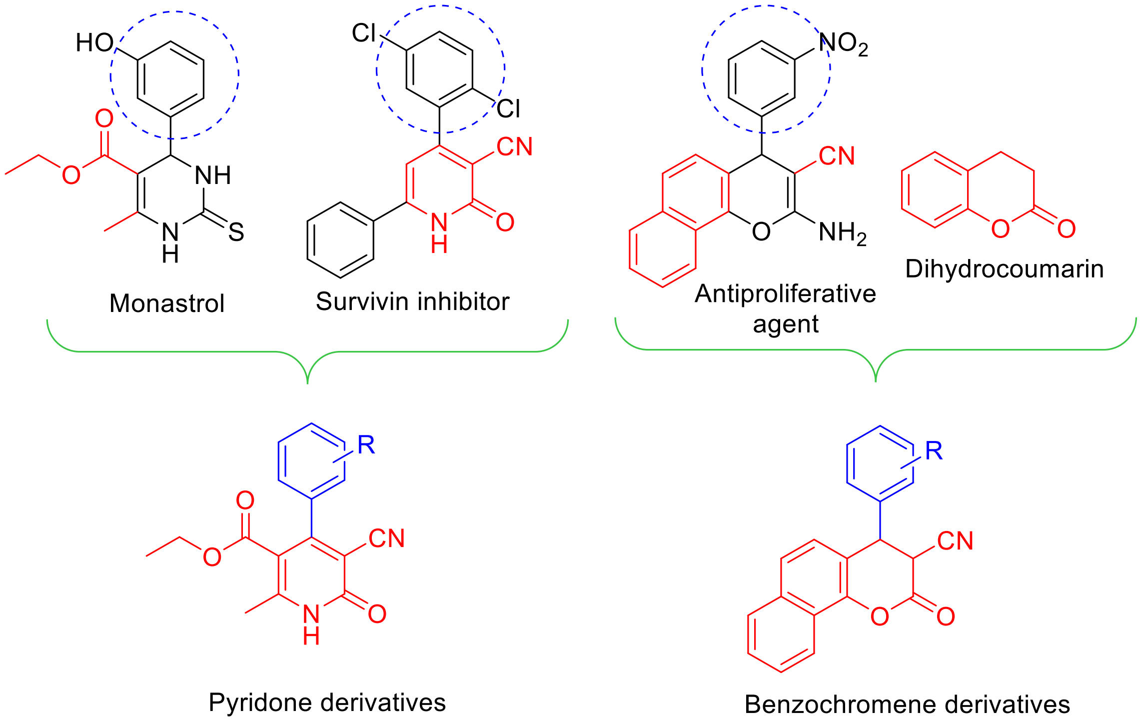

Figure 2.3: Pyridone and benzochromene derivatives: A compound of interest containing a hybrid of two structural moieties

The present work in chapter 2 deals with a simple and convenient method for synthesizing hetero-polycyclic 3,4-dihydropyridones and 2-pyridones from 4H-pyran derivatives. It also include the conversion of traditional 2-amino-4H-benzo[h]chromene derivatives into 2-oxo-3,4-dihydro-2H-benzo[h]chromene derivatives. The compounds synthesized in this chapter incorporate a hybrid of two biologically active structural moieties as shown in **Figure 2.3.** All the products obtained were collected and recrystallized in an appropriate solvent. Those compounds which provide a suitable crystal were studied by SC-XRD and Hirshfeld surface analysis to interpret the non-covalent interactions involved in the supramolecular structures.

2.3. Synthesis of hetero-polycyclic 3,4-dihydro-2-pyridone and 2-pyridone derivatives

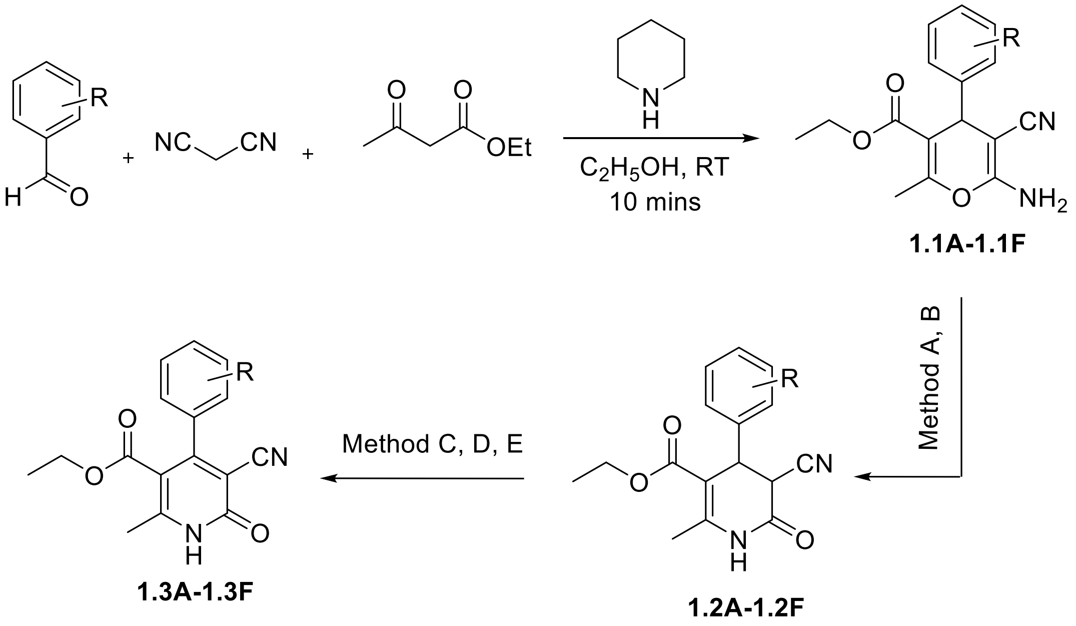

R= 3-NO_2, 3-OCH_3, 4-Cl, 3-Cl, 4-CH_3, 4-OCH_3

Entry= A, B, C, D, E, F

Method A: I_2, Reflux, Method B: Formic acid, Reflux, Method C: DDQ, Microwave, Method D: DDQ, Thermal, Method E: 1/2O_2, RT

Scheme 1

In scheme 1, 4H-pyran derivatives **(1.1A-1.1F)** were synthesized and then further subjected to a catalyst to undergo ring rearrangement of the 4H-pyrans to form 3,4-dihydro-2-pyridones **(1.2A-1.2F)**. The obtained 3,4-dihydro-2-pyridones **(1.2A-1.2F)** were again oxidized to give 2-pyridone derivatives **(1.3A-1.3F)**.

2.4. Experimental

^{1}H NMR (300 MHz) and ^{13}C NMR (75 MHz) spectra were recorded on JEOL AL300 FTNMR spectrometer using TMS as an internal reference, and chemical shift values are expressed in δ, ppm units. Melting points of all the compounds were recorded on the electrically heated instrument and are uncorrected. All the reactions were monitored by thin-layer chromatography (TLC) on pre-coated aluminum sheets of Merck using an appropriate solvent system, and chromatograms were visualized under UV light. The compound was purified by flash column chromatography using silica gel size 230-400 mesh.

2.4.1. General procedure for the synthesis of 4H-pyrans (1.1A-1.1F)

To a 100 mL RB, ethanol (40 mL) was taken, and aldehyde (10 mmol) and malononitrile (10 mmol) were added and stirred. To the mixture, ethyl acetoacetate (10 mmol) was added, followed by piperidine (0.2 mL, 2 mmol). The mixture was then stirred at room temperature in an open atmosphere for 10 mins. The precipitate was filtered in a sintered glass funnel and washed with ice-cold methanol to obtain a pure product of 4H-pyran derivatives **(1.1A-1.1F)**.

2.4.1.1. Ethyl 6-amino-5-cyano-2-methyl-4-(3-nitrophenyl)-4H-pyran-3-carboxylate (1.1A): Pale yellow solid, yield: 89%, m.p. 188°C; **^{1}H NMR (300 MHz, $CDCl_3$):** δppm 1.10 – 1.15 (3H, t, CH_3, J = 7.2 Hz); 2.41 (3H, s, CH_3); 4.02 – 4.09 (2H, q, CH_2, J = 7.2 Hz); 4.58 (1H, s, CH); 4.65 (2H, s, NH_2); 7.46 – 7.52 (1H, t, Ar-H, J = 7.8 Hz); 7.57 – 7.60 (1H, d, Ar-H, J = 7.8 Hz); 8.06 (1H, s, Ar-H); 8.09 – 8.12(1H, d, Ar-H, J = 7.8 Hz).

2.4.1.2. Ethyl 6-amino-5-cyano-4-(3-methoxyphenyl)-2-methyl-4H-pyran-3-carboxylate (1.1B): White solid, yield: 87%, m.p. 173-175°C; **^{1}H NMR (300 MHz, $CDCl_3$):** δppm 1.08 – 1.13 (3H, t, CH_3, J = 7.2Hz); 2.35 (3H, t, CH_3); 3.78 (3H, t, CH_3); 4.00 – 4.07 (2H, m, CH2); 4.4 (1H,s, CH); 4.59 (2H, s, NH_2); 6.73 (1H, s, Ar-H); 6.76 – 6.80 (2H, m, Ar-H); 7.17 – 7.26 (1H, m ,Ar-H).

2.4.1.3. Ethyl 6-amino-4-(4-chlorophenyl)-5-cyano-2-methyl-4H-pyran-3-carboxylate (1.1C): White solid, yield: 93%, m.p. 195°C; **^{1}H NMR (300 MHz, $CDCl_3$):** δppm 1.09 – 1.13 (3H, t, CH_3, J = 7.2 Hz); 2.37 (3H, s, CH_3); 4.01 – 4.08 (2H, q, CH_2, J = 7.2 Hz); 4.42 (1H, s, CH); 4.58 (2H, s, NH_2); 7.12 – 7.15 (2H, d, Ar-H, J = 8.4 Hz); 7.25 – 7.28 (2H, d, Ar-H, 8.4 Hz).

2.4.1.4. Ethyl 6-amino-4-(3-chlorophenyl)-5-cyano-2-methyl-4H-pyran-3-carboxylate (1.1D): White solid, yield: 93%, m.p. 207°C; **^{1}H NMR (300 MHz, $CDCl_3$):** δppm 1.09 – 1.14 (3H. t, CH_3, J = 7.2 Hz); 2.37 (3H, s, CH_3); 4.00 – 4.10 (2H, q, 7.2 Hz); 4.42 (1H, s, CH); 4.63 (2H, s, NH_2); 7.08 – 7.27 (4H, m, Ar-H).

2.4.1.5. Ethyl 6-amino-5-cyano-2-methyl-4-(p-tolyl)-4H-pyran-3-carboxylate (1.1E): White solid, yield: 85%, m.p. 201°C; **^{1}H NMR (300 MHz, $CDCl_3$):** δppm 1.08 – 1.13 (3H, t, CH_3, *J* = 7.2 Hz); 2.30 (3H, s, CH_3); 2.35 (3H, s, CH_3); 4.00 – 4.07 (2H, q, CH_2, *J* = 7.2 Hz); 4.40 (1H, s, CH); 4.54 (2H, s, NH_2); 7.10 (4H, s, Ar-H).

2.4.1.6. Ethyl 6-amino-5-cyano-4-(4-methoxyphenyl)-2-methyl-4H-pyran-3-carboxylate (1.1F): White solid, yield: 83%, m.p. 187-191°C; **^{1}H NMR (300 MHz, $CDCl_3$):** δppm 1.09 – 1.14 (3H, t, CH_3, *J* = 7.2 Hz); 2.35 (3H, s, CH_3); 3.78 (3H, s, CH_3); 4.00 – 4.07 (2H, q, CH_2, *J* = 7.2 Hz); 4.40 (1H, s, CH); 4.45 (2H, s, NH_2); 6.82 – 6.84 (2H, d, Ar-H, *J* = 8.7); 7.10 – 7.13 (2H, d, Ar-H, *J* = 8.7).

2.4.2. General procedure for the synthesis of 3,4-dihydro-2-pyridones (1.2A-1.2F)

Method A: To a 2-neck 150 mL RB, each of the synthesized 4H-pyrans **(1.1A-1.1F)** (6.7 mmol) was dissolved in ethanol (50 mL) at 80°C. Iodine (10 mol %) was added to the reaction vessel and refluxed at 85°C for 2-4 hours, monitored by TLC (EtOAc/hexane 3:7). After the reaction, the mixture was concentrated under reduced pressure and then treated with sodium thiosulphate solution (5 mol%) to remove unreacted iodine. The organic layer was back-extracted with ethyl acetate (twice), usual workup and purification over silica gel column using Hexane: EtOAc (70:30) afforded 3,4-dihydro-2-pyridones **(1.2A-1.2F)**.

Method B: The 4H-pyrans **(1.1A-1.1F)** (10 mmol) and excess formic acid (20 mL) was heated under reflux at 115°C for 3-4 hours. After the reaction was completed, the formic acid was reduced under a rotary evaporator, and the precipitate obtained was recrystallized in ethanol to obtain pure products **(1.2A-1.2F)**.

Additional technique: The organic layer (ethyl acetate) obtained from the workup process in method A was concentrated in a rotary evaporator to prevent precipitate formation. The solution was collected in a conical flask, sealed with rubber septa, and then placed inside a freezer (-20 to -25°C) for 2 hours. The precipitate of 3,4-dihydro-2-pyridones **(1.2A-1.2F)** was formed (confirmed by TLC) and collected by filtration. The filtrate, which contains the remaining 3,4-dihydro-2-pyridones **(1.2A-1.2F)**, was purified using column chromatography. This method facilitates the pure precipitate of 3,4-dihydro-2-pyridones **(1.2A-1.2F)** and reduces the working time and the amount of solvent required for purification.

2.4.2.1. Ethyl 5-cyano-2-methyl-4-(3-nitrophenyl)-6-oxo-1,4,5,6-tetrahydropyridine-3-carboxylate (1.2A): White solid, yield: 96%, m.p. 193-15°C; **^{1}H NMR (300 MHz, $CDCl_3$):** δppm 1.19 – 1.24 (3H, t, CH_3, J =7.2 Hz); 2.50 (3H, s, CH_3); 4.10 – 4.18 (2H, q, CH_2, J = 6.9 Hz); 4.19 – 4.22 (1H, d, CH, J = 6.9 Hz); 4.61 – 4.63 (1H, d, CH, J = 6.9 Hz); 7.52 – 7.59 (2H, m, Ar-H); 7.63 – 7.66 (1H, m, Ar-H); 8.08 (1H. s, Ar-H); 8.19 (1H, s, NH); **^{13}C NMR (75 MHz, $CDCl_3$):** δppm 14.2, 18.1, 23.3, 37.8, 61.7, 104.3, 116.8, 124.8, 126.8, 128.3, 128.6, 134.0, 148.0, 148.9, 167.2, 171.8. **MS (m/z):** 333.40 (M+1).

2.4.2.2. Ethyl 5-cyano-4-(3-methoxyphenyl)-2-methyl-6-oxo-1,4,5,6-tetrahydropyridine-3-carboxylate (1.2B): White solid, yield: 97%, m.p. 185-188°C; **^{1}H NMR (300 MHz, $CDCl_3$):** δppm 1.19 – 1.23 (3H, t, CH_3, J = 7.2 Hz); 2.41 (3H, s, CH_3); 3.79 (3H, s, CH_3); 4.08 – 4.18 (3H, m, CH_2, CH); 4.45 – 4.48 (1H, d, CH, J = 6.9 Hz); 6.79 – 6.86 (3H, m, Ar-H); 7.23 – 7.28 (1H, m, Ar-H); 8.30 (1H, s, NH); **^{13}C NMR (75 MHz, $CDCl_3$):** δppm 14.2, 18.1, 22.0, 39.1, 56.1, 61.7, 104.3, 112.2, 116.8, 120.9, 126.2, 126.9, 128.7, 148.9, 155.8, 167.2, 171.8. **MS (m/z):** 315.36 (M+1).

2.4.2.3. Ethyl 4-(4-chlorophenyl)-5-cyano-2-methyl-6-oxo-1,4,5,6-tetrahydropyridine-3-carboxylate (1.2C): White solid, yield: 93%, m.p. 198-200°C; **^{1}H NMR (300 MHz, $CDCl_3$):** δppm 1.18 – 1.23 (3H, t, CH_3, J = 7.2 Hz); 2.44 (3H, s, CH_3); 4.08 – 4.17 (3H, m, CH_2, CH); 4.46 – 4.49 (1H, d, CH, J = 7.2 Hz); 7.18 – 7.20 (2H, d, Ar-H, J = 8.4 Hz); 7.30- 7.33 (2H, d, Ar-H, J = 8.4 Hz); 8.42 (1H,s, -NH,); **^{13}C NMR (75 MHz, $CDCl_3$):** δppm 14.2, 18.1, 27.9, 38.8, 61.7, 104.3, 116.8, 128.7, 129.1, 131.5, 138.7, 148.9, 167.2, 171.8. **MS (m/z):** 319.75 (M+1).

2.4.2.4. Ethyl 4-(3-chlorophenyl)-5-cyano-2-methyl-6-oxo-1,4,5,6-tetrahydropyridine-3-carboxylate (1.2D): White solid, yield: 96%, m.p. 193-

195°C; **^{1}H NMR (300 MHz, $CDCl_3$):** δppm 1.19 – 1.23 (3H, t, CH_3, *J* = 7.2 Hz); 2.43 (3H, s, CH_3); 4.10 – 4.19 (3H, m, CH2, CH); 4.45 – 4.47 (1H, d, CH, *J* = 7.2 Hz); 7.16 – 7.20 (2H, m, Ar-H); 7.26 – 7.30 (2H, m, Ar-H); 8.57 (1H, s, NH); **^{13}C NMR (75 MHz, $CDCl_3$):** δppm 14.2, 18.1, 27.4, 38.8, 61.7, 104.3, 116.8, 125.8, 126.0, 127.5, 130.0, 134.2, 142.0, 148.9, 167.2, 171.8. **MS (m/z):** 319.75 (M+1).

2.4.2.5. Ethyl 5-cyano-2-methyl-6-oxo-4-(p-tolyl)-1,4,5,6-tetrahydropyridine-3-carboxylate (1.2E): White solid, yield: 92%, m.p. 187-189°C; **^{1}H NMR (300 MHz, $CDCl_3$):** δppm 1.19 – 1.24 (3H, t, CH_3, *J* = 7.2 Hz); 2.33 (3H,s, CH_3); 2.43 (3H, s, CH_3); 4.04 – 4.20 (3H, m, CH_2, CH); 4.46 – 4.48 (1H, d, CH, *J* = 6.9 Hz); 7.14 (4H, s, Ar-H); 8.39 (1H, s, NH); **^{13}C NMR (75 MHz, $CDCl_3$):** δppm 14.2, 18.1, 21.1, 27.2, 38.8, 61.7, 103.3, 116.8, 127.5, 127.5, 129.2, 129.2, 135.6, 137.7, 148.4, 167.2, 171.8. **MS (m/z):** 319.75 (M+1).

2.4.2.6. Ethyl 5-cyano-4-(4-methoxyphenyl)-2-methyl-6-oxo-1,4,5,6-tetrahydropyridine-3-carboxylate (1.2F): White solid, yield: 94%, m.p. 173-175°C; **^{1}H NMR (300 MHz, $CDCl_3$):** δppm 1.19 – 1.23 (3H, t, CH_3, *J* = 7.2 Hz); 2.44 (3H, s, CH_3); 3.79 (3H, s, CH_3); 4.07 – 4.18 (3H, m, CH_2, CH); 4.45 – 4.47 (1H, d, CH, *J* = 6.9 Hz); 6.84 – 6.87 (2H, d, Ar-H, *J* = 8.7 Hz); 7.15 – 7.18 (2H, d, Ar-H, *J* = 8.7 Hz); 7.62 (1H, s, NH); **^{13}C NMR (75 MHz, $CDCl_3$):** δppm 14.2, 18.1, 22.0, 39.1, 56.1, 61.7, 104.3, 112.2, 116.8, 120.9, 126.2, 126.9, 128.7, 148.9, 155.8, 167.2, 171.8. **MS (m/z):** 315.36 (M+1).

2.4.3. General procedure for the synthesis of 2-pyridones (1.3A-1.3F)

Method C (microwave-assisted reaction): To each of the solution of 3,4-dihydro-2-pyridone **(1.2A-1.2F)** (3.52 mmol) in ethanol (15 ml), DDQ (3.52 mmol) was added and was irradiated in microwave oven for 2 minutes. The reaction was monitored by TLC (EtOAc/hexane 5:5). After the reaction was completed, ethanol (10 ml) was added to the reaction vessel, which allowed to form pure crystals of 2-pyridone **(1.3A-1.3F)** (which was further collected). The remaining solvents that contain 2-pyridone **(1.3A-1.3F)** were collected and purified over silica gel by column chromatography Hexane: EtOAc (50:50).

Method D (thermal assisted reaction): To a solution of 3,4-dihydro-2-pyridone **(1.2A-1.2F)**(3.52 mmol) in ethanol (15 ml), DDQ (3.52 mmol) was added and was heated on a heating mantle at 100° C for 8-10 minutes. The reaction was monitored by TLC (EtOAc/hexane 5:5). After the reaction was completed, ethanol (10 ml) was added to the reaction vessel, which allowed to form pure crystals of 2-pyridone **(1.3A-1.3F)** (which was further collected). The remaining solvents that contain 2-pyridone **(1.3A-1.3F)** were collected and purified over silica gel by column chromatography Hexane: EtOAc (50:50).

Method E (auto-oxidation process): The powdered form of 3,4-dihydro-2-pyridones **(1.2A-1.2F)** was placed on a conical flask and exposed to an open atmosphere at the room temperature. It allows the compound to interact with atmospheric oxygen to undergo self-oxidation from 2-pyridone compounds **(1.3A-1.3F)**. The formation of 2-pyridone **(1.3A-1.3F)** was monitored by TLC (EtOAc/hexane 5:5). Compounds were separated using column chromatography Hexane: EtOAc (50:50). However, this synthesis method was not favored over methods A and B since it was time-consuming, and the yield of the product 2-pyridone **(1.3A-1.3F)** was poor.

Additional technique: For both methods C and D, after the reaction of 3,4-dihydro-2-pyridone **(1.2A-1.2F)** with DDQ, ethanol was reduced in a rotary evaporator, and methanol (30 ml) was added and was heated to dissolve the product 2-pyridone **(1.3A-1.3F)**. The solution was cooled at -20 to -25°C stand to form a pure precipitate of 2-pyridone **(1.3A-1.3F)**. Filtered and washed with methanol. The filtrate was collected and concentrated. The process was repeated until the concentration of 2-pyridone **(1.3A-1.3F)** in the filtrate was minimized (confirmed by TLC). The final filtration was then subjected to purification by column chromatography.

2.4.3.1. Ethyl 5-cyano-2-methyl-4-(3-nitrophenyl)-6-oxo-1,6-dihydropyridine-3-carboxylate (1.3A): White solid, yield: 89%, m.p. 201-203°C; **^{1}H NMR (300 MHz, $CDCl_3$):** δppm 0.90 – 0.94 (3H, t, CH_3, J = 7.2 Hz); 2.68 (3H, s, CH_3); 3.96 – 4.03 (2H, q, CH_2, J = 7.2 Hz); 7.72 – 2.75 (2H, d, Ar-H, J = 7.5 Hz); 8.23 (1H, s, Ar-H);

8.36 – 8.39 (1H, m, Ar-H); 13.61 (1H, s, NH); **^{13}C NMR (75 MHz, CDCl$_3$):** δppm 14.2, 19.6, 61.8, 109.0, 115.3, 115.8, 123.8, 127.3, 128.8, 130.0, 134.7, 145.0, 151.4, 161.5, 165.0, 169.4. **MS (m/z):** 328.09 (M+1).

2.4.3.2. Ethyl 5-cyano-4-(3-methoxyphenyl)-2-methyl-6-oxo-1,6-dihydropyridine-3-carboxylate (1.3B): White solid, yield: 90%, m.p. 193-195°C; **^{1}H NMR (300 MHz, CDCl$_3$):** δppm 0.84 – 0.89 (3H, t, CH_3, *J* = 7.2 Hz); 2.62 (3H, s, CH_3); 3.83 (3H, s, CH_3); 3.92 – 3.99 (2H, q, CH_2, *J* = 7.2 Hz); 6.89 – 7.03 (2H, m, Ar-H); 7.27 (1H, s, Ar-H); 7.36 – 7.41 (1H, t, Ar-H, *J* = 8.1 Hz); 13.67 (1H, s, NH); **^{13}C NMR (75 MHz, CDCl$_3$):** δppm 14.2, 19.6, 55.7, 61.9, 108.9, 114.3, 11.43, 115.2, 115.8, 124.8, 130.1, 130.1, 151.3, 159.8, 161.6, 165.0, 169.7. **MS (m/z):** 312.09 (M+1).

2.4.3.3. Ethyl 4-(4-chlorophenyl)-5-cyano-2-methyl-6-oxo-1,6-dihydropyridine-3-carboxylate (1.3C): White solid, yield: 94%, m.p. 207-209°C; **^{1}H NMR (300 MHz, CDCl$_3$):** δppm 0.88 – 0.93 (3H, t, CH_3, *J* = 7.2 Hz); 2.63 (3H, s, CH_3-); 3.93 - 4.0 (2H, q, CH_3, *J* = 7.2 Hz); 7.30 – 7.32 (2H, d, Ar-H, *J* = 8.4 Hz); 7.46 – 7.49 (2H, d, Ar-H, *J* = 8.4 Hz); 13.63 (1H, s, -NH); **^{13}C NMR (75 MHz, CDCl$_3$):** δppm 14.04, 18.91, 40.91, 41.02, 60.90, 107.35, 113.87, 129.18, 129.18, 129.21, 129.21, 134.36, 134.44, 146.06, 162.89, 165.16. **MS (m/z):** 316.09 (M+1).

2.4.3.4. Ethyl 4-(3-chlorophenyl)-5-cyano-2-methyl-6-oxo-1,6-dihydropyridine-3-carboxylate (1.3D): White solid, yield: 86%, m.p. 201-203°C; **^{1}H NMR (300 MHz, CDCl$_3$):** δppm 0.87 – 0.92 (3H, t, CH_3, *J* = 7.2 Hz); 2.64 (3H, s, CH_3); 3.94 – 4.01 (2H, q, CH_2, *J* = 7.2 Hz); 7.26 – 7.28 (1H, d, Ar-H, *J* = 5.4 Hz); 7.33 (1H, s, Ar-H), 7.40 – 7.7.49 (2H, m, Ar-H) ; 13.61 (1H, s, NH); **^{13}C NMR (75 MHz, CDCl$_3$):** δppm 14.04, 18.91, 40.91, 41.02, 60.90, 107.35, 113.87, 129.18, 129.18, 129.21, 129.21, 134.36, 134.44, 146.06, 162.89, 165.16. **MS (m/z):** 316.09 (M+1).

2.4.3.5. Ethyl 5-cyano-2-methyl-6-oxo-4-(p-tolyl)-1,6-dihydropyridine-3-carboxylate (1.3E): White solid, yield: 93%, m.p. 193-195°C; **^{1}H NMR (300 MHz, CDCl$_3$):** δppm 0.84 – 0.89 (3H, t, CH_3, *J* = 7.2 Hz); 2.41 (3H, s, CH_3); 2.60 (3H, s, CH_3); 3.91 – 3.98 (2H, q, CH_2, *J* = 7.2 Hz); 7.27 (4H, s, Ar-H); 13.65 (1H, s, NH); **^{13}C NMR (75 MHz, CDCl$_3$):** δppm 14.3, 19.6, 21.3, 61.3, 109.1, 115.3, 115.9, 128.7, 128.7, 129.5, 134.7, 136.6, 152.4, 160.7, 167.0, 169.4. **MS (m/z):** 297.12 (M+1).

2.4.3.6. Ethyl 5-cyano-4-(4-methoxyphenyl)-2-methyl-6-oxo-1,6-dihydropyridine-3-carboxylate (1.3F): White solid, yield: 95%, m.p. 187-189°C; **^{1}H NMR (300 MHz, $CDCl_3$):** δppm 0.90 – 0.94 (3H, t, CH_3, J = 7.2 Hz); 2.60 (3H, s, CH_3); 3.85 (3H, s, CH_3); 3.94 – 4.01 (2H, q, CH_2, J = 7.2 Hz); 6.97 – 7.00 (2H, d, Ar-H, J = 8.7 Hz); 7.32 – 7.35 (2H, d, Ar-H, J = 8.7 Hz); 13.58 (1H, s, NH); **^{13}C NMR (75 MHz, $CDCl_3$):** δppm 14.2, 19.6, 55.7, 61.9, 108.9, 114.3, 11.43, 115.2, 115.8, 124.8, 130.1, 130.1, 151.3, 159.8, 161.6, 165.0, 169.7. **MS (m/z):** 312.09 (M+1).

2.5. Results and discussions

In scheme 1, a series of polycyclic 3,4-dihydropyridone derivatives **(1.2A-1.2F)** were synthesized from 4H-pyrans. The conversion of 4H-pyrans into 3,4-dihydropyridone by using iodine and formic acid as a catalyst was reported for the first time. Both methods, A and B, gave a high yield of product. However, method B was more favored since the catalyst could be easily recovered using a rotary evaporator. From those polycyclic 3,4-dihydropyridone derivatives, four compounds **(1.2A, 1.2C, 1.2E, and 1.1F)** gave a suitable crystal for the analysis. Also, from the synthesized 2-pyridone derivatives **(1.3A-1.3F)**, five compounds **(1.3A, 1.3C, 1.3D, 1.3E, and 1.3F)** gave a suitable crystal for the analysis. The crystal obtained in scheme 1 was studied by single-crystal X-ray diffraction (SC-XRD) and Hirshfeld surface analysis.

2.5.1. X-ray crystallographic studies and Hirshfeld surface analysis of compounds 1.2A, 1.2C, 1.2E, 1.2F, 1.3A, 1.3C, 1.3D, 1.3E and 1.3F

2.5.1.1. Crystal analysis of compound 1.2A

The compound **1.2A** was recrystallized in methanol at room temperature by slow evaporation of the solvent. The chiral asymmetric compound **1.2A** was analyzed using SC-XRD **(Figure 2.4)**. The compound crystallized with cell lengths **a** = 7.20280(18)Å, **b** = 8.5465(3)Å, **c** = 14.0887(4)Å, i.e., **a ≠ b ≠ c** and cell angles $\boldsymbol{\alpha}$ **=**

102.125(3)°, $\boldsymbol{\beta}$ = 93.523(2)°, $\boldsymbol{\gamma}$ = 108.714(3)°, i.e., $\boldsymbol{\alpha \neq \beta \neq \gamma \neq 90}$**°** which indicate that the compound is exhibiting a triclinic crystal system, with space group P-1 that contains two molecules per unit cell.

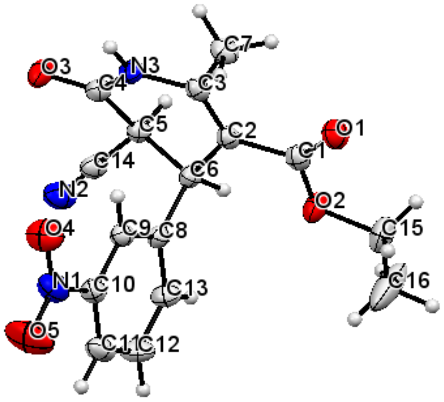

Figure 2.4: ORTEP diagram of compound **1.2A**

In the crystal analysis of compound **1.2A**, the 3,4-dihydro-2-pyridone ring is non-planar and adopts a puckered ring of slightly twisted half chair conformation. It is due to the sp^3 hybridization of C5 and C6. The benzenoid ring is almost perpendicular to the 3,4-dihydro-2-pyridone ring, where the dihedral angle between the plane of the two rings is 89.99°. Both rings are arranged in the AB pattern and the crystal packing orthogonal pattern. The crystallographic information is summarized in **Table 2.1**.

Table 2.1: Crystal data on compounds **1.2A, 1.2C,** and **1.2E**

Compound	**1.2A**	**1.2C**	**1.2E**
Identification code	2170439	2035460	2170453
Empirical formula	$C_{16}H_{15}N_3O_5$	$C_{16}H_{15}ClN_2O_3$	$C_{17}H_{18}N_2O_3$
Formula weight	329.31	318.75	298.33
Temperature(K)	293(2)	293(2)	296(2)
Crystal system	Triclinic	Triclinic	monoclinic
Space group	P-1	P-1	P21/c
a(Å)	7.20280(18)	9.48809(19)	15.713(5)
b(Å)	8.5465(3)	12.9444(3)	11.590(3)
c(Å)	14.0887(4)	14.9410(3)	8.823(3)
α(°)	102.125(3)	104.0971(19)	90
β(°)	93.523(2)	106.3634(18)	95.309(6)
γ(°)	108.714(3)	105.5962(18)	90
Volume(Å^3)	795.29(4)	1591.42(6)	1599.9(8)
Z	2	4	4
ρ (g/cm^3)	1.375	1.330	1.239
μ(mm^{-1})	0.104	0.253	0.700
F(000)	344.0	664.0	632.0
Crystal size(mm^3)	0.22 × 0.2 × 0.18	0.17 × 0.16 × 0.14	0.24 × 0.2 × 0.18

Radiation	MoKα (λ = 0.71073)	MoKα (λ = 0.71073)	CuKα (λ = 1.54178)
2Θ range for data collection(°)	6.346 to 54.76	6.562 to 54.894	9.496 to 67.046
Index ranges	-9 ≤ h ≤ 8, -10 ≤ k ≤ 9, -17 ≤ l ≤ 17	-11 ≤ h ≤ 11, -16 ≤ k ≤ 16, -17 ≤ l ≤ 19	-9 ≤ h ≤ 11, -8 ≤ k ≤ 8, -6 ≤ l ≤ 6
Reflections collected	8972	20721	2360
Independent reflections	3279	6757	610
Data/restraints/parameters	3279/0/219	6757/0/401	610/0/203
Goodness-of-fit on F^2	1.063	1.091	1.111
Final R indexes [I>=2σ (I)]	R_1 = 0.0519, wR_2 = 0.1356	R_1 = 0.0493, wR_2 = 0.1235	R1 = 0.0303, wR2 = 0.0798
Final R indexes [all data]	R_1 = 0.0651, wR_2 = 0.1472	R_1 = 0.0716, wR_2 = 0.1373	R1 = 0.0314, wR2 = 0.0807
Largest diff. peak/hole/e $Å^{-3}$	0.26/-0.23	0.23/-0.40	0.09/-0.09

The supramolecular framework of compound 1.2A: The molecular packing of compound **1.2A** display a strong non-covalent N-H…O bond, which assists the self-assembly of the molecule in forming supramolecular structures. This N-H…O intermolecular interaction arises between the hydrogen of the amine group with the carbonyl oxygen (O3) (in short, within the amide group) within the 3,4-dihydro-2-pyridone ring at a bond distance of 2.000Å. It leads to the formation of an unsymmetrical dimer giving $R_2^2(8)$ graph set notation **(Figure 2.5 (b))**. The oxygen (O4) of the nitro group acts as a bifurcated acceptor. It forms C-H…O bonds with the hydrogen from the 3,4-dihydro-2-pyridone ring and hydrogen from the ester moiety at a distance of 2.718Å and 2.688Å, respectively. These two C-H…O bonds, along with one C-H…O bond between the carbonyl oxygen (O1) and the other hydrogen from the 3,4-dihydro-2-pyridone ring altogether, forms a new graph set of $R_3^2(10)$ **(Figure 2.5 (b))**. C-H…N interaction which forms between the nitrile nitrogen (N2) and the hydrogen of the benzenoid ring at a distance of 2.639Å, also forms the $R_2^2(18)$ graph set **(Figure 2.5 (c))**. The other driving forces which facilitate the supramolecular assembly are C-H…π and lone pair…π interactions that arise from the hydrogen (H16B) and the nitrogen (N2) with the benzenoid ring at an interaction distance of 3.224Å and 3.519Å respectively **(Figure 2.5 (d) and (e))**. The different non-covalent interactions are given in **Table 2.2**.

Table 2.2: Hydrogen bonds and other interactions in compound **1.2A**

Donor-H...Acceptor	**D – H, Å**	**H...A, Å**	**D...A, Å**	**D - H...A, º**
N3-H3…O3	0.860	2.000	2.833	162.88
C5-H5…O1	0.980	2.586	3.293	129.04
C6-H6…O4	0.980	2.718	3.676	165.90

C11-H11…N2	0.930	2.639	3.315	129.99
C15-H15A…O4	0.970	2.688	3.355	126.30
C16-H16B…C10	0.960	2.772	3.695	161.51
C16-H16B…π(C8-C13)	0.960	3.224	4.199	173.46
Other contacts				
N2…π(C8-C13)	1.135	3.519	4.538	150.08
Intramolecular				
C15-H15A…O1	0.970	2.680	2.687	79.96
C15-H15B…O1	0.970	2.660	2.687	81.08
C7H7B…O1	0.960	2.360	2.878	113.30
C9-H9…N3	0.930	2.733	3.404	129.78

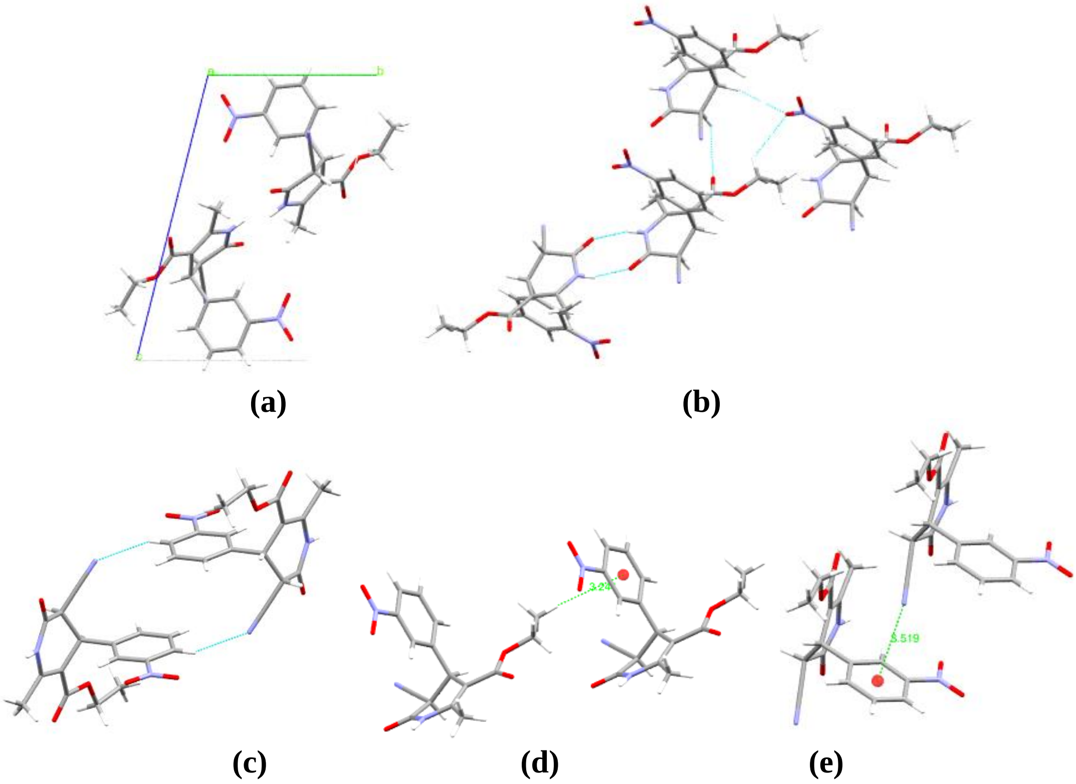

(a) (b)

(c) (d) (e)

Figure 2.5: (a) Packing diagram of **1.2A**, (b) and (c) Graph sets, (d) C-H…π interaction, and (d) Lone pair…π interaction in compound **1.2A**

Hirshfeld surface analysis of compound 1.2A: The Hirshfeld surface mapped over the d_{norm} in the range of -0.58 to 1.40Å for compound **1.2A** is displayed in **Figure 2.6 (a) and (b)**. The region of bright red spots corresponds to short contacts, which are more dominant intermolecular N-H…O interactions. A region of lighter dull red spots was due to C-H…O, C-H…N, and C-H…C interactions.

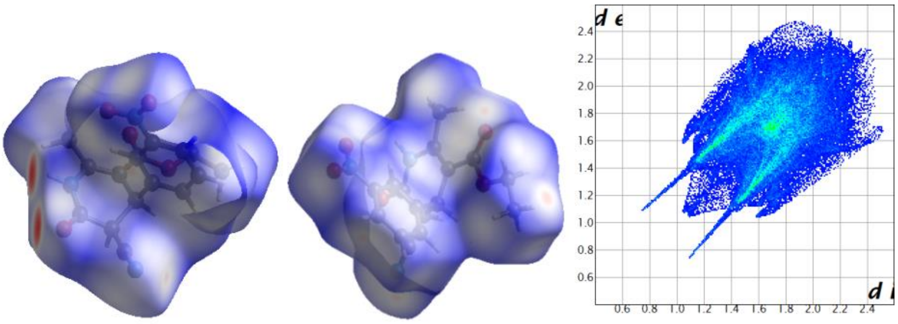

(a) **(b)** **(c)**

Figure 2.6: (a) and (b) d_{norm} both side view, (c) 2-D fingerprint plot, of compound **1.2A**

The relative percentage contributions of non-covalent interaction to the Hirshfeld surface is represented by the 2-D fingerprint plot of compound **1.2A (Figure 2.6 (c))**. Those are O…H (39.8%), H…H (27.8%), N…H (12.7%), C…H (10.9%), C…N (3.7%), C…C (1.5%), N…O (1.5%), C…O (1.3%) and O…O (0.9%). O…H/H…O has the highest contribution and appears as a pair of distinct spikes in the 2-D fingerprint plot of compound **1.2A** in the region of di + de = 1.8-2.5Å. However, N…H/H…N contacts occupy the region of brighter areas which also appears as a spike within the fingerprint plot in the region of di + de = 2.5-3.2Å. C…H/H…C and C-H…π also appear as a characteristic wing-like pattern in the region of di + de = 2.6-3.4Å. The C…N/N…C, which accounts for 3.7%, also indicates the presence of lone pair…π interactions between the nitrogen (N2) of the nitrile group and the benzenoid ring.

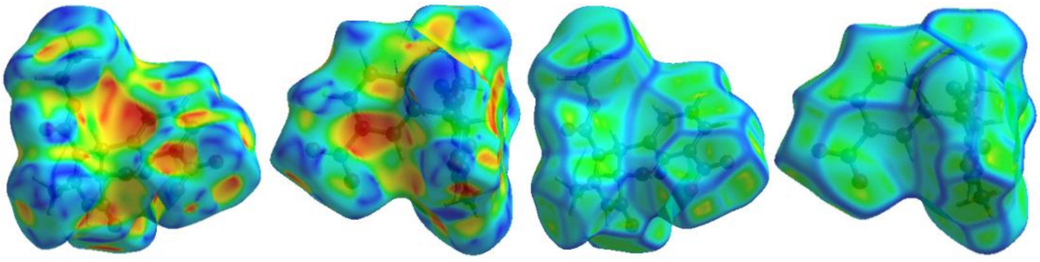

(a) **(b)** **(c)** **(d)**

Figure 2.7: (a) and (b) Shape-index, (c) and (d) Curvedness, both side views of compound **1.2A**

The Hirshfeld surface mapped over the shape-index in a range of -1 to 1Å for compound **1.2A** does not have complimentary pair of red and blue triangles around the aromatic benzenoid ring surface, which indicate the absence of π...π stacking interactions. The yellowish-red colored concave regions around the surface of the benzenoid ring in compound **1.2A** indicate the acceptor region where weak C-H...π and N…π (lone pair…π) interactions occur **(Figure 2.7 (a) and (b))**. Similarly, the Hirshfeld surface mapped over the curvedness in a range of -4 to 0.4 Å for compound **1.2A** also does not display an area of the flat green region with a yellowish spot around the benzenoid ring surface, which again indicate the absence of π…π stacking interactions between the benzenoid ring **(Figure 2.7 (c) and (d))**.

The presence of N-H…O, C-H…O, C-H…N, C-H…C and other short contacts such as C-H…π and lone pair…π (N…π) found in the supramolecular are also supported by the Hirshfeld weak non-covalent intermolecular interactions calculation within the cluster of radius 3.8Å around a single crystal fragment. Those interactions are illustrated in **Figure 2.8**.

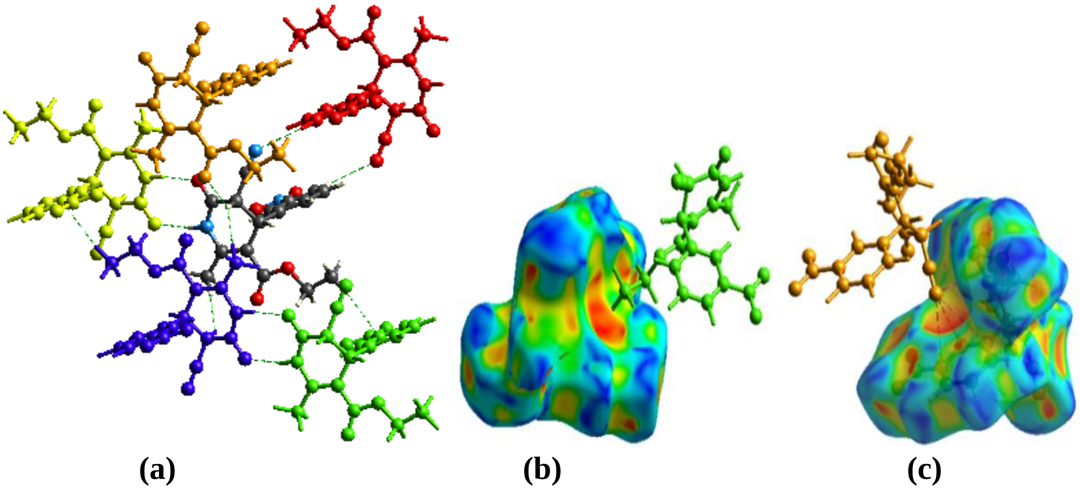

Figure 2.8: (a) Non-covalent Hydrogen bonds (b) C-H…π and (c) Lone pair…π interaction, in compound **1.2A**

2.5.1.2. Crystal analysis of compound 1.2C

The compound **1.2C** was recrystallized in methanol at room temperature by slow evaporation of the solvent. The chiral asymmetric compound **1.2C** was analyzed using SC-XRD **(Figure 2.9)**. The **1.2C** compound has two symmetry-independent molecules (Z'=2) in a 1:1 ratio in its asymmetric unit with four molecules per unit cell. The compound crystallized in a triclinic crystal system in a

P-1 space group with cell lengths **a** = 9.4919(8)Å, **b** = 12.9828(11)Å, **c** = 14.9912(13)Å and cell angles $\boldsymbol{\alpha}$ = 104.030(3)Å, $\boldsymbol{\beta}$ = 106.305(3)Å, $\boldsymbol{\gamma}$ = 105.518(3)Å.

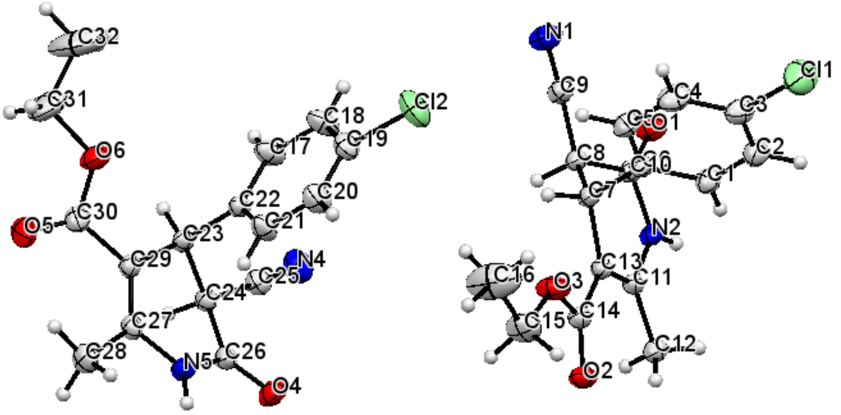

A **B**

Figure 2.9: ORTEP diagram of compound **1.2C**

The crystal structural studies indicated that the phenyl ring moiety is aromatic and planar in symmetry-independent molecules. However, the dihydro-2-pyridone ring is non-planar and adopts a puckered ring of slightly twisted half-chair conformation. The phenyl rings of both the symmetry-independent molecules are almost perpendicular to the dihydro-2-pyridone ring as the dihedral angles between their mean planes are about 89.74° and 85.96°. The crystallographic information is summarized in **Table 2.1**.

The supramolecular framework of compound 1.2C: The hydrogen-bonding network of enantiomeric molecules A & B and crystal packing is shown in the **Figure 2.10**. Enantiomers A (RS) and B (SR) are linked with H5A…O2 hydrogen bonding **(Figure 2.10 (b))**, whereas pyridone group nitrogen is involved in different types of weak interactions in both enantiomers. Both enantiomers exist as co-crystal in a 1:1 ratio in crystal packing. In addition to intermolecular C-H…O interactions, the extended structure of enantiomers A & B has intramolecular C-H…O interactions in the flexible arm of the compound. The C-H...π interaction is also exhibited in the crystal packing between the alkyl group and π-electrons of the ring of the adjacent molecule. In an extensive hydrogen-bonding network, terminal carbonyl oxygen, pyridone oxygen & nitrogen of the cyano group are involved in three weak interactions that formed 8, 12 & 8 membered $R_2^2(8)$, $R_2^2(12)$ and $R_2^2(8)$

rings due to C-H…O and C-H…N interactions respectively **(Figure 2.10 (c))**. The non-covalent hydrogen bonding interactions found for compound **1.2C** are given in **Table 2.3**.

Table 2.3: Hydrogen bonds and other interactions in compound **1.2C**

Donor-H...Acceptor	**D – H, Å**	**H...A, Å**	**D...A, Å**	**D - H...A, º**
N2-H2A…O1	0.783	2.266	3.036	168.27
C8-H8…O2	0.980	2.447	3.307	146.34
N5-H5…O2	0.803	2.245	3.044	173.59
C21-H21…N1	0.930	2.722	3.353	125.85
C32-H32C…N4	0.960	2.700	3.553	148.43
C1-H1…O4	0.930	2.481	3.294	146.11
C24-H24…O5	0.980	2.367	3.211	143.85
C16-H16A…π(C1-C6)		3.376		
C12-H12C…π(C17-C22)		2.928		
Intramolecular				
C12-H12B…O2	0.960	2.274	2.931	124.85
C28-H28B…O5	0.960	2.238	2.938	129.05

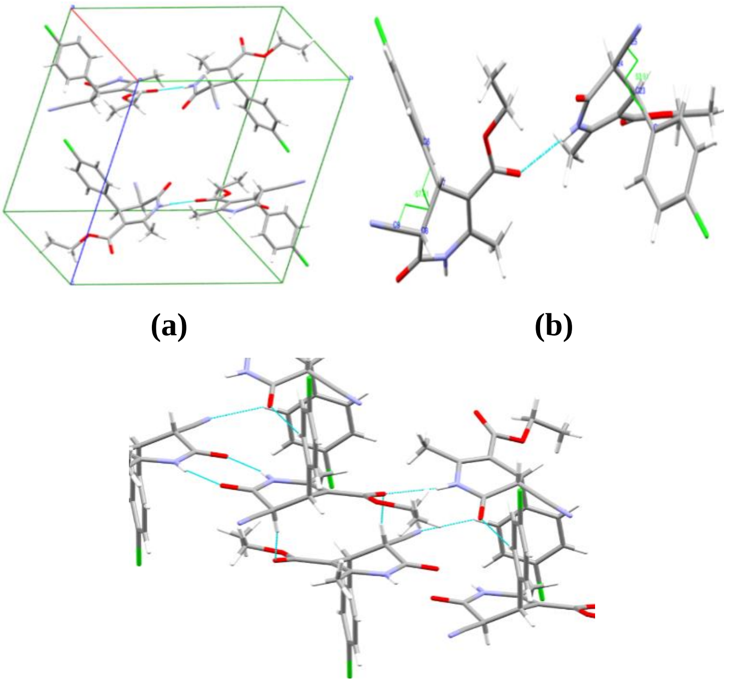

(a) (b)

(c)

Figure 2.10: (a) Packing diagram of compound **1.2C**, (b) C-H...O interaction between enantiomers A and B, (c) Graph sets in compound **1.2C**

Hirshfeld surface analysis of compound 1.2C: The Hirshfeld surface mapped over the d_{norm} in the range of -0.57 to 1.66Å for compound **1.2C** is presented in **Figure 2.11 (a) and (c)**. The bright red spots on the Hirshfeld surfaces of **1.2C**

correspond to the short interactions of N-H...O, whereas the lighter red spots indicate the C-H…O interactions. The enantiomers A & B have their own distinct Hirshfeld surface and fingerprint plot, which are not identical **(Figure 2.11 (a) and (c))**. The yellowish-red bin is absent on the fingerprint plots of both enantiomers A & B, which indicates the absence of weak π...π stacking in the crystal structure **(Figure 2.11 (b) and (d))**. The spoke-like pattern in the fingerprint plots of enantiomer A represents the C-H…O interactions in the region of di + de = 2.00–2.9Å **(Figure 2.11 (b))**. In contrast, the C-H…O interactions in enantiomer B appear in the region of di + de = 2.30-2.70Å **(Figure 2.11 (d))**. The C-H...π interactions in enantiomer A can be seen as a pair of unique blue-colored wings in the region of di + de = 3.2–3.6Å, while in enantiomer B, it is observed in the region of di + de = 3.2–3.5Å. The C-H…N pair of contacts also appear as a pair of two characteristic wings in the region of di + de = 3.2–3.4 Å and 3.1-3.4 Å in enantiomers A and B, respectively.

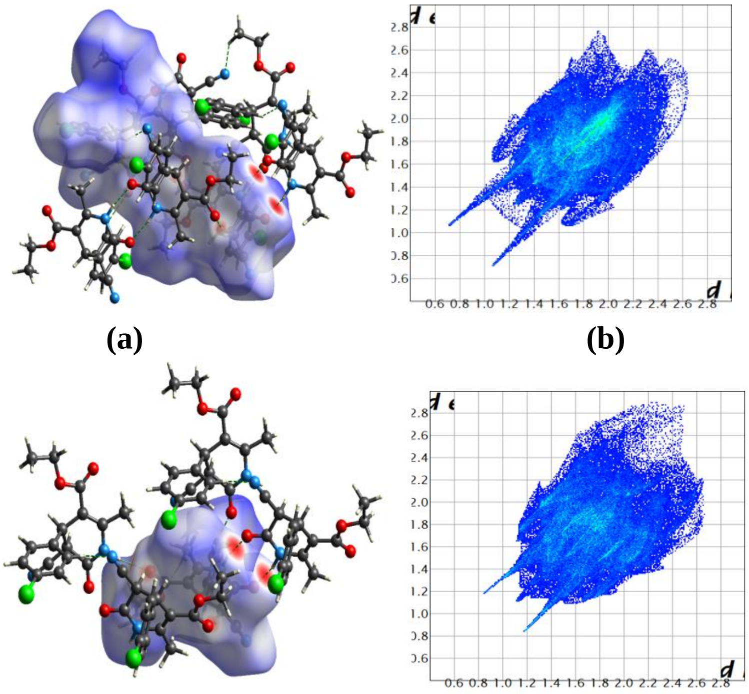

(a) **(b)**

(c) **(d)**

Figure 2.11: (a) d_{norm} and (b) 2-D fingerprint of compound **1.2C** enantiomer A, (c) d_{norm}, and (d) 2-D fingerprint of compound **1.2C** enantiomer B

The enantiomers A and B showed differences in their surface coverage. For enantiomer A, the contribution of different interactions to Hirshfeld Surface are H…H (30.0%), Cl…N (1.6%), Cl…H (15.0%), O…H (21.4%), C…H (16.5%), and

N…H (11.4%), and N…O (5.0%), and other interactions are less than 1.0%. Whereas for enantiomer B, they are H…H (37.8%), Cl…N (2.0%), Cl…H (12.6%), O…H (15.1%), C…H (13.7%), and N…H (14.6%), and C…O (1.0%), and other interactions are less than 1.0%.This study also showed that the contribution of CH...π interactions is about 16.5% & 13.7% for enantiomers A & B, respectively. The calculation of interaction energies indicated that the dispersion component and electrostatic forces are the dominating factors due to aromatic electronic redistribution in the compound and weak interactions in enantiomers A and B.

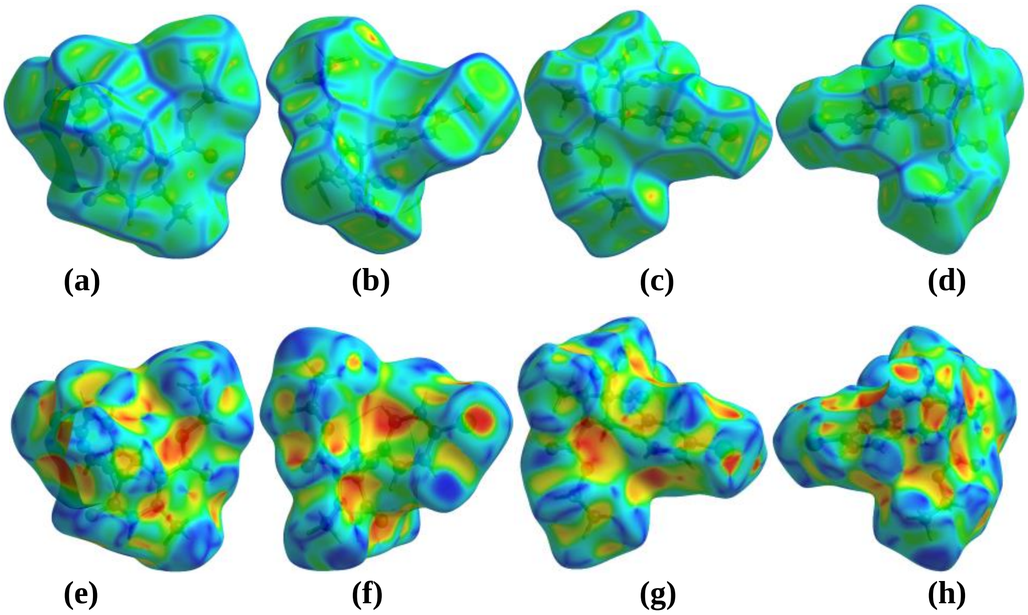

Figure 2.12: (a) and (b) Curvedness, (e) and (f) Shape-index, both side views of compound **1.2C** enantiomer A, (c) and (d) Curvedness, (g) and (h) Shape-index, both side views of compound **1.2C** enantiomer B

The curvedness plots and the shape index plots of the 3-D Hirshfeld surface also revealed weak intermolecular interactions in enantiomers A and B. On the curvedness surface, the yellow spots represent the weak interactions in the crystal structure. The red-yellow colored spots in curvedness plots show strong hydrogen-bonding interactions in the crystal structure **(Figure 2.12 (a)-(d))**. In the shape-index of enantiomers A and B, red and blue areas represent the acceptor and the donor property, respectively. Yellowish-red colored concave regions indicate the presence of weak intermolecular interactions. The red and blue colored triangles on the surface of the rings of the molecule indicated the presence of weak $\pi...\pi$ stacking in the crystal structure **(Figure 2.12 (e)-(h))**. Hirshfeld surface analysis gives evidence of weak intermolecular interactions, and all these weak interactions stabilize and strengthen the crystal packing structure of enantiomers A and B.

The presence of C-H…O, C-H…N, and C-H…π interactions in the supramolecular framework is supported by the Hirshfeld weak non-covalent intermolecular interactions calculation within the cluster of radius 3.8Å around a single crystals fragments. Those interactions are illustrated in **Figure 2.13**.

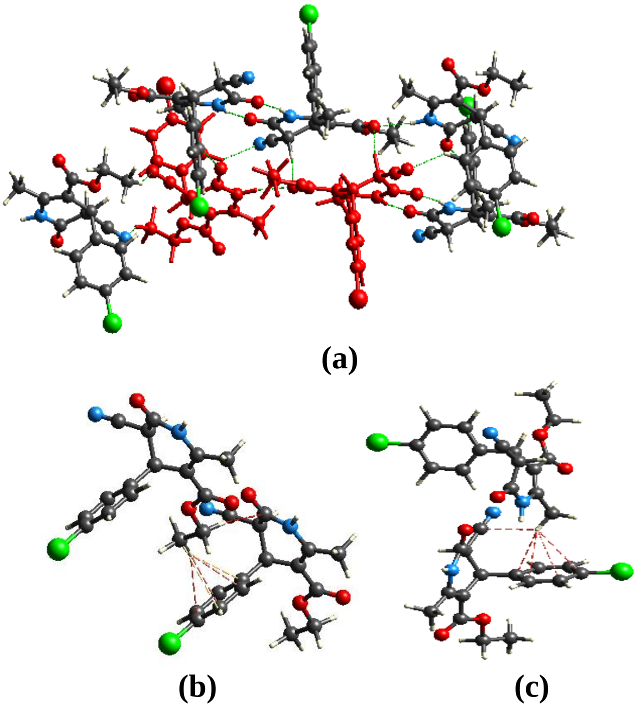

Figure 2.13: (a) C-H…O and C-H…N interactions, (b) and (c) C-H…π interactions, in compound **1.2C**

2.5.1.3. Crystal analysis of compound 1.2E

The compound **1.2E** was recrystallized in methanol at room temperature by slow evaporation of the solvent. The chiral asymmetric compound **1.2E** was analyzed using SC-XRD **(Figure 2.14)**. The compound crystallized with cell lengths **a** = 15.713(5)Å, **b** = 11.590(3)Å, **c** = 8.823(3)Å, i.e., **a** ≠ **b** ≠ **c** and cell angles $\boldsymbol{\alpha}$ = 90°, $\boldsymbol{\beta}$ = 95.309(6)°, $\boldsymbol{\gamma}$ = 90°, i.e., $\boldsymbol{\alpha = \gamma = 90°, \beta \neq 90°}$ which indicate that the compound is exhibiting a monoclinic crystal system, with space group $P2_1/c$ that contains four molecules per unit cell.

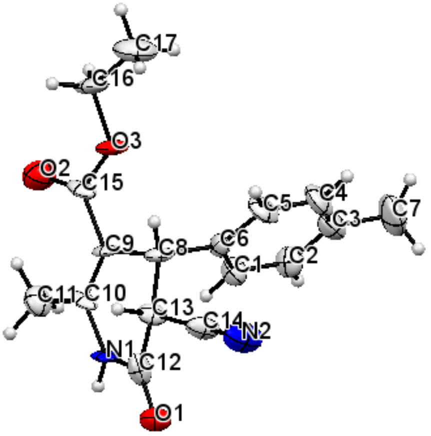

Figure 2.14: ORTEP diagram of compound **1.2E**

In the crystal analysis of compound **1.2E**, the 3,4-dihydro-2-pyridone ring is non-planar and adopts a puckered ring of slightly twisted half chair conformation. It is due to the sp^3 hybridization of C8 and C13. The benzenoid ring is almost perpendicular to the 3,4-dihydro-2-pyridone ring, where the dihedral angle between the plane of the two rings is 87.60°. Both rings are arranged in the ABAB pattern in the orthogonal pattern in the crystal packing. The crystallographic information is summarized in **Table 2.1**.

The supramolecular framework of compound 1.2E: The molecular association of compound **1.2E** displays a strong non-covalent N-H…O bond, which assists the self-assembly of the molecule in forming supramolecular structures. This N-H…O intermolecular interaction between the hydrogen of the amine group with the carbonyl oxygen (O3) (in short, within the amide group) within the 3,4-dihydro-2-pyridone ring with a bond distance of 2.008Å lead to the formation of unsymmetrical dimer giving $R_2^2(8)$ graph set notation **(Figure 2.15 (b))**. The oxygen (O1) of the carbonyl group within the 3,4-dihydro-2-pyridone ring acts as a bifurcated acceptor. It forms C-H…O bonds with the hydrogen from the ester moiety, having a bond distance of 2.586Å. Thus, these N-H…O and C-H…O bond from the bifurcated oxygen involving four molecules forms a graph set notation of $R_4^2(18)$ **(Figure 2.15 (c))**. This bifurcated acceptor O1 plays a significant role in linking the interlayer chain. Altogether the C-H…N bond with a bond distance of

2.556Å and C-H…O bond with a bond distance of 2.586Å facilitate the interlayer connectivity and forms two graph sets with $R_3^3(17)$ notation **(Figure 2.15 (d))**. The molecular arrangement of **1.2E** also displays C-H…C intermolecular interaction with the benzenoid carbon at a distance of 2.887Å which assists the interlayer connectivity. This C-H…C contact is also responsible for bringing the hydrogen close enough to have C-H…π interaction with the benzenoid ring current at a bond distance of 2.829Å. Apart from these, another C-H...π interaction is observed within the benzenoid hydrogen. Its intermolecular ring at a 3.552Å bond distance also acts as an additional force in bringing the molecules together to form a supramolecular network **(Figure 2.15 (e))**. The non-covalent hydrogen bonding is listed in **Table 2.4**.

Table 2.4: Hydrogen bonds and other interactions in compound **1.2E**

Donor-H...Acceptor	**D – H, Å**	**H...A, Å**	**D...A, Å**	**D - H...A, º**
N1-H1…O1	0.859	2.008	2.899	162.43
C8-H8…N2	0.980	2.566	3.496	158.35
C11-H11A…O2	0.960	2.586	3.463	152.01
C16-H16A…O1	0.970	2.559	3.528	177.14
C17-H17C…C2	0.960	2.887	3.577	129.65
C17-H17C…π(C1-C6)	0.960	2.829	3.729	156.64
C2-H2…π(C1-C6)	0.930	3.552	4.730	148.08
Intramolecular				
C1-H1…N1	0.930	2.829	3.481	128.20
C11-H11B…O2	0.960	2.169	2.903	132.27
C16-H16A…O2	0.970	2.755	2.714	77.39
C16-H16B…O2	0.970	2.649	2.714	83.38

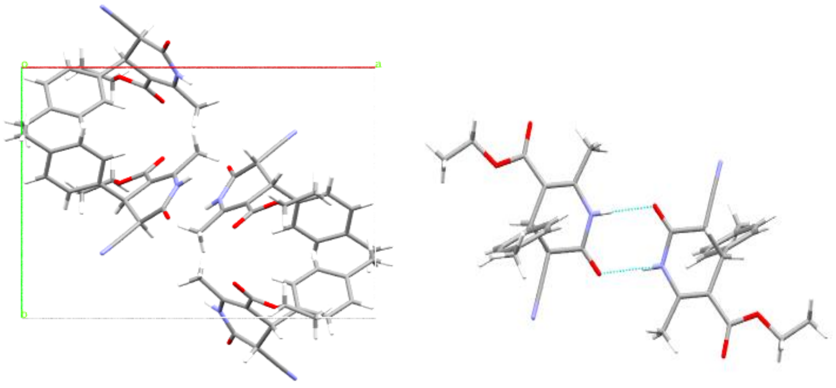

(a) **(b)**

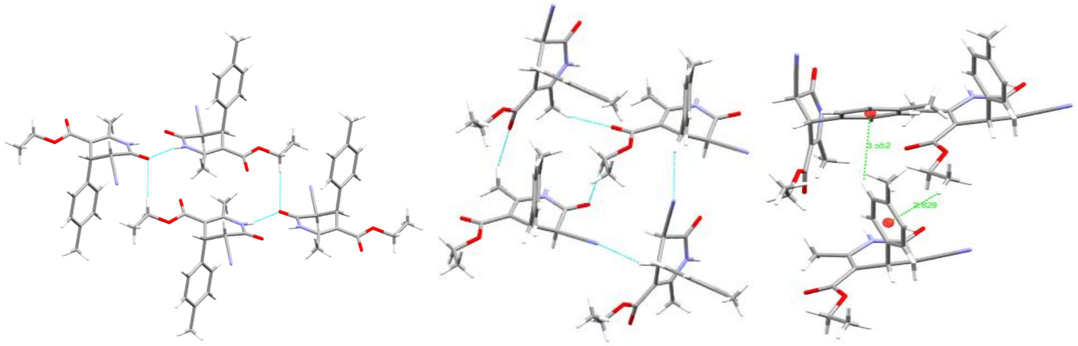

(c) (d) (e)

Figure 2.15: (a) Packing diagram of **1.2E**, (b) (c) and (d) Graph sets and (e) C-H…π interactions, in compound **1.2E**

Hirshfeld surface analysis of compound 1.2E: The Hirshfeld surface mapped over the d_{norm} in the range of -0.53 to 1.69Å for compound **1.2E** is displayed in **Figure 2.16 (a) and (b)**. The region of bright red spots corresponds to short contacts, which are more dominant intermolecular N-H…O interactions. The other lighter red spots are due to C-H…O, C-H…N, and C-H…C interactions.

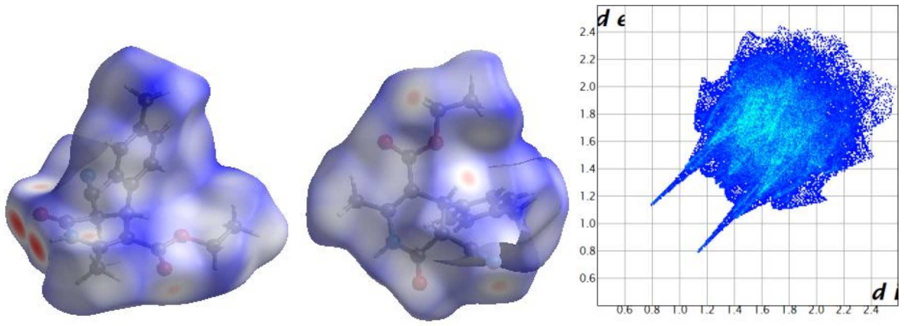

(a) (b) (c)

Figure 2.16: (a) and (b) d_{norm} both side view, (c) 2-D fingerprint plot, of compound **1.2E**

The relative percentage contributions of non-covalent interaction to the Hirshfeld surface is represented by the 2-D fingerprint plot of compound **1.2E (Figure 2.16 (c))**. Those are H…H (46.5%), O…H (20.1%), N…H (14.4%), C…H (17.8%), N…O (0.9%), C…O (0.2%) and C…N (0.1%). The O…H/H…O appears as a pair of distinct spikes in the region of di + de = 1.9-2.5Å. However, N…H/H…N contacts are not distinguishable in the fingerprint plot but occupies the region of di + de = 2.5-3.2Å. Since C-H…π decomposed within the C…H/H…C contacts, they occupy the same region in the 2-D fingerprint plot and are not separable. Therefore, the C…H/H…C and C-H…π contacts appear as a characteristic wing-like pattern in the 2-D fingerprint plot in the region of di + de = 2.8-3.6Å. Since there is no C…C contact contribution, it means there is no significant contribution by π...π stacking interactions.

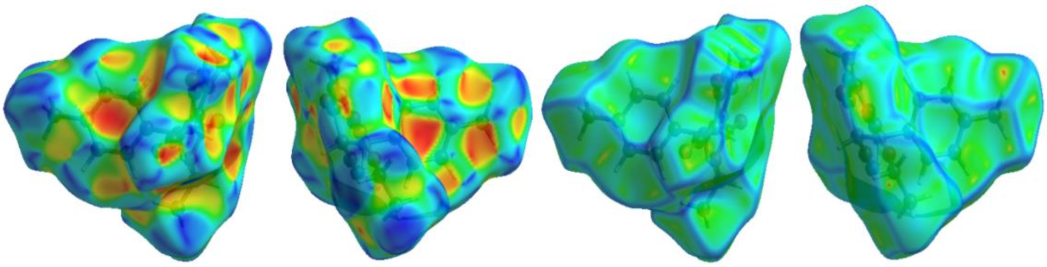
(a) **(b)** **(c)** **(d)**

Figure 2.17: (a) and (b) Shape-index, (c) and (d) Curvedness, both side views of compound **1.2E**

The shape-index mapped over in a range of -1 to 1Å for compound **1.2E** does not have complimentary pair of red and blue triangles around the aromatic benzenoid ring surface, which indicate the absence of π…π stacking interactions. Yellowish-red colored concave regions in the shape index around the surface of the benzenoid ring in compound **1.2E** indicate the acceptor region where weak C-H...π interactions occur **(Figure 2.17: (a) and (b))**. The Hirshfeld curvedness surface in a range of -4 to 0.4 Å for compound **1.2E** also does not display an area of the flat green region with a yellowish spot around the benzenoid ring surface, which again indicate the absence of π…π stacking interactions between the benzenoid ring **(Figure 2.17: (c) and (d))**.

The Hirshfeld weak non-covalent intermolecular interactions calculation within the cluster of radius 3.8Å around a single crystals fragments also supports the presence of N-H…O, C-H…O, C-H…N, C-H…C, and C-H…π interactions found in the supramolecular framework of compound **1.2E**. Those interactions are illustrated in **Figure 2.18**.

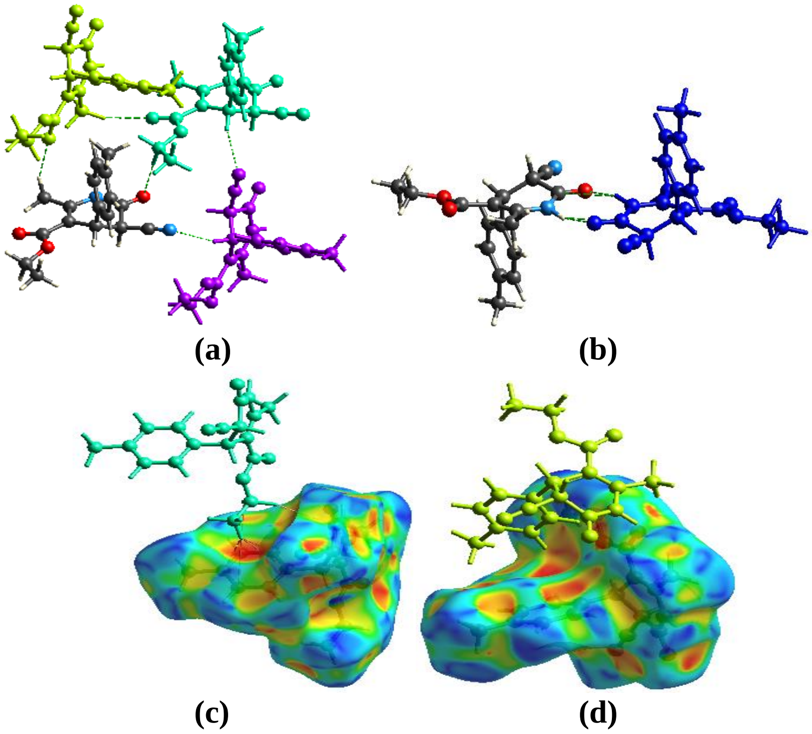
(a) (b)
(c) (d)

Figure 2.18: (a) and (b) Non-covalent interactions, (c) and (d) C-H…π interactions, in compound **1.2E**

2.5.1.4. Crystal analysis of compound 1.2F

The compound **1.2F** was recrystallized in methanol at room temperature by slow evaporation of the solvent. The chiral asymmetric compound **1.2F** was analyzed using SC-XRD **(Figure 2.19)**. The compound crystallized with cell lengths **a** = 10.2948(9)Å, **b** = 11.3659(8)Å, **c** = 27.177(2)Å, i.e., **a ≠ b ≠ c** and cell angles $\boldsymbol{\alpha}$ = 90°, $\boldsymbol{\beta}$ = 90°, $\boldsymbol{\gamma}$ = 90°, i.e., $\boldsymbol{\alpha = \beta = \gamma = 90}$°, which indicate that the compound is exhibiting an orthorhombic crystal system, with space group Pbca that contains eight molecules per unit cell.

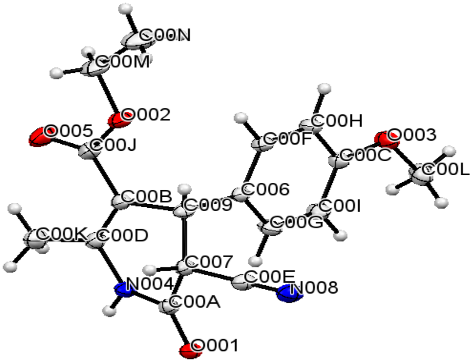

Figure 2.19: ORTEP diagram of compound **1.2F**

In the crystal analysis of compound **1.2F**, the 3,4-dihydro-2-pyridone ring is non-planar and adopts a puckered ring of slightly twisted half chair conformation. This is due to the sp^3 hybridization of C007 and C009. The benzenoid ring is almost perpendicular to the 3,4-dihydro-2-pyridone ring, where the dihedral angle between the plane of the two rings is 87.03°. The crystallographic information is summarized in **Table 2.5**.

Table 2.5: Crystal data on compounds **1.2F, 1.3A,** and **1.3C**

Compound	**1.2F**	**1.3A**	**1.3C**
Identification code	2170447	2170457	2035549
Empirical formula	$C_{17}H_{18}N_2O_4$	$C_{16}H_{13}N_3O_5$	$C_{16}H_{13}ClN_2O_3$
Formula weight	314.33	327.29	316.73
Temperature(K)	296.15	296.15	296.15
Crystal system	Orthorhombic	Triclinic	triclinic
Space group	Pbca	P-1	P-1
a(Å)	10.2948(9)	8.184(4)	9.264(5)
b(Å)	11.3659(8)	13.805(2)	9.923(5)
c(Å)	27.177(2)	14.268(2)	10.327(5)
α(°)	90	91.48(3)	64.060(5)
β(°)	90	91.10(3)	73.767(5)
γ(°)	90	105.32(3)	66.810(5)
Volume(Å^3)	3180.0(4)	1553.6(8)	778.1(7)
Z	8	4	2
ρ (g/cm^3)	1.313	1.399	1.352
μ(mm^{-1})	0.780	0.106	0.259
F(000)	1328.0	680.0	328.0
Crystal size(mm^3)	0.23 × 0.21 × 0.17	0.25 × 0.21 × 0.18	0.2 × 0.18 × 0.14
Radiation	CuKα (λ = 1.54178)	MoKα (λ = 0.71073)	MoKα (λ = 0.71073)
2Θ range for data collection(°)	10.782 to 102.408	5.258 to 55.828	4.424 to 57.932
Index ranges	$-9 \le h \le 8$, $-10 \le k \le 10$, $-27 \le l \le 13$	$-10 \le h \le 10$, $-17 \le k \le 17$, $-18 \le l \le 18$	$-12 \le h \le 12$, $-13 \le k \le 13$, $-13 \le l \le 13$
Reflections collected	3805	27030	24274
Independent reflections	1558	7130	4048
Data/restraints/parameters	1558/0/216	7130/3/440	4048/0/205
Goodness-of-fit on F^2	1.051	0.875	1.057
Final R indexes [I>=2σ (I)]	R_1 = 0.0394, wR_2 = 0.0952	R_1 = 0.0631, wR_2 = 0.1475	R1 = 0.0503, wR2 = 0.1223
Final R indexes [all data]	R_1 = 0.0470, wR_2 = 0.1000	R_1 = 0.1375, wR_2 = 0.1827	R1 = 0.0873, wR2 = 0.1406
Largest diff.peak/hole/e Å^{-3}	0.24/-0.14	0.45/-0.32	0.21/-0.42

The supramolecular framework of compound 1.2F: The molecular association of compound **1.2F** displays a strong non-covalent N-H…O bond between the hydrogen (H004) of the amine group with the carbonyl oxygen (O001) within the 3,4-dihydro-2-pyridone ring at a bond distance of 2.076Å. These N-H…O bonds lead to the formation of an unsymmetrical dimer, giving $R_2^2(8)$ graph set notation **(Figure**

2.20 (b)) which also assists the self-assembly of the molecule in forming supramolecular structures. The hydrogen (H004) of the amine group within the 3,4-dihydro-2-pyridone ring acts as bifurcated hydrogen and forms an N-H…N bond with the nitrogen (N008) from the cyano group having a bond distance of 2.712Å. The nitrogen (N008) also acts as a bifurcated acceptor and forms a C-H…N bond with the hydrogen from the benzenoid ring at a distance of 2.592Å. These N-H…N and C-H…N bonds formed by the bifurcated hydrogen and bifurcated acceptor nitrogen along with the N-H…O dominant bond altogether result in the formation of the $R_2^2(8)$ graph set **(Figure 2.20 (c))**. Furthermore, these N-H...N together with the C-H…N bond within the crystal packing involving four **1.2F** molecules also forms another $R_4^4(26)$ graph set **(Figure 2.20 (d))**. Other stabilizing non-covalent interactions involved in the supramolecular structures are C-H…C contacts with a bond distance of 2.758Å and2.769Å and C-H…π interaction with an interactions distance of 2.730Å, 3.356Å and 3.901Å **(Figure 2.20 (e) and (f))**. Intermolecular and intramolecular hydrogen bonding is given in **Table 2.6**.

Table 2.6: Hydrogen bonds and other interactions in compound **1.2F**

Donor-H...Acceptor	**D – H, Å**	**H...A, Å**	**D...A, Å**	**D - H...A, º**
N004-H004…O001	0.847	2.076	2.906	165.99
N004-H004…N008	0.847	2.712	3.075	107.48
C007-H007…C00C	0.945	2.758	3.575	145.32
C007-H007…C00H	0.970	2.769	3.584	145.02
C00G-H00G…N008	0.926	2.592	3.402	146.41
C007-H007…π(benzenoid ring)	0.970	2.730	3.670	173.50
C00N-H00m….π(benzenoid ring)	0.871	3.356	3.999	132.85
C00L-H00e…π(benzenoid ring)	0.984	3.901	4.831	158.61
Intramolecular				
C00G-H00G…O001	0.926	2.959	3.756	145.07
C00K-H00a…O005	0.897	2.235	2.858	126.21
C00F-H00F…O002	1.007	2.572	3.235	123.22
C00M…H00k…O005	0.939	2.656	2.658	79.93
C00M…H00l…O005	0.966	2.483	2.658	89.59

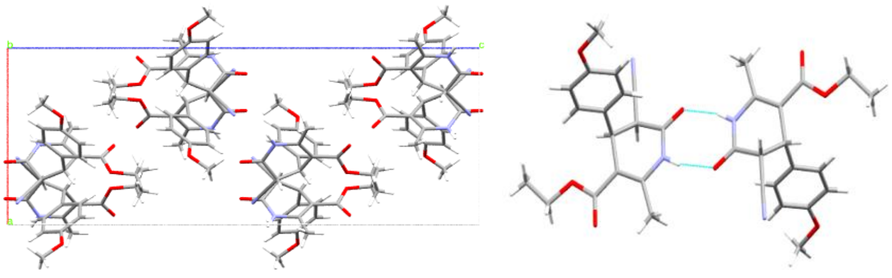

(a) **(b)**

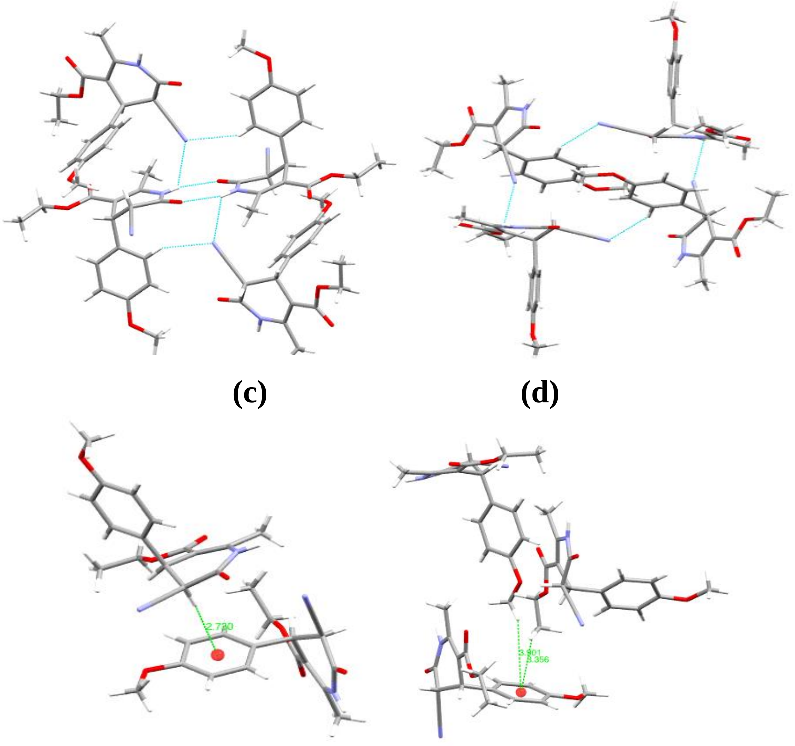

(c) (d)

(e) (f)

Figure 2.20: (a) Packing diagram of **1.2F**, (b) (c) and (d) Graph sets, (e) and (f) C-H…π interactions, in compound **1.2F**

Hirshfeld surface analysis of compound 1.2F: The Hirshfeld surface mapped over the d_{norm} in the range of -0.53 to 1.41Å for compound **1.2F** is displayed in **Figure 2.21 (a) and (b)**. The region of bright red spots corresponds to short contacts, which are more dominant intermolecular N-H…O interactions. The lighter red spots were due to C-H…N and C-H…C interactions.

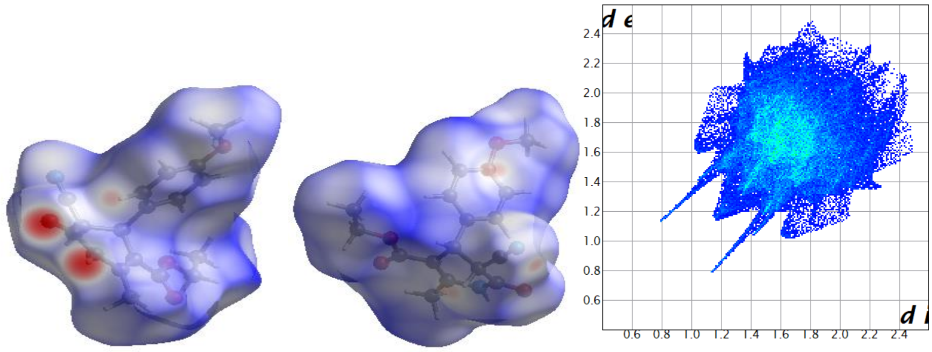

(a) (b) (c)

Figure 2.21: (a) and (b) d_{norm} both side view, (c) 2-D fingerprint plot, of compound **1.2F**

The2-D fingerprint plots of compound **1.2F** show the relative percentage contributions of non-covalent interaction to the Hirshfeld surface **(Figure 2.21 (c))**. Those are H…H (43.4%), O…H (23.7%), C…H (18.4%), N…H (11.5%), N…O (1.1%), N…N (0.6%), C…C (0.6%) and C…N (0.5%) and C...O (0.1%). The O…H/H…O interaction appears as a pair of distinct pairs of spikes in the 2-D fingerprint plot in the region of di + de = 1.9-2.5Å. Also, N…H/H…N contacts occupy the region of spikes but are not very distinguishable in the fingerprint plot in the region of di + de = 2.5-3.0Å. Although C-H…π intermolecular interactions are observed in the supramolecular framework, its relative contribution is decomposed within the C…H/H…C contacts. They appear as a characteristic wing-like pattern in the 2-D fingerprint plot in the region of di + de = 2.7-4.0Å.

The shape-index mapped in a range of -1 to 1Å for compound **1.2F** does not have complimentary pair of red and blue triangles around the aromatic benzenoid ring surface, which indicate the absence of π…π stacking interactions. The yellowish-red colored concave regions in the shape index around the surface of the benzenoid indicate the acceptor region where weak C-H...π interactions occur **(Figure 2.22 (a) and (b))**. The Hirshfeld surface mapped over the curvedness in a range of -4 to 0.4 Å for compound **1.2F** also does not display an area of the flat green region with a yellowish spot around the benzenoid ring surface, which again indicate the absence of π…π stacking interaction **(figure 2.22 (c) and (d))**.

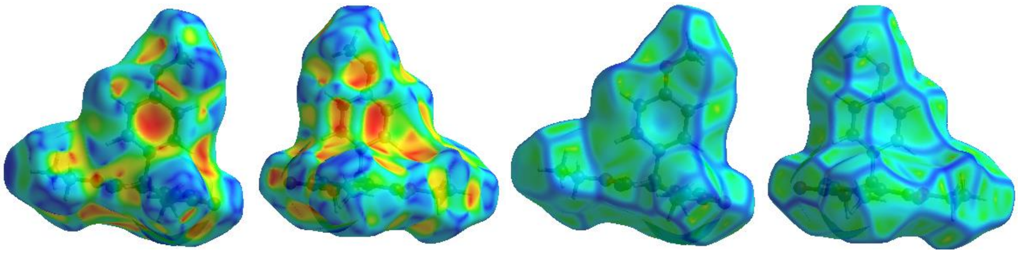
(a) **(b)** **(c)** **(d)**

Figure 2.22: (a) and (b) Shape-index, (c) and (d) Curvedness, both side views of compound **1.2F**

The presence of N-H…O, C-H…O, C-H…N, C-H…C, and C-H…π interactions in the supramolecular framework which also result in forming the respective graph sets motifs are also supported by the Hirshfeld weak non-covalent intermolecular interactions calculation within the cluster of radius 3.8Å around a single crystals fragments. Those interactions are illustrated in **Figure 2.23**.

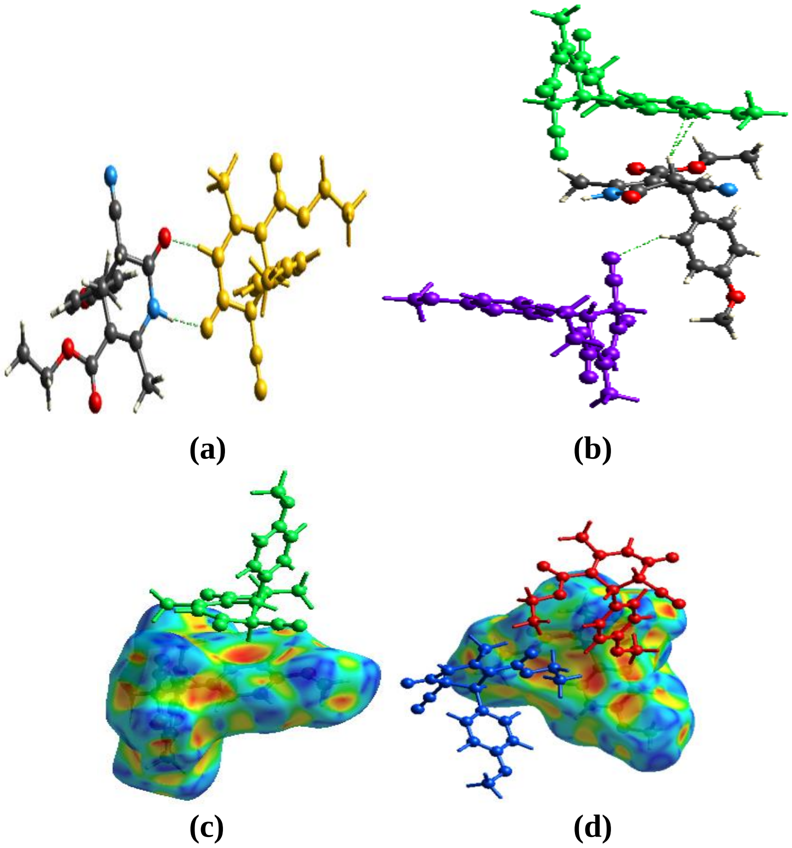

Figure 2.23: (a) N-H…O interaction, (b) C-H…N and C-H…C interactions, (c) and (d) C-H…π interactions in compound **1.2F**

2.5.1.5. Crystal analysis of compound 1.3A

The compound **1.3A** was recrystallized in ethyl acetate at room temperature by slow evaporation of the solvent. The chiral asymmetric compound **1.3A** was analyzed using single-crystal X-ray diffraction **(Figure 2.24)**. The compound **1.3A** has two symmetry-independent molecules (Z'=2) in its asymmetric unit with four molecules per unit cell. The compound crystallized in a triclinic crystal system in a P-1 space group with cell lengths **a** = 8.184(4)Å, **b** = 13.805(2)Å, **c** = 14.268(2)Å, and cell angles $\boldsymbol{\alpha}$= 91.48(3)°, $\boldsymbol{\beta}$ = 91.10(3)°, $\boldsymbol{\gamma}$ = 105.32(3)°. In both the symmetry-independent molecules of the asymmetric unit, the pyridone and phenyl rings are planar. The dihedral angles between mean planes of pyridone and phenyl rings are 61.87° and 56.32°. The crystallographic information is summarized in **Table 2.5**.

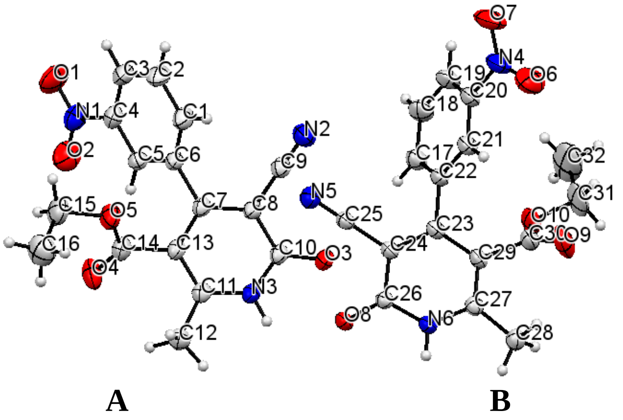

Figure 2.24: ORTEP diagram of compound **1.3A**

The supramolecular framework of compound 1.3A: Both the molecules A and B in the asymmetric unit involved strong N-H…O hydrogen bond interactions with distances of 1.883Å and 1.875Å, and bond angles of 173.76° and 177.36°, respectively. The N-H…O interactions, i.e., N6-H6…O8 and N3-H3…O3 between two molecules formed a dimer which has a graph set of $R_2^2(8)$ motif in both molecules A and B **(Figure 2.25 (c) and (d))**. The C10=O3…C25, C25-N5…C4, and N5…C8 interactions connects the two symmetry-independent molecules having an interaction distances of 3.063Å, 3.124Å and 3.195Å respectively **(Figure 2.25 (b))**. The N1-O2…C11 interactions in molecule A lead to the formation of infinite chains that propagate parallel to the crystallographic a-direction (**Figure 2.25 (c))**. Oxygen O3 acts as a bifurcated acceptor, establishes hydrogen bond interaction with the N3-H3A and C12-H12B donors, and forms a six-membered graph set of $R_2^1(6)$ motif. On the contrary, the interaction between nitro groups of two molecules due to their differences in dipole moments and N-H…O hydrogen bond interactions results in the propagation of infinite chains of molecule B (**Figure 2.25 (d))**. Like in molecule A, O6 acts as a bifurcated acceptor and forms hydrogen bond interactions in B, which results in the formation of a six-membered graph set of $R_2^1(6)$ and eight-membered $R_2^2(8)$ motif. Further, the two C-H...π interactions between molecule A and the pyridone ring of B, i.e., C12-H12...π interaction, and between molecule A and phenyl ring of B, i.e., C3-H3...π interaction with the distances 3.282 Å and 3.084Å respectively assists in the self-assembly of molecules A and B (**Figure 2.25 (e))**. Hydrogen bonds and other interactions in the compound are given in **Table 2.7**.

Table 2.7: Hydrogen bonds and other interactions in compound **1.3A**

Donor-H...Acceptor	**D-H, Å**	**H...A, Å**	**D...A, Å**	**D-H...A, º**
N3-H3A...O3	0.860	1.883	2.740	173.76
C12-H12B...O3	0.960	2.667	3.471	141.65
N3-H3...C10	0.860	2.775	3.579	156.24
N6-H6...O8	0.860	1.875	2.717	177.36
N6-H6...C26	0.860	2.730	3.538	157.05
C28-H28B...O8	0.960	2.590	3.412	142.50
C31-H31B…O4	0.970	2.623	3.276	124.87
C12-H12...π (N6, C23, C24, C26, 27, C29)		3.282		
C12-H12...π(C17-C22)		3.084		
C2-H2…N5	0.931	2.663	3.348	131.03
Other interactions				
C9…C26		3.344		
C25…O3		3.063		
C25…C10		3.295		
N5…C8		3.195		
C14=O…C28	1.181	3.217	3.951	120.24
N4-O7…N4	1.203	3.059	3.522	102.55
C10=03…C25	1.240	3.063	3.295	89.51
N1-O2...C11	.200	3.178	4.123	135.69
C25-N5...C4	1.123	3.124	3.614	106.98
Intramolecular				
C15-H15B…O4	0.970	2.430	2.655	92.49
C15-H15A…O5	0.970	1.992	1.448	43.30
C3-H3…O1	0.930	2.424	2.703	97.25
C5-H5…O2	0.930	2.378	2.674	98.14
C15-H15B…π(C2-C6)		4.217		
C31-H31A…O9	0.970	2.895	1.437	95.79
C31-H31B…O9	0.970	2.343	1.437	42.58
C32-H32A…O10	0.960	2.491	2.331	69.23
C32-H32…π(C17-C22)		3.148		

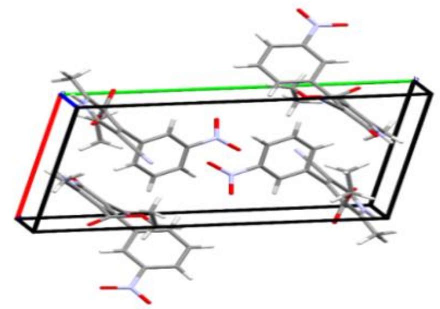

(a)

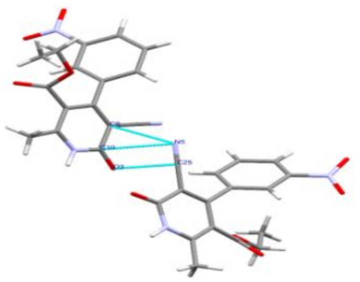

(b)

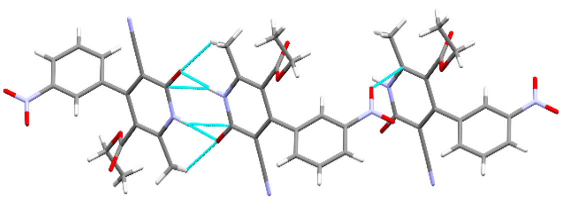

(c)

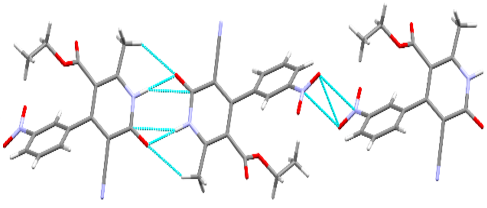

(d)

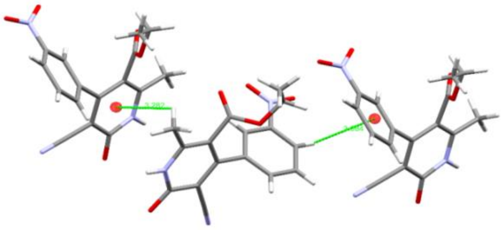

(e)

Figure 2.25: (a) Packing diagram of **1.3A**, (b) dipole…dipole interactions,(c) and (d) graph sets and dipole…dipole interactions, (e) C-H…π interactions, in compound **1.3A**

Hirshfeld Surface analysis of compound 1.3A: The bright red spots on the Hirshfeld surfaces of **1.3A** mapped over a d_{norm} range of -0.5152 to 1.1464Å correspond to the short interactions of N-H...O, whereas the lighter red spots indicate the C-H…O interactions **(Figure 2.26 (a) and (c))**.

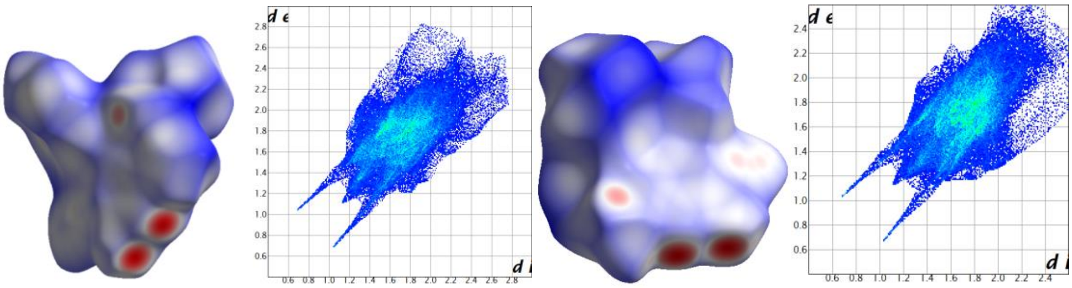

(a) **(b)** **(c)** **(d)**

Figure 2.26: (a) d_{norm} and (b) 2-D fingerprint of compound **1.3A** molecule A, (c) d_{norm} and (d) 2-D fingerprint of compound **1.3A** molecule B

In the 2-D fingerprint plots of compound **1.3A**, the presence of H...H and O...H intermolecular interactions appear as pair of distinct spikes, where the lower spike (di>de) represents the acceptor character of the atom, and the upper spike (di<de) corresponds to the donor character of the atom **(Figure 2.26 (b) and (d))**. A pair of long distinct pointed spikes at (di, de) ≈ (1.05, 0.7 Å) and (di, de) ≈ (1.15, 1.1Å) represents the O...H/H...O and H...H/H...H interactions. Moreover, the presence of N…H and C…H interactions appear as a pair of characteristic wings in a 2-D fingerprint plot at the regions (di, de) ≈ (1.1, 1.5 Å) and (di, de) ≈ (1.8, 1.2 Å) in molecule A and (di, de) ≈ (1.5, 1.1 Å) and (di, de) ≈ (1.7, 1.18 Å) respectively in molecule B. The 2-D fingerprint plots of compound **1.3A** show the relative

contribution of intermolecular interactions to the Hirshfeld surface. Those are H…H (28.1%), O…H (31.2%), N…H (10.8%), C…H (8.5%), C…C (2.7%), C…N (5.9%), C…O (4.0%), N…N (0.9%), O…N (3.7 %), O…O (4.2%).

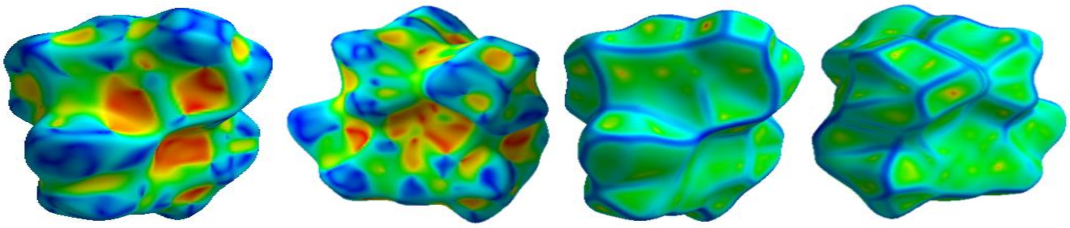
(a) **(b)** **(c)** **(d)**

Figure 2.27: (a) and (b) Shape-index, (c) and (d) Curvedness, both side views of compound **1.3A**

Hirshfeld surfaces mapped over the shape-index in a range of -1.0 to 1.0 Å for compound **1.3A** have deformed complementary pairs of touching red and blue triangles, which indicates the possible C-H...π interactions in the crystal structure. Further, red and blue areas in the shape index represent the acceptor, and the donor property of molecules A and B. Yellowish-red colored concave regions indicate the presence of weak intermolecular interactions in the Shape index plots **(Figure 2.27 (a) and (b))**. In contrast, yellow spots on the curved surface represent the molecules' weak interactions. The red-yellow colored spots in curvedness plots indicate the presence of strong hydrogen-bonding interactions in the crystal structure **(Figure 2.27 (c) and (d))**.

The different non-covalent hydrogen bonding within the 3.8Å radius from a single fragment found from the Hirshfeld calculations are given in **Figure 2.28**.

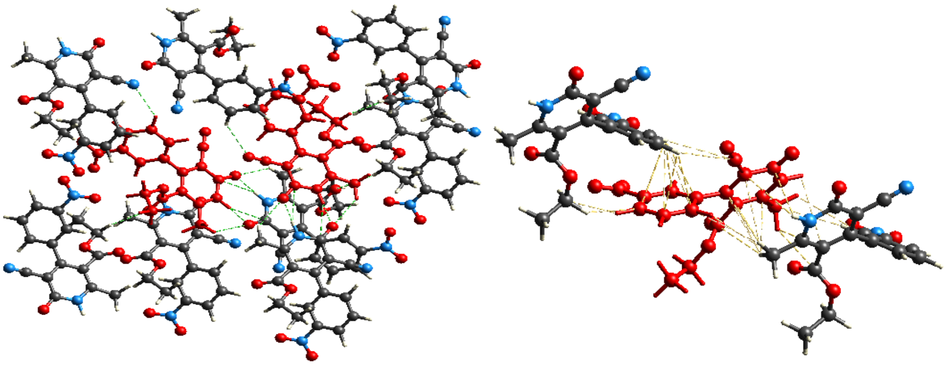
(a) **(b)**

Figure 2.28: (a) Non- covalent interactions and (b) C-H…π interactions in compound **1.3A**

2.5.1.6. Crystal analysis of compound 1.3C

The compound **1.3C** was recrystallized in ethanol at room temperature by slow evaporation of the solvent. The chiral asymmetric compound **1.3C** was analyzed using SC-XRD **(Figure 2.29)**. The compound crystallized with cell lengths **a** = 9.264(5)Å, **b** = 9.923(5)Å, **c** = 10.327(5)Å, i.e., $\mathbf{a} \neq \mathbf{b} \neq \mathbf{c}$ and cell angles $\boldsymbol{\alpha}$ = 64.060(5)°, $\boldsymbol{\beta}$ = 73.767(5)°, $\boldsymbol{\gamma}$ = 66.810(5)°, i.e., $\boldsymbol{\alpha} = \boldsymbol{\gamma} = \mathbf{90^\circ}, \boldsymbol{\beta} \neq \mathbf{90^\circ}$, which indicate that the compound is exhibiting a triclinic crystal system, with space group P-1 that contains two molecules per unit cell.

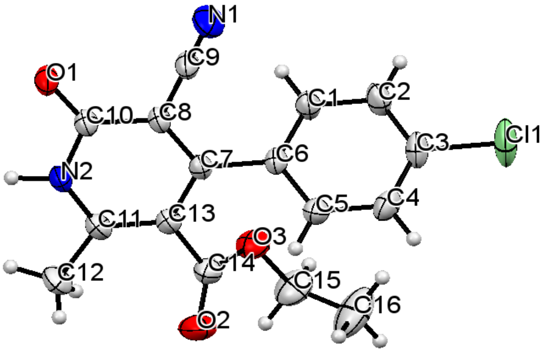

Figure 2.29: ORTEP diagram of compound **1.3C**

The chiral asymmetric compound **1.3C** crystal structure shows that both the pyridone and phenyl ring adopt planar cyclic systems. The plane of the two aromatic rings twisted way from each other at a torsion angle of 51.26°. Both rings are arranged in the ABAB pattern in the orthogonal pattern in crystal packing. The crystallographic information is summarized in **Table 2.5**.

The supramolecular framework of compound 1.3C: The crystal packing within the unit cell is stabilized by $\pi \ldots \pi$ stacking between the aromatic rings at a distance of 3.951Å **(Figure 2.30 (a))**. The pyridone ring also interacts with the hydrogen (H1) from the benzenoid ring giving C-H…π interaction at a distance of 2.761Å **(Figure 2.30 (b))**. The supramolecular framework of compound **1.3C** involves a strong non-covalent N-H…O intermolecular hydrogen bond with a bond distance of 1.836Å that results in the formation of an asymmetric dimer. The carbonyl carbon (C10) of the pyridone ring also interacts with the hydrogen of the amine within the pyridone moiety, forming N-H…C interactions with a bond distance of 2.701Å. These N-H…O and N-H…C interactions arise from the pyridone ring's carboxyl and amine moiety. It forms an unsymmetrical dimer and also adopts the formation of $R_2^2(6)$ and $R_2^2(8)$ graph sets **(Figure 2.30 (c))**. Bifurcated hydrogen bonding is also observed between the carbonyl oxygen (O1) of the pyridone ring with the hydrogen from its pyridone alkyl substituent at a distance of 2.662Å which forms $R_2^1(6)$ graph sets **(Figure 2.30 (c))**. This bifurcated hydrogen bonding assists the linear chain formation and interlayer connectivity. Hydrogen (H5) from the benzenoid ring interacts with the carbonyl oxygen (O2) of the ester substituents from the successive layer of the crystal packing also forms an intermolecular hydrogen bond at a distance of 2.389Å which results in the formation of $R_2^2(14)$ graph set **(Figure 2.30 (c))**. Apart from these, C-H…π interactions were also observed in the aromatic pyridone ring. Other interactions such as dipole-dipole and halogen-halogen are also found, facilitating the supramolecular framework **(Figure 2.30 (d))**. The weak non-covalent interactions are given in **Table 2.8**.

Table 2.8: Hydrogen bonds and other interactions in compound **1.3C**

Donor-H...Acceptor	**D-H, Å**	**H...A, Å**	**D...A, Å**	**D-H...A, º**
N2-H2…O1	0.961	1.836	2.784	167.99
N2-H2…C10	0.961	2.701	3.628	162.23
C12-H12C….O1	0.960	2.662	3.481	143.48
C5-H5…O2	0.930	2.389	3.259	156.48
C1-H1…π(C7-C10,C11,C13,N2)	0.930	2.761	3.403	126.97
Other interactions				
N1…C12	1.141	3.180	4.261	158.14
Cl1…Cl1	1.741	3.195	4.935	177.76
π(C1-C6)…π(C1-C6)		3.951		
Intramolecular				
C5-H5…O2	0.930	3.337	3.842	116.36
C12-H12A…O2	0.960	2.801	2.920	87.45
C12-H12B…O2	0.960	2.617	2.920	98.64
C16-H16A…π(C1-C6)	0.960	3.389	4.071	129.85

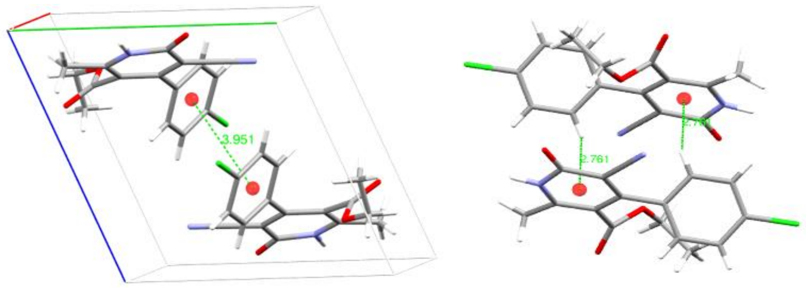

(a) **(b)**

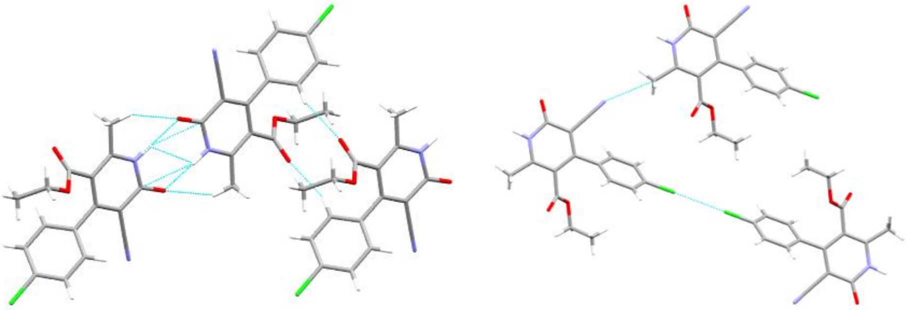

(c) (d)

Figure 2.30: (a) Packing diagram of **1.3C**, (b) C-H…π interaction (c) Graph sets and (d) dipole-dipole and halogen interactions, in compound **1.3C**

Hirshfeld surface analysis of compound 1.3C: The Hirshfeld surface mapped over the d_{norm} in the range of -0.63 to 1.37Å for compound **1.3C** is displayed in **Figure 2.31 (a) and (b)**. The region of bright red spots, which are comparatively larger than other red bumps, represents more dominant non-covalent strong N-H…O intermolecular interactions between the carbonyl (C=O) and the amine (N-H) group of the pyridone ring. The other red light spots arise due to C-H…O interactions.

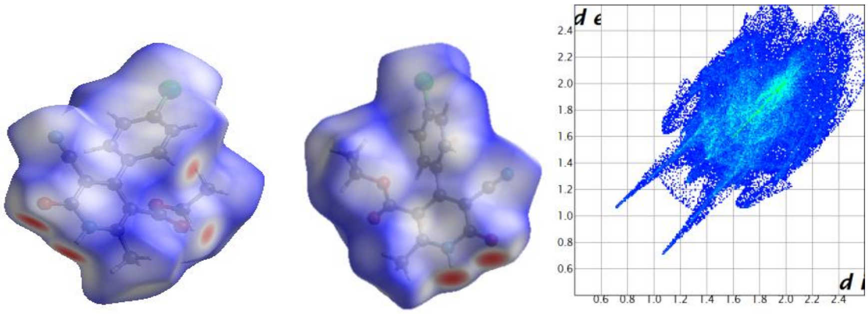

(a) (b) (c)

Figure 2.31: (a) and (b) d_{norm} both side view, (c) 2-D fingerprint plot, of compound **1.3C**

The other lighter white and blue regions of the Hirshfeld surface indicate weaker interactions due to more extended contacts, which are more significant or equal to the van der Waals interatomic distances.

The 2-D fingerprint plots of compound **1.3C** show the relative percentage contributions of non-covalent interaction to the Hirshfeld surface **(Figure 2.31 (c))**. Those interactions are H…H (32.4%), O…H (18.3%), N…H (14.6%), C…H (11.4%), H...Cl (7.2%), C...Cl (5.8%), C…C (2.5%), Cl...Cl (2.5%), C…O (2.1%), N…Cl (1.2%), N…O (0.9%), O…O (0.8%), O...Cl (0.2%) and C...N (0.1%). O…H/H...O interactions appear as a pair of distinct spikes in the 2-D fingerprint plot of compound **1.3C** in the region of di + de = 1.8-2.8Å. The existence of C-H...π intermolecular interactions decompose within the C...H contacts in the region of di + de = 2.7-3.4Å, which appears as a characteristic of distinct wings. Similarly, N...H/H...N intermolecular interactions are also reflected close to the characteristic wing occupied in the region of di + de = 2.6-2.8Å as a distinct point in the 2-D fingerprint plot. The relative contribution of C…C close contacts, which account for 2.5% in the region of di + de = 3.4-4.0 in compound **1.3C**, indicates aromatic ring π…π stacking interactions.

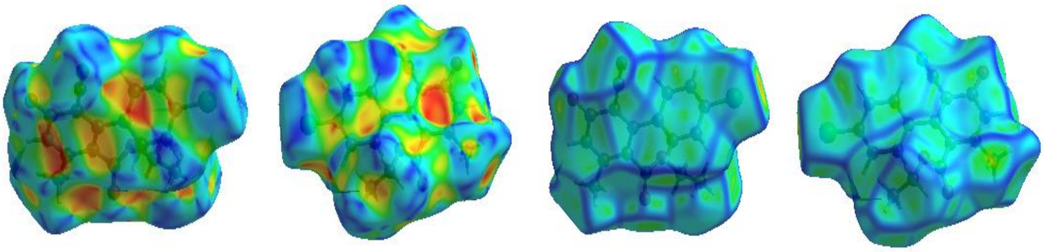
(a) **(b)** **(c)** **(d)**

Figure 2.32: (a) and (b) Shape-index, (c) and (d) Curvedness, both side views of compound **1.3C**

The shape-index mapped over a range of -1 to 1Å for compound **1.3C** shows the presence of complementary pair of red and blue triangles having an edge-to-edge connection around the aromatic benzenoid ring surface which indicates the presence of π...π stacking interactions (**Figure 2.32 (a))**. The yellowish-red colored concave regions around the surface of the pyridone ring in compound **1.3C** indicate the acceptor region where weak C-H...π interaction occurs (**Figure 2.32 (b))**. The curvedness mapped over a range of -4 to 0.4 Å for compound **1.3C** also displays a flat green region with a yellowish spot around the benzenoid ring surface, which indicates the presence of π…π stacking interactions between the benzenoid rings (**Figure 2.32 (c))**.

The Hirshfeld weak interactions calculation also supports the presence of weak non-covalent intermolecular interactions as in crystal packing. Where N-H…O, N-H…C, C-H…O, C-H…π, π…π stacking, and other intermolecular interactions are found within the cluster of radius 3.8Å around a single crystals fragments. Those interactions are in figure **2.33**.

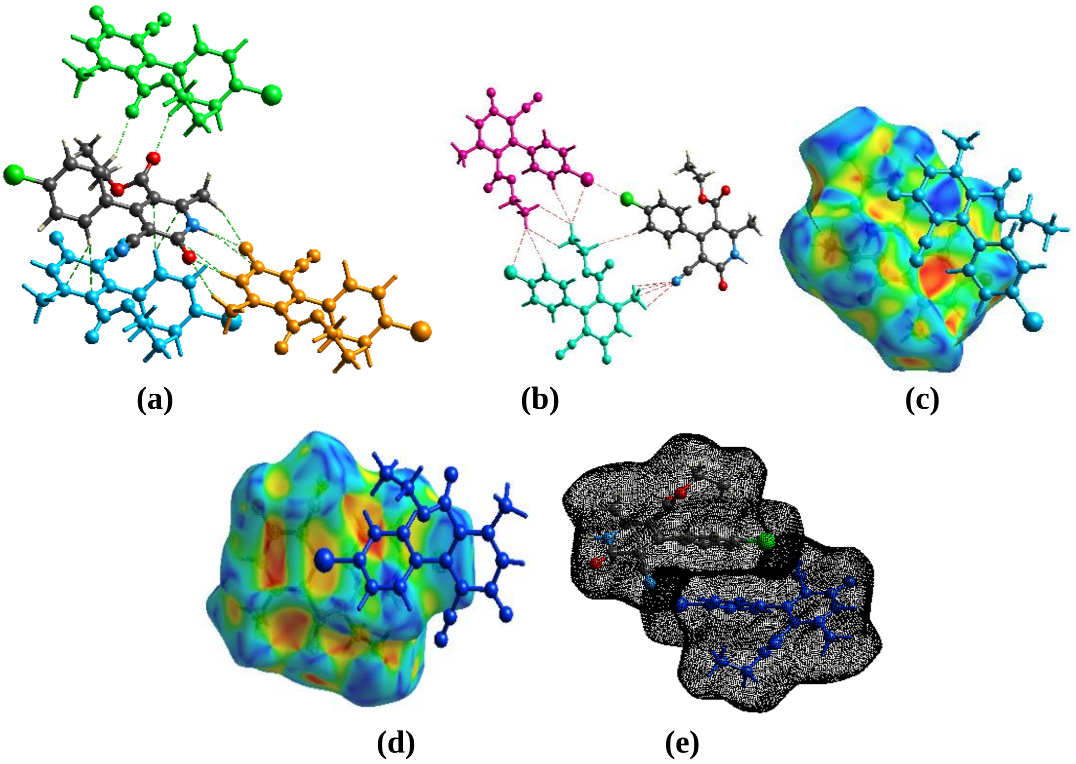
(a) (b) (c)

(d) (e)

Figure 2.33: (a) N-H…O, N-H…C, and C-H…O interactions, (b) dipole-dipole and halogen interactions, (c) C-H…π interactions, (d) and (e) $\pi…\pi$ interaction, in compound **1.3C**

2.5.1.7. Crystal analysis of compound 1.3D

The compound **1.3D** was recrystallized in acetic acid at room temperature by slow evaporation of the solvent. The chiral asymmetric compound **1.3D** was analyzed using SC-XRD **(Figure 2.34)**. The compound crystallized with cell lengths **a** = 13.893(5), **b** = 6.745(2), **c** = 16.893(6) i.e., **a ≠ b ≠ c** and cell angles $\boldsymbol{\alpha}$ = 90°, $\boldsymbol{\beta}$ = 97.405(5)°, $\boldsymbol{\gamma}$ = 90° i.e., $\boldsymbol{\alpha = \gamma = 90°}$, $\boldsymbol{\beta \neq 90°}$, which indicate that the compound is exhibiting a monoclinic crystal system, with space group $P2_1/c$ that contains four molecules per unit cell.

The crystal structure of the chiral asymmetric compound **1.3D** shows that both the pyridone and phenyl ring adopts a planar cyclic system. The phenyl ring twisted away from the parent pyridone ring plane at a dihedral angle of 61.67°. The summary of crystallographic information is listed in **Table 2.9**.

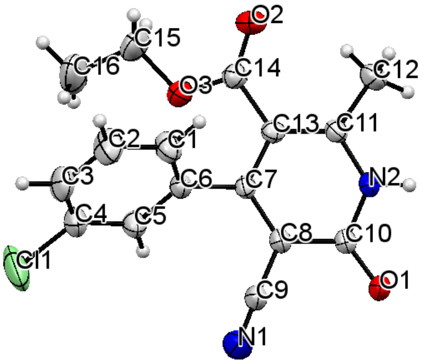

Figure 2.34: ORTEP diagram of compound **1.3D**

Table 2.9: Crystal data on compounds **1.3D**, **1.3E** and **1.3F**

Compound	1.3D	1.3E	1.3F
Identification code	2064030	2062954	2062953
Empirical formula	$C_{16}H_{13}ClN_2O_3$	$C_{17}H_{16}N_2O_3$	$C_{17}H_{16}N_2O_4$
Formula weight	316.73	296.32	312.32
Temperature(K)	296.15	296.15	296.15
Crystal system	Monoclinic	monoclinic	monoclinic
Space group	$P2_1/c$	$P2_1/n$	I2/a
a(Å)	13.893(5)	15.502(6)	18.470(3)
b(Å)	6.745(2)	6.588(3)	8.456(4)
c(Å)	16.893(6)	17.198(7)	23.200(3)
α(°)	90	90	90
β(°)	97.405(5)	115.496(5)	109.360(2)
γ(°)	90	90	90
Volume(Å^3)	1569.7(10)	1585.2(11)	3418.5(18)
Z	4	4	8
ρ (g/cm^3)	1.340	1.242	1.214
μ(mm^{-1})	0.257	0.086	0.088
F(000)	656.0	624.0	1312.0
Crystal size(mm^3)	0.19 × 0.16 × 0.13	0.24 × 0.19 × 0.15	0.24 × 0.17 × 0.14
Radiation	MoKα (λ = 0.71073)	MoKα (λ = 0.71073)	MoKα (λ = 0.71073)
2Θ range for data collection(°)	5.914 to 54.496	5.824 to 55.686	5.164 to 56.942
Index ranges	$-17 \le h \le 17$, $-8 \le k \le 8$, $-21 \le l \le 21$	$-19 \le h \le 20$, $-8 \le k \le 8$, $-22 \le l \le 22$	$-23 \le h \le 23$, $-10 \le k \le 10$, $-29 \le l \le 31$
Reflections collected	20770	24041	25769
Independent reflections	3490	3722	3762
Data/restraints/parameters	3490/0/205	3722/0/206	3762/1/216
Goodness-of-fit on F^2	1.046	0.952	1.038
Final R indexes [I>=2σ (I)]	R_1 = 0.0589, wR_2 = 0.1650	R1 = 0.0537, wR2 = 0.1343	R1 = 0.0761, wR2 = 0.1643
Final R indexes [all data]	R_1 = 0.0900, wR_2 = 0.1901	R1 = 0.0947, wR2 = 0.1566	R1 = 0.0978, wR2 = 0.1982
Largest diff.peak/hole/e Å^{-3}	0.50/-0.33	0.19/-0.26	0.44/-0.47

The supramolecular framework of compound 1.3D: The molecular packing in compound **1.3D** involves a strong non-covalent N-H…O intermolecular hydrogen bond with a bond distance of 1.913Å, which facilitates the asymmetric dimerization as well as the self-assembly of the compound that forms a supramolecular network. The carbonyl carbon also interacts with the hydrogen of the amine within the pyridone moiety, forming N-H…C interactions with a bond distance of 2.82(3)Å. These N-H…O and N-H…C interactions that arise from the carbonyl and amine moiety of the pyridone ring also adopts the formation of $R_2^2(6)$ and $R_2^2(8)$ graph sets **(Figure 2.35 (b))**. The intermolecular hydrogen bond interactions observed in the single crystal structure of **1.3D** are summarized in **Table 2.10**.

Table 2.10: Hydrogen bonds and other interactions in compound **1.3D**

Donor-H...Acceptor	**D – H, Å**	**H...A, Å**	**D...A, Å**	**D - H...A, º**
N2-H2…O1	0.863	1.913	2.775	175.65
N2-H2…C10	0.863	2.816	3.638	159.55
C1-H1…N1	0.930	2.718	3.641	172.16
C3-H3…N1	0.930	2.625	3.287	128.56
C5-H5…O2	0.930	2.542	3.452	166.19
C12-H12A…O1	0.960	2.683	3.642	177.17
C15-H15A…O1	0.970	2.676	3.451	137.16
C15-H15A…C10	0.970	2.820	3.534	131.11
C2H2…π(C1-C6)	0.930	3.251	4.014	140.58
C12-H12B…π (C7,C8,C10,C11,C13,N2)	0.960	3.118	4.022	157.60
C16-H16B…π (C7,C8,C10,C11,C13,N2)	0.960	3.169	3.787	123.70
Intramolecular				
C12-H12B…O2	0.960	2.410	2.921	112.92
C15-H15B…O2	0.970	2.530	2.703	89.60
C15-H16C…π(C1-C6)	0.960	3.083	3.892	142.80

The pyridone moiety's carbonyl oxygen (O1) also acts as trifurcated hydrogen acceptor. The nitrogen (N1) from the nitrile substituent of the pyridone ring had a partial negative character in interacting with intermolecular atoms. The trifurcated acceptor (O1), the nitrogen (N1) of the nitrile group, and the carbonyl oxygen (O2) of the ester substituent established hydrogen interactions which assist the polymeric linear chain connectivity forming C12-H12A…O1, C5-H5…O2 and C1-H1…N1 at an interaction distance of 2.683Å, 2.542Å and 2.718Å that leads to the formation of $R_2^2(13)$ and $R_2^2(14)$ graph sets **(Figure 2.35 (c))**. C-H…O interactions between the alkyl hydrogen with the trifurcated acceptor oxygen (O2) in a parallel displace fashion also binds together the pair of asymmetric dimer, together along with the N-H…O interactions form $R_4^2(12)$ graph set **(Figure 2.35 (d))**. It is also observed that the nitrogen (N1) acts as a bifurcated acceptor and forms C-H…N interactions with the phenyl hydrogen from the same polymeric chain and with the phenyl hydrogen from a different layer, thus playing a crucial role in linking between the two polymeric chain layers. The polymeric interlayer connectivity adopted by the bifurcated acceptor N1 results in the formation of anti-parallel interlayer connections between the polymeric chain giving the $R_3^2(15)$ graph set **(Figure 2.35 (e))**. C-H…N interactions formed the bifurcated acceptor N1 assists the interaction between the consecutive crystal packing, together with the C-H…O intermolecular interactions between the ester substituent and the trifurcated acceptor O2 also give rise to $R_4^4(32)$ graph set **(Figure 2.35 (f))**. C-H…π interaction is also formed between the hydrogen (H2) and the benzenoid ring at a distance of 3.251 Å. Another two C-H…π interactions between the pyridone ring with the hydrogen (H12B) from the alkyl substituent and the hydrogen (H16B) from the ester moiety at a distance of 3.118Å and 3.169Å respectively, also stabilizes the crystal packing within the unit cell.

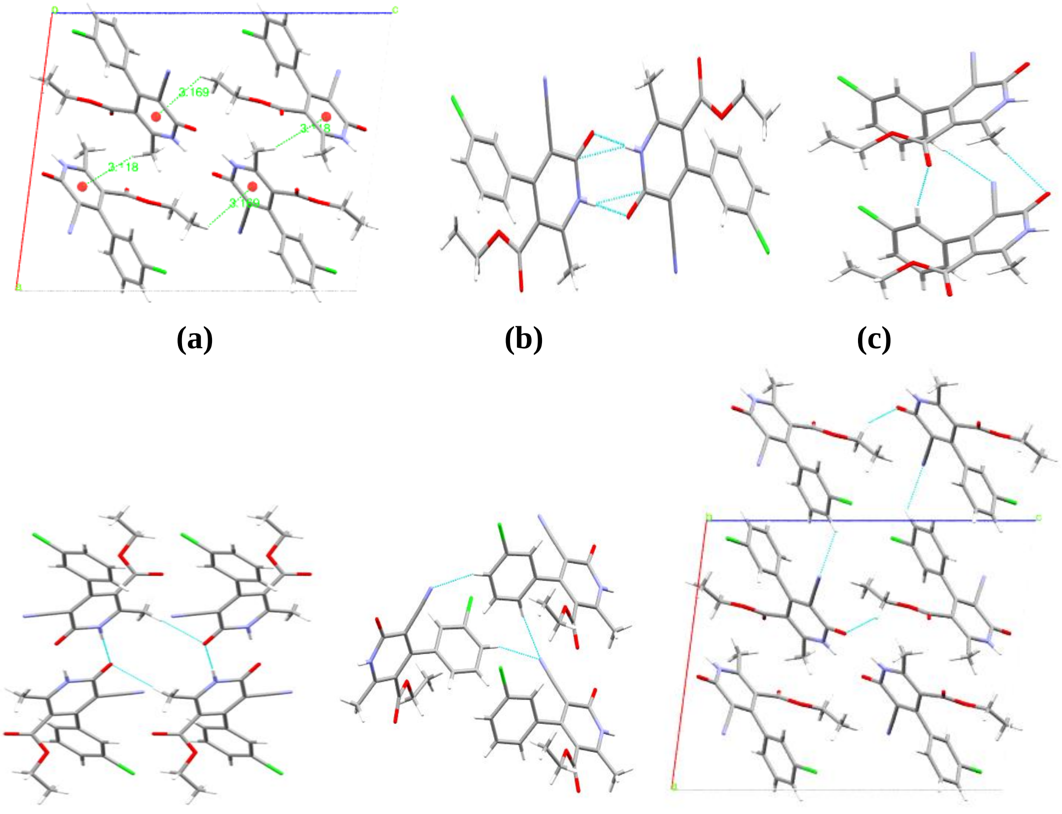

(a) (b) (c)

(c) (e) (f)

Figure 2.35: (a) Packing diagram of **1.3D**, (b), (c), (d), (e) and (f) Graph sets with non-covalent interactions in compound **1.3D**

Hirshfeld surface analysis of compound 1.3D: The Hirshfeld surface of compound **1.3D** mapped over a d_{norm} range of -0.65 to 1.49 is demonstrated in **Figure 2.36 (a) and (b)**. The region of bright red spots, which are comparatively larger than other red bumps, represents more dominant non-covalent strong N-H…O intermolecular interactions. The other red light spots on the d_{norm} surface arise due to C-H…O, C-H…C, and C-H…N interactions. The 2-D fingerprint plots of compound **1.3D** are shown in figure **(Figure 2.36 (c))**. The presence of O…H/H...O appears as a pair of distinct spikes, where the lower spike indicates an acceptor spike (O-atoms interacting with H-atoms, di>de). In contrast, the upper spike corresponds to a donor spike (H-atoms interacting with the O-atoms, di<de). The C…H intermolecular interactions in compound **1.3D** occupy a distinct region on the 2-D fingerprint plot. Similarly, other intermolecular interactions like H...H and N...H also appear at distinct points in the 2-D fingerprint plot. The yellowish-red bin is absent on the fingerprint plots, which means the absence of weak $\pi...\pi$ stacking in crystal packing. The relative percentage contributions to the Hirshfeld surface by different interactions in the descending values are as follows. In compound **1.3D** there are H...H (24.5 %), O...H (20.7%), C...H (18.5%), N...H (15.5%), Cl...H (14.6%), C…O (1.8%), Cl…Cl (1.7%), N…O (1%), C…N (0.7%), Cl...N (0.5%), Cl...C (0.4%), C…C (0.1%). The existence of C-H…π intermolecular interactions in compound **1.3D** displays a characteristic flipped wing-like pattern in the 2-D fingerprint plot. However, these weak C-H…π interactions decomposed into the C…H contacts in the 2-D fingerprint plot. The relative contribution of C…C close contacts, which account for 0.1% in **1.3D**, also indicates no significant aromatic $\pi...\pi$ stacking interaction.

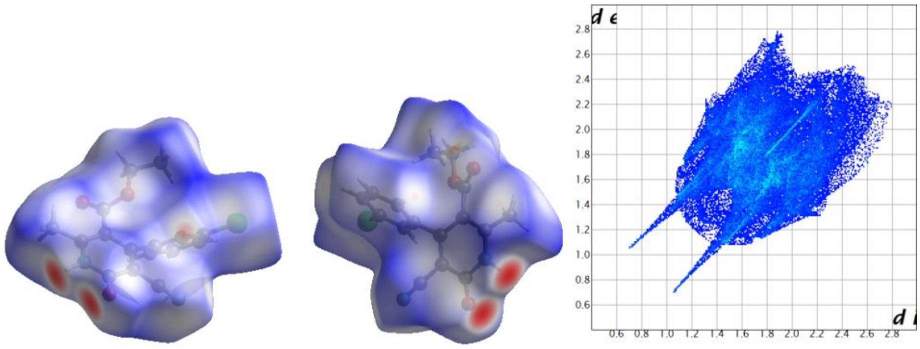

(a) **(b)** **(c)**

Figure 2.36: (a) and (b) d_{norm} both side view, (c) 2-D fingerprint plot, of compound **1.3D**

The Hirshfeld surface mapped over the shape-index in a range of -1 to 1Å for compound **1.3D** does not have red and blue triangles with edge-to-edge reciprocal connections in the region of the aromatic ring surface **(Figure 2.37 (a) and (b))**. Thus, indicating the absence of π...π stacking interactions between the aromatic ring within the crystal packing and the supramolecular structures. Similarly, the Hirshfeld surface mapped over the curvedness in a range of -4 to 0.4 Å for compound **1.3D** also display the absence of a flat green region around the two aromatic ring surface **(Figure 2.37 (c) and (d))**, which also again signifies the lack of π...π stacking interactions between the aromatic rings.

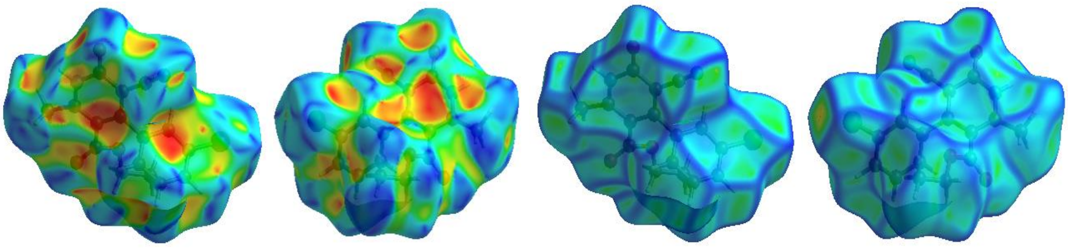

(a) **(b)** **(c)** **(d)**

Figure 2.37: (a) and (b) Shape-index, (c) and (d) Curvedness, both side views of compound **1.3D**

Although C-H…π interactions decompose within the C…H contacts in the 2-D fingerprint plot, however, the single-crystal analysis, as well as the supramolecular self-assembly within the 3.8 Å radius calculated for the Hirshfeld, shows the evidence of C-H…π intermolecular interaction within the pyridone ring and benzenoid ring surface.

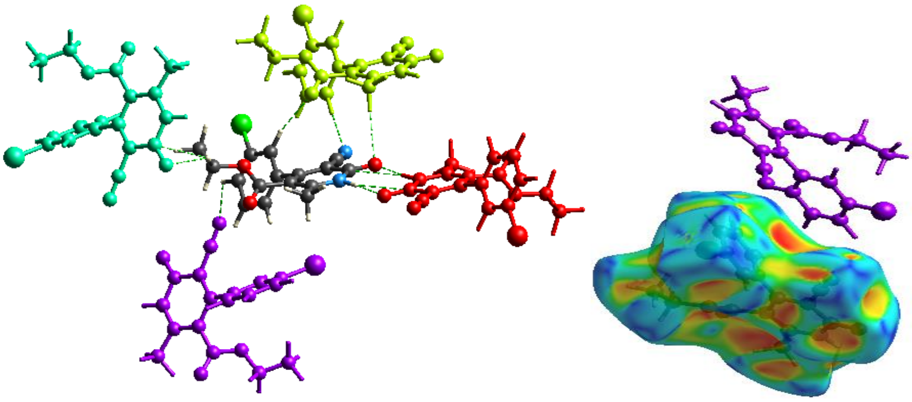

(a) **(b)**

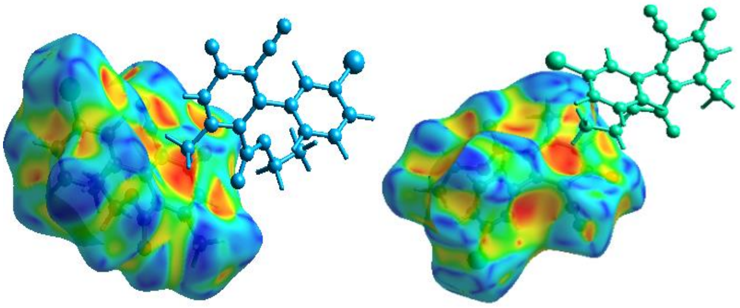

(c) **(d)**

Figure 2.38: (a) Non-covalent Hydrogen bonding, (b),(c) and (d) C-H…π interactions, in compound **1.3D**

The Hirshfeld surface mapped over the shape index shows a distinct yellowish-red colored concave surface around the benzenoid and pyridone rings surface. The red concave region around the aromatic ring surface is reserved for C-H…π interaction that fits and occupies that region. The C-H...π mentioned above and other non-covalent interactions found from the Hirshfeld analysis are illustrated in **Figure 2.38**.

2.5.1.8. Crystal analysis of compound 1.3E

The compound **1.3E** was recrystallized in ethanol at room temperature by slow evaporation of the solvent. The chiral asymmetric compound **1.3E** was analyzed using SC-XRD **(Figure 2.39)**. The compound crystallized with cell lengths **a** = 15.502(6), **b** = 6.588(3), **c** = 17.198(7) i.e., $\mathbf{a} \neq \mathbf{b} \neq \mathbf{c}$ and cell angles $\boldsymbol{\alpha}$ = 90°, $\boldsymbol{\beta}$ = 115.496(5)°, $\boldsymbol{\gamma}$ = 90° i.e., $\boldsymbol{\alpha = \gamma = 90}$°, $\boldsymbol{\beta \neq 90}$° which indicate that the compound is exhibiting a monoclinic crystal system, with space group $P2_1/n$ that contains four molecules per unit cell.

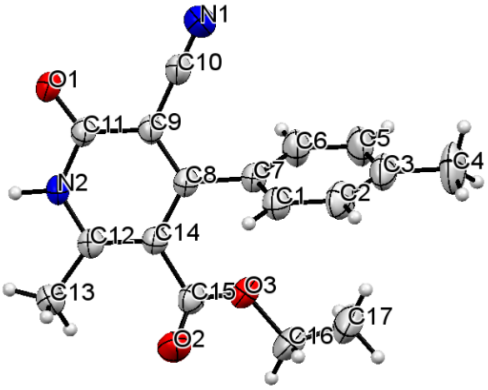

Figure 2.39: ORTEP diagram of compound **1.3E**

The crystal structure of the asymmetric chiral compound **1.3E** shows that both the pyridone and phenyl ring adopts a planar cyclic system. The phenyl ring twisted away from the parent pyridone ring plane at a torsion angle of 57.17°. Both rings are arranged in the AB pattern in the orthogonal pattern in crystal packing. The summary of crystallographic information is listed in **Table 2.9**.

The supramolecular framework of compound 1.3E: The molecular packing in compound **1.3E** involves a strong non-covalent N-H…O intermolecular hydrogen bond with a bond distance of 1.916Å, which facilitates the asymmetric dimerization as well as the self-assembly of the compound that forms a supramolecular network. The carbonyl carbon of the pyridone ring also interacts with the hydrogen of the amine within the pyridone moiety, forming N-H…C interactions with a bond distance of 2.815Å. These N-H…O and N-H…C interactions that arise from the carbonyl and amine moiety of the pyridone ring also adopts the formation of $R_2^2(6)$ and $R_2^2(8)$ graph sets **(Figure 2.40 (b))**. The hydrogen bonds and other interactions observed in the single crystal structure of **1.3E** are summarized in **Table 2.11**.

Table 2.11: Hydrogen bonds and other interactions in compound **1.3E**

Donor-H...Acceptor	**D – H,Å**	**H...A,Å**	**D...A,Å**	**D - H...A,°**
N2-H2…O1	0.913	1.916	2.821	170.74
N2-H2…C11	0.913	2.815	3.668	155.99
C6-H6…O2	0.930	2.403	3.313	166.10
C16-H16A…O1	0.970	2.718	3.464	134.11
C13-H13A…π(C8,C9,C11,C12,C14,N2)	0.960	3.835	4.750	160.87
C13-H13B…π(C8,C9,C11,C12,C14,N2)	0.960	3.294	4.239	168.31
C17-H17A…π(C8,C9,C11,C12,C14,N2)	0.960	3.040	3.818	139.06
Other interactions				
π(C1-C3,C5-C7)…π(C1-C3,C5-C7)		4.266		
O3…C13			3.146	
Intramolecular				
C13-H13A…O2	0.960	2.788	2.888	86.21
C13-H13B…O2	0.960	2.562	2.888	99.98
C16-H16A…O2	0.970	2.717	2.701	78.77
C16-H16B…O2	0.970	2.642	2.701	82.98
C17-H17B…π(C1-C3,C5-C7)	0.960	3.152	3.923	138.53

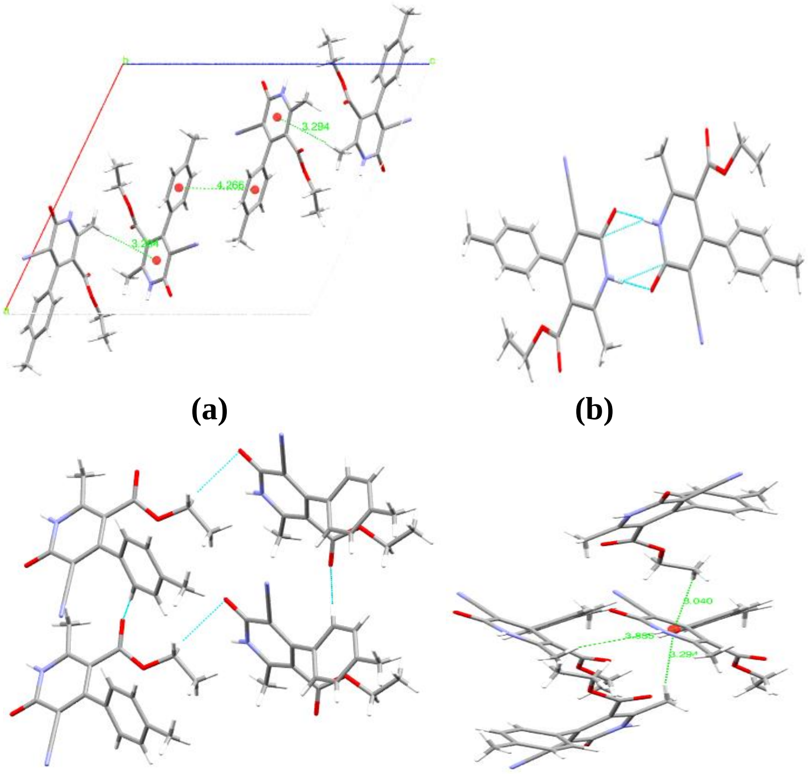

(a) **(b)**

(c) **(d)**

Figure 2.40: (a) Packing diagram of compound **1.3E**, (b) and (c) Graph sets, and (d) C-H…π interactions in compound **1.3E**

The pyridone's carbonyl oxygen (O1) acts as a bifurcated acceptor and forms C-H…O interaction with the hydrogen from the ester substituents at a distance of 2.718Å. The carbonyl oxygen (O2) of the ester substituent also forms a C-H…O bond with the benzenoid hydrogen at a distance of 2.403Å. These two C-H…O bond acts as interlayer connectivity between different polymeric chain and also forms another graph set of $R_4^4(28)$ **(Figure 2.40 (c))**. The crystal packing is also stabilized by dipole-dipole interaction that arises between the alkyl substituents of the pyridone and the oxygen (O3) of the ester substituents at an interaction distance of 3.146Å. C-H…π and π...π stacking also assist the crystal packing of compound **1.3E (Figure 2.40 (a))**. The hydrogen (H13A) and (H13B) from the pyridone alkyl substituents interacts with the pyridone ring from the same side and forms C-H…π interaction at a distance of 3.835Å and 3.294Å respectively. The hydrogen (H17A) from the ester moeity forms C-H…π interactions with the pyridone ring at a distance of 3.040Å **(Figure 2.40 (d))**. The overall structure supramolecular network of compound **1.3E** thus exhibits a combination of parallel displaced $\pi...\pi$, C-H…π, C-H…O, N-H…O, N-H…C, and dipole-dipole interaction.

Hirshfeld surface analysis of compound 1.3E: The Hirshfeld surface mapped over the d_{norm} in the range of -0.60 to 1.45Å for compound **1.3E** is displayed in **Figure 2.41 (a) and (b)**. The region of bright red spots, which are comparatively more significant than the other, corresponds to N-H…O contacts which are more dominant intermolecular interactions. The regions of pale red spots were due to weaker C-H…N and C-H…C interactions. The other lighter white and blue regions of the Hirshfeld surface indicate weaker interactions due to more extended contacts, which are more significant or equal to the van der Waals interatomic distances.

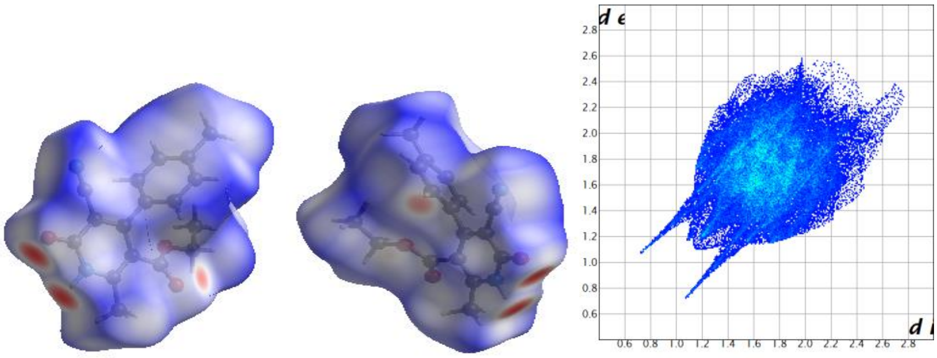

(a) **(b)** **(c)**

Figure 2.41: (a) and (b) d_{norm} both side view, (c) 2-D fingerprint plot, of compound **1.3E**

The 2-D fingerprint plots of compound **1.3E** show the relative percentage contributions of non-covalent interaction to the Hirshfeld surface **(Figure 2.41 (c))**. Those are H…H (42.3%), O…H (21.1%), N…H (17.3%), C…H (15.3%), C…O (1.4%), C…C (1.3%), C…N (0.7%) and N…O (0.6%). The O…H/H...O interactions appear as a pair of distinct spikes in the 2-D fingerprint plot of compound **1.3E** in the region of di + de = 1.8-2.8Å. C…H/H...C intermolecular interactions also occupy the basal region of the spike in the 2-D fingerprint plot in the region of di + de = 2.8-3.9Å. C-H…π interactions found within the supramolecular framework decomposed within the C…H contacts in the 2-D fingerprint plot. Similarly, N...H/H...N intermolecular interactions are also reflected close to the C…H contacts but closer to the O…H contacts in the 2-D fingerprint plot in the region of di + de = 2.6-3.2Å as distinct points in the 2-D fingerprint plot. The relative contribution of C…C close contacts, which account for 1.3% in the region of di + de = 3.7-4.3Å, indicates aromatic ring π…π stacking interactions.

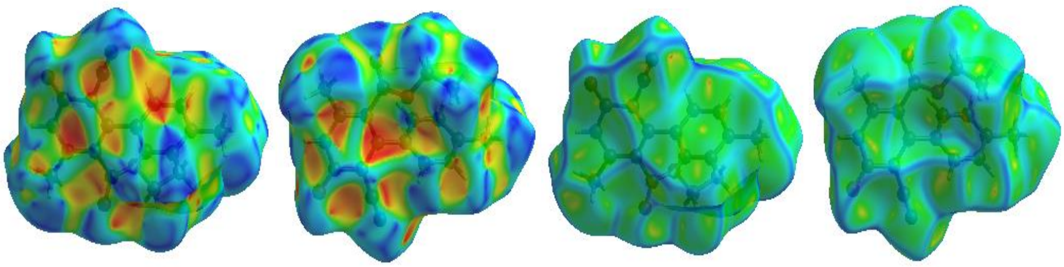

Figure 2.42: (a) and (b) Shape-index, (c) and (d) Curvedness, both side views of compound **1.3E**

The red region indicates acceptor property in the shape index, and the blue region indicates donor property. The Hirshfeld surface mapped over the shape-index in a range of -1 to 1Å for compound **1.3E** shows the presence of red and blue triangles with edge-to-edge reciprocal connection in the region of the pyridone ring surface **(Figure 2.42 (a))**. Thus, indicating the presence of π...π stacking interactions between the benzenoid rings within the crystal packing. The yellowish-red colored bins in the shape index around the surface of the pyridone ring in compound **1.3E** indicate the presence of C-H...π interactions **(Figure 2.42 (b))**. Similarly, the Hirshfeld surface mapped over the curvedness in a range of -4 to 0.4 Å also display the presence of a flat green region with a yellowish spot around the benzenoid ring surface, which indicate the presence π...π stacking interactions between the benzenoid rings **(Figure 2.42(c))**.

The intermolecular interactions within the cluster of 3.8Å around a single crystal fragment calculated for the Hirshfeld interactions also confirm the presence of weak non-covalent intermolecular interactions as in crystal packing, where N-H…O, N-H…C, C-H…O, C-H…π and π…π stacking intermolecular interactions and are shown in **Figure 2.43**.

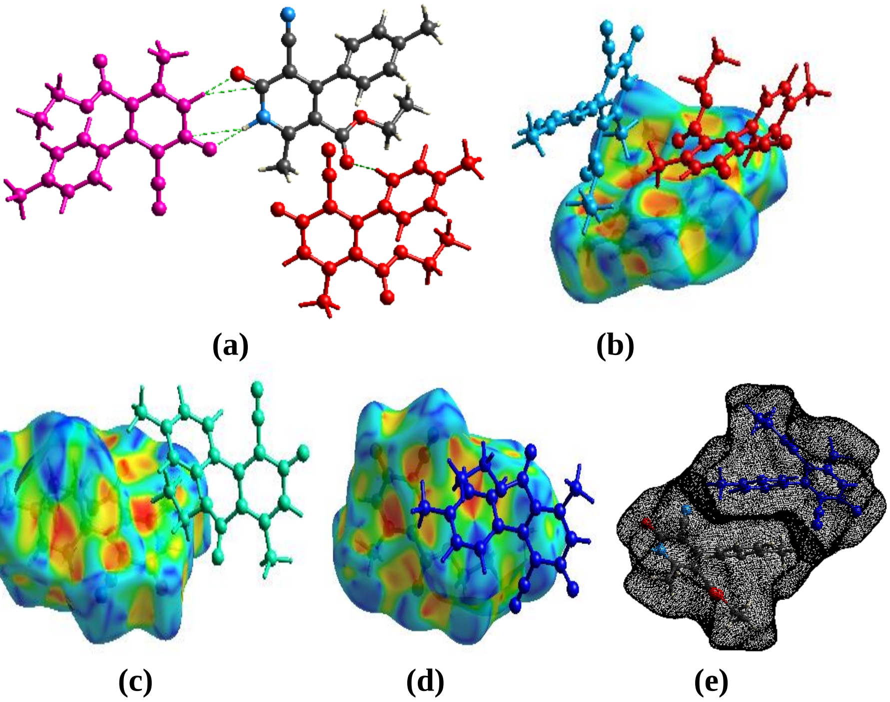

(a) (b)

(c) (d) (e)

Figure 2.43: (a) N-H…O, N-H…C and C-H…O interactions, (b) and (c) C-H…π interactions, (d) and (e) π…π interaction, in compound **1.3E**

2.5.1.9. Crystal analysis of compound 1.3F

The compound **1.3F** was recrystallized in ethanol at room temperature by slow evaporation of the solvent. The chiral asymmetric compound **1.3F** was analyzed using SC-XRD **(Figure 2.44)**. The compound crystallized with cell lengths **a** = 18.470(3)Å, **b** = 8.456(4)Å, **c** = 23.200(3)Å, i.e., **a** ≠ **b** ≠ **c** and cell angles $\boldsymbol{\alpha}$ = 90°, $\boldsymbol{\beta}$ = 109.360(2)°, $\boldsymbol{\gamma}$ = 90°, i.e., $\boldsymbol{\alpha = \gamma = 90°, \beta \neq 90°}$ which indicate that the compound is exhibiting a monoclinic crystal system, with space group I2/a that contains eight molecules per unit cell.

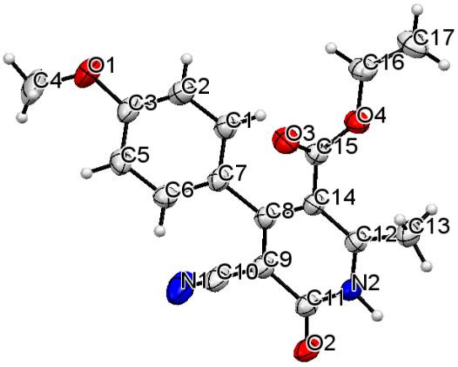

Figure 2.44: ORTEP diagram of compound **1.3F**

The chiral asymmetric compound **1.3F** crystal structure shows that both the pyridone and phenyl ring adopt planar cyclic systems. The plane of the two aromatic rings twisted way from each other at a dihedral angle of 54.23°. Both rings are arranged in the AB pattern in the orthogonal pattern in crystal packing. The crystallographic information is summarized in **Table 2.9**.

The supramolecular framework of compound 1.3F: The supramolecular framework of compound **1.3F** involves a strong non-covalent N-H…O intermolecular hydrogen bond with a bond distance of 1.942Å that results in the formation of an asymmetric dimer. The carbonyl carbon (C11) of the pyridone ring also interacts with the hydrogen of the amine within the pyridone moiety, forming N-H…C interactions with a bond distance of 2.892Å. These N-H…O and N-H…C interactions that arise from the carbonyl and amine moiety of the pyridone ring also adopts the formation of $R_2^2(6)$ and $R_2^2(8)$ graph sets **(Figure 2.45 (b))**. The carbonyl oxygen (O3) from the ester substituents also forms an intermolecular hydrogen bond at a distance of 2.676Å with hydrogen (H16A) from the ester group of the successive layer of the crystal packing. Hydrogen (H2) from the benzenoid ring interacts with the pyridone p-orbital, for which the C-H…π interaction distance is 3.471Å. There are also two C-H…π intermolecular interactions observed within the benzenoid ring at an interaction distance of 3.343Å and 3.114Å, respectively, from the methoxy hydrogen (H4C) and hydrogen (H13C) from the alkyl substituent of the pyridone ring**(Figure 2.45 (c) and (d))**. Apart from these, an overlapping of the pyridone ring has been observed and the resultants $\pi…\pi$ stacking interaction distance is 4.455Å which is much weaker than the usual $\pi…\pi$ stacking interactions found for another benzenoid ring **(Figure 2.45 (d))**. The hydrogen bonds and other interactions observed in the single crystal structure of **1.3F** are summarized in **Table 2.23**.

Table 2.12: Hydrogen bonds and other interactions in compound **1.3F**

Donor-H...Acceptor	**D – H, Å**	**H...A, Å**	**D...A, Å**	**D - H...A, °**
N2-H2…O2	0.928	1.942	2.870	179.23
N2-H2…C11	0.928	2.892	3.779	160.15
C16-H16A…O3	0.970	2.676	3.645	177.42
C2-H2A…π(C8,C9,C11,C12,C14,N2)	0.930	3.471	4.371	163.54
C4-H4C…π(C1-C3, C5-C7)	0.960	3.343	4.291	170.16
C13-H13C…π(C1-C3, C5-C7)	0.960	3.114	4.034	161.13
Other contact				

π(C8,C9,C11,C12,C14,N2)…π (C8,C9,C11,C12,C14,N2)		4.455		
Intramolecular				
C1-H1…O4	0.930	2.983	3.598	125.02
C13-H13B…O4	0.960	2.897	3.172	97.73
C16-H16A…O3	0.970	2.784	2.748	77.82
C16-H16B…O3	0.970	2.665	2.748	85.54

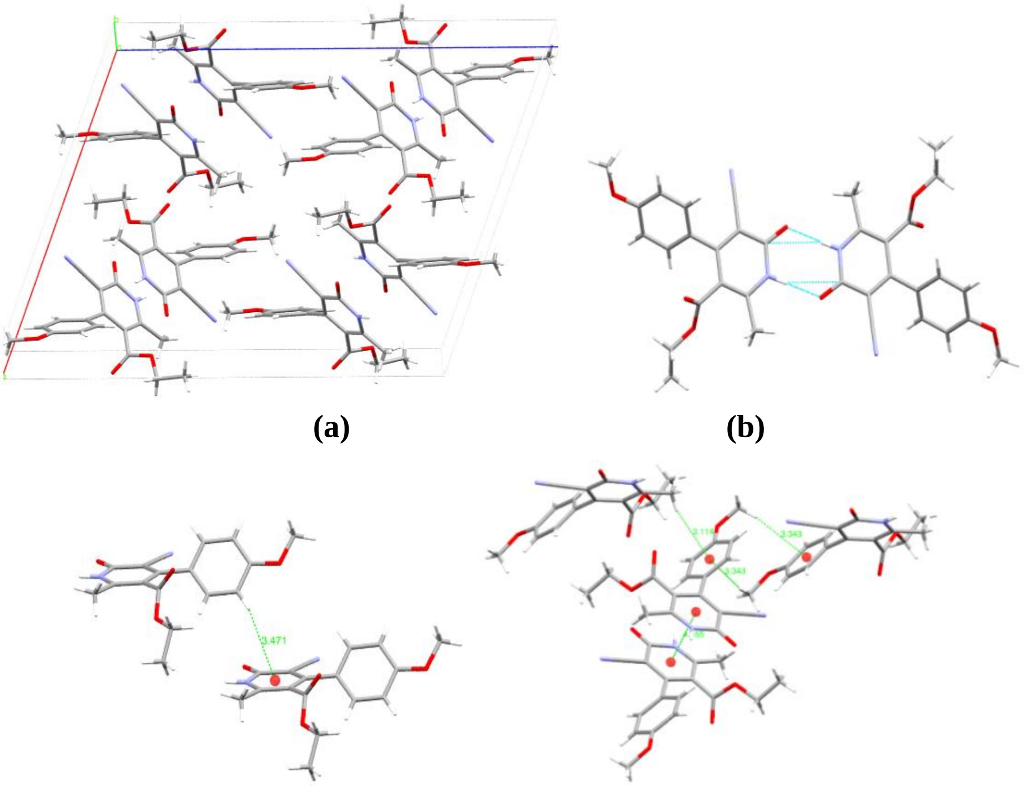

(a) (b)

(c) (d)

Figure 2.45: (a) Packing diagram of compound **1.3F**, (b) Graph sets, (c) C-H…π, and (d) C-H…π and π…π interactions in compound **1.3F**

Hirshfeld surface analysis of compound 1.3F: The Hirshfeld surface mapped over the d_{norm} in the range of -0.57 to 1.66Å for compound **1.3F** is displayed in **Figure 2.46 (a) and (b)**. The lighter white and blue regions of the Hirshfeld surface indicate weaker interactions due to more extended contacts, which are more significant or equal to the van der Waals interatomic distances. The region of bright red spots represents more dominant non-covalent strong N-H…O intermolecular interactions. The other red light spot on the d_{norm} surface arises due to C-H…O interactions.

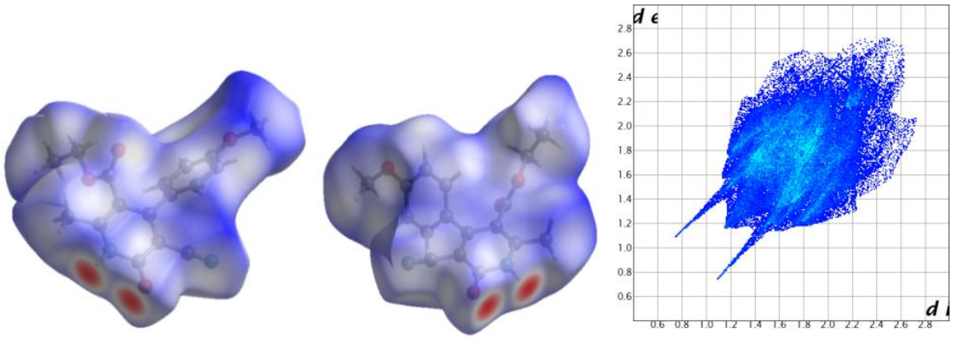

(a) **(b)** **(c)**

Figure 2.46: (a) and (b) d_{norm} both side view, (c) 2-D fingerprint plot, of compound **1.3F**

The 2-D fingerprint plots of compound **1.3F** show the relative percentage contributions of non-covalent interaction to the Hirshfeld surface **(Figure 2.46 (c))**. Those are H…H (35.6%), O…H (24.9%), C…H (18.3%), N…H (15.7%), C…O (2.7%), C…C (1.7%), O…O (0.7%), N…O (0.4%). The presence of O…H/H...O interactions appears as a pair of distinct spikes in the 2-D fingerprint plot of compound **1.3F** in the region of di + de = 1.8-2.8Å, C…H/H...C intermolecular interactions also appear as a characteristic wing-like pattern in the 2-D fingerprint plot in the region of di + de = 2.8-3.8Å. Although C-H…π intermolecular interactions in compound **1.3F**, however these weak C-H…π interactions decomposed within the C…H contacts in the 2-D fingerprint plot. Similarly, N...H/H...N intermolecular interactions are also reflected around characteristic wings occupied in the region of di + de = 2.6-3.2Å as distinct points in the 2-D fingerprint plot. The relative contribution of C…C close contacts, which account for 1.7%, indicates aromatic ring π…π stacking interactions.

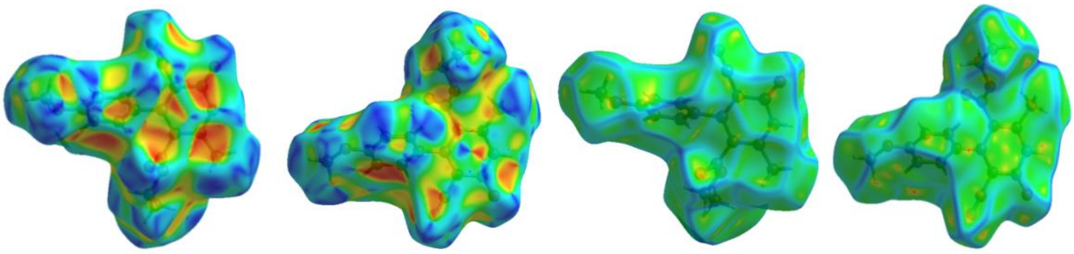

(a) **(b)** **(c)** **(d)**

Figure 2.47: (a) and (b) Shape-index, (c) and (d) Curvedness, both side views of compound **1.3F**

The Hirshfeld surface mapped over the shape-index in a range of -1 to 1Å for compound **1.3F** shows the presence of red and blue triangles around the pyridone ring's surface, which indicates the presence of π...π stacking interactions between the pyridone rings **(Figure 2.47 (b))**. The yellowish-red colored bins in the shape-index around the surface of the pyridone and the benzenoid rings in compound **1.3F** indicate the region of weak interactions compatible for C-H...π to occur **(Figure 2.47 (a) and (b))**. The curvedness Hirshfeld surface in a range of -4 to 0.4Å also displays the presence of a flat green region with a yellowish spot around the pyridone ring surface, which again confirms the presence of π...π stacking interactions between the pyridone rings **(Figure 2.47 (d))**.

The Hirshfeld weak interactions calculation also supports the presence of weak non-covalent intermolecular interactions as in crystal packing, where N-H…O, C-H…O, C-H…π, and π…π stacking intermolecular interactions are found within the cluster of radius 3.8Å around a single crystal fragment. Those interactions are in **Figure 2.48.**

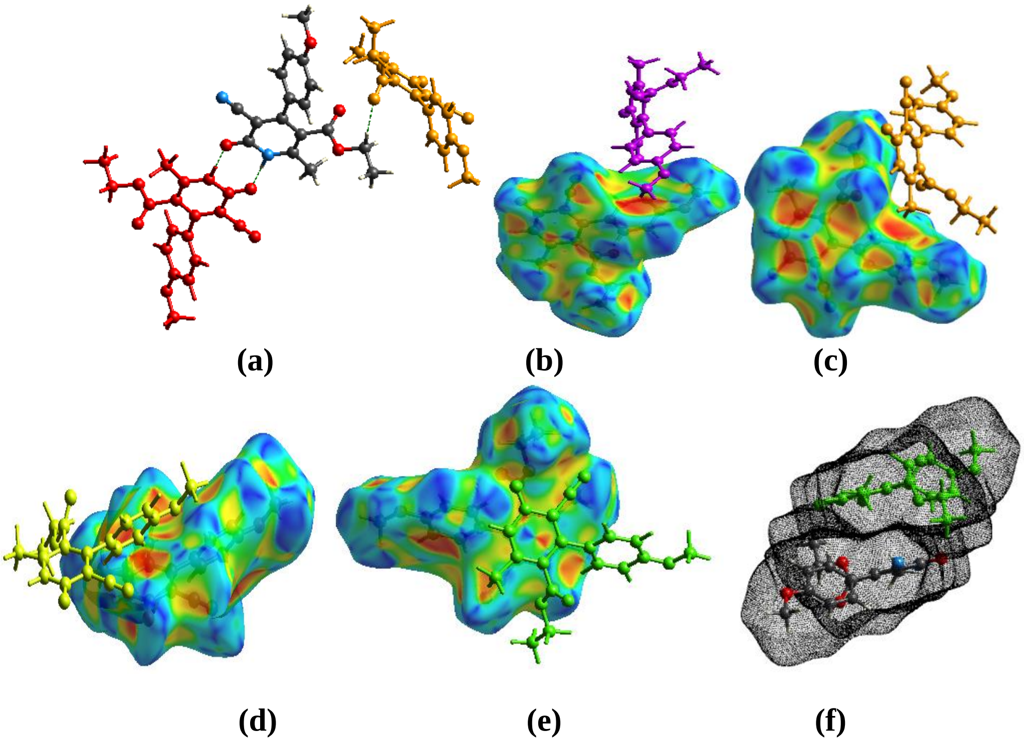
(a) **(b)** **(c)**

(d) **(e)** **(f)**

Figure 2.48: (a) N-H…O and C-H…O interactions, (b), (c) and (d) C-H…π interactions, (e) and (f) π…π interaction, in compound **1.3F**

2.6. Synthesis of hetero-polycyclic 2-oxo-3,4-dihydro-2H-benzo[h]chromene derivatives

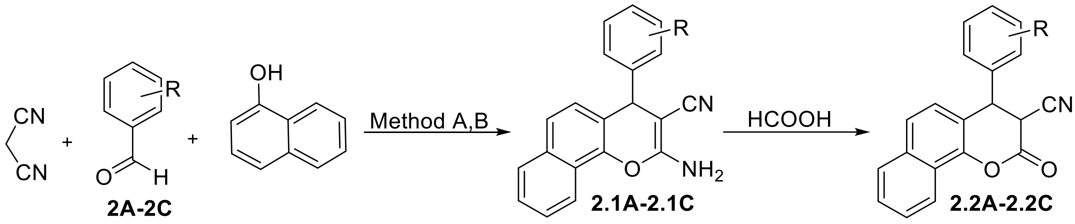

R= 3-OH, 2,5-OCH$_3$, 4-Cl
Entry= A, B, C

Scheme 2

In scheme 2, traditional 2-amino-4H-benzo[h]chromene **(2.1A-2.1C)** was synthesized by two different methods using piperidine and sodium carbonate as a catalyst under reflux and grinding techniques, respectively. The product 2-amino-4H-benzo[h]chromene **(2.1A-2.1C)** was then reacted with formic acid to obtain 3,4-dihydro-2H-benzo[h]chromene derivatives **(2.2A-2.2C)**.

2.7. Experimental

^{1}H NMR (300 MHz) and ^{13}C NMR (75 MHz) spectra were recorded on JEOL AL300 FTNMR spectrometer using TMS as an internal reference, and chemical shift values are expressed in δ, ppm units. Melting points of all the compounds were recorded on the electrically heated instrument and are uncorrected. All the reactions were monitored by thin-layer chromatography (TLC) on pre-coated aluminum sheets of Merck using ethyl acetate and hexane as an eluent, and chromatograms were visualized under UV light.

2.7.1. General procedure for the synthesis of 2-amino-4H-benzo[h]chromenes (2.1A-2.1C)

Method A: To a 100 mL RB, malononitrile (1.5 mmol), aldehyde (1.5 mmol), and 1-naphthol (1.5 mmol) were taken and dissolved in 50 mL of ethyl alcohol. Piperidine (20 mol%) was added to the mixture and then refluxed at 80°C for 6 hours. The reaction was monitored by TLC (eluent ethyl acetate and hexane). After completion of the reaction, the ethyl alcohol solvent was reduced in a rotary evaporator, and the precipitate obtained was filtered with ice-cooled methanol to get the pure product **(2.1A-2.1C)**.

Method B: A stoichiometric mixture of aldehyde (1.5 mmol), malononitrile (1.5 mmol), 1-naphthol (1.5 mmol), and anhydrous sodium carbonate (1.5 mmol) were added to a mortar, and then ground with a pestle at room temperature for 30 minutes. The reaction was monitored by TLC (eluent ethyl acetate and hexane). After completion of the reaction, the mixture was subjected to a vacuum sintered funnel and washed with hot distilled water to remove unreacted sodium carbonate and its by-product. The precipitate product was dried and then recrystallized from ethanol to get the pure product **(2.1A-2.1C)**.

2.7.1.1. 2-amino-4-(3-hydroxyphenyl)-4H-benzo[h]chromene-3-carbonitrile (2.1A): Pale yellow solid, yield: 87%, m.p. 252-254°C; **^{1}H NMR (300 MHz, $CDCl_3$+DMSO):** δppm 4.74 (1H, s, CH); 5.99 (2H, s, NH_2); 6.66 – 6.68 (1H, d, Ar-H, J = 8.2 Hz); 6.72 – 6.74 (1H, d, Ar-H, J = 7.6 Hz); 7.05 – 7.12 (2H, m, Ar-H); 7.48 – 7.55 (3H, m, Ar-H); 7.57 (1H, s, Ar-H); 7.76 – 7.78 (1H, d, Ar-H, J = 7.8 Hz); 8.23- 8.25 (1H, d, Ar-H, J = 8.1 Hz); 8.86 (1H, s, OH).

2.7.1.2. 2-amino-4-(2,5-dimethoxyphenyl)-4H-benzo[h]chromene-3-carbonitrile (2.1B): White solid, yield: 86%, m.p. 261-260°C; **^{1}H NMR (300 MHz, $CDCl_3$):** δppm 3.66 (3H, s, CH_3); 3.83 (3H, s, CH_3); 4.73 (2H, s, NH_2); 6.59 (1H, s, CH); 6.60 (1H, s, Ar-H); 6.70 – 6.73 (1H, d, Ar-H, J = 8.7 Hz); 6.83 – 6.86 (1H, d, Ar-H, J = 8.7 Hz); 7.11 – 7.14 (1H, d, Ar-H, J = 8.7 Hz); 7.46 – 7.57 (3H, m, Ar-H); 7.75 – 7.78 (1H, d, Ar-H, J = 8.7 Hz); 8.13 – 8.16 (1H, d, Ar-H, J = 8.7 Hz).

2.7.1.3. 2-amino-4-(4-chlorophenyl)-4H-benzo[h]chromene-3-carbonitrile (2.1C): Pale yellow solid, yield: 93%, m.p. 231-233°C; **^{1}H NMR (300 MHz, $CDCl_3$):** δppm 4.78 (2H, s, NH_2); 4.86 (1H, s, CH); 6.96 – 6.99 (1H, d, Ar-H, J = 8.7 Hz); 7.14 – 7.19 (2H, m, Ar-H); 7.26 – 7.31 (2H, m, Ar-H); 7.50 – 7.61 (3H, m, Ar-H); 7.78 – 7.81 (1H, d, Ar-H, J = 8.7 Hz); 8.13 – 8.16 (1H, d, Ar-H, J = 8.7 Hz).

2.7.2. General procedure for the synthesis of 2-oxo-3,4-dihydro-2H-benzo[h]chromenes (2.2A-2.2C)

To a 50 mL RB, each of the 2-amino-4H-benzo[h]chromene derivatives **(2.1A-2.1C)** (3 mmol) and excess formic acid (20 mL) was taken and refluxed at 115°C for 3 hours. The reaction was monitored by TLC (eluent ethyl acetate and hexane). After completion of the reaction, it was subjected to a rotary evaporator to reduce the formic acid. The precipitate was then recrystallized from acetone to get pure crystals of the product **(2.2A-2.2C)**.

2.7.2.1. 4-(3-hydroxyphenyl)-2-oxo-3,4-dihydro-2H-benzo[h]chromene-3-carbonitrile (2.2A): Yellow solid, yield: 97%, m.p. 260-262°C; **^{1}H NMR (300 MHz, $CDCl_3$):** δppm 4.14 – 4.17 (1H, d, CH, *J* = 8.7); 4.70 – 4.73 (1H, d, CH, *J* = 8.7 Hz); 6.65 (1H, s, Ar-H); 6.70 – 6.99 (3H, m, Ar-H); 7.20 – 7.23 (1H, d, Ar-H, *J* = 8.7 Hz); 7.32 – 7.35 (1H, d, Ar-H, *J* = 8.7 Hz); 7.59 – 7.70 (3H, m, Ar-H); 7.84 – 7.87 (1H, d, Ar-H, *J* = 8.7 Hz); 8.30 (1H, s, OH); **^{13}C NMR (75 MHz, $CDCl_3$):** δppm 35.1, 43.3, 113.3, 113.7, 115.7, 120.8, 125.1, 125.4, 125.6, 125.8, 126.7, 127.5, 130.1, 130.6, 132.7, 133.0, 137.6, 143.9, 157.5, 170.1. **MS (m/z):** 315.32 (M+1).

2.7.2.2. 4-(2,5-dimethoxyphenyl)-2-oxo-3,4-dihydro-2H-benzo[h]chromene-3-carbonitrile (2.2B): White solid, yield: 95%, m.p. 267-269°C; **^{1}H NMR (300 MHz, $CDCl_3$):** δppm 3.69 (3H, s, CH_3); 3.86 (3H, s, CH_3); 4.20 (1H, d, CH, *J* = 8.7 Hz); 4.61 (1H, d, CH, *J* = 8.7 Hz); 6.72 – 6.89 (3H, m, Ar-H); 7.12 – 7.15 (1H, d, Ar-H, *J* = 8.7 Hz); 7.39 – 7.69 (3H, m, Ar-H); 7.91 – 7.94 (1H, d, Ar-H, *J* = 8.7 Hz); 8.16 – 8.19 (1H, d, Ar-H, *J* = 8.7 Hz); **^{13}C NMR (75 MHz, $CDCl_3$):** δppm 30.1, 40.3, 55.8, 56.9, 112.6, 112.8, 113.4, 115.8, 125.1, 125.4, 125.6, 125.9, 126.7, 127.4, 127.7, 132.6, 132.3, 133.3, 138.7, 153.4, 156.9, 170.2. **MS (m/z):** 359.37 (M+1).

2.7.2.3. 4-(4-chlorophenyl)-2-oxo-3,4-dihydro-2H-benzo[h]chromene-3-carbonitrile (2.2C): Yellow solid, yield: 94%, m.p. 239-241°C; **^{1}H NMR (300 MHz, $CDCl_3$):** δppm 4.21 – 4.24 (1H, d, CH, *J* = 8.7 Hz); 4.69 – 4.72 (1H, d, CH, *J* = 8.7 Hz); 7.08 – 7.13 (3H, m, Ar-H); 7.42 – 7.70 (4H, m, Ar-H); 7.74 – 7.77 (1H, d, Ar-H, *J* = 8.7 Hz); 7.93 – 7.96 (1H, d, Ar-H, *J* = 8.7 Hz); 8.10 – 8.13 (1H, d, Ar-H, *J* = 8.7 Hz); **^{13}C NMR (75 MHz, $CDCl_3$):** δppm 36.7, 43.2, 116.4, 125.1, 125.4, 125.6, 125.9, 126.5, 127.3, 127.5, 129.4, 129.4, 129.9, 129.9, 131.8, 133.2, 133.9, 138.5, 141.1, 168.9. **MS (m/z):** 333.79 (M+1).

2.8. Results and discussions

In scheme 2, a series of 2-oxo-3,4-dihydro-2H-benzo[h]chromenederivatives **(2.2A-2.2C)** were synthesized from 2-amino-4H-benzochromene derivatives **(2.1A-2.1C)**. These hetero-polycyclic 2-oxo-3,4-dihydro-2H-benzo[h]chromene derivatives **(2.2A-2.2C)** were recrystallized in an appropriate solvent to give a suitable crystal for the analysis. The crystal obtained was studied by single-crystal X-ray diffraction (SC-XRD) and Hirshfeld surface analysis.

2.8.1. X-Ray Crystallographic studies and Hirshfeld surface analysis of compounds 2.2A, 2.2B and 2.2C

2.8.1.1. Crystal analysis of compound 2.2A

The compound **2.2A** was recrystallized in acetone at room temperature by slow evaporation of the solvent. The chiral asymmetric compound **2.2A** was analyzed using SC-XRD **(Figure 2.49)**. The compound crystallized with cell lengths **a** = 13.0954(5)Å, **b** = 11.9629(4)Å, **c** = 10.0736(3)Å, i.e., $\mathbf{a \neq b \neq c}$ and cell angles $\boldsymbol{\alpha}$ = 90°, $\boldsymbol{\beta}$ = 100.992(4)°, $\boldsymbol{\gamma}$ = 90°, i.e., $\boldsymbol{\alpha = \gamma = 90°, \beta \neq 90°}$ which indicate that the compound is exhibiting a monoclinic crystal system, with space group $P2_1/c$ that contains four molecules per unit cell.

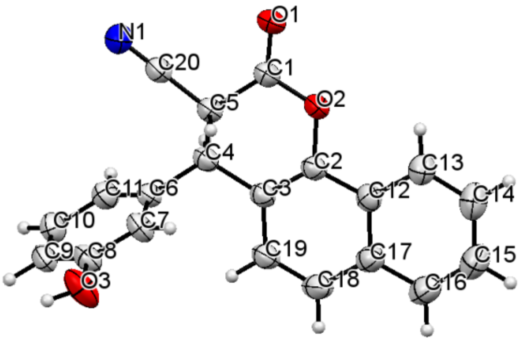

Figure 2.49: ORTEP diagram of compound **2.2A**

The chiral asymmetric compound **2.2A** crystal structure shows that the 2H-pyran ring moiety within the benzo[h]chromene is non-planar due to the sp^3 hybridization at C4 and C5 carbon atoms. Due to this sp^3 hybridization, the 2H-pyran ring moiety within the benzo[h]chromene is distorted and adopts a half chair conformation. The atoms C2, C3, C4, and O2 are coplanar, and the atoms C1 and C5 deviate from the plane by 0.303Å and 0.817Å, respectively. The benzenoid ring is twisted away from the plane of the naphthalene ring moiety with a dihedral angle of 71.66°. The crystallographic information is summarized in **Table 2.13**.

Table 2.13: Crystal data on compounds **2.2A**, **2.2B** and **2.2C**

Compound	**2.2A**	**2.2B**	**2.2C**
Identification code	2170677	2170676	2170675
Empirical formula	$C_{20}H_{13}NO_3$	$C_{22}H_{17}NO_4$	$C_{20}H_{12}ClNO_2$
Formula weight	315.31	359.36	333.76
Temperature(K)	293(2)	293(2)	293(2)
Crystal system	Monoclinic	Triclinic	Monoclinic
Space group	$P2_1/c$	P-1	Pc
a(Å)	13.0954(5)	7.1525(2)	9.4512(4)
b(Å)	11.9629(4)	11.6419(4)	5.8620(3)
c(Å)	10.0736(3)	11.7099(3)	15.0441(6)
α(°)	90	104.998(3)	90
β(°)	100.992(4)	96.077(3)	104.826(4)
γ(°)	90	106.017(3)	90
Volume($Å^3$)	1549.17(10)	888.64(5)	805.74(6)
Z	4	2	2
ρ (g/cm^3)	1.352	1.343	1.376
μ(mm^{-1})	0.092	0.093	0.248
F(000)	656.0	376.0	344.0
Crystal size(mm^3)	0.36 × 0.34 × 0.3	0.22 × 0.2 × 0.18	0.2 × 0.18 × 0.17
Radiation	MoKα (λ = 0.71073)	MoKα (λ = 0.71073)	MoKα (λ = 0.71073)
2Θ range for data collection(°)	6.604 to 54.708	6.438 to 54.884	6.952 to 54.974
Index ranges	$-16 \le h \le 16, -15 \le k \le 15, -12 \le l \le 12$	$-8 \le h \le 9, -14 \le k \le 15, -13 \le l \le 15$	$-10 \le h \le 12, -6 \le k \le 7, -19 \le l \le 18$
Reflections collected	21523	11941	6555
Independent reflections	3338	3786	2552
Data/restraints/parameters	3338/0/226	3786/0/246	2552/2/217
Goodness-of-fit on F^2	1.096	1.086	1.006
Final R indexes [I>=2σ (I)]	$R_1 = 0.0446$, $wR_2 = 0.1135$	$R_1 = 0.0482$, $wR_2 = 0.1145$	$R_1 = 0.0397$, $wR_2 = 0.0911$
Final R indexes [all data]	$R_1 = 0.0668$, $wR_2 = 0.1259$	$R_1 = 0.0730$, $wR_2 = 0.1294$	$R_1 = 0.0649$, $wR_2 = 0.1045$
Largest diff.peak/hole/e $Å^{-3}$	0.12/-0.16	0.16/-0.19	0.12/-0.22

The supramolecular framework of compound 2.2A: The supramolecular structure of compound **2.2A** involves a strong O-H…O intermolecular interaction at a bond distance of 2.136Å between the hydroxyl hydrogen (H3) and the carbonyl oxygen (O1) of the benzo[h]chromene ring, which results in the formation of a continuous chain of **2.2A** compounds. The hydrogen (H3) is bifurcated and interacts with the partially positive charge carbonyl carbon (C1) to form a hydrogen bond with a distance of 2.782Å. The C-H...N interaction between the benzenoid hydrogen (H9) and the nitrogen (N1) of the nitrile group at a distance of 2.539Å results in the formation of the $R_2^2(18)$ graph set **(Figure 2.50 (b))**. The two continuous chains of **2.2A** running anti-parallel to each other are interconnected by C-H…C between the bifurcated hydrogen (H16) and the benzenoid carbons (C8 and C9) at a distance of 2.857Å and 2.756Å respectively forming $R_2^2(22)$ and $R_2^2(24)$ graph sets **(Figure 2.50 (c))**. This C-H…C interactions also bring the naphthalene ring moiety close enough to have intermolecular $\pi \ldots \pi$ stacking interactions at a distance of 3.698Å **(Figure 2.50 (d))**. Similarly, the C-H…N interactions mentioned above also allow $\pi \ldots \pi$ stacking interactions between the benzenoid rings in a parallel displaced fashion at a distance of 4.225Å **(Figure 2.50 (e))**. The two C-H…C interactions stabilizes the crystal packing within the unit cell through the bifurcated hydrogen (H16). The C-H…O interactions between the hydroxyl oxygen (O3) and the hydrogen (H5) from the sp^3 hybridized carbon (C5) of benzo[h]chromene ring at a distance of 2.335Å, and dipole-dipole interactions between the oxygen (O3) with the carbon (C5) and (C1) at a distance of 3.112Å and 3.140Å respectively, also stabilize the crystal packing. In addition to this, the crystal packing is also stabilized by C-H…π intermolecular interactions between the hydrogen (H13 and H14) with the naphthalene ring current at a distance of 3.621Å and 3.481Å **(Figure 2.50 (f))**. The C-H…C interactions which stabilized the crystal packing also bring its bifurcated hydrogen (H16) of the naphthalene ring moiety to have C-H…π interactions with the benzenoid ring at a distance of 3.332Å **(Figure 2.50 (g))**. Thus, the overall structure of the **2.2A** compound exhibits different intermolecular hydrogen interactions and dipole-dipole interactions. The non-covalent interactions found in the analysis of compound **2.2A** are in **Table 2.14**.

Table 2.14: Hydrogen bonds and other interactions in compound **2.2A**

Donor-H...Acceptor	**D – H, Å**	**H...A, Å**	**D...A, Å**	**D - H...A, °**
O3-H3…O1	0.820	2.136	2.913	158.01
O3-H3…C1	0.820	2.782	3.528	152.27
C16-H16…C8	0.930	2.857	3.772	168.08
C16-H16….C9	0.930	2.756	3.653	162.20
C9-H9…N1	0.930	2.539	3.467	175.12

C4-H4…N1	0.980	2.703	3.471	135.49
C5-H5…O3	0.980	2.335	3.112	135.58
C13-H13…π(C2,C3,C12,C17-C19)	0.928	3.621	4.274	129.67
C14-H14…π(C12-C17)	0.943	3.481	4.354	155.02
C16-H16…π(C6-C11)	0.930	3.332	4.236	164.87
Other contacts				
π(C6-C11)…π(C6-C11)		4.225		
π(C2,C3,C12-C19)…π(C2,C3,C12-C19)		3.698		
O3…C1		3.140		
O3…C5		3.112		
Intramolecular				
C7-H7…π(C2,C3,C12C17-C19)	0.930	3.730	4.103	107.30
C4-H4…O2	0.980	3.098	2.859	66.88

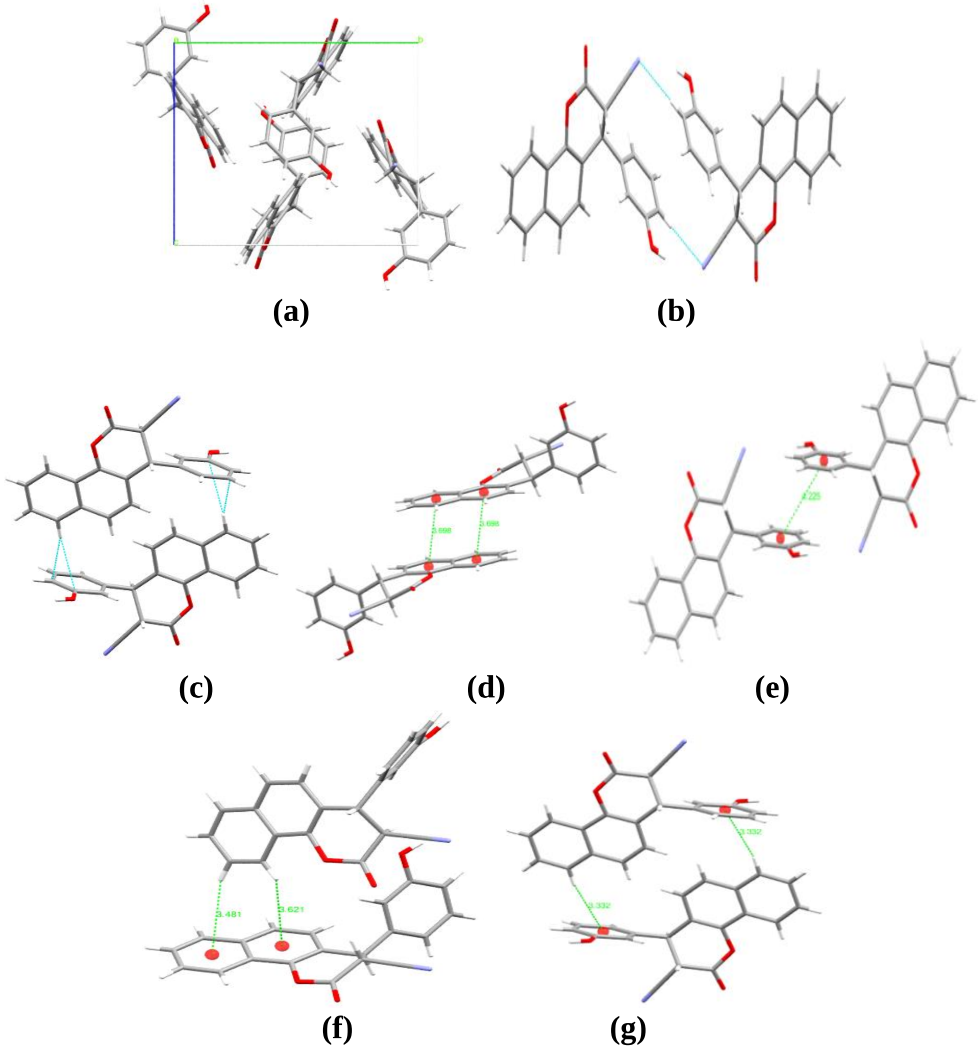

(a) **(b)**

(c) **(d)** **(e)**

(f) **(g)**

Figure 2.50: (a) Packing diagram of compound **2.2A**, (b) and (c) Graph sets, (d) and (e) π…π interactions, (f) and (g) C-H…π interactions, in compound **2.2A**

Hirshfeld surface analysis of compound 2.2A: The Hirshfeld surface mapped over the d_{norm} in the range of -0.48 to 1.39Å for compound **2.2A** is displayed in **(Figure 2.51 (a) and (b))**. The brightest red spot corresponds to the closest and most dominant contact, which arises from O-H…O interactions between the hydroxyl hydrogen and carbonyl oxygen (O1) within the benzo[h]chromene ring. The other lighter red spots are due to short contacts due to O-H…C, C-H…O, C-H…N, and C-H…C interactions.

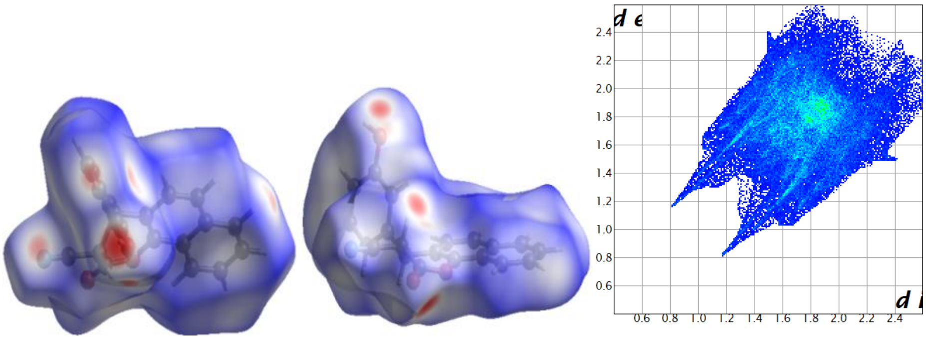

(a) **(b)** **(c)**

Figure 2.51: (a) and (b) d_{norm} both side view, (c) 2-D fingerprint plot, of compound **2.2A**

The relative percentage contributions of non-covalent interaction to the Hirshfeld surface by compound **2.2A** is represented by the 2-D fingerprint plot **(Figure 2.51 (c))**. Those are H…H (32.9%), C…H (22.5%), O…H (21.9%), N…H (11.8%), C…C (6.1%), C…O (1.7%), C…N (1.3%), O…N (1.3%) and O...O (0.5%). The two spoke-like patterns in the 2-D fingerprint plot in the region of di + de = 1.95-2.8Å represent the O…H/H...O interactions. N…H\H…N interactions also appear within the spikes in the 2-D fingerprint plot in the region of di + de = 2.8-3.2Å. Since C-H...π intermolecular interactions decompose within the C...H contacts, it appears in the same region on the 2-D fingerprint plot in the region of di + de = 2.5-3.7Å, which appears as hooks and clamp like pattern. The relative contribution of C…C close contacts, which account for 6.1%, represents significant π...π stacking interactions within the aromatic rings.

The shape-index mapped over a range of -1 to 1Å for compound **2.2A** shows the presence of complementary red and blue triangles around the bicyclic surface of the naphthalene ring and the benzenoid ring, which indicate the presence of π...π stacking interactions **(Figure 2.52 (a) and (b))**.

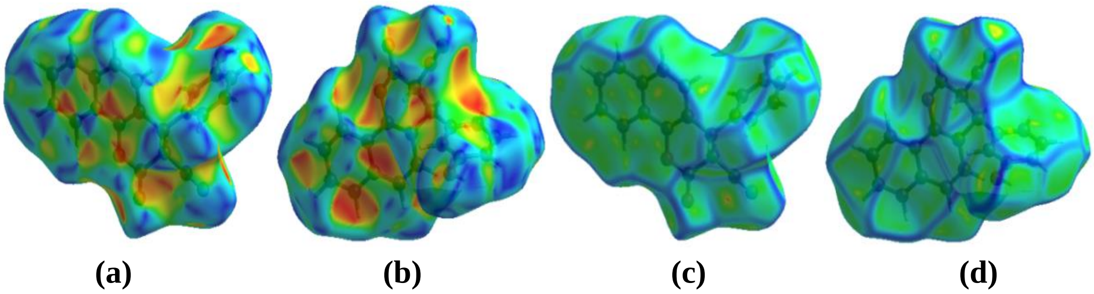
Figure 2.52: (a) and (b) Shape-index, (c) and (d) Curvedness, both side views of compound **2.2A**

The yellowish-red colored concave regions around the surface of the naphthalene ring and the benzenoid ring in compound **2.2A** indicate the acceptor region where weak C-H...π interaction occurs **(Figure 2.52 (a) and (b))**. The Hirshfeld curvedness surface mapped over a range of -4 to 0.4 Å also reveals the presence of a flat green region with a yellowish spot around the naphthalene and the benzenoid ring surfaces, which indicate the presence of π...π stacking interactions **(Figure 2.52 (c) and (d))**.

The presence of weak non-covalent O-H…O, O-H…C, C-H…N, C-H…C, C-H…π, and π…π stacking interactions is also supported by the Hirshfeld weak intermolecular interactions calculation in the crystal packing around the cluster of radius 3.8Å from a single crystals fragments. Those interactions are in **Figure 2.53**.

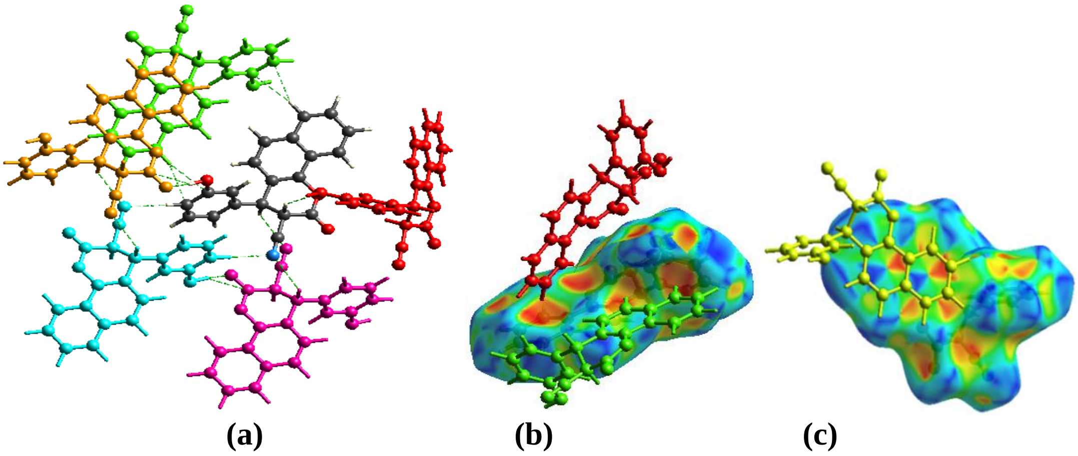

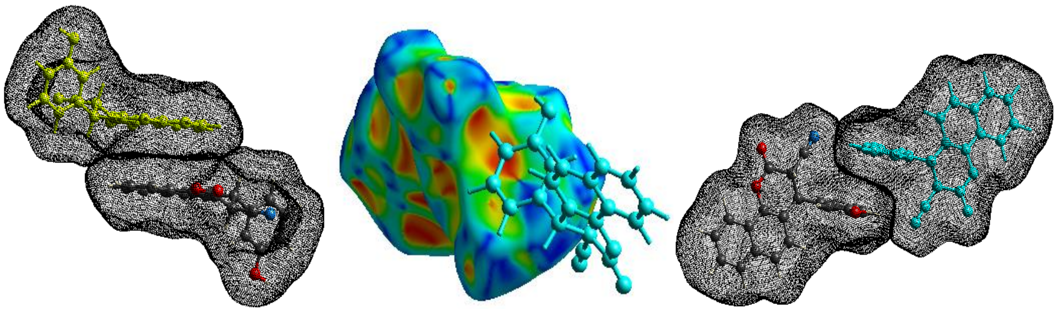

(d) (e) (f)

Figure 2.53: (a) Non-covalent hydrogen bonding, (b) C-H…π interactions, (c), (d), (e) and (f) π…π interactions, in compound **2.2A**

2.8.1.2. Crystal analysis of compound 2.2B

The compound **2.2B** was recrystallized in acetone at room temperature by slow evaporation of the solvent. The chiral asymmetric compound **2.2B** was analyzed using SC-XRD **(Figure 2.54)**. The compound crystallized with cell lengths **a** = 7.1525(2)Å, **b** = 11.6419(4)Å, **c** = 11.7099(3)Å, i.e., **a ≠ b ≠ c** and cell angles $\boldsymbol{\alpha}$ = 104.998(3)°, $\boldsymbol{\beta}$ = 96.077(3)°, $\boldsymbol{\gamma}$ = 106.017(3)°, i.e., $\boldsymbol{\alpha \neq \beta \neq \gamma \neq 90°}$ which indicate that the compound is exhibiting a triclinic crystal system, with space group P-1 that contains two molecules per unit cell.

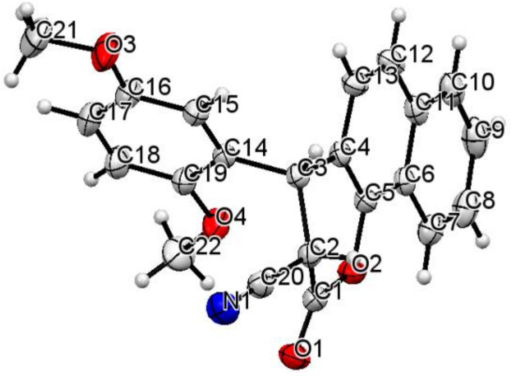

Figure 2.54: ORTEP diagram of compound **2.2B**

The chiral asymmetric compound **2.2B** crystal structure shows that the 2H-pyran ring moiety within the benzo[h]chromene is non-planar due to the sp^3 hybridization at C2 and C3 carbon atom. Due to these sp^3 hybridizations, the 2H-pyran ring moiety within the benzo[h]chromene is distorted and adopts a half chair conformation. The atoms C1, C3, C4, C5, and O2 are coplanar, and atom C2 deviates from the plane by 0.520Å. The benzenoid ring is twisted and flips away from the plane of the naphthalene ring moiety with a dihedral angle of 82.05°. The crystallographic information is summarized in **Table 2.13**.

The supramolecular framework of compound 2.2B: The crystal association of compound **2.2B** involves a C-H…N and C-H…O intermolecular interactions having the same interaction distance of 2.595Å. The C-H…N interaction arises between the hydrogen (H10) of the naphthalene ring moiety and the nitrile nitrogen (N1). Also, the C-H…O interaction arises between the benzenoid hydrogen (H15) and the carbonyl oxygen (O1) of the benzo[h]chromene ring. The nitrile group's nitrogen (N1) atom acts as a bifurcated acceptor and forms one more C-H…N bond with the hydrogen (H8) from the naphthalene ring moiety, at a bond distance of 2.630Å. These two C-H…N interactions, along with the C-H…O interaction, results in the formation of symmetrically arranged sheets which also leads to the formation of $R_3^3(17)$ and $R_3^3(19)$ graph sets **(Figure 2.55 (b))**. The hydrogen (H2) from the sp^3 hybridized carbon (C2) acts as bifurcated hydrogen. It forms C-H…C bond with carbon (C9 and C10) from the naphthalene ring moiety at an interaction distance of 2.826Å and 2.775Å, respectively, resulting in the formation of $R_2^2(16)$ and $R_2^2(18)$ graph set notations **(Figure 2.55 (c))**. It also forms $R_4^4(14)$, and $R_4^4(16)$ graph sets together with the C-H…N bond **(Figure 2.55 (c))**. These two C-H…C interactions also serve as interlinkages between different sheets. It also brings the naphthalene ring moiety close enough to have $\pi \ldots \pi$ intermolecular stacking interaction at a distance of 3.827Å **(Figure 2.55 (d))**. The C-H…π intermolecular interaction between the six membered benzenoid hydrogen (H17 and H18) and the naphthalene ring at a distance of 2.805Å and 3.009Å, respectively stabilizes the crystal packing within the unit cell. Also, the methoxy hydrogen (H22A) interacts with the benzenoid ring current. It forms a C-H…π interaction at a distance of 3.191Å, which also assists in stabilizing the crystal packing **(Figure 2.55 (a))**. Beyond these interactions, the supramolecular self-assembly of compound **2.2B** also exhibits one more C-H…π interaction between the hydrogen (H21B) from the other methoxy group with the benzenoid ring current on the other side of the plane at a distance of 3.152Å **(Figure 2.55 (e))**. The interactions found in the crystal analysis are in **Table 2.15**.

Table 2.15: Hydrogen bonds and other interactions in compound **2.2B**

Donor-H...Acceptor	**D – H, Å**	**H...A, Å**	**D...A, Å**	**D - H...A, º**
C10-H10…N1	0.930	2.595	3.447	152.68
C15-H15…O1	0.930	2.595	3.387	143.39
C8-H8…N1	0.930	2.630	3.429	144.39
C2-H2…C10	0.980	2.775	3.670	152.10
C2-H2…C9	0.980	2.826	3.688	147.20
C17-H17…π(C6-C11)	0.930	2.805	3.604	144.58
C18-H18…π(C4-C6,C11-C13)	0.930	3.009	3.790	142.66
C22-H22A…π(C14-C19)	0.960	3.191	3.936	135.83
C21-H21B…π(C14-C19)	0.960	3.152	3.914	137.52
Other Contact				
π(C4-C13)…π(C4-C13)		3.827		
Intramolecular				
O2…O4		2.853		
C22-H22B…O2	0.960	3.307	3.633	102.22

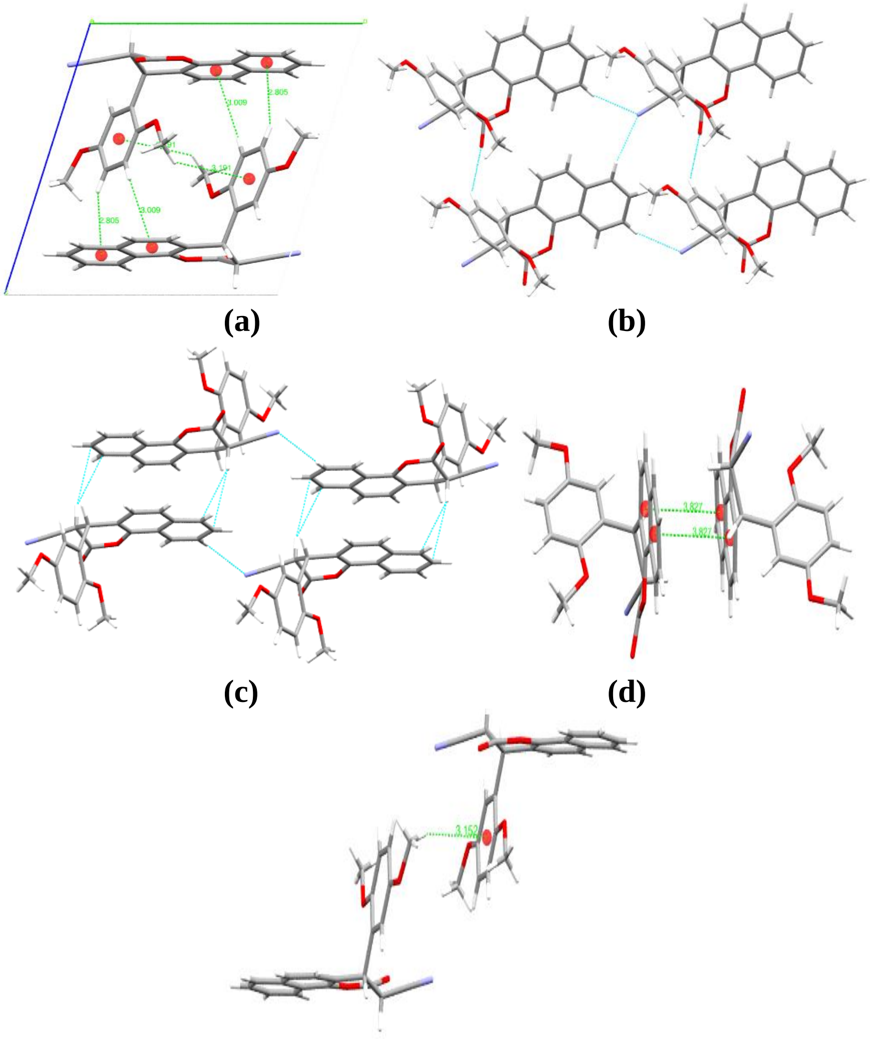

(a) **(b)**

(c) **(d)**

(e)

Figure 2.55: (a) Packing diagram of **2.2B** with C-H…π interactions, (b) and (c) Graph sets, (d) π…π interactions, and (e) C-H…π interaction in compound **2.2B**

Hirshfeld surface analysis of compound 2.2B: The Hirshfeld surface mapped over the d_{norm} in the range of -0.13 to 1.62Å for compound **2.2B** is displayed in **Figure 2.56 (a) and (b)**. The red-colored spots arise due to C-H…N, C-H…O, and C-H…C interactions. The intensity of the color and size of the red spots differs depending on the strength of interaction. The more dominant the interaction, the more intense the color and size of the spot and vice versa in Hirshfeld surface analysis.

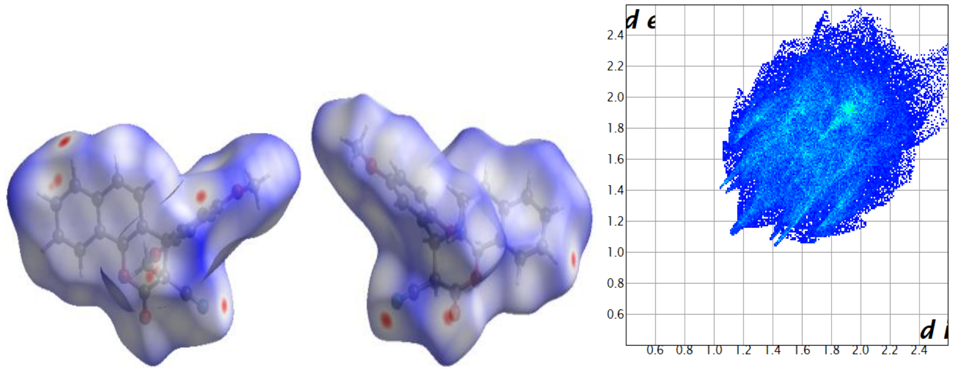

(a) **(b)** **(c)**

Figure 2.56: (a) and (b) d_{norm} both side view, (c) 2-D fingerprint plot, of compound **2.2B**

The 2-D fingerprint plot of the compound **2.2B** represents the relative percentage contributions of non-covalent interaction to the Hirshfeld surface **(Figure 2.56 (c))**. Those are H…H (40.1%), C…H (23.9%), O…H (18.4%), N…H (11.7%), C…C (4.4%), C…O (0.8%), N…O (0.6%) and C…N (0.1%). The two outer spoke-like patterns in the 2-D fingerprint plot in the region of di + de = 1.45-3.20Å represent the N…H/H...N interactions. O…H\H…O interactions also appear at the inner side as a spokes-like pattern in the 2-D fingerprint plot in the region of di + de = 2.5-2.8Å. The C-H...π intermolecular interactions decompose within the C...H contacts. It appears in the same region on the 2-D fingerprint plot in the region of di + de = 2.7-3.4Å, which appears like a pair of hooks or small fins. The relative contribution of C…C close contacts, which account for 4.4%, indicate the presence of π…π stacking interactions.

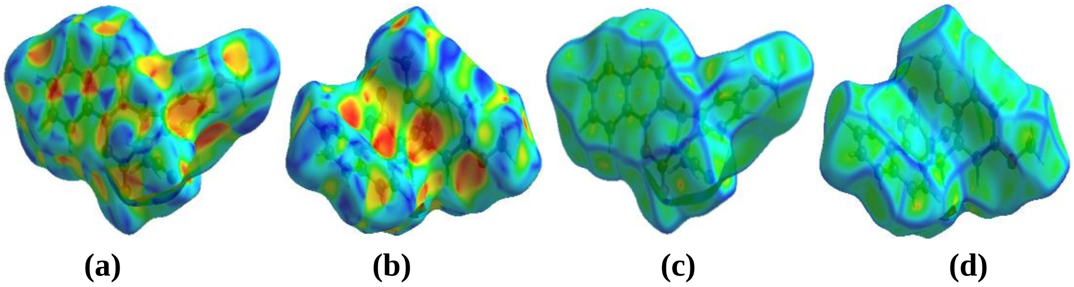
(a) (b) (c) (d)

Figure 2.57: (a) and (b) Shape-index, (c) and (d) Curvedness, both side views of compound **2.2B**

The Hirshfeld shape-index in a range of -1 to 1Å for compound **2.2B** shows the presence of complementary red and blue triangles around the surface of the naphthalene ring, which indicate the presence of intermolecular π...π stacking interactions between the rings **(Figure 2.57 (a))**. The yellowish-red colored concave regions around the surface of the naphthalene ring and the benzenoid ring in compound **2.2B** indicate the acceptor region where weak C-H...π interaction occurs **(Figure 2.57 (a) and (b))**. Again, the curvedness in a range of -4 to 0.4 Å for compound **2.2B** also displays the presence of a flat green region with a yellowish spot around the naphthalene ring surface which supports the presence of intermolecular π…π stacking interactions between the naphthalene rings **(Figure 2.57 (c))**.

The weak non-covalent C-H…N, C-H…O, C-H…C, C-H…π, and π…π stacking interactions found within the supramolecular structures is also supported by the Hirshfeld weak intermolecular interactions calculation for a single crystal fragment around the cluster of radius 3.8Å. Those interactions are in **Figure 2.58**.

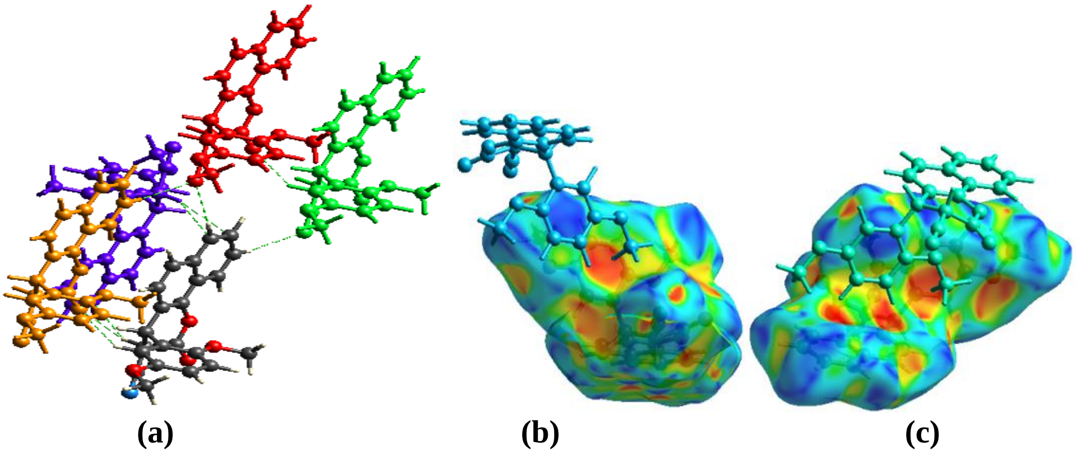
(a) (b) (c)

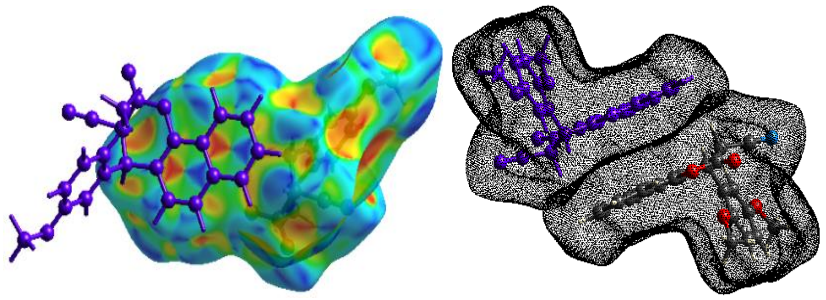

(d) **(e)**

Figure 2.58: (a) C-H…N, C-H…C and C-H…O interactions, (b) and (c) C-H…π interactions, (d) and (e) π…π interaction, in compound **2.2B**

2.8.1.3. Crystal analysis of compound 2.2C

The compound **2.2C** was recrystallized in acetone at room temperature by slow evaporation of the solvent. The chiral asymmetric compound **2.2C** was analyzed using SC-XRD **(Figure 2.59)**. The compound crystallized with cell lengths **a** = 9.4512(4)Å, **b** = 5.8620(3)Å, **c** = 15.0441(6)Å, i.e., **a ≠ b ≠ c** and cell angles $\boldsymbol{\alpha}$ = 90°, $\boldsymbol{\beta}$= 104.826(4)°, $\boldsymbol{\gamma}$ = 90°, i.e., $\boldsymbol{\alpha = \gamma = 90°, \beta \neq 90°}$, which indicate that the compound is exhibiting monoclinic crystal system, with space group Pc that contains two molecules per unit cell.

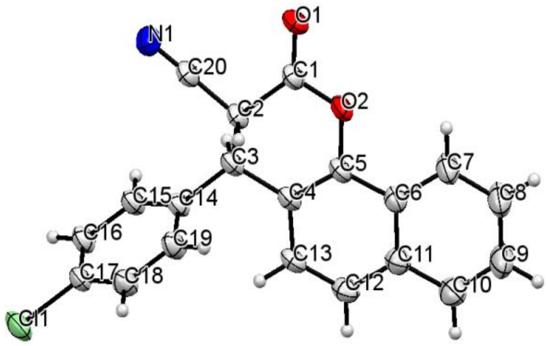

Figure 2.59: ORTEP diagram of compound **2.2C**

The chiral asymmetric compound **2.2C** crystal structure shows that the 2H-pyran ring moiety within the benzo[h]chromene is non-planar due to the sp^3 hybridization at C2 and C3 carbon atom. Due to these sp^3 hybridizations, the 2H-pyran ring moiety within the benzo[h]chromene is distorted and adopts a half chair conformation. The atoms C1, C3, C4, C5, and O2 are coplanar, and atom C2 deviates from the plane by 0.683Å. The benzenoid ring twisted and flipped away from the plane of the naphthalene ring moiety with a dihedral angle of 72.92°. The crystallographic information is summarized in **Table 2.13**.

The supramolecular framework of compound 2.2C: The nitrogen (N1) of the cyano group acts as a bifurcated acceptor and forms C-H…N interactions with hydrogen (H16) and (H19) from the chlorobenzene ring at an interaction distance of 2.522Å and 2.420Å respectively. The hydrogen (H3) from the pyran ring moiety also forms C-H…C interaction with the carbon (C12) of the naphthalene ring at a distance of 2.712Å. The hydrogen (H13) from the naphthalene ring also forms C-H…O interaction at a distance of 2.542Å with the oxygen (O1) from the pyran ring moiety. These C-H…N, C-H…O, and C-H…C interactions altogether forms graph sets of $R_2^2(12)$, $R_3^2(16)$, and $R_3^3(20)$ **(Figure 2.60 (b))**. The hydrogen (H10) acts as bifurcated hydrogen and interacts with the chlorine atom (Cl1) and the carbon (C17) of the chlorobenzene ring and forms C-H…Cl and C-H…C interactions at a distance of 2.920Å and 2.896Å, respectively, and this extensive interaction between the molecules forms a polymeric chain of compound **2.2C**. The polymeric chains from different layers are interconnected by the C-H…C contacts having a 2.712Å interaction distance between the pyran ring hydrogen (H3) and the naphthalene ring carbon (C12). Also, different polymeric chains run perpendicularly along the other chain's plane, and these different chains having different orientations are interconnected through the C-H…N and C-H…O contacts. The crystal packing within the unit cell is stabilized by the C-H…O interaction and by lone pair…π interaction between the oxygen (O1) and the chlorobenzene p-orbitals **(Figure 2.60 (c))**. The supramolecular associations of compound **2.2C** also display C-H…π interaction between the naphthalene ring hydrogen (H9) and the chlorobenzene ring at a distance of 3.252Å **(Figure 2.60 (d))**. The hydrogen (H18) from the chlorobenzene ring also interacts with the naphthalene p-orbital and forms a C-H…π interaction having distance of 3.344Å **(Figure 2.60 (e))**. Furthermore, since the carbon atom (C1) within the pyran ring moiety has a partially positive charge, it also interacts with the naphthalene p-orbitals on a different side of the plane, forming cation…π interaction with an interaction distance of 3.733Å **(Figure 2.60 (f))**. The weak non-covalent interactions are given in **Table 2.16**.

Table 2.16: Hydrogen bonds and other interactions in compound **2.2C**

Donor-H...Acceptor	**D – H, Å**	**H...A, Å**	**D...A, Å**	**D - H...A, º**
C10-H10…C17	0.930	2.896	3.623	136.02
C10-H10…Cl1	0.930	2.920	3.863	168.74
C3-H3…C12	0.980	2.712	3.689	175.07
C19-H19…N1	0.930	2.420	3.345	173.21
C16-H16…N1	0.930	2.552	3.423	156.18
C13-H13…O1	0.929	2.542	3.424	158.46
C9-H9…π(C14-C19)	0.930	3.252	3.877	126.43
C18-H18… π(C6-C11)	0.930	3.344	4.126	143.06
Other contacts				
O1… π(C14-C19)		3.450		
C1…π(C6-C11)		3.733		
Intramolecular				
C2-H2…O2	0.980	2.749	2.420	60.40
C19-H19…O2	0.930	4.473	4.851	108.66

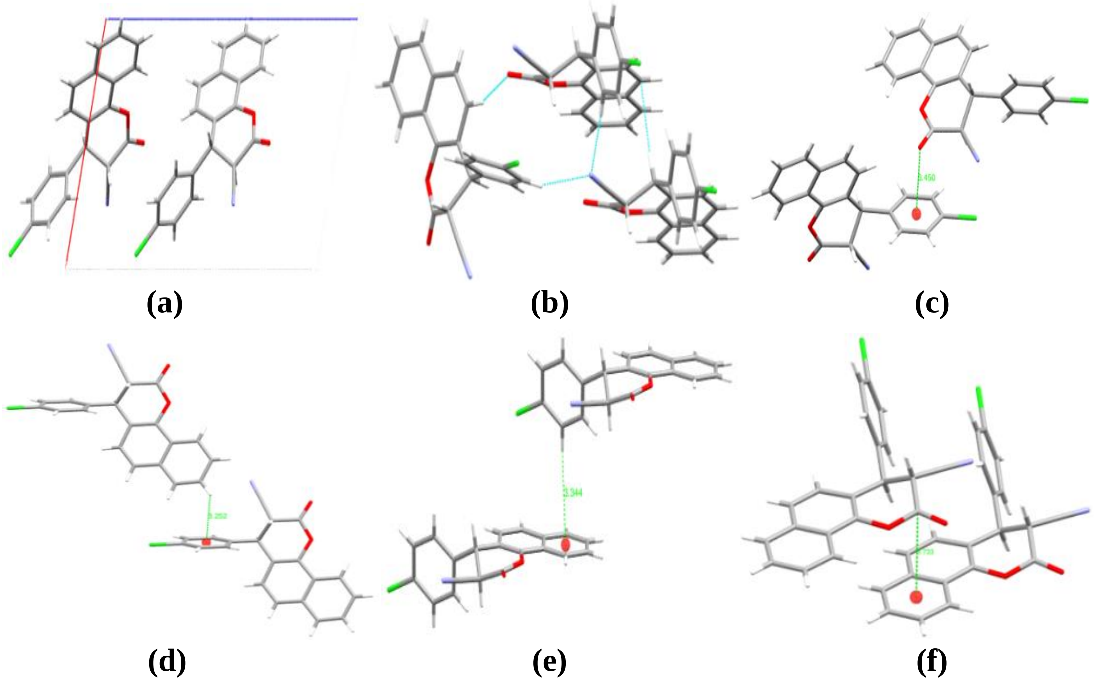
(a) **(b)** **(c)**

(d) **(e)** **(f)**

Figure 2.60: (a) Packing diagram of **2.2C**, (b) Graph sets, (c) Lone pair…π, (d) and (e) C-H…π interactions and (f) Cation…π interaction, in compound **2.2C**

Hirshfeld surface analysis of compound 2.2C: The Hirshfeld surface mapped over the d_{norm} in the range of -0.28 to 1.35Å for compound **2.2C** is displayed in **Figure 2.61 (a) and (b)**. The white and blue regions of the Hirshfeld surface indicate weaker interactions due to more extended contacts, which are more significant or equal to the van der Waals interatomic distances. The region of red spots corresponds to short contacts due to C-H…N, C-H…C, and C-H…O interactions. The intensity and size of the red spots increases for those contacts which are more dominant and vice versa.

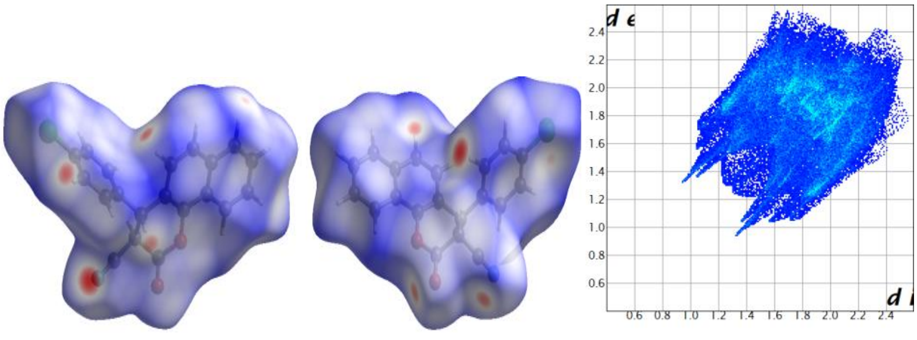

(a) **(b)** **(c)**

Figure 2.61: (a) and (b) d_{norm} both side view, (c) 2-D fingerprint plot, of compound **2.2C**

The relative percentage contributions of non-covalent interaction to the Hirshfeld surface by compound **2.2C** is are represented by the 2-D fingerprint plot **(Figure 2.61 (c))**. Those interactions are H…H (26.9%), C…H (21.7%), H…Cl (14.3%), N…H (13.6%), O…H (10.3%), C…O (7.2%), C…C (2.6%), C…Cl (1.9%), C…N (0.9%) and N…Cl (0.5%). The outer two spoke-like patterns in the 2-D fingerprint plot in the region of di + de = 2.2-2.8Å represent the N…H interactions. O…H interactions also appear as a shorter spoke-like pattern in the region of di + de = 2.5-3.0Å. Since C-H...π intermolecular interactions decompose within the C...H contacts, it appears in the same region in the 2-D fingerprint plot as a clamp-like pattern in the region of di + de = 2.7-3.4Å. C…C close contacts' relative contribution, which accounts for 2.6%, represents cation…π interaction. Also, the C…O contacts contributing 7.2% in the 2-D fingerprint plot represents lone pair…π interactions.

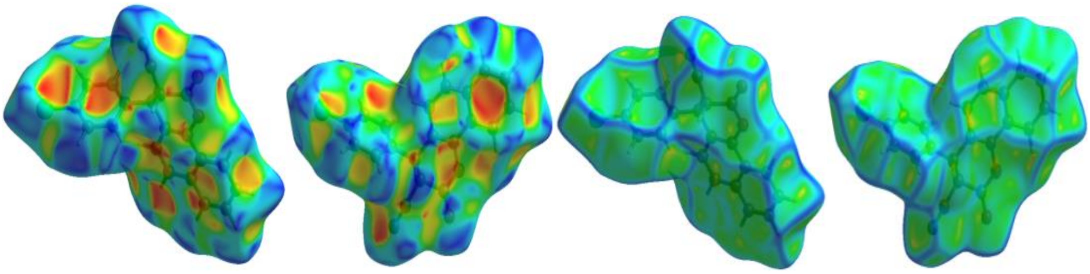

(a) **(b)** **(c)** **(d)**

Figure 2.62: (a) and (b) Shape-index, (c) and (d) Curvedness, both side views of compound **2.2C**

The shape-index in a range of -1 to 1Å for compound **2.2C** shows the lack of complementary red and blue triangles having an edge-to-edge connection around the aromatic ring surface which indicates the absence of π...π stacking interactions. The yellowish-red colored concave regions around the surface of the naphthalene ring and the chlorobenzene ring in compound **2.2C** indicate the acceptor region where weak C-H...π, lone pair…π, and cation…π interactions occur **(Figure 2.62 (a) and (b))**. The curvedness surface in a range of -4 to 0.4 Å for compound **2.2C** also does not have a flat green region with a yellowish spot around the surface of the naphthalene ring and the chlorobenzene ring, which indicate the absence of π...π stacking interactions **(Figure 2.62 (c) and (d))**.

The different types of interactions found within the supramolecular framework of compound **2.2C** are also supported by the Hirshfeld calculations of weak interaction within a radius of 3.8Å from the single crystal fragments, as shown in **Figure 2.63**.

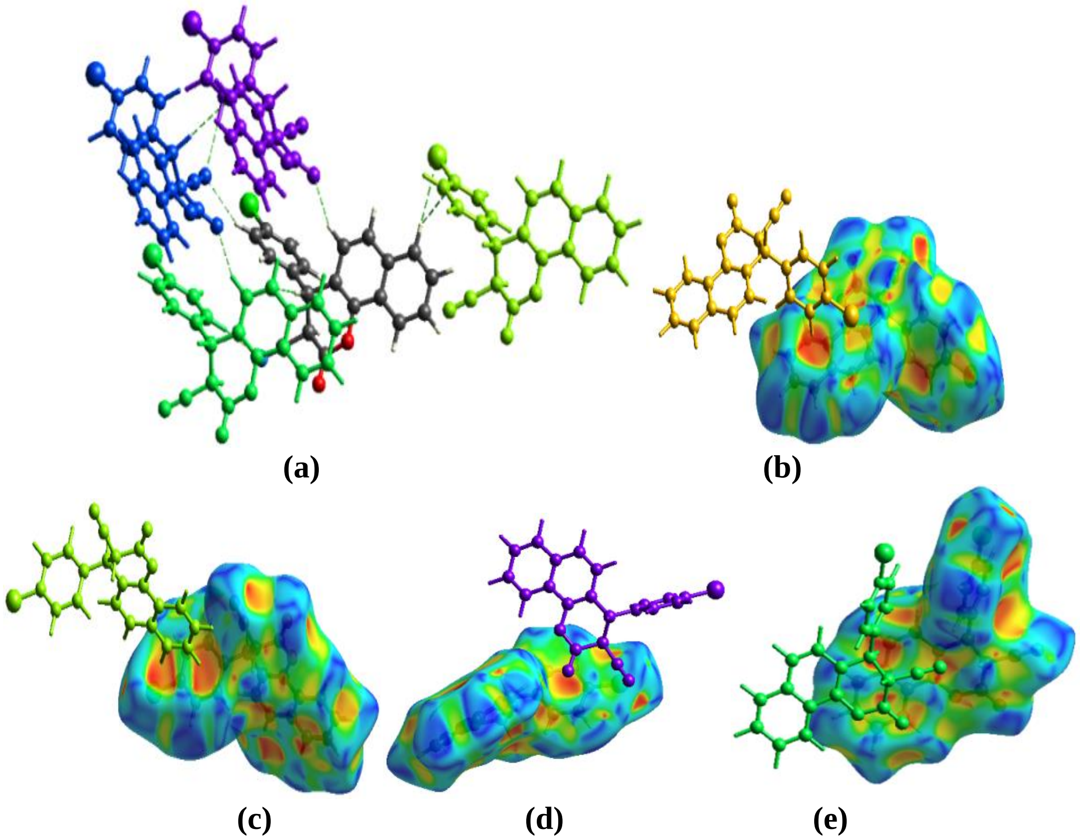

(a) **(b)**

(c) **(d)** **(e)**

Figure 2.63: (a) C-H…C, C-H…N and C-H…O interactions, (b),(c) C-H…π interactions, (d) Lone pair…π and (e) Cation…π interactions, in compound **2.2C**

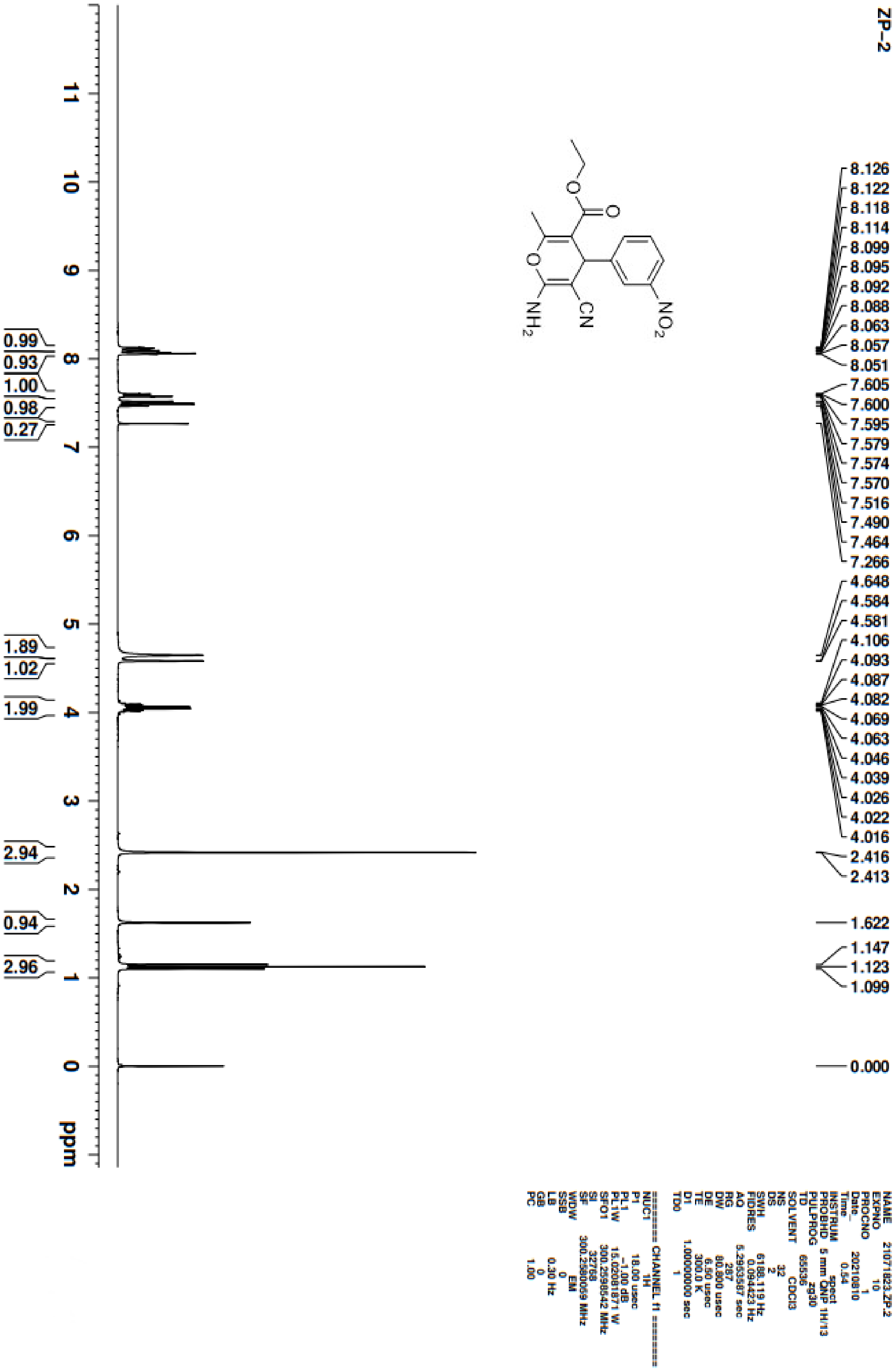

Figure 2.64: ^{1}H NMR spectra of compound **1.1A**

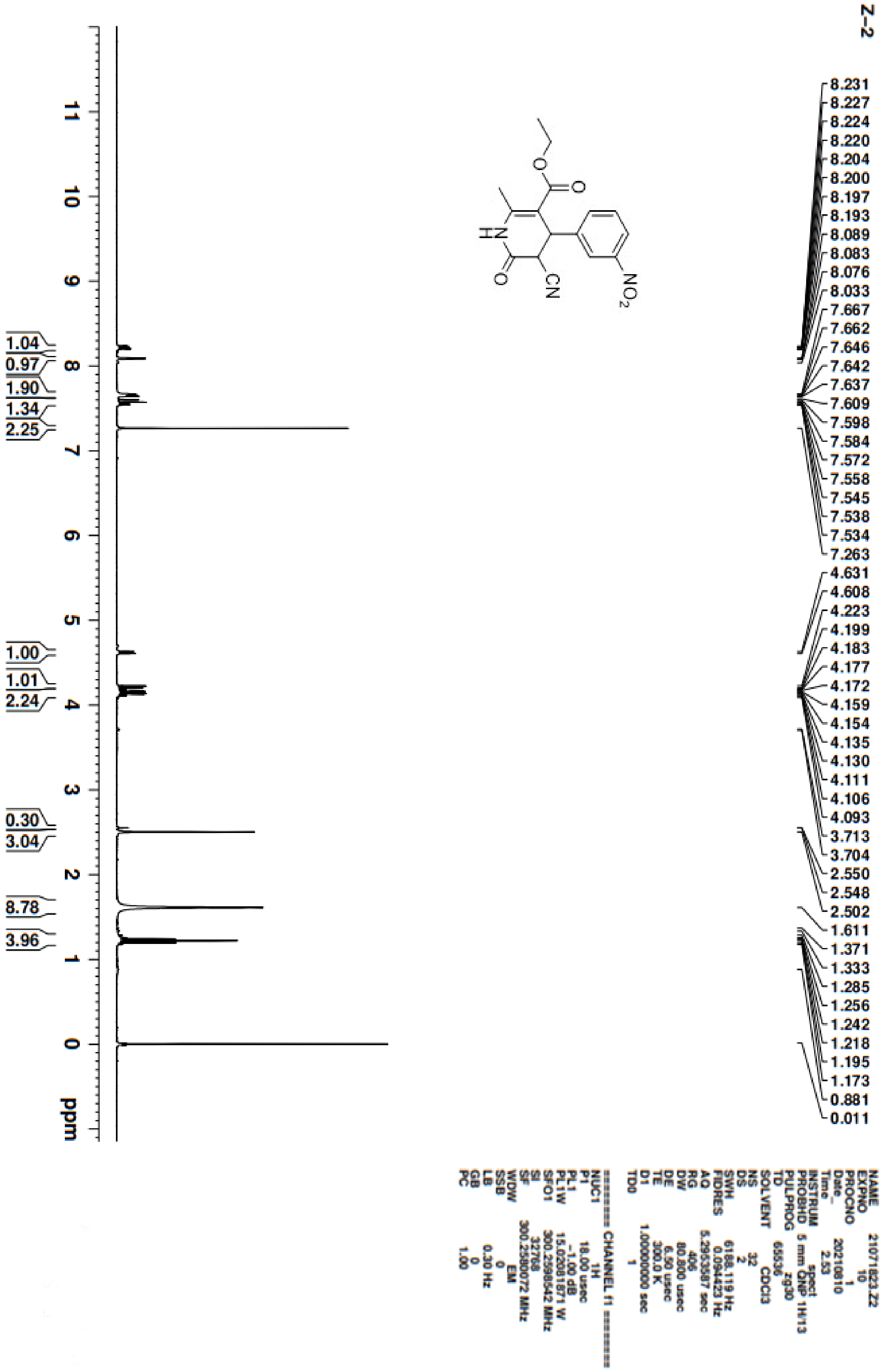

Figure 2.65: ^{1}H NMR spectra of compound **1.2A**

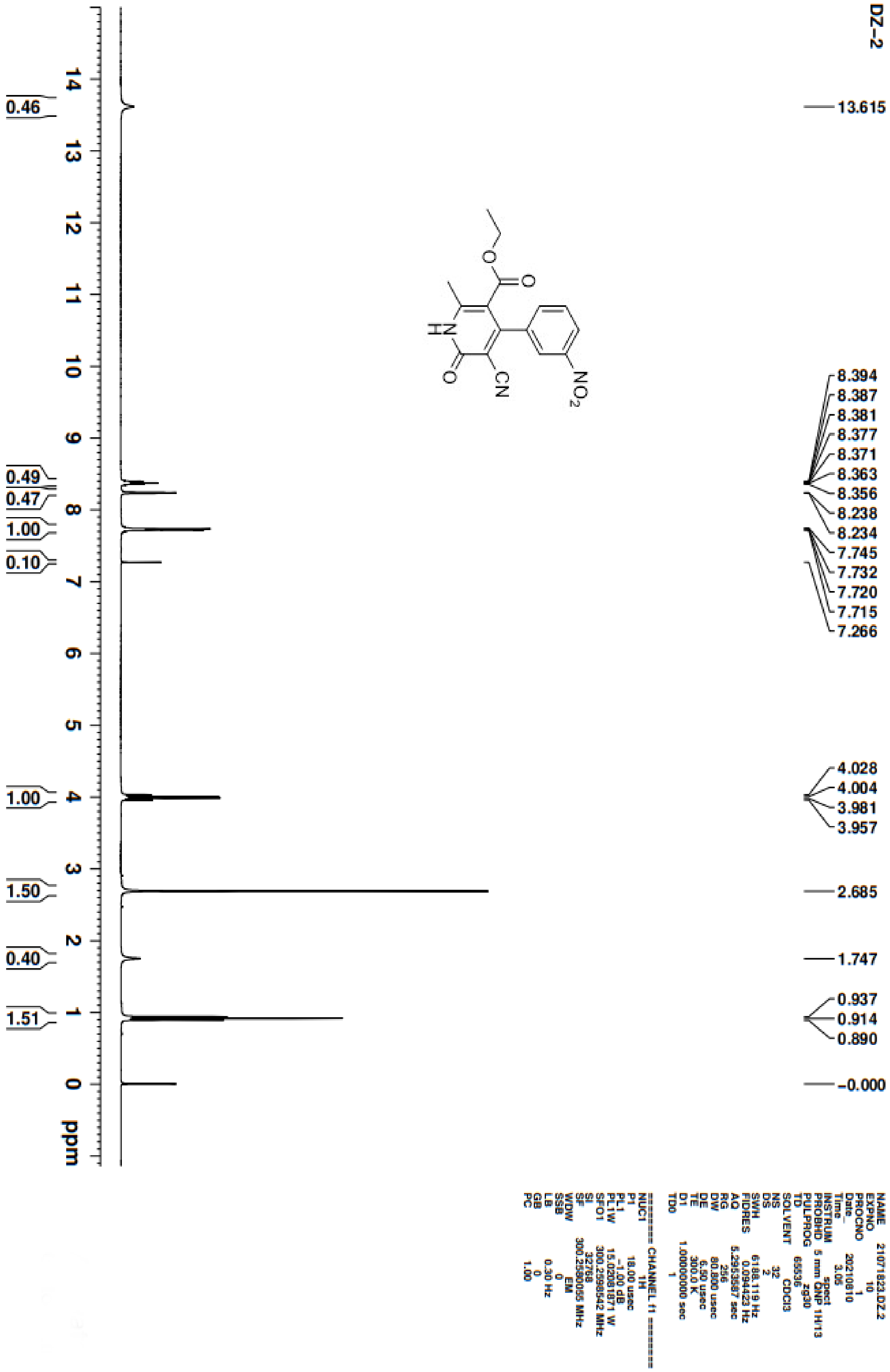

```
NAME       21071823.DZ.2
EXPNO                 10
PROCNO                 1
Date_           20210810
Time                3.05
INSTRUM            spect
PROBHD   5 mm QNP 1H/13
PULPROG             zg30
TD                 65536
SOLVENT            CDCl3
NS                    32
DS                     2
SWH          6188.119 Hz
FIDRES       0.094423 Hz
AQ          5.2953587 sec
RG                   256
DW            80.800 usec
DE              6.50 usec
TE               300.0 K
D1        1.00000000 sec
TD0                    1

======== CHANNEL f1 ========
NUC1                  1H
P1            18.00 usec
PL1             -1.00 dB
PL1W       15.02081871 W
SFO1   300.2598542 MHz
SI                 32768
SF     300.2580055 MHz
WDW                   EM
SSB                    0
LB               0.30 Hz
GB                     0
PC                  1.00
```

Figure 2.66: ^{1}H NMR spectra of compound **1.3A**

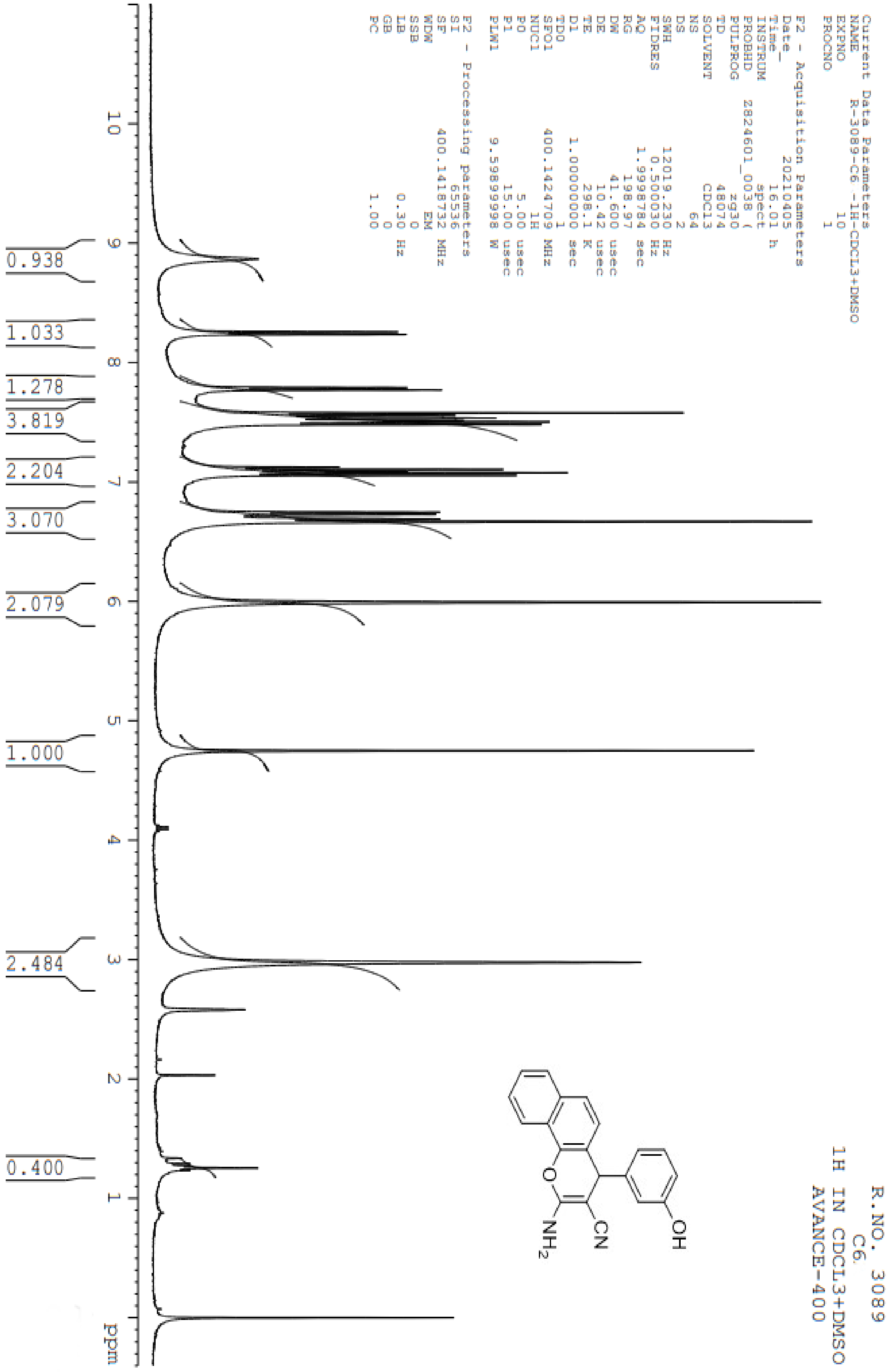

```
Current Data Parameters
NAME       R-3089-C6 -1H-CDCL3+DMSO
EXPNO                   10
PROCNO                   1

F2 - Acquisition Parameters
Date_             20210405
Time                 16.01 h
INSTRUM              spect
PROBHD   2824601_0038 (
PULPROG               zg30
TD                   48074
SOLVENT              CDCl3
NS                      64
DS                       2
SWH              12019.230 Hz
FIDRES            0.500030 Hz
AQ               1.9998784 sec
RG                  198.97
DW                  41.600 usec
DE                   10.42 usec
TE                   298.1 K
D1              1.00000000 sec
TD0                      1
SFO1           400.1424709 MHz
NUC1                    1H
P0                    5.00 usec
P1                   15.00 usec
PLW1            9.59899998 W

F2 - Processing parameters
SI                   65536
SF             400.1418732 MHz
WDW                     EM
SSB                      0
LB                    0.30 Hz
GB                       0
PC                    1.00
```

Figure 2.67: ^{1}H NMR spectra of compound **2.1A**

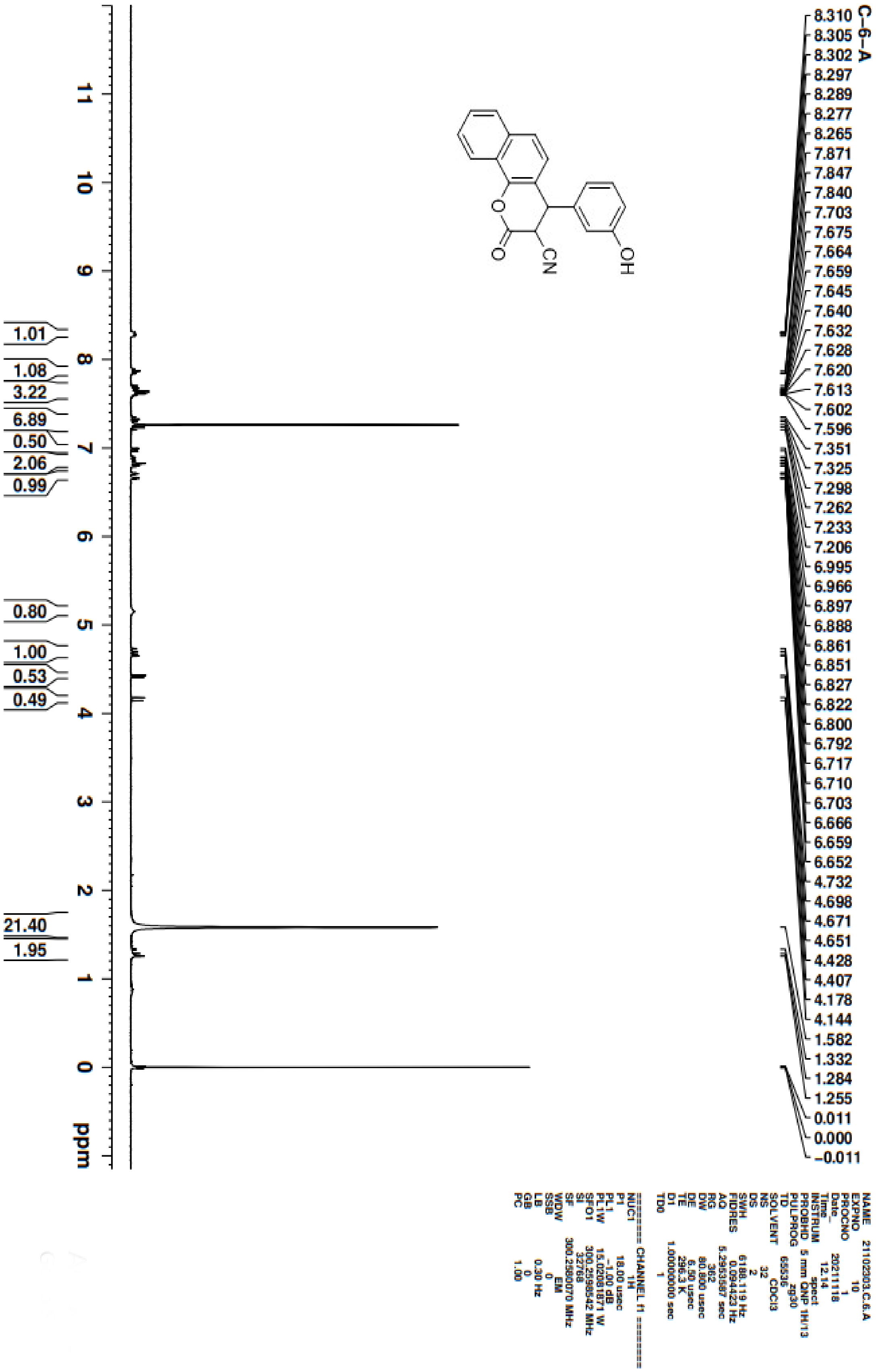

Figure 2.68: ^{1}H NMR spectra of compound **2.2A**

CHAPTER 3

SYNTHESIS AND STUDY OF POLYCYCLIC AROMATIC FLEXIMERS

3.1. Introduction

Polycyclic ring structures serve as a convenient starting scaffold in medicinal chemistry programs to develop multi-functional drugs. They may also be valuable moieties added to existing structures to improve the pharmacokinetic properties of drugs currently used in the clinic or under development. Some polycyclic aromatic compounds have exhibited carcinogenic and mutagenic properties. The development of such compounds as antitumor drugs may raise concerns. Nevertheless, many clinically active anticancer drugs not derived from polycyclic aromatic compounds are carcinogenic and demonstrate other harmful properties. Benzene is highly carcinogenic, but many compounds derived from benzene are life-saving drugs. It has been shown that altering polycyclic aromatic compounds' structure can help interact with specific organelles to evoke selective cytotoxic reactions (Cherubim et al., 1993; Palmer et al., 1988). Many scientists use this simple but crucial concept; due to these approaches, many carbazoles, anthracenes, and related structures are in current clinical use (Bandyopadhyay et al., 2012; Rescifina et al., 2006).

Heterocyclic compounds symbolize a vital source of pharmacologically active molecules, and more than 85% of all biologically active compounds contain heterocyclic scaffolds (Heravi&Zadsirjan, 2020). They are frequently used to alter physicochemical properties of molecules, such as lipophilicity, polarity, and hydrogen bonding capacity. That can improve the pharmacodynamic and pharmacokinetic profile (Gomtsyan, 2012). Pyridone is a heterocyclic 6-membered aromatic ring with a carbonyl group and nitrogen that have been used in drug discovery strategies (Zhang & Pike, 2021). Relevant characteristics associated with structure have been described by Y. Zhan and A. Pike, such as its ability to act as both a hydrogen bond acceptor and donor. They act as a bioisostere of amides, phenyls, and other nitrogen and oxygen-containing heterocycles. Pyridone can modulate lipophilicity, solubility, and metabolic stability (Zhang & Pike, 2021). Pyridone is structurally similar to thymine and uracil bases, and 2-pyridone exhibits lactam–lactim (keto/enol) tautomerization like thymine and uracil bases. Flexible dipyridone incorporates an extensive non-covalent interaction and shows donor-acceptor property through weak interactions (Singh et al., 2020).

2-pyridone analouges have been observed to possess different pharmacological activities such as antibacterial (Fujita et al., 2005; Li et al., 2000), antifungal (Breinholt et al., 1997), antiviral (Dragovich et al., 2002; Parreira et al., 2001), antitumor (Sharma et al., 2016) and antiplatelet (Parlow& South, 2003). Moreover, 2-pyridone analouges have also been used to manufacture paints (Mijin et al., 2014), pigments, additives for fuels and lubricants, acid-base indicators, and stabilizers for polymers, and coatings (Litvinov et al., 1999). 2-pyridone-based flexible dimers have also been reported as active anti-inflammatory agents (Dubey et al., 2014; Rai et al., 2016; Semple et al., 2003).

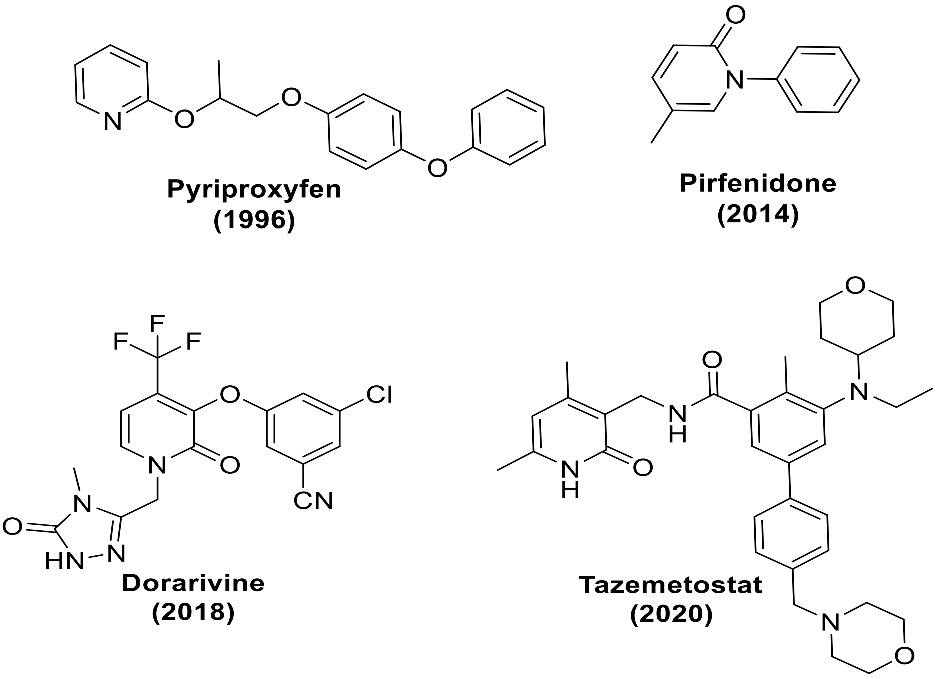

Figure 3.1: Biologically active 2-pyridone derivatives

Recently, the Food and Drug Administration (FDA) had approved 2-pyridone derivative drugs. Pirfenidone in 2014 for the treatment of idiopathic pulmonary fibrosis, Dovarivine in 2018 as a new non-nucleoside reverse transcriptase inhibitor for the treatment of HIV infection (Talwani&Temesgen, 2020) and Tazemetostat in 2020 for the treatment of epithelioid sarcoma. Pyriproxyfen, a pesticide introduced to the United States in 1996, was effective against insect varieties by mimicking their natural hormone, disturbing their growth, and containing 2-pyridone moiety in its structure (**Figure 3.1)**.

3.2. Present work

The present work in chapter 3 deals with the synthesis of 2-pyridone derivative fleximers by introducing aromatic rings to the 2-pyridone active functional group. The aromatic ring was introduced by alkylating the 2-pyridone derivatives at the nitrogen and the oxygen atom in the presence of the base. The methylene group links the pyridine/pyridone and the aromatic rings (**Figure 3.2)**.

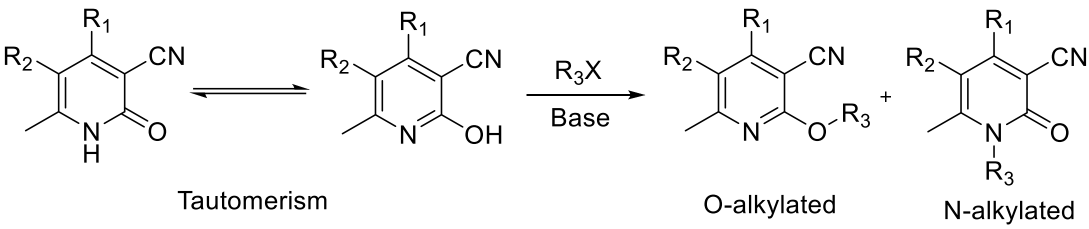

R_1= 2-$NO_2C_6H_4$, 3-ClC_6H_4, 4-$CH_3C_6H_4$, 4-$OCH_3C_6H_4$, CH_3
R_2= H, COOEt
R_3= O or N linked with aromatic ring

Figure 3.2: Basic structural representation of the designed polycyclic aromatic fleximers

3.3. Synthesis of methylene linked aromatic ring with bromide

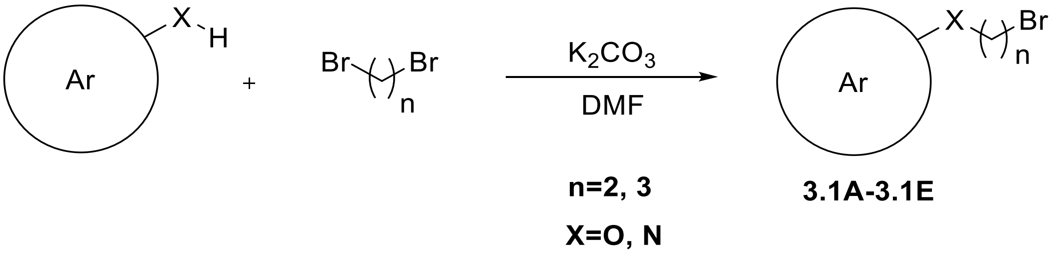

Scheme 3

In scheme 3, we have synthesized a series of aromatic rings linked with an alkyl halide **(Figure 3.3)**. The aromatic compounds are those of polycyclic aromatic ring that contains hydroxy group as its ring substituent or either imide group that contains nitrogen as a part of the ring atom. The alkyl halide moieties come from either 1,2-dibromoethane or 1,3-dibromopropane.

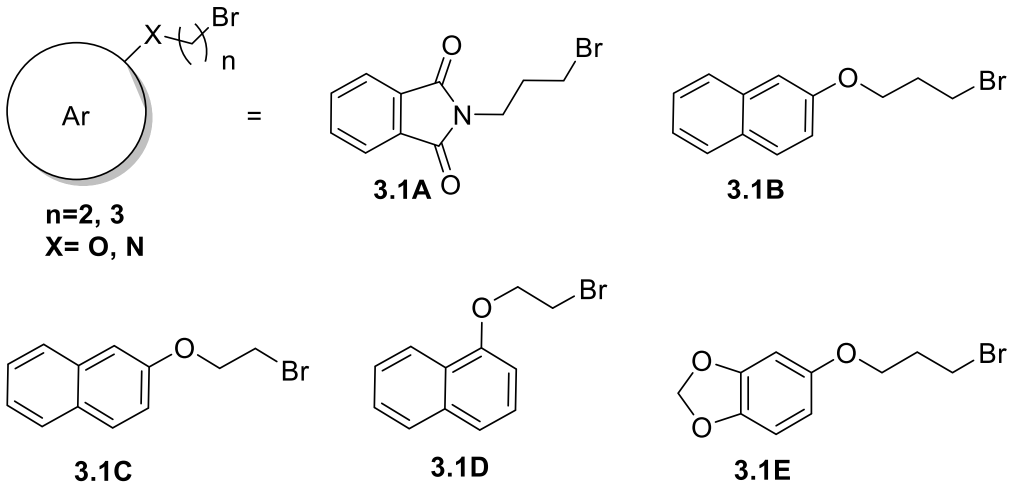

Figure 3.3: Structures of methylene-linked aromatic ring with bromide

3.4. Experimental

^{1}H NMR (300 MHz) and ^{13}C NMR (75 MHz) spectra were recorded on JEOL AL300 FTNMR spectrometer using TMS as an internal reference, and chemical shift values are expressed in δ, ppm units. All the reactions were monitored by thin-layer chromatography (TLC) on pre-coated aluminum sheets of Merck using an appropriate solvent system, and chromatograms were visualized under UV light. Silica gel (60-120 and 230-400 mesh) was employed for column chromatography and flash chromatography, and eluents were ethyl acetate/hexane mixtures.

3.4.1. General procedure for the synthesis of methylene linked aromatic ring with bromide (3.1A-3.1E)

In a 100 mL round bottom flask, either phthalimide, 2-naphthol, 1-naphthol, or sesamol (40.98 mmol) and potassium carbonate (40.98 mmol) were dissolved in 25 mL of dimethylformamide (DMF). Furthermore, the reaction mixture was stirred for 30 minutes at room temperature. After 30 minutes of the reaction, either 1,3-dibromopropane or 1,2-dibromoethane (204.8 mmol) was added to the reaction mixture, and the reaction was continued for 12 h. TLC monitored the completion of the reaction. Solvent DMF was removed by rotary evaporator, and the residue was extracted with chloroform (3 × 200 mL) and washed with water (3 × 100 mL). The combined organic layer was collected and dried over anhydrous sodium sulfate. The crude solid product was then mixed with silica gel (230-400 mesh) and subjected to flash chromatography using ethyl acetate and hexane as eluent. The pure compounds **(3.1A-3.1E)** were collected at 10 % EtOAc/Hexane.

3.4.1.1. 2-(3-bromopropyl)isoindoline-1,3-dione (3.1A): Yield: 0.49g (89%); **^{1}H NMR (300 MHz, $CDCl_3$):** δppm 3.77 – 3.81 (2H, t, CH_2); 4.47 – 4.51 (2H, t, CH_2); 7.15 – 7.17 (1H, d, CH); 7.36 (1H, s, CH); 7.45 – 7.49 (3H, m, CH); 8.34 – 8.36 (2H, dd, CH).

3.4.1.2. 2-(3-bromopropoxy)naphthalene (3.1B): Yield: 0.45g (87%); **^{1}H NMR (300 MHz, $CDCl_3$):** δppm 2.14 – 2.18 (2H, m, CH_2); 3.51 – 3.55 (2H, t, CH_2); 4.20 – 4.24 (2H, t, CH_2); 7.13 – 7.16 (1H, d, CH); 7.34 (1H, s, CH); 7.45 – 7.49 (3H, m, CH); 7.79 – 7.84 (2H, m, CH).

3.4.1.3. 2-(2-bromoethoxy)naphthalene (3.1C): Yield: 0.49g (89%); **^{1}H NMR (300 MHz, $CDCl_3$):** δppm 3.77 – 3.81 (2H, t, CH_2); 4.47 – 4.51 (2H, t, CH_2); 7.15 – 7.17 (1H, d, CH); 7.36 (1H, s, CH); 7.45 – 7.49 (3H, m, CH); 8.34 – 8.36 (2H, dd, CH).

3.4.1.4. 1-(2-bromoethoxy)naphthalene (3.1D): Yield: 0.49g (93%); **^{1}H NMR (300 MHz, $CDCl_3$):** δppm 3.50 – 3.54 (2H, t, CH_2); 4.29 – 4.33 (2H, t, CH_2); 6.19 – 6.21 (1H, d, CH); 7.40 – 7.50 (4H, m, CH); 8.08 – 8.10 (1H, d, CH); 8.36 – 8.38 (1H, d, CH).

3.4.1.5. 5-(3-bromopropoxy)benzo[d][1,3]dioxole (3.1E): Yield: 0.47g (83%); **^{1}H NMR (300 MHz, $CDCl_3$):** δppm 2.51 – 2.55 (2H, m, CH_2); 3.67 – 3.71 (2H, t, CH_2); 4.08 – 4.12 (2H, t, CH_2); 6.32 (2H, s, CH_2); 6.57 (1H, s, CH); 6.67 – 6.69 (1H, d, CH); 7.10 – 7.12 (1H, d, CH)

3.5. Synthesis of polycyclic aromatic fleximers from polycyclic aromatic 2-pyridone derivatives

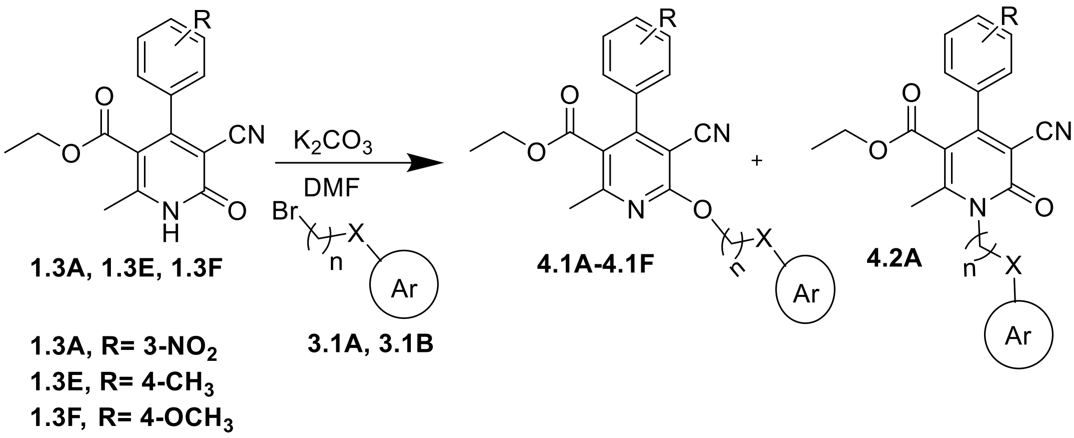

Scheme 4

In scheme 4, the polycyclic 2-pyridone **(1.3A, 1.3E, and 1.3F)** from Scheme 1 was reacted with the methylene-linked aromatic ring with bromide **(3.1A** and **3.1B)** obtained from Scheme 3. This reaction was done in the presence of potassium carbonate as a base and DMF as a solvent to give polycyclic aromatic fleximers for studying nature's interactions by these models **(Figure 3.4)**.

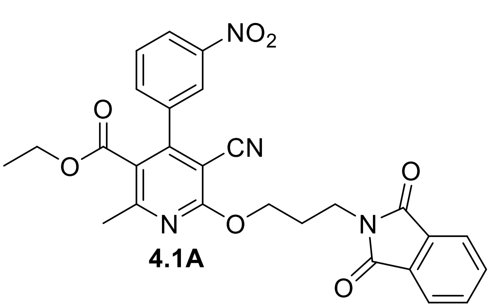

4.1A

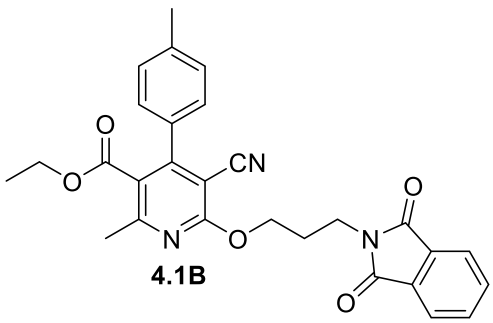

4.1B

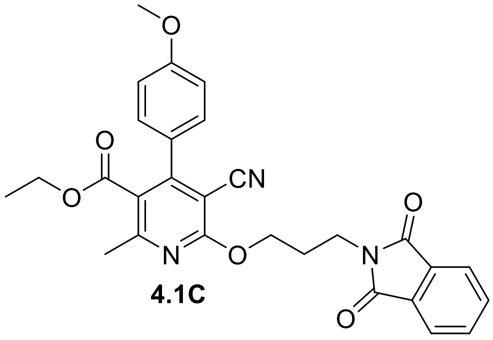

4.1C

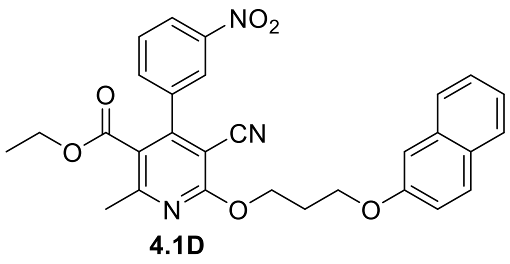

4.1D

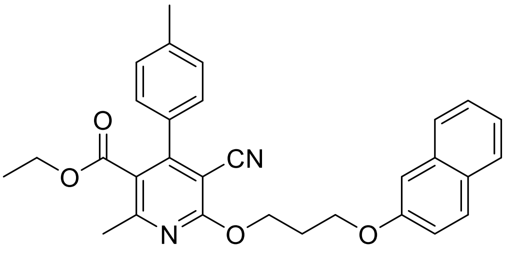

4.1E

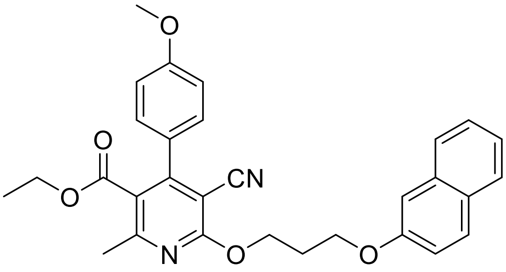

4.1F

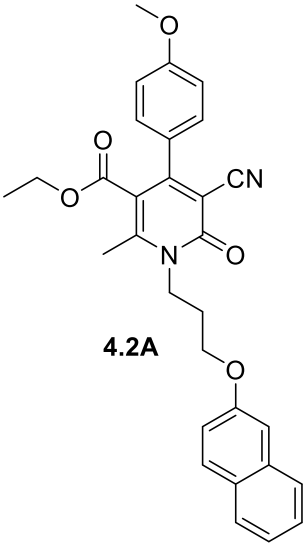

4.2A

Figure 3.4: Structures of polycyclic 2-pyridone derivative fleximers

3.6. Experimental

^{1}H NMR (300 MHz) and ^{13}C NMR(75 MHz) spectra were recorded on JEOL AL300 FTNMR spectrometer using TMS as an internal reference, and chemical shift values are expressed in δ, ppm units. All the reactions were monitored by thin-layer chromatography (TLC) on pre-coated aluminum sheets of Merck using an appropriate solvent system, and chromatograms were visualized under UV light. The product obtained in scheme 5 was purified using ethyl acetate and hexane as eluent by flash column chromatography, employing silica gel (230-400 mesh).

3.6.1 General procedure for the synthesis of polycyclic aromatic fleximers from polycylic 2-pyridone derivatives (4.1A-4.1F, 4.2A)

In a 100 ml round bottom flask, any of the compounds **1.3A, 1.3E** or **1.3F** (0.0068 mol) and potassium carbonate (1 g, 0.0072 moles) were taken in DMF (30 mL) and stirred for 20 min. After 20 min, either compound **3.1A** or **3.1B** (0.0068 mol) was added and stirred for 12 h. Completion of the reaction was checked via TLC (30% EtOAc& Hexane). After completion of the reaction, DMF was removed under reduced pressure through a rotary evaporator, and the reaction mixture was extracted with EtOAc/ H2O (100/ 100 X 3 ml).). The EtOAc layer was dried with anhydrous Na2SO4 and filtered. EtOAc was removed, and the product was purified via SiO_2-flash chromatography. The pure compounds **(4.1A-4.1F)** were collected at 10 % EtOAc/Hexane. The compound **4.2A** was also collected at 25 % ethyl acetate-hexane.

3.6.1.1. Ethyl 5-cyano-6-(3-(1,3-dioxoisoindolin-2-yl)propoxy)-2-methyl-4-(3-nitrophenyl) nicotinate (4.1A): White solid, yield: 89%, m.p. 213-215°C; **^{1}H NMR (300 MHz, $CDCl_3$):** δppm 0.96 – 1.00 (3H, t, CH_3, J = 7.2 Hz); 2.22 – 2.31 (2H, m, CH_2); 2.56 (3H, s, CH_3); 3.91 – 3.96 (2H, t, CH_2, J = 6.4 Hz); 4.01 – 4.08 (2H, q, CH_2, J = 7.2 Hz); 4.56 – 4.60 (2H, t, CH_2, J = 6.4 Hz); 7.64 – 7.75 (4H, m, Ar-H); 7.81 – 7.86 (2H, dd, Ar-H); 8.21 (1H, s, Ar-H); 8.32 – 8.36 (1H, m, Ar-H); **^{13}C NMR (75 MHz, $CDCl_3$):** δppm 14.3, 22.3, 28.7, 38.6, 59.8, 65.3, 91.5, 109.3, 113.8, 121.5, 123.1, 124.4, 129.6, 131.8, 132.2, 133.9, 138.4, 148.3, 154.2, 164.5, 164.9, 166.2, 169.7; **MS (m/z):** 515.16 (M+1).

3.6.1.2. Ethyl 5-cyano-6-(3-(1,3-dioxoisoindolin-2-yl)propoxy)-2-methyl-4-(p-tolyl)nicotinate (4.1B): White solid, yield: 92%, m.p. 197-200°C; **^{1}H NMR (300 MHz, $CDCl_3$):** δppm 0.90 – 0.95 (3H, t, CH_3, J = 7.2 Hz); 2.20 – 2.29 (2H, m, CH_2); 2.39 (3H, s, CH_3); 2.50 (3H, s, CH_3); 3.90 – 3.94 (2H, t, CH_2, J = 6.6 Hz); 3.97 – 4.04 (2H, q, CH_2, J = 7.2 Hz); 4.52 – 4.56 (2H, t, CH_2, J = 6.0 Hz); 7.23 (4H, s, Ar-H); 7.69 – 7.73 (2H, m, Ar-H); 7.81 – 7.86 (2H, m, Ar-H); **^{13}C NMR (75 MHz, $CDCl_3$):** δppm 14.5, 19.8, 22.3, 26.5, 38.7, 61.3, 65.4, 92.1, 108.9, 116.1, 123.7, 127.1, 129.5, 131.0, 132.6, 135.0, 154.3, 164.8, 166.1, 166.9, 168.7; **MS (m/z):** 484.52 (M+1).

3.6.1.3. Ethyl 5-cyano-6-(3-(1,3-dioxoisoindolin-2-yl)propoxy)-4-(4-methoxyphenyl)-2-methylnicotinate (4.1C): White solid, yield: 94%, m.p. 209-211°C; **^{1}H NMR (300 MHz, $CDCl_3$):** δppm 0.95 – 1.00 (3H, t, CH_3, J = 7.2 Hz); 2.21 – 2.29 (2H, m, CH_2); 2.49 (3H, s, CH_3); 3.84 (3H, s, CH_3); 3.90 – 3.95 (2H, t,

CH_2, *J* = 6.6 Hz); 4.00 – 4.07 (2H, q, CH_2, *J* = 7.2 Hz); 4.52 – 4.56 (2H, t, CH_2, *J* = 6.0 Hz); 6.94 – 6.98 (2H, m, Ar-H); 7.28 – 7.32 (2H, m, Ar-H); 7.68 – 7.74 (2H, m, Ar-H); 7.81 – 7.87 (2H, m, Ar-H); **^{13}C NMR (75 MHz, $CDCl_3$):** δppm 13.9, 21.7, 26.5, 38.9, 55.9, 60.9, 65.3, 91.2, 109.2, 113.6, 114.8, 132.0, 129.5, 130.0, 132.1, 133.1, 154.2, 160.6, 164.1, 164.8, 166.0, 168.1; **MS (m/z):** 500.15 (M+1).

3.6.1.4. Ethyl 5-cyano-2-methyl-6-(3-(naphthalen-2-yloxy)propoxy)-4-(3-nitrophenyl) nicotinate (4.1D): White solid, yield: 94%, m.p. 206-208°C;**^{1}H NMR (300 MHz, $CDCl_3$):** δppm 0.96 – 1.00 (3H, t, CH_3, *J* = 7.2 Hz); 2.22 – 2.31 (2H, m, CH_2); 2.56 (3H, s, CH_3); 3.91 – 3.96 (2H, t, CH_2, *J* = 6.4 Hz); 4.01 – 4.08 (2H, q, CH_2, *J* = 7.2 Hz); 4.56 – 4.60 (2H, t, CH_2, *J* = 6.4 Hz); 7.12 (1H, s, Ar-H); 7.81 – 7.95 (4H, m, Ar-H); 8.21-8.26 (2H, dd, Ar-H); 8.30 (1H, s, Ar-H); 8.34 – 8.38 (3H, m, Ar-H); **^{13}C NMR (75 MHz, $CDCl_3$):** δppm 14.1, 21.6, 30.1, 61.3, 64.1, 65.0, 91.5, 106.2, 109.7, 114.6, 118.1, 122.7, 124.1, 124.6, 126.3, 126.9, 127.5, 129.2, 129.4, 129.8, 130.1, 133.5, 140.1, 148.9, 154.4, 155.6, 164.2, 164.9, 167.0; **MS (m/z):** 512.53 (M+1).

3.6.1.5. Ethyl 5-cyano-2-methyl-6-(3-(naphthalen-2-yloxy)propoxy)-4-(p-tolyl)nicotinate (4.1E): White solid, yield: 89%, m.p. 218-220°C; **^{1}H NMR (300 MHz, $CDCl_3$):** δppm 0.97-1.01(3H, t, CH_3, *J* = 7.2 Hz); 2.20 – 2.29 (2H, m, CH_2); 2.39 (3H, s, CH_3); 2.54 (3H, s, CH_3); 3.90 – 3.95 (2H, t, CH_2, *J* = 6.4 Hz); 4.02 – 4.09 (2H, q, CH_2, *J* = 7.2 Hz); 4.55 – 4.60 (2H, t, CH_2, *J* = 6.4 Hz); 7.11 (1H, s, Ar-H); 7.80 – 7.94 (4H, m, Ar-H); 8.20-8.25 (2H, dd, Ar-H); 8.31 (1H, s, Ar-H); 8.35 – 8.40 (3H, m, Ar-H); **^{13}C NMR (75 MHz, $CDCl_3$):** δppm 14.5, 21.3, 22.1, 30.2, 59.9, 63.9, 65.0, 91.6, 107.3, 109.5, 114.5, 118.3, 124.0, 126.8, 127.1, 127.9, 129.4, 129.6, 130.1, 132.2, 135.0, 154.5, 155.6, 164.7, 165.3, 166.7; **MS (m/z):** 481.22 (M+1).

3.6.1.6. Ethyl 5-cyano-4-(4-methoxyphenyl)-2-methyl-6-(3-(naphthalen-2-yloxy)propoxy) nicotinate (4.1F): White solid, yield: 79%, m.p. 237-239°C; **^{1}H NMR (300 MHz, $CDCl_3$):** δppm 0.95 – 1.00 (3H, t, CH_3, *J* = 7.2 Hz); 2.21 – 2.29 (2H, m, CH_2); 2.49 (3H, s, CH_3); 3.84 (3H, s, CH_3);3.87 – 3.93 (2H, t, CH_2, *J* = 6.4 Hz); 4.00 – 4.07 (2H, q, CH_2, *J* = 7.2 Hz); 4.56 – 4.61 (2H, t, CH_2, *J* = 6.4 Hz); 7.13 (1H, s, Ar-H); 7.79 – 7.93 (4H, m, Ar-H); 8.23-8.28 (2H, dd, Ar-H); 8.31 (1H, s, Ar-

H); 8.37 – 8.42 (3H, m, Ar-H); **^{13}C NMR (75 MHz, $CDCl_3$):** δppm 13.9, 23.1, 30.3, 55.7, 61.5, 65.1, 91.6, 107.3, 164.8, 114.3, 114.9, 118.5, 124.5, 126.4, 126.9, 127.8, 129.1, 129.6, 130.4, 133.6, 154.5, 155.6, 161.0, 164.1, 164.9, 167.3; **MS (m/z):** 497.23 (M+1).

3.6.1.7. Ethyl 5-cyano-4-(4-methoxyphenyl)-2-methyl-1-(3-(naphthalen-2-yloxy)propyl)-6-oxo-1,6-dihydropyridine-3-carboxylate (4.2A): White solid, yield: 19%, m.p. 232-234°C; **^{1}H NMR (300 MHz, $CDCl_3$):** δppm 0.94 – 0.99 (3H, t, CH_3, $J = 7.2$ Hz); 2.27 – 2.35 (2H, m, CH_2); 2.53 (3H, s, CH_3); 3.42 – 3.47 (2H, t, CH_2, $J = 6.4$ Hz); 3.84 (3H, s, CH_3);4.05 – 4.12 (2H, q, CH_2, $J = 7.2$ Hz); 4.59 – 4.64 (2H, t, CH_2, $J = 6.4$ Hz); 6.95 (1H, s, Ar-H); 7.69 – 7.83 (4H, m, Ar-H); 8.13-8.18 (2H, dd, Ar-H); 8.25 (1H, s, Ar-H); 8.32 – 8.37 (3H, m, Ar-H); **^{13}C NMR (75 MHz, $CDCl_3$):** δppm 13.7, 14.3, 26.5, 42.3, 55.6, 62.8, 73.9, 106.3, 109.0, 113.9, 115.2, 116.3, 118.7, 124.0, 124.8, 126.3, 126.9, 127.8, 129.1, 129.7, 130.1, 140.7, 155.6, 156.9, 159.9, 165.3, 170.1; **MS (m/z):** 497.55 (M+1).

3.7. Results and Discussions

In scheme 4, a series of polycyclic aromatic fleximers were synthesized by reacting pyridone derivatives of scheme 2 with compounds **(3.1A** and **3.1B**). Alkylation of the pyridones **(1.3A** and **1.3E)** occurs mainly at the carbonyl group's oxygen. However, in the case of the pyridine **(1.3F)**, the reaction takes place on both the nitrogen atom and the carbonyl oxygen, giving both N-linked fleximer and O-linked fleximer. All the products obtained in scheme 4 were recrystallized in ethyl acetate, and the crystal obtained was studied by single-crystal X-ray diffraction (SC-XRD) and Hirshfeld surface analysis.

3.7.1. X-Ray Crystallographic studies and Hirshfeld surface analysis of compounds 4.1A, 4.1B, 4.1C, 4.1D, 4.1E, 4.1F and 4.2A

3.7.1.1. Crystal analysis of compound 4.1A

The compound **4.1A** was recrystallized in ethyl acetate at room temperature by slow evaporation of the solvent. The chiral asymmetric compound **4.1A** was analyzed using SC-XRD **(Figure 3.5)**. The compound crystallized with cell lengths **a**

= 8.2660(2)Å, **b** = 9.7941(2)Å, **c** = 15.4631(3)Å, i.e., $\mathbf{a} \neq \mathbf{b} \neq \mathbf{c}$ and cell angles $\boldsymbol{\alpha}$ = 80..114(2)°, $\boldsymbol{\beta}$ = 85.324(2)°, $\boldsymbol{\gamma}$ = 89.370(2)°, i.e., $\boldsymbol{\alpha} \neq \boldsymbol{\beta} \neq \boldsymbol{\gamma} \neq \mathbf{90°}$ which indicate that the compound is exhibiting triclinic crystal system, with space group P-1 that contains two molecules per unit cell.

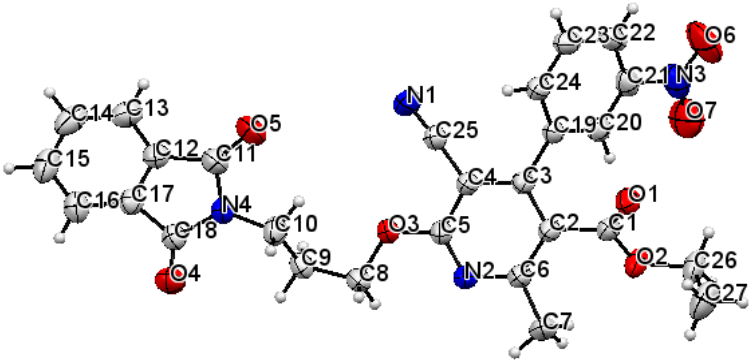

Figure 3.5: ORTEP diagram of compound **4.1A**

Table 3.1: Crystal data on compounds **4.1A**, **4.1B** and **4.1C**

Compound	**4.1A**	**4.1B**	**4.1C**
Identification code	2170484	2170486	2170483
Empirical formula	$C_{27}H_{22}N_4O_7$	$C_{28}H_{25}N_3O_5$	$C_{28}H_{25}N_3O_6$
Formula weight	514.48	483.52	499.51
Temperature(K)	293(2)	293(2)	293(2)
Crystal system	Triclinic	Monoclinic	Triclinic
Space group	P-1	$P2_1/c$	P-1
a(Å)	8.2660(2)	22.7134(14)	8.2728(2)
b(Å)	9.7941(2)	8.2757(5)	12.8622(3)
c(Å)	15.4631(3)	13.0718(8)	23.6886(6)
α(°)	80.114(2)	90	95.533(2)
β(°)	85.324(2)	94.562(5)	92.120(2)
γ(°)	89.370(2)	90	90.398(2)
Volume(Å^3)	1229.16(5)	2449.3(3)	2507.02(11)
Z	2	4	4
ρ (g/cm^3)	1.390	1.295	1.323
μ(mm^{-1})	0.103	0.091	0.094
F(000)	536.0	992.0	1048.0
Crystal size(mm^3)	0.2 × 0.19 × 0.18	0.18 × 0.16 × 0.14	0.16 × 0.15 × 0.13
Radiation	MoKα (λ = 0.71073)	MoKα (λ = 0.71073)	MoKα (λ = 0.71073)
2Θ range for data collection(°)	6.494 to 54.808	6.368 to 54.994	6.124 to 55.13
Index ranges	$-10 \le h \le 10, -11 \le k \le 12, -19 \le l \le 19$	$-29 \le h \le 29, -10 \le k \le 10, -16 \le l \le 16$	$-10 \le h \le 10, -16 \le k \le 12, -26 \le l \le 30$
Reflections collected	16294	21898	29373
Independent reflections	5254	5329	10372
Data/restraints/parameters	5254/0/345	5329/0/325	10372/0/673
Goodness-of-fit on F^2	1.077	1.016	0.975
Final R indexes [I>=2σ (I)]	$R_1 = 0.0469$, $wR_2 = 0.1151$	$R_1 = 0.0905$, $wR_2 = 0.2492$	$R_1 = 0.0584$, $wR_2 = 0.1335$
Final R indexes [all data]	$R_1 = 0.0649$, $wR_2 = 0.1276$	$R_1 = 0.1810$, $wR_2 = 0.3060$	$R_1 = 0.1294$, $wR_2 = 0.1648$
Largest diff.peak/hole/e Å^{-3}	0.15/-0.24	0.45/-0.28	0.22/-0.20

The chiral asymmetric compound **4.1A** crystal structure shows that the nitrobenzene rings twisted away from the plane of the parent pyridine ring and with a dihedral angle of 52.35°. The phthalimide ring also flips away from the parent pyridine ring plane at a dihedral angle of 15.32°. All three rings are planar and have sp^2 hybridized atoms, facilitating the delocalization of π-orbitals. The crystallographic information is summarized in **Table 3.1**.

The supramolecular framework of compound 4.1A: The molecular association of compound **4.1A** involves C-H…O and C-H…N interactions horizontally along the plane of the rings. C-H...O interactions arise between the phthalimide oxygen (O5) and hydrogen (H13), having an interaction distance of 2.500Å. C-H…N interactions with a distance of 2.726Å emerge between the phthalimide hydrogen (H14) and the nitrogen (N1) of the cyano group. These C-H…O and C-H…N interactions along the plane of the rings result in the formation of $R_2^2(10)$ and $R_2^2(15)$ graph set notations **(Figure 3.6 (b))**. The resulted graph sets motif is linked with another graph set of the same motif through C-H…O interactions between the hydrogen (H22) of the nitrogen nitrobenzene ring and the oxygen (O4) of the phthalimide ring at a distance of 2.531Å, which leads to the formation of a polymeric layer of sheets. This C-H…O interaction, in combination with the C-H…N interactions, also forms a graph set of $R_4^4(32)$ **(Figure 3.6 (b))**. The oxygen (O1) of the ester moiety acts as a bifurcated acceptor. It forms a C-H…O interlayer bond with the hydrogen (H16) of the phthalimide ring and the hydrogen (H23) of the nitrobenzene ring. These bonds have an interaction distance of 2.547Å and 2.717Å, respectively. This two interlayer C-H…O interaction results in the formation of $R_2^2(16)$ and $R_2^2(30)$ graph sets **(Figure 3.6 (c) and (d))**. The molecular self-assembly of compound **4.1A** also displays C-H…C interlayer interaction between the nitrobenzene hydrogen (H20) and the phthalimide ring carbons (C15) and (C16) at a distance of 2.823Å and 2.837Å **(Figure 3.6 (e))**. The molecular packing within the unit cell is stabilized by C-H...O interaction which has an interaction distance of 2.547Å and lone pair…π interaction between the phthalimide oxygen (O4) and the pyridine ring at a distance of 3.263Å. The supramolecular framework of compound **4.1A** also displays two C-H…π interactions from both sides of the benzenoid moiety of the phthalimide ring and one C-H…π interaction from one side of the nitrobenzene ring. The C-H…π interaction distance found for these are 3.187Å, 3.282Å and 3.228Å **(Figure 3.6 (a), (f), and (g))**. The C-H…π interaction with an interaction distance of 3.187Å also assists the stabilization of the crystal packing. In addition, π…π parallel displaced staking interaction is also found between the nitrobenzene rings **(Figure 3.6 (h))**. The non-covalent interactions are listed in **Table 3.2**.

Table 3.2: Hydrogen bonds and other interactions in compound **4.1A**

Donor-H...Acceptor	**D – H, Å**	**H...A, Å**	**D...A, Å**	**D - H...A, º**
C22-H22…O4	0.930	2.531	3.314	142.00
C20-H20…C15	0.930	2.823	3.705	158.69
C20-H20…C16	0.930	2.837	3.517	130.89
C13-H13…O5	0.930	2.500	3.327	148.17
C14-H14…N1	0.930	2.726	3.654	175.20
C23-H23…O1	0.930	2.717	3.629	167.10
C16-H16…O1	0.930	2.547	3.210	128.55
C7-H7B…π(C12-C17)	0.930	3.187	3.890	131.49
C27-H27A…π(C19-C24)	0.960	3.282	4.206	162.01
C20-H20…π(C12-C17)	0.930	3.228	3.960	137.04
Other interactions				
π(C19-C24)…π(C19-C24)		4.600		
O4…π(C2-C6, N2)		3.263		
Intramolecular				
C9-H9A…O3	0.970	2.509	2.345	69.14
C10-H10B…O3	0.970	2.456	2.848	103.85
C26-H26A…O1	0.970	2.440	2.680	93.50
C27-H27C…O1	0.960	2.668	3.153	111.84

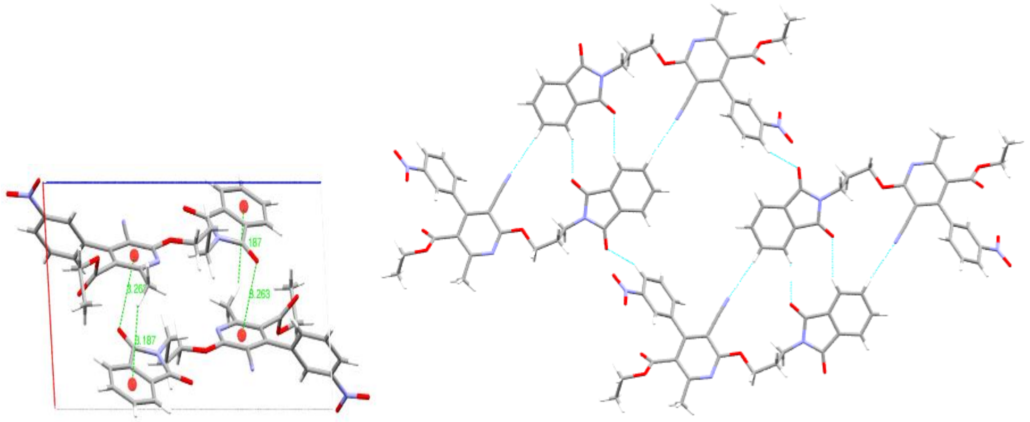

(a) (b)

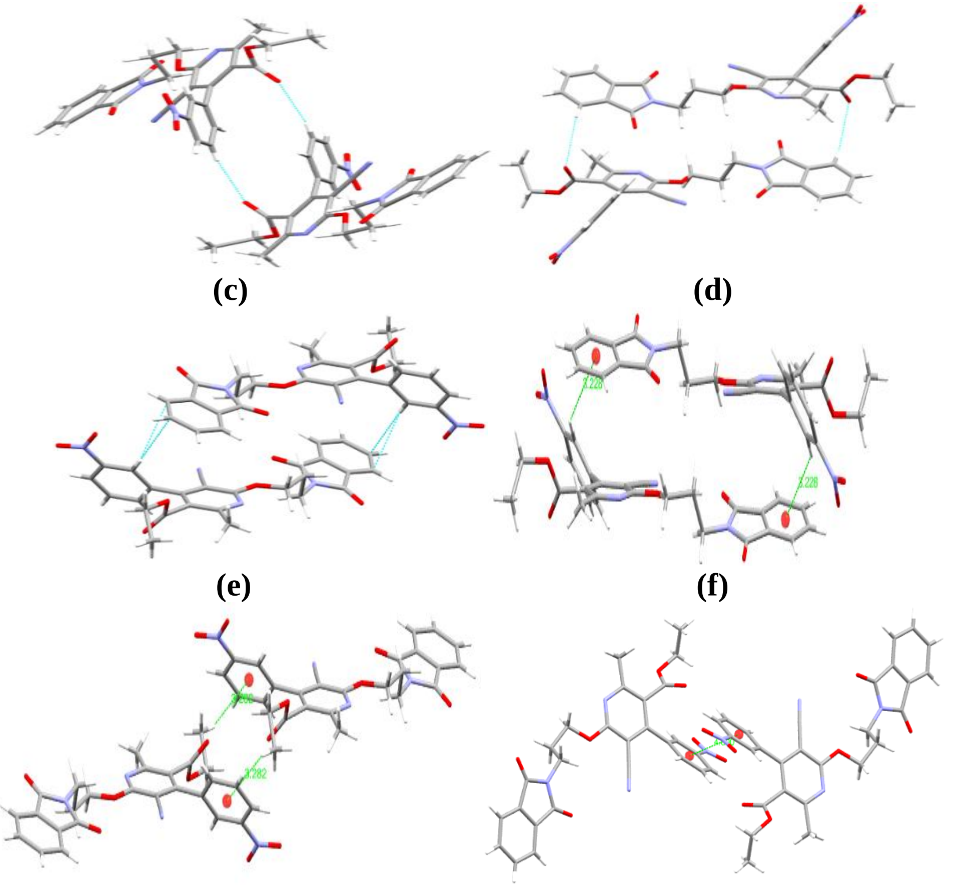

(c) (d)

(e) (f)

(g) (h)

Figure 3.6: (a) Packing diagram of compound **4.1A**, (b), (c) and (d) graph sets, (e) C-H…C, (f) and (g) C-H…π interactions, (h) π…π interactions, in compound **4.1A**

Hirshfeld surface analysis of compound 4.1A: The Hirshfeld surface mapped over the $_{\text{norm}}$ in the range of -0.17 to 1.50Å for compound **4.1A** is displayed in **Figure 3.7 (a) and (b)**. The region of red spots corresponds to shorter contacts due to C-H…O, C-H…N, and C-H…C interactions.

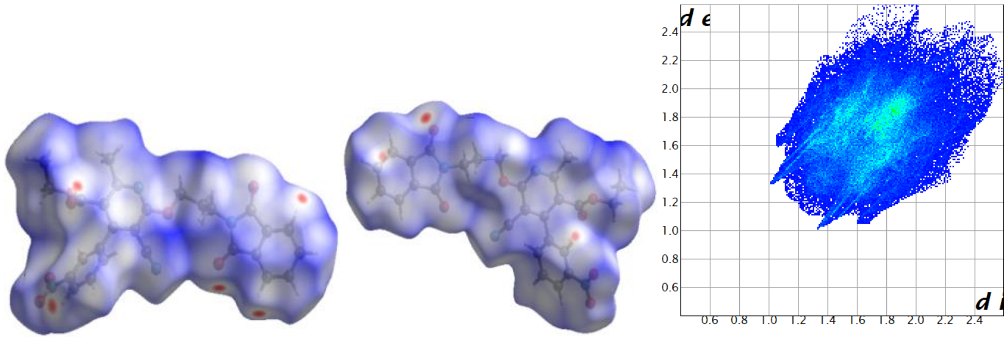

(a) (b) (c)

Figure 3.7: (a) and (b) d_{norm} both side view, (c) 2-D fingerprint plot, of compound **4.1A**

The intensity of the red color and the size of the spots depends on interaction distance. The more dominant the interaction, the more intense the red color and the larger the size of the spots and vice versa in Hirshfeld surface analysis.

The 2-D fingerprint plot of the compound **4.1A** represents the relative percentage contributions of non-covalent interaction to the Hirshfeld surface **(Figure 3.7 (c))**. Those are H…H (33.5%), O...H (28.8%), C…H (14.5%), N…H (9.1%), C…C (5.4%), O…C (4.0%), C…N (1.4%), N…O (1.4%), O…O (1.3%), N…N (0.5%). The pair of spokes-like patterns in the region of di + de = 2.3-2.8Å represents O…H interactions. Similarly, N…H interaction is also reflected around the spoke in the region of di + de = 2.6-3.2Å. The C-H...π and C…H contacts appear in the same region in the 2-D fingerprint, which appears as a characteristic flip wing-like pattern in the region of di + de = 2.7-3.6Å. The C…C and O…C contacts which account for 5.4% and 4.0%, respectively, signify the presence of π...π stacking interactions and lone pair...π interaction within the aromatic ring.

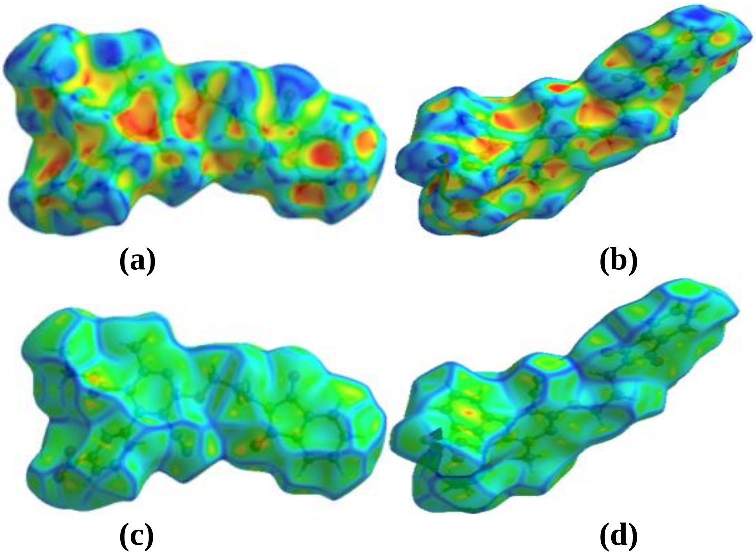

Figure 3.8: (a) and (b) Shape-index, (c) and (d) Curvedness, both side views of compound **4.1A**

The shape-index is in a range of -1 to 1Å for compound **4.1A** shows the presence of complementary pair of red and blue triangles having an edge-to-edge connection at the surface of the nitrobenzene ring, which indicates the presence of π...π stacking interactions between the rings **(Figure 3.8 (b))**. The yellowish-red colored concave regions around the surface of the aromatic rings represent the acceptor region where C-H...π and lone pair…π interactions occur **(Figure 3.8 (a) and (b))**. The curvedness in a range of -4 to 0.4 Å for compound **4.1A** also display a flat green region with a yellowish spot around the surface of the nitrobenzene, which indicates the presence of π…π stacking interaction between the rings **(Figure 3.8 (d))**.

The C-H…O, C-H…N, C-H…C, C-H…π , π…π and lone pair…π interactions found within the supramolecular association of compound **4.1A** are also supported by the Hirshfeld calculation for weak non-covalent intermolecular interactions within the cluster of radius 3.8Å from a single crystals fragment is shown in **Figure 3.9**.

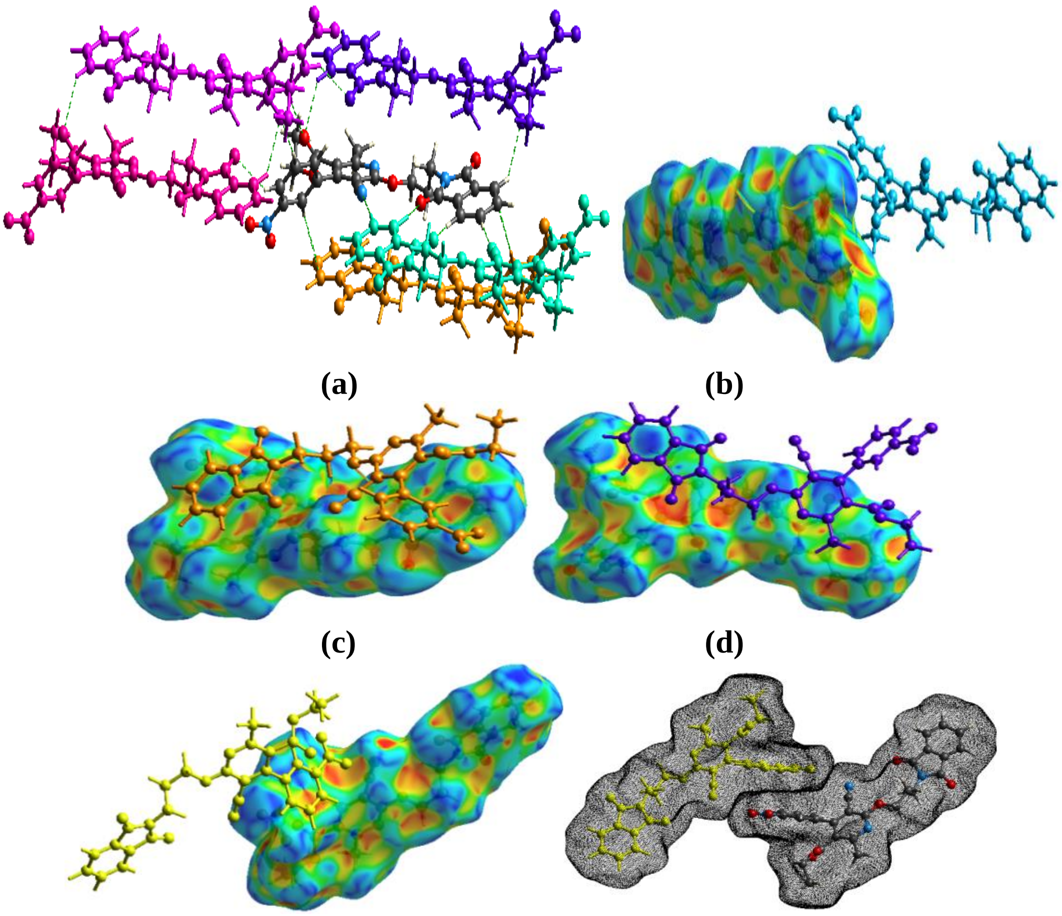
(a) **(b)**

(c) **(d)**

(e) **(f)**

Figure 3.9: (a) C-H…O, C-H…N and C-H…C interactions, (b) and (c) C-H…π interactions, (d) Lone pair…π and C-H…π interactions, (e) and (f) π…π interaction, in compound **4.1A**

3.7.1.2. Crystal analysis of compound 4.1B

The compound **4.1B** was recrystallized in ethyl acetate at room temperature by slow evaporation of the solvent. The chiral asymmetric compound **4.1B** was analyzed using SC-XRD **(Figure 3.10)**. The compound crystallized with cell lengths **a** = 22.7134(14)Å, **b** = 8.2757(5)Å, **c** = 13.0718(8)Å, i.e., $\mathbf{a} \neq \mathbf{b} \neq \mathbf{c}$ and cell angles $\boldsymbol{\alpha}$ = 90°, $\boldsymbol{\beta}$ = 94.562(5)°, $\boldsymbol{\gamma}$ = 90°, i.e., $\boldsymbol{\alpha = \gamma = 90°}$, $\boldsymbol{\beta \neq 90°}$. It indicates that the compound exhibits a monoclinic crystal system, with space group P2$_1$/c containing four molecules per unit cell.

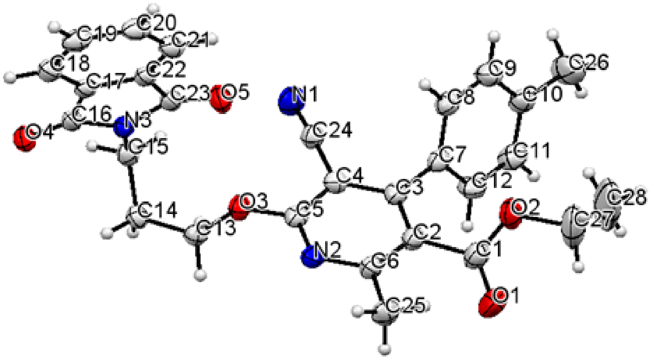

Figure 3.10: ORTEP diagram of compound **4.1B**

The chiral asymmetric compound **4.1B** crystal structure shows that the toluene rings twisted away from the plane of the parent pyridine ring and with a dihedral angle of 64.58°. The phthalimide ring also twisted and flipped away from the parent pyridine ring plane at a dihedral angle of 87.82°. Maximum flexibility is achieved through the C14 atom. The crystallographic information is summarized in **Table 3.1**.

The supramolecular framework of compound 4.1B: The molecular association of compound **4.1B** involves C-H…O and C-H…N interactions. The oxygen (O4) acts and forms two C-H…O bonds with the phthalimide ring hydrogen (H21) and the linker hydrogen (H13A) from two different molecules at an interaction distance of 2.573Åand 2.476Å, respectively. These two C-H…O interactions serves as the stabilizing force within the crystal packing, and the C-H…O network between them forms a graph set notation of $R_4^2(20)$ **(Figure 3.11 (b))**. The hydrogen (H27A) from the alkyl group of the ester moiety interacts with the nitrogen (N1) of the cyano group and forms C-H…N interactions at an interaction distance of 2.665Å. This C-H…N interactions, together with the C-H…O interactions at a distance of 2.476Å involving three molecules of compound **4.1B**, also result in the formation of $R_3^3(29)$ graph set **(Figure 3.11 (c))**. The crystal packing within the unit cell also displays lone pair…π interaction between the oxygen (O4) and the pyrrole ring moiety of the phthalimide ring at a distance of 3.262Å. It is facilitated by the C-H…π interaction between the linker hydrogen (H14A) and the phthalimide benzenoid ring at a distance of 3.542Å **(Figure 3.11 (d))**. In addition to this, the pyridine ring p-orbital also forms two C-H…π interactions with the toluene ring hydrogen (H9) and the phthalimide ring hydrogen (H19) at an interaction distance of 3.348Å and 3.047Å respectively **(Figure 3.11 (f) and (g))**. The extensive network of C-H...O and C-H…N interactions also display weak π…π interaction between the pyrrole ring moiety at an interaction distance of 3.717Å **(Figure 3.11 (e))** as well as C-H…π interaction between the hydrogen (H27A) from the alkyl group of the ester moiety and the toluene ring p-orbital at a distance of 3.410Å **(Figure 3.11 (h))**. The non-covalent interactions found in the crystal structures of compound **4.1B** are given in **Table 3.3.**

Table 3.3: Hydrogen bonds and other interactions in compound **4.1B**

Donor-H...Acceptor	**D – H, Å**	**H...A, Å**	**D...A, Å**	**D - H...A, º**
C27-H27A…N1	0.970	2.665	3.261	120.07
C13-H13A…O4	0.970	2.476	3.347	149.38
C21-H21…O4	0.930	2.573	3.373	144.38
C12-H12…H26A	0.930	2.351	3.061	132.88
C14-H14A…π(C17-C22)	0.970	3.542	3.922	106.00
C9-H9…π(C1-C6,N2)	0.930	3.348	4.018	130.85
C19-H19…π(C1-C6,N2)	0.930	3.407	4.047	128.08
C27-H27A…πC7-C12)	0.970	3.410	4.086	128.57
Other contacts				
O4…π(C16,C17,C22,C23,N3)		3.262		
π(C16,C17,C22,C23,N3)… π(C16,C17,C22,C23,N3)		3.717		
Intramolecular				
C13-H13A…O5	0.970	2.945	3.389	109.16
C14-H14A…O4	0.970	3.077	3.517	109.18
C25-H25A…O1	0.960	2.698	3.071	103.72
C27-H27B…O1	0.969	2.212	2.666	107.32
C28-H28C…π(C7-C12)	0.960	3.251	4.083	146.07

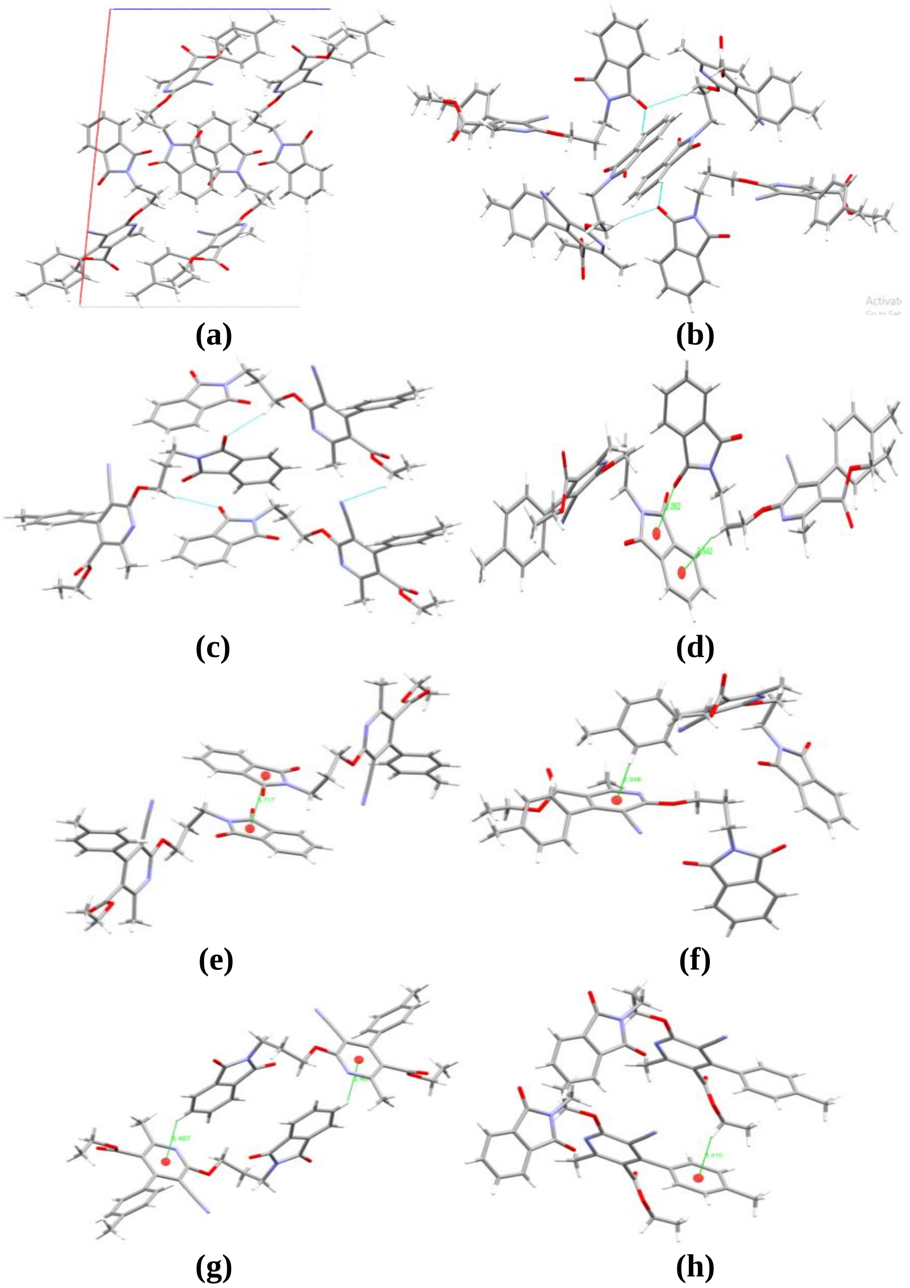

(a) (b)

(c) (d)

(e) (f)

(g) (h)

Figure 3.11: (a) Packing diagram of compound **4.1B**, (b) and (c) graph sets, (d) Lone pair…π and C-H…π interactions, (e) π…π interaction, (f), (g) and (h) C-H…π interactions, in compound **4.1B**

Hirshfeld surface analysis of compound 4.1B: The Hirshfeld surface mapped over the d_{norm} in the range of -0.16 to 1.44Å for compound **4.1B** is displayed in **Figure 3.12 (a) and (b)**. The region of red spots corresponds to shorter contacts due to C-H…O, C-H…N, and C-H…H interactions. The intensity of the red color and the size of the spots depends on interaction distance. The more dominant the interaction, the more intense the red color and the larger the size of the spots and vice versa.

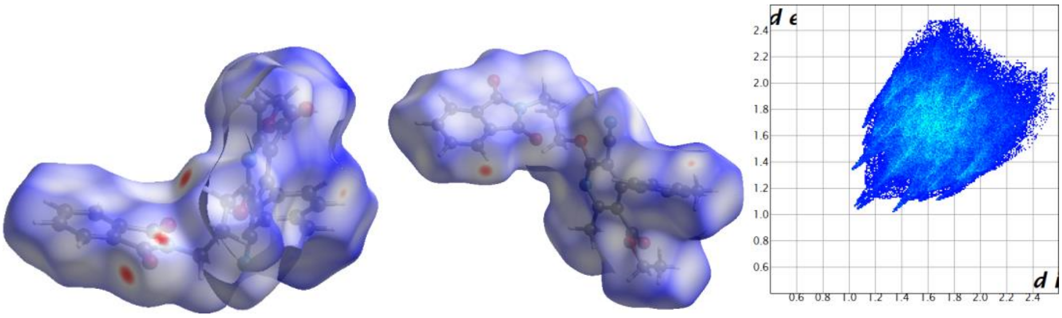

(a) **(b)** **(c)**

Figure 3.12: (a) and (b) d_{norm} both side view, (c) 2-D fingerprint plot, of compound **4.1B**

The 2-D fingerprint plot of the compound **4.1B** represents the relative percentage contribution of non-covalent interaction to the Hirshfeld surface **(Figure 3.12 (c))**. Those are H…H (46.4%), C…H (19.6%), O...H (18.3%), N…H (9.9%), C…C (1.3%), O…C (2.5%),N…O (0.9%), C…N (0.7%) and N…N (0.4%). The pair of spoke-like patterns in the region of di + de = 2.3-2.6Å represents O…H interactions. Also, N…H interaction is also reflected in the region of di + de = 2.6-3.2Å. The C-H...π and C…H contacts appear in the same region and appear like a characteristic flip wing-like pattern in the region of di + de = 2.8-3.6Å. The C…C and O…C contacts account for 1.3%, signifying the presence of very weak π...π stacking interaction.

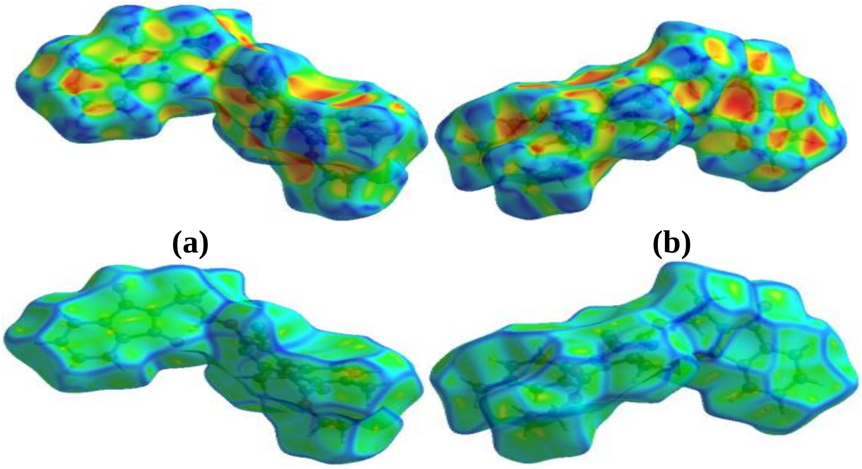

(a) **(b)**

(c) **(d)**

Figure 3.13: (a) and (b) Shape-index, (c) and (d) Curvedness, both side views of compound **4.1B**

The shape-index surface mapped over a range of -1 to 1Å for compound **4.1B** shows the presence of complementary pair of red and blue triangles at the surface of the pyrrole ring moiety, which indicates the presence of π...π stacking interactions between the rings **(Figure 3.13 (a))**. The yellowish-red colored concave regions around the surface of the aromatic rings represent the acceptor region where C-H...π and lone pair…π interactions occur **(Figure 3.13 (a) and (b))**. The curvedness surface in a range of -4 to 0.4 Å for compound **4.1B** also displays a flat green region with a yellowish spot around the surface of the pyrrole ring, which indicates the presence of π…π stacking interaction between the rings **(Figure 3.13 (c))**.

The C-H…O, C-H…N, C-H…H, C-H…π, π…π, and lone pair…π interactions found within the supramolecular association of compound **4.1B** are also supported by the Hirshfeld calculation for weak non-covalent intermolecular interactions within the cluster of radius 3.8Å from a single crystals fragment is shown in **Figure 3.14**.

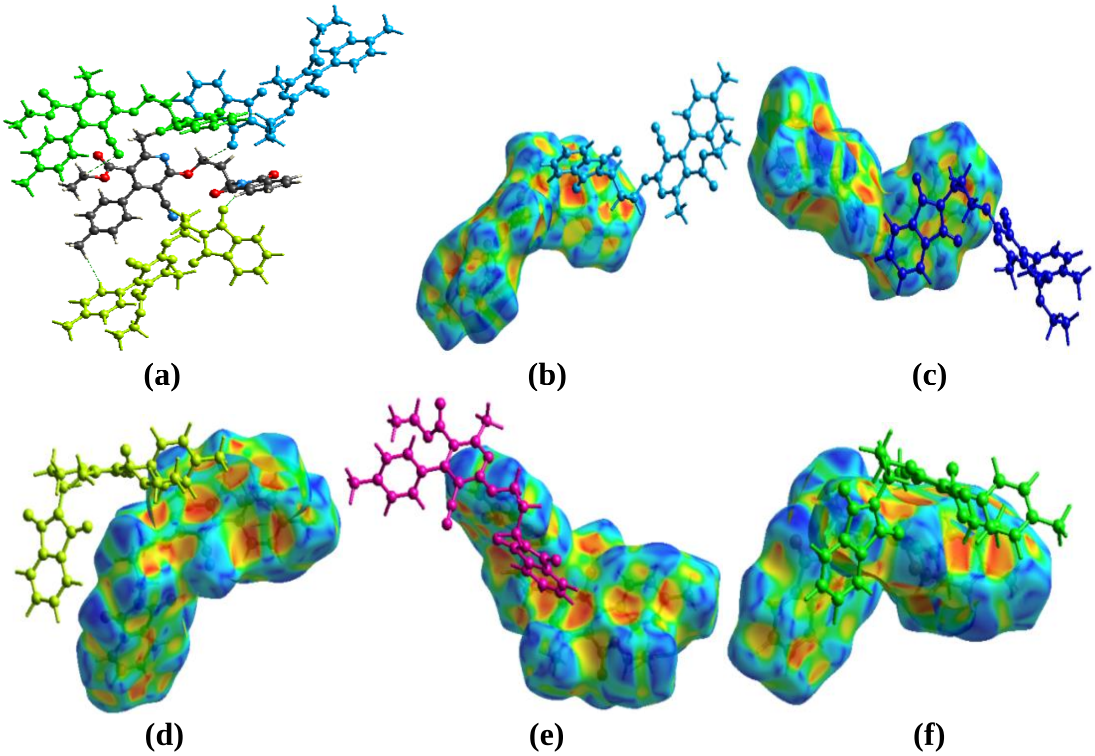

Figure 3.14: (a) C-H…O, C-H…N and C-H…H interactions, (b) Lone pair…π and C-H…π interactions, (c) π…π interaction, (d), (e) and (f) C-H…π interactions, in compound **4.1B**

3.7.1.3. Crystal analysis of compound 4.1C

The compound **4.1C** was recrystallized in ethyl acetate at room temperature by slow evaporation of the solvent. The chiral asymmetric compound **4.1C** was analyzed using SC-XRD **(Figure 3.15)**. The compound crystallized with cell lengths **a** = 8.2728(2)Å, **b** = 12.8622(3)Å, **c** = 23.6886(6)Å, i.e., **a** ≠ **b** ≠ **c** and cell angles $\boldsymbol{\alpha}$ = 95.533(2)°, $\boldsymbol{\beta}$ = 92.120(2)°, $\boldsymbol{\gamma}$ = 90.398(2)°, i.e., $\boldsymbol{\alpha \neq \beta \neq \gamma \neq 90°}$ which indicate that the compound is exhibiting triclinic crystal system, with space group P-1 that contains four molecules per unit cell.

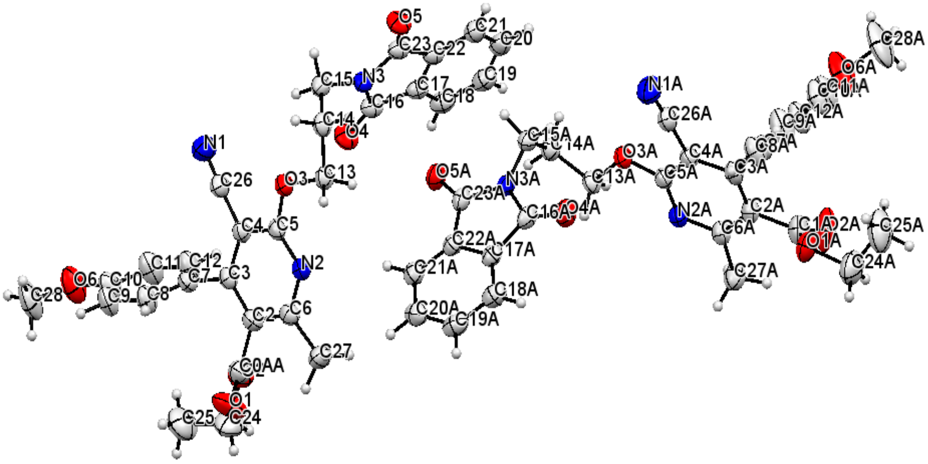

Figure 3.15: ORTEP diagram of compound **4.1C**

The chiral asymmetric compound **4.1C** crystal structure shows that the anisole ring twisted away from the plane of the parent pyridine ring with a dihedral angle of 69.27° and 75.53° for the two crystals. The phthalimide rings also twisted and flipped towards the pyridone, where maximum flexibility is observed at C14 and C14A. The dihedral angle between the phthalimide ring and the pyridone ring in both the crystals are 77.89° and 77.69°. The crystallographic information is summarized in **Table 3.1**.

The supramolecular framework of compound 4.1C: The oxygen (O5) and (O5A) in both the crystal forms two C-H...O bonds with the linker hydrogen and hydrogen of the phthalimide ring at a distance of 2.481Å, 2.550Å, 2.476Å, and 2.558Å respectively in both the crystals. The oxygen (O4) and (O4A) also form C-H…O interactions with the linker hydrogen at a distance of 2.691Å and 2.672Å, respectively. The anisole ring hydrogen also interacts with the methoxy oxygen

(O6A), forming C-H…O interaction at a distance of 2.702Å. These C-H…O interactions between the two crystals form a graph set notation of $R_2^2(11)$ and $R_2^2(25)$ **(Figure 3.16 (b))**. The C-H…O interactions found between the phthalimide oxygen and the linker hydrogen also forms $R_4^2(20)$ and $R_4^4(26)$ graph sets **(Figure 3.16 (c))**. The crystal packing within the unit cell is also stabilized by these C-H…O interactions. The molecular arrangement of compound **4.1C** also displays lone pair…π interaction at a distance of 3.202Å and 3.224Å and $\pi \ldots \pi$ interaction at a distance of 3.680Å and 3.646Å **(Figure 3.16 (d) and (e))**. Also, C-H…π interactions on both side of the anisole ring surface by the same mode is found for both the crystal **(Figure 3.16 (f) and (g))**. The hydrogen bonding and other weak interactions are given in **Table 3.4**.

Table 3.4: Hydrogen bonds and other interactions in compound **4.1C**

Donor-H...Acceptor	**D – H, Å**	**H...A, Å**	**D...A, Å**	**D - H...A, ^{o}**
C13-H13C…O5A	0.970	2.476	3.339	148.12
C13A-H13A…O5	0.970	2.481	3.345	148.33
C18-H18…O5A	0.930	2.558	3.362	144.90
C14A-H14A…O4	0.970	2.691	3.448	135.28
C14-H14C…O4A	0.970	2.672	3.438	136.14
C8-H8…O6A	0.930	2.702	3.539	150.06
C18A-H18A…O5	0.930	2.550	3.352	144.74
C9A-H9A…C4	0.930	2.876	3.704	148.99
C25A-H25B…O1	0.960	2.663	3.468	141.69
C14-H14A…π(C17-C22)	0.970	3.455	3.824	105.11
C15A-H15A….π(C17A-C22A)	0.970	3.247	3.679	108.99
C20A-H20A…π(C2A-C6A,N2A)	0.930	3.425	4.066	128.17
C24A-H24A…π(C7A-C12A)	0.971	3.463	3.938	112.50
C24A-H24B…π(C7A-C12A)	0.970	3.531	3.938	107.88
C15-H15C….π(C17-C22)	0.970	3.221	3.648	108.62
C20-H20…π(C2-C6,N2)	0.930	3.467	4.100	127.47
C24-H24C…π(C7-C12)	0.970	3.412	3.924	115.15
C24-H24D…π(C7-C12)	0.970	3.533	3.924	106.76
Other contacts				
O5A…π(C16,C17,C22,C23,N3)		3.202		
π(C16A,C17A,C22A,C23A,N3A)… π(C16A,C17A,C22A,C23A,N3A)		3.680		
O5…π(C16A,C17A,C22A,C23A,N3A)		3.224		
π(C16,C17,C22,C23,N3)… π(C16,C17,C22,C23,N3)		3.646		
Intramolecular				
C27-H27E…O1	0.960	2.425	3.128	129.90
C24-H24D…O1	0.970	2.322	2.681	100.95

C25-H25D…π(C7-C12)	0.960	3.280	3.913	125.18
C27A-H27B…O2A	0.960	2.427	3.124	129.27
C24A-H24B…O2A	0.970	2.316	2.672	100.71
C25A-H25B… π(C7A-C12A)	0.960	3.388	3.938	118.50

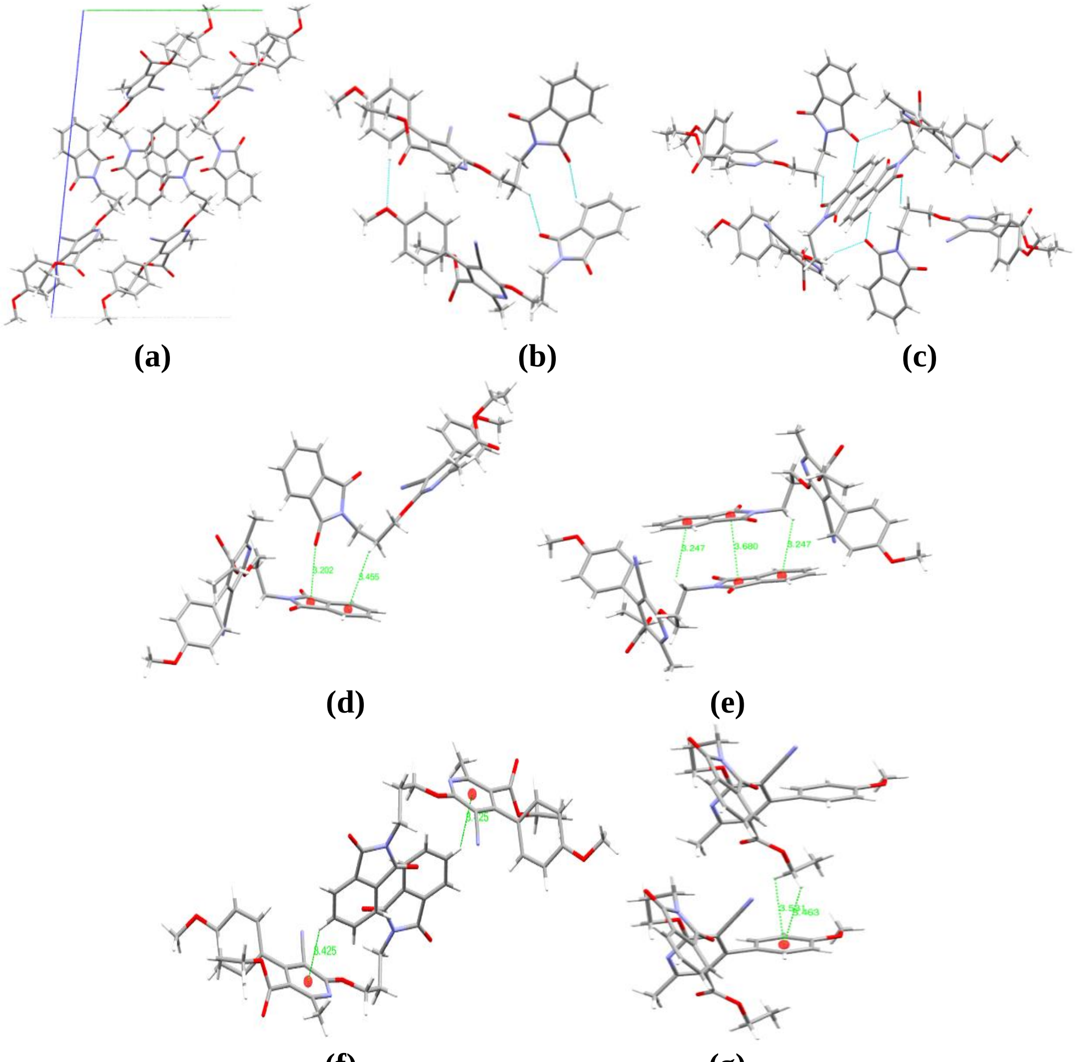

(a) (b) (c)

(d) (e)

(f) (g)

Figure 3.16: (a) Packing diagram of compound **4.1C**, (b) and (c) graph sets, (d) Lone pair…π and C-H…π interactions, (e) C-H…π and π…π interactions, (f) and (g) C-H…π interaction, in compound **4.1C**

Hirshfeld surface analysis of compound 4.1C: The Hirshfeld surface mapped over the d_{norm} in the range of -0.16 to 1.45Å for compound **4.1C** is displayed in **Figure 3.17 (a) and (b)**. The region of red spots corresponds to shorter dominant contacts due to C-H…O interactions. A very light red spot also corresponds to weaker C-H…O and C-H…C interactions.

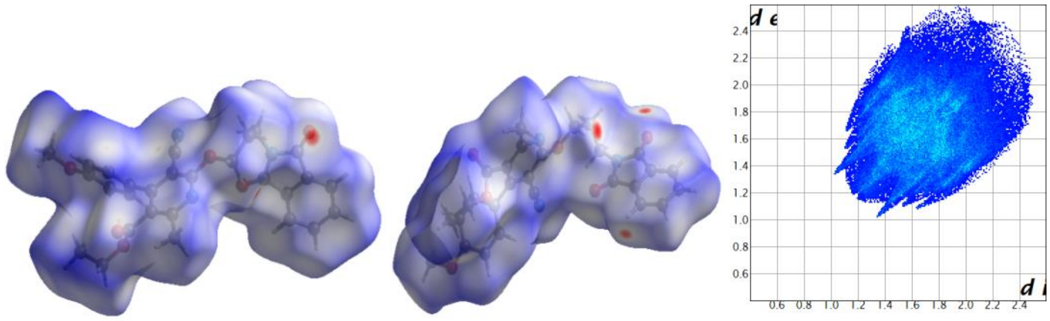

(a) **(b)** **(c)**

Figure 3.17: (a) and (b) d_{norm} both side view, (c) 2-D fingerprint plot, of compound **4.1C**

The relative percentage contributions of non-covalent interaction to the Hirshfeld surface are summarized by the 2-D fingerprint plot of compound **4.1C** **(Figure 3.17 (c))**. Those are H…H (44.3%), O...H (22.0%), C…H (18.1%), N…H (10.3%), C…O (1.7%), C…C (1.3%), N…O (1.0%), O…O (0.1%), C…N (0.8%) and N…N (0.3%). A pair of longer spoke-like patterns in the region of di + de = 2.3-2.8Å represents O…H interactions. The shorter pair of spoke-like patterns in the region of di + de = 2.6-3.2Å also represents N…H interaction. C-H...π and C…H contacts also appear as a characteristic flipped wing-like pattern in the region of di + de = 2.7-3.6Å. The C…C contacts which contribute 1.3%, indicates the presence of very weak π...π stacking interactions within the ring.

The Hirshfeld shape-index in a range of -1 to 1Å for compound **4.1C** shows the presence of complementary pair of red and blue triangles at the surface of the pyrrole ring moiety within the phthalimide ring, which indicates the presence of π...π stacking interactions between the aromatic rings **(Figure 3.18 (b))**. The yellowish-red colored concave regions around the surface of the aromatic rings represent the acceptor region where C-H...π and lone pair…π interactions occur **(Figure 3.18 (a) and (b))**. Again, the Hirshfeld surface mapped over the curvedness in a range of -4 to 0.4 Å for compound **4.1C** also display a flat green region with a yellowish spot around the pyrrole ring surface, which indicates the presence of π…π stacking interaction between the aromatic rings **(Figure 3.18 (d))**.

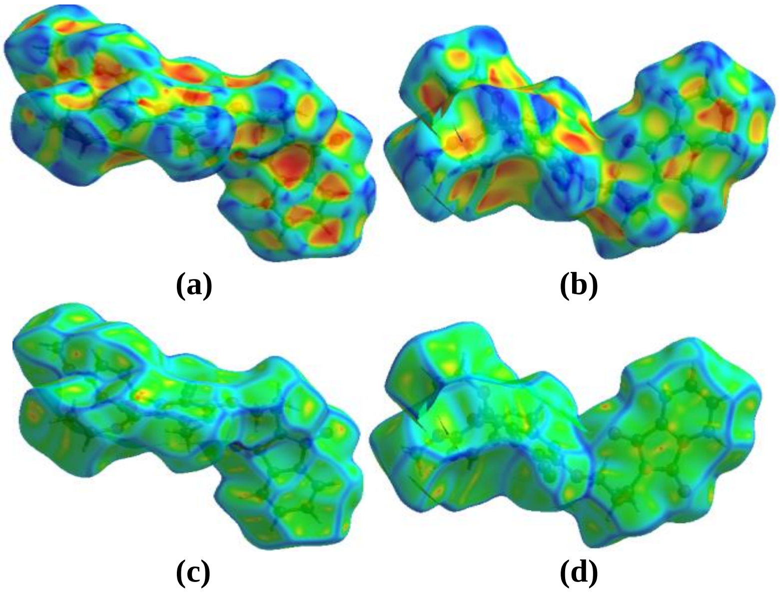

Figure 3.18: (a) and (b) Shape-index, (c) and (d) Curvedness, both side views of compound **4.1C**

The C-H…O, C-H…C, lone pair…π, and π…π stacking interactions found within the supramolecular framework are also supported by the Hirshfeld calculation for weak non-covalent intermolecular interactions in the crystal packing within the cluster of radius 3.8Å from a single crystals fragment is shown in **Figure 3.19**.

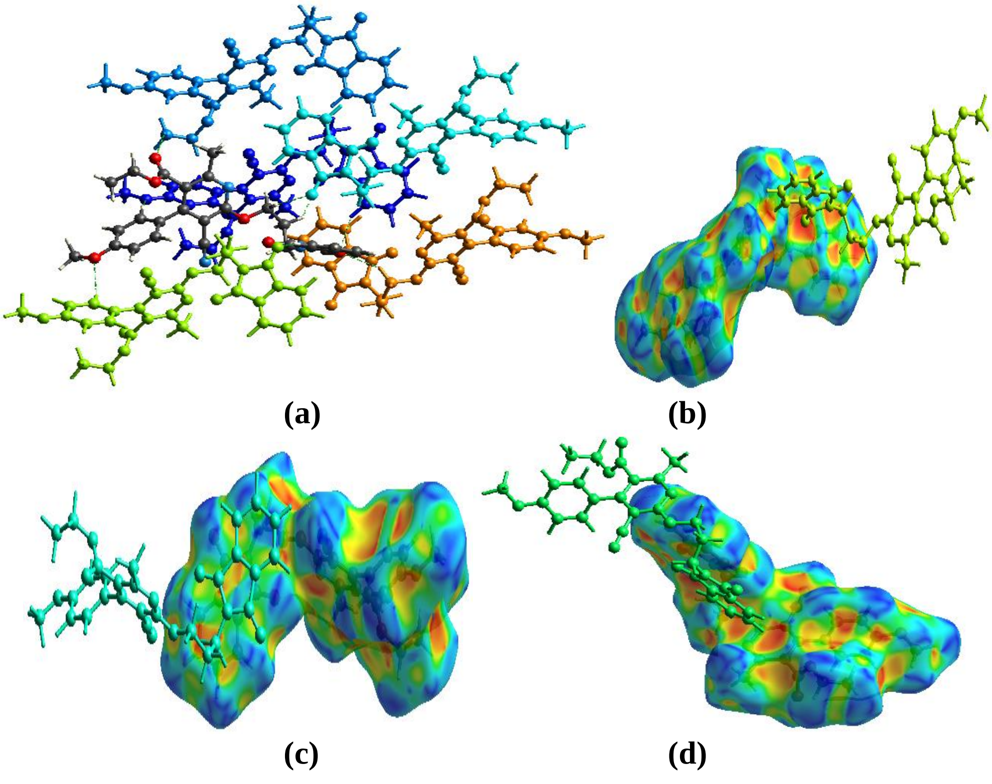

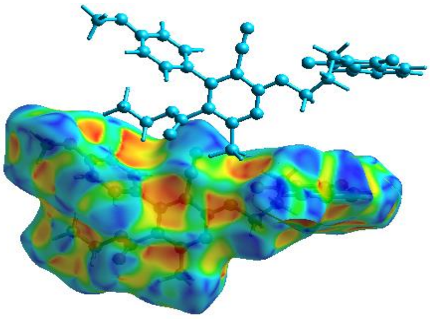

(e)

Figure 3.19: (a) C-H…O and C-H…C interactions, (b) Lone pair…π and C-H…π interactions, (c) π…π interaction, (d) and (e) C-H…π interactions, in compound **4.1C**

3.7.1.4. Crystal analysis of compound 4.1D

The compound **4.1D** was recrystallized in ethyl acetate at room temperature by slow evaporation of the solvent. The chiral asymmetric compound **4.1D** was analyzed using SC-XRD **(Figure 3.20)**. The compound crystallized with cell lengths **a** = 8.6636(2)Å, **b** = 9.9919(3)Å, **c** = 16.2401(5)Å, i.e., **a ≠ b ≠ c** and cell angles $\boldsymbol{\alpha}$ = 85.130(3)°, $\boldsymbol{\beta}$ = 86.656(2)°, $\boldsymbol{\gamma}$ = 68.591(3)°, i.e., $\boldsymbol{\alpha \neq \beta \neq \gamma \neq 90°}$. This indicates that the compound is exhibiting a triclinic crystal system, with space group P-1 containing two molecules per unit cell.

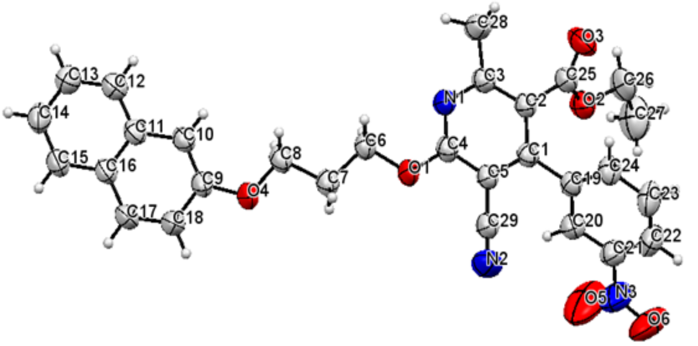

Figure 3.20: ORTEP diagram of compound **4.1D**

The chiral asymmetric compound **4.1D** crystal structure shows that the 6-membered benzenoid ring twisted away from the plane of the parent pyridine ring and with a dihedral angle of 59.80°. The 10-membered naphthalene ring also flips away from the parent pyridine ring plane at an angle of 6.84°. The nitrogen (N1) on the pyridine ring is sp^2 hybridized and facilitates the current ring delocalization. The crystallographic information is summarized in **Table 3.5**.

Table 3.5: Crystal data on compounds **4.1D**, **4.1E** and **4.1F**

Compound	**4.1D**	**4.1E**	**4.1F**
Identification code	2170459	2170485	2170468
Empirical formula	$C_{29}H_{25}N_3O_6$	$C_{30}H_{28}N_2O_4$	$C_{30}H_{28}N_2O_5$
Formula weight	511.52	480.54	496.54
Temperature(K)	293(2)	293(2)	293(2)
Crystal system	Triclinic	Triclinic	Triclinic
Space group	P-1	P-1	P-1
a(Å)	8.6636(2)	8.5493(5)	9.2109(5)
b(Å)	9.9919(3)	10.2675(5)	10.3814(4)
c(Å)	16.2401(5)	16.2273(8)	15.3885(8)
α(°)	85.130(3)	76.660(4)	98.418(4)
β(°)	86.656(2)	85.576(4)	90.090(5)
γ(°)	68.591(3)	69.711(5)	116.208(5)
Volume($Å^3$)	1303.55(7)	1300.00(13)	1302.34(12)
Z	2	2	2
ρ (g/cm^3)	1.303	1.228	1.266
μ(mm^{-1})	0.093	0.082	0.087
F(000)	536.0	508.0	524.0
Crystal size(mm^3)	0.2 × 0.18 × 0.16	0.28 × 0.26 × 0.24	0.36 × 0.32 × 0.14
Radiation	MoKα (λ = 0.71073)	MoKα (λ = 0.71073)	MoKα (λ = 0.71073)
2Θ range for data collection(°)	6.452 to 54.902	6.414 to 54.682	6.378 to 54.886
Index ranges	$-11 \le h \le 10, -12 \le k \le 12, -20 \le l \le 20$	$-10 \le h \le 10, -13 \le k \le 13, -20 \le l \le 20$	$-11 \le h \le 10, -12 \le k \le 12, -18 \le l \le 19$
Reflections collected	19390	18586	9384
Independent reflections	5544	5498	4608
Data/restraints/parameters	5544/0/345	5498/0/347	4608/0/337
Goodness-of-fit on F^2	1.075	1.063	1.067
Final R indexes [I>=2σ (I)]	R_1 = 0.0511, wR_2 = 0.1325	R_1 = 0.0545, wR_2 = 0.1413	R_1 = 0.0602, wR_2 = 0.1540
Final R indexes [all data]	R_1 = 0.0814, wR_2 = 0.1501	R_1 = 0.0913, wR_2 = 0.1658	R_1 = 0.0815, wR_2 = 0.1732
Largest diff. peak/hole/e $Å^{-3}$	0.19/-0.28	0.17/-0.21	0.27/-0.29

The supramolecular framework of compound 4.1D: The overall structure of compound **4.1D** involves C-H…O, C-H…N, C-H…C, C-H…π intermolecular interactions and $\pi \ldots \pi$ stacking interaction. These weak non-covalent intermolecular interactions assist in stabilizing the supramolecular structure. The molecules exhibit C-H…O and C-H…N intermolecular with the plane of the pyridine ring and the naphthalene ring, resulting in the formation of sheet layer. The C-H…O interactions between the naphthalene hydrogen (H18) and the oxygen (O4) and C-H…N interaction between the naphthalene hydrogen (H15) with the nitrogen (N2) of the cyano group at a distance of 2.711Å and 2.654Å respectively, interconnect the two **4.1D** compounds in an anti-parallel manner to form graph sets of $R_2^2(8)$ and $R_2^2(15)$ **(Figure 3.21 (b))**. The other hydrogen (H13) from the naphthalene ring also forms C-H…O interaction with the oxygen (O6) of the nitro group at a distance of 2.639Å.

This C-H…O interaction together with C-H…N interaction at 2.654Å involving four molecules of **4.1D** also adopts the formation of $R_4^4(28)$ motif (**Figure 3.21 (c))**. Furthermore, the different layer of sheets are interconnected through C-H…O bond between the oxygen (O5) of the nitro group and the hydrogen (H27B) from the ester moiety with a distance of 2.562Å also lead to the formation of $R_2^2(24)$ graph set notation (**Figure 3.21 (d))**. Beyond this, the C-H…C interactions with a distance of 2.866 Å and 2.841Å, and C-H…N interaction with a distance of 2.749Å arises from the bifurcated acceptor (N2), stabilize the interlayer connection between different sheets. The molecules within the crystal packing are stabilized by the two mentioned C-H…C interactions and by another two C-H…π interactions at a distance of 2.824Å and 2.610Å between the naphthalene ring of the 6-membered benzenoid hydrogen (**Figure 3.21 (a))**. Apart from these, the naphthalene ring also forms another C-H…π interaction with the polycyclic linked hydrogen at a distance of 3.141Å. Moreover, the 6-membered benzenoid ring also displays two C-H…π interactions from both sides of the plane at a distance of 3.588Å and 3.569Å (**Figure 3.21 (e))**. The molecular association of compound **4.1D** also exhibits π…π stacking interaction between the naphthalene and the pyridine ring, where the distance between the two centroids is 3.674Å (**Figure 3.21 (f))**. The weak interactions are listed in **Table 3.6**.

Table 3.6: Hydrogen bonds and other interactions in compound **4.1D**

Donor-H...Acceptor	**D – H, Å**	**H...A, Å**	**D...A, Å**	**D - H...A, º**
C13-H13…O6	0.930	2.639	3.493	153.12
C15-H15…N2	0.930	2.654	3.567	167.70
C18-H18…O4	0.930	2.711	3.638	174.37
C24-H24…C16	0.930	2.866	3.490	125.64
C24-H24…C17	0.930	2.841	3.700	154.08
C27-H27B…O5	0.960	2.562	3.520	175.28
C28-H28B…N2	0.960	2.749	3.698	170.10
C6-H6B…π(C9-C11, C16-C18)	0.970	3.141	4.084	164.31
C22-H22…π(C19-C24)	0.930	3.588	4.095	117.01
C23-H23…π(C11-C16)	0.930	2.824	3.467	127.26
C24-H24…π(C9-C11, C16-C18)	0.930	2.610	3.347	136.60
C26-H26B…π(C19-C24)	0.970	3.569	4.371	141.57
Other contact				
π(N1, C1-C5)…π(C11-C16))		3.674		
Intramolecular				
C7-H7A…O1	0.970	2.529	2.363	69.07
C7-H7B…O1	0.970	2.551	2.363	67.84

C7-H7A…O4	0.970	2.513	2.345	68.94
C7-H7B…O4	0.970	2.544	2.345	67.18
C26-H26A…O3	0.970	2.664	2.672	79.97
C26-H26B…O3	0.970	2.645	2.672	81.03
C27-H27C…π(C19-C24)	0.960	3.780	4.508	134.75

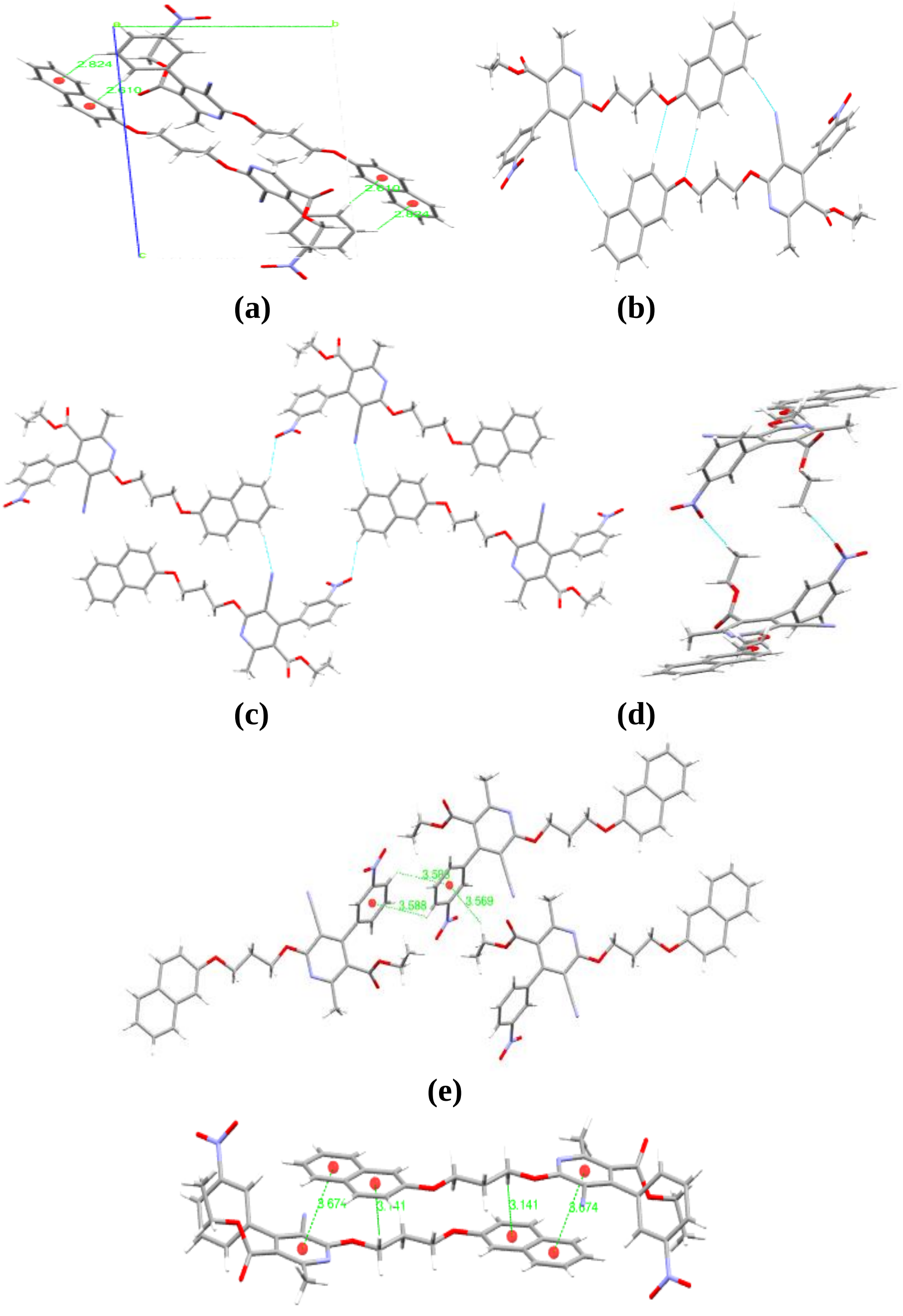

(a) **(b)**

(c) **(d)**

(e)

(f)

Figure 3.21: (a) Packing diagram of **4.1D**, (b), (c), and (d) graph sets, (e) C-H…π interactions, and (f) C-H…π and π…π interactions in compound **4.1D**

Hirshfeld surface analysis of compound 4.1D: The Hirshfeld surface mapped over the d_{norm} in the range of -0.12 to 1.71Å for compound **4.1D** is displayed in **Figure 3.22 (a) and (b)**. The region of bright red spots corresponds to shorter dominant contacts due to C-H…O and C-H…N interactions. The lighter dull red spots also arise due to weaker C-H…O and C-H…C contacts with longer bond lengths.

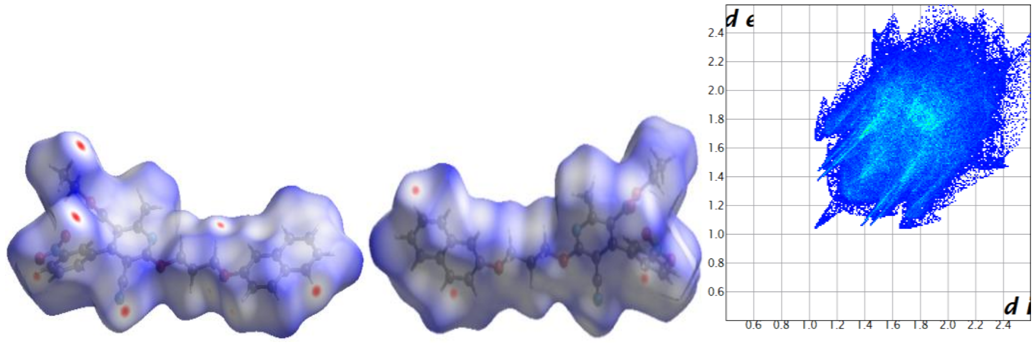

(a) **(b)** **(c)**

Figure 3.22: (a) and (b) d_{norm} both side view, (c) 2-D fingerprint plot, of compound **4.1D**

The relative percentage contributions of non-covalent interaction to the Hirshfeld surface are summarized by the 2-D fingerprint plot of compound **4.1D** (**Figure 3.22 (c)**). Those are H…H (40.4%), O…H (22.6%), C...H (20.2%), N…H (9.6%), C…C (2.9%), N…O (1.8%), C…O (1.1%), C…N (0.9%) and O…O (0.6%). The string-like pattern in the 2-D fingerprint plot represents H…H contacts. The spoke-like pattern in the region of di + de = 2.4-3.0Å represents O…H interactions. N…H interaction also appears in a shorter in region of di + de = 2.5-3.4Å. The presence of CH...π interaction decomposes within the C…H contacts in the 2-D fingerprint plot. Thus the C-H…π and C…H contacts appear as a characteristic wing-like pattern on the 2-D fingerprint plot in the region of di + de = 2.7-3.7Å. The relative contribution of C…C contacts which account for 2.9%, confirms the existence of π...π stacking interaction between the aromatic pyridine ring and the naphthalene ring.

Complementary pair of red and blue triangles are found at the surface of the pyridine ring and the naphthalene ring in the Hirshfeld shape-index range of -1 to 1Å for compound **4.1D**. It indicates the presence of π...π stacking interaction between the pyridine ring and the naphthalene ring **(Figure 3.23 (b))**. However, yellowish-red colored concave regions in the shape index around the surface of the naphthalene and 6-membered benzenoid rings represent the acceptor region where C-H...π interactions occur **(Figure 3.23 (a) and (b))**.

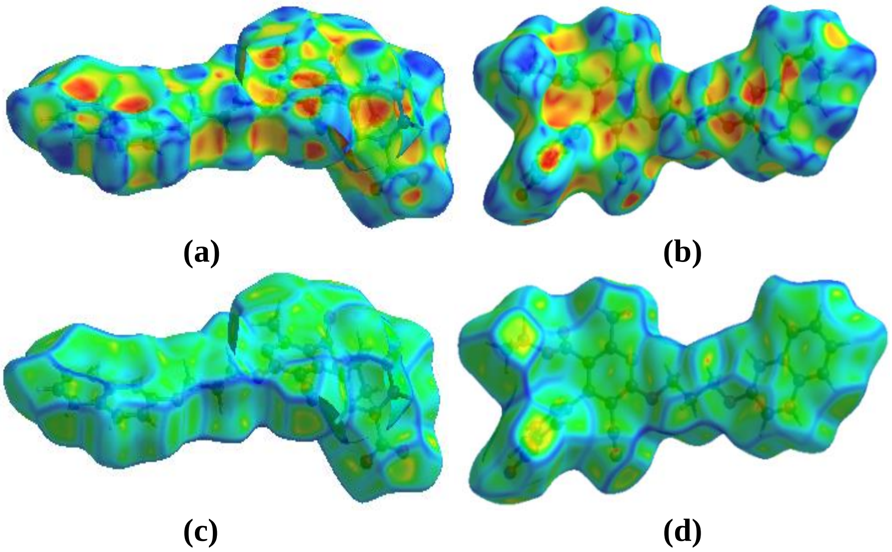
(a) **(b)**

(c) **(d)**

Figure 3.23: (a) and (b) Shape-index, (c) and (d) Curvedness, both side views of compound **4.1D**

The Hirshfeld curvedness surface in a range of -4 to 0.4 Å for compound **4.1D** also display the presence of a somewhat green flat region with a yellowish spot around the aromatic ring surface, which indicate the absence of π…π stacking interaction between the aromatic rings **(Figure 3.23 (c) and (d))**. Since there is an unequal electronic distribution between the pyridine and the naphthalene ring, the Hirshfeld shape-index, and curvedness surfaces, respectively, do not display sharp blue and red triangles with edge-to-edge connections with exemplary green flat surface.

The presence of C-H…O, C-H…N, C-H…C, and C-H…π interactions within the molecular assembly is also supported by the Hirshfeld calculation of weak non-covalent intermolecular interactions in the crystal packing within the cluster of radius 3.8Å from a single crystals fragment as shown in **Figure 3.24**.

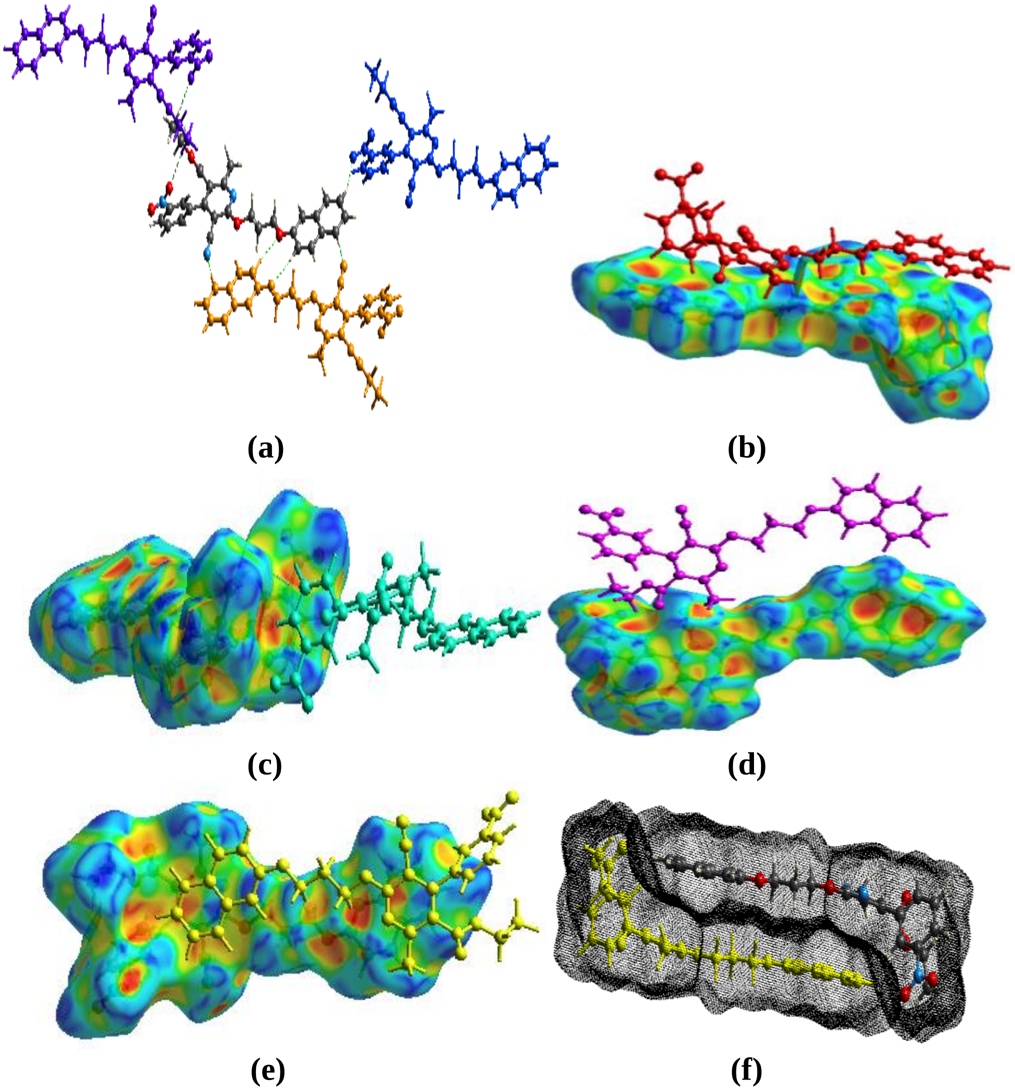
(a) (b) (c) (d) (e) (f)

Figure 3.24: (a) C-H…O, C-H…N and C-H…C interactions, (b), (c) and (d) C-H…π interactions, (e) and (f) π…π interaction, in compound **4.1D**

3.7.1.5. Crystal analysis of compound 4.1E

The compound **4.1E** was recrystallized in ethyl acetate at room temperature by slow evaporation of the solvent. The chiral asymmetric compound **4.1E** was analyzed using SC-XRD **(Figure 3.25)**. The compound crystallized with cell lengths **a** = 8.5493(5)Å, **b** = 10.2675(5)Å, **c** = 16.2273(8)Å, i.e., **a** ≠ **b** ≠ **c** and cell angles $\boldsymbol{\alpha}$ = 76.660(4)°, $\boldsymbol{\beta}$ = 85.576(4)°, $\boldsymbol{\gamma}$ = 69.711(5)°, i.e., $\boldsymbol{\alpha} \neq \boldsymbol{\beta} \neq \boldsymbol{\gamma} \neq \mathbf{90°}$ which indicate that the compound is exhibiting triclinic crystal system, with space group P-1 that contains two molecules per unit cell.

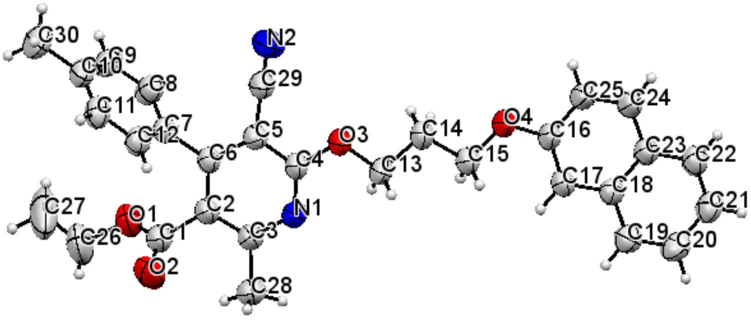

Figure 3.25: ORTEP diagram of compound **4.1E**

The chiral asymmetric compound **4.1E** crystal structure shows that the 6-membered benzenoid ring twisted away from the plane of the parent pyridine ring and with a dihedral angle of 58.06°. The 10-membered naphthalene ring also flips away from the parent pyridine ring plane at a dihedral angle of 7.52°. The nitrogen (N1) on the pyridine ring is also sp^2 hybridized, facilitating current ring delocalization within the ring. The crystallographic information is summarized in **Table 3.5**.

The supramolecular framework of compound 4.1E: The molecular association of compound **4.1E** involves C-H…O and C-H…N interactions that link the molecules along the plane of the aromatic rings to form sheets of the dimer. The C-H…O interaction arises between the oxygen (O4) and the hydrogen (H17) of the naphthalene ring at an interaction distance of 2.640Å and forms a graph set notation of $R_2^2(8)$ **(Figure 3.26 (b))**. The nitrogen (N2) from the cyano group also interacts with the hydrogen (H20) of the naphthalene ring, forming C-H…N interactions at a distance of 2.643Å. This C-H…N interaction, along with the C-H…O interactions together, also forms a graph set of $R_2^2(15)$ **(Figure 3.26 (b))**. The different dimeric sheets are interconnected by C-H…H interactions at a distance of 2.338Å, which forms a polymeric layer of compound **4.1E**. The different polymeric layers are interconnected through C-H…N interactions between the hydrogen (H26A) from the alkyl group of the ester moiety and the nitrogen (N2) of the cyano group at a distance of 2.673Å. C-H…π interactions between the hydrogen (H11) and (H12) of the toluene ring with naphthalene p-orbitals stabilizes the crystal packing within the unit cell at a distance of 2.896Å and 2.667Å respectively **(Figure 3.26 (c))**. The extensive network of compounds also displays π…π interaction between the naphthalene and pyridine rings at a distance of 3.751Å. It is facilitated by C-H…π interaction between the linker hydrogen (H13B) and the naphthalene p-orbital at a distance of 3.101Å **(Figure 3.26 (d))**. The hydrogen (H26A) that interacts with the nitrogen (N2) of the cyano group also has sufficient distance to interact with the p-orbitals of the toluene ring and forms C-H…π interaction at a distance of 3.460Å **(Figure 3.26 (e))**. Different weak interactions are given in **Table 3.7**.

Table 3.7: Hydrogen bonds and other interactions in compound **4.1E**

Donor-H...Acceptor	**D – H, Å**	**H...A, Å**	**D...A, Å**	**D - H...A, º**
C17-H17…O4	0.930	2.640	3.569	177.71
C20-H20…N2	0.930	2.643	3.571	175.96
C26-H26A…N2	0.970	2.673	3.417	133.82
C23-H23…H26B	0.930	2.338	2.951	123.17
C13-H13B…π(C16-C19, C24, C25)	0.970	3.101	4.038	163.01
C11-H11…π(C19-C24)	0.930	2.896	3.569	130.35
C12-H12…π(C16-C19, C24, C25)	0.930	2.667	3.418	138.34
C26-H26B…π(C7-C12)	0.970	3.460	4.146	129.61
Other contacts				
π(C2-C6, N2)…π(C19-C24)		3.751		
Intramolecular				
C14-H14A…O3	0.970	2.535	2.358	68.44
C14-H14B…O3	0.970	2.533	2.358	68.54
C14-H14A…O4	0.970	2.525	2.338	67.77
C14-H14B…O4	0.970	2.513	2.338	68.41
C26-H26A…O1	0.970	2.260	2.646	102.57
C2H-27A…π(C7-C12)	0.961	3.739	4.027	100.56
C2H-27C…π(C7-C12)	0.960	3.505	4.027	116.55

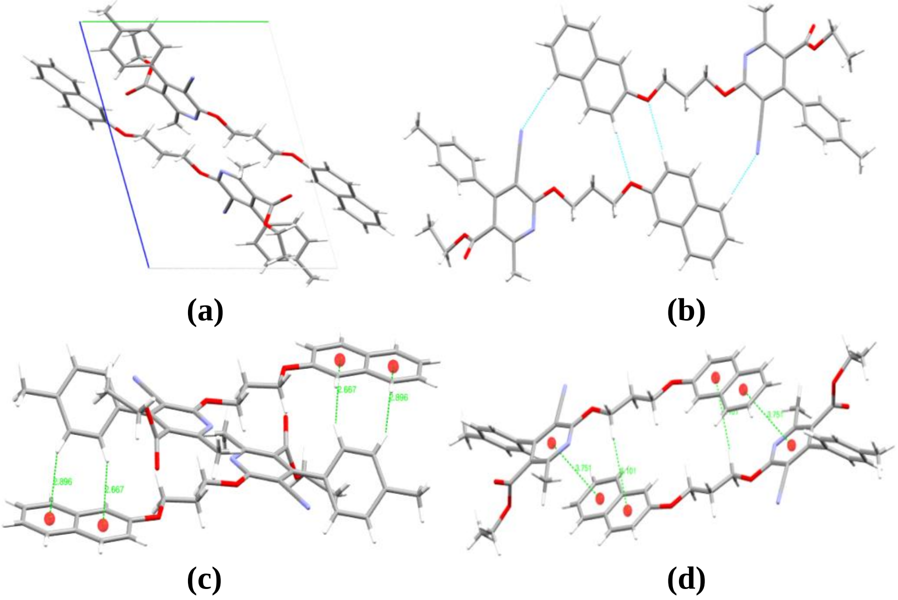

(a) (b)

(c) (d)

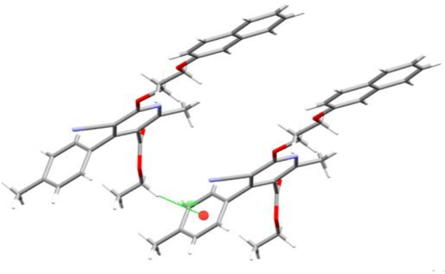

(e)

Figure 3.26: (a) Packing diagram of compound **4.1E**, (b) Graph sets, (c) C-H…π interactions, (d) C-H…π and π…π interactions and (e) C-H…π interaction, in compound **4.1E**

Hirshfeld surface analysis of compound 4.1E: Hirshfeld surface mapped over the d_{norm} in the range of -0.10 to 1.60Å for compound **4.1E** is displayed in **Figure 3.27 (a) and (b)**. The region of bright red spots corresponds to shorter contacts due to C-H…O and C-H…N interactions. The lighter red spots also arise due to weaker C-H…N and C-H…H contacts and have longer interaction distances.

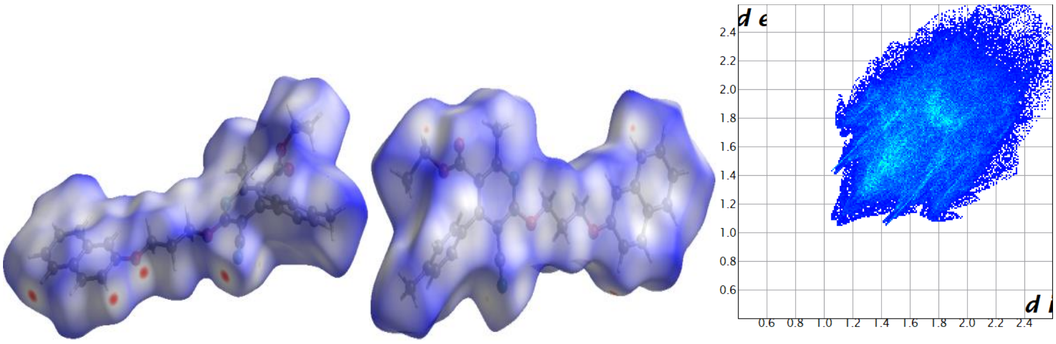

(a) **(b)** **(c)**

Figure 3.27: (a) and (b) d_{norm} both side view, (c) 2-D fingerprint plot, of compound **4.1E**

The relative percentage contributions of non-covalent interaction to the Hirshfeld surface are summarized by the 2-D fingerprint plot of compound **4.1E** **(Figure 3.27 (c))**. Those are H…H (54.9%), C...H (20.3%), O…H (10.4%),N…H (9.9%), C…C (2.3%),C…O (1.2%),C…N (0.9%) and N…O (0.2%). Both O...H and N...H appears within a short spoke-like pattern in the region of di + de = 2.5-3.0Å. Also, C-H...π and C…H contacts appear as a hooks-like pattern on the 2-D fingerprint plot in the region of di + de = 2.7-3.6Å. The C…C contacts contribute 2.3%, indicating the presence of π...π stacking interactions between the ring.

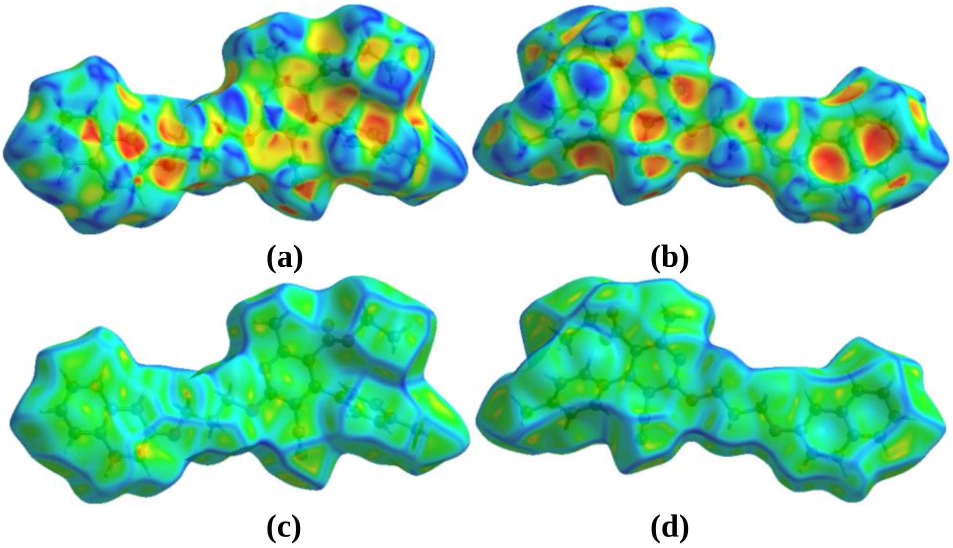
(a) (b)
(c) (d)

Figure 3.28: (a) and (b) Shape-index, (c) and (d) Curvedness, both side views of compound **4.1E**

The Hirshfeld surface mapped over the shape-index in a range of -1 to 1Å for compound **4.1E** shows the presence of complementary red and blue triangles around the pyridine and naphthalene ring surfaces which indicate the presence of significant π...π stacking interactions between the aromatic rings **(Figure 3.28 (a))**. The yellowish-red colored concave regions in the shape index around the surface of the naphthalene and the toluene rings represent the acceptor region where C-H...π interactions occur **(Figure 3.28 (a) and (b))**. Likewise, the Hirshfeld curvedness surface in the range of -4 to 0.4 Å also displays the presence of a flat green region around the aromatic ring surface, which again validates the presence of π...π stacking interaction between the aromatic rings **(Figure 3.28 (c))**.

The C-H…O, C-H…N, C-H…H, C-H…π, and π…π interactions within the supramolecular framework of compound **4.1E** are also supported by the Hirshfeld calculation of weak non-covalent intermolecular interactions in the crystal packing within the cluster of radius 3.8Å from a single crystals fragment is shown in **Figure 3.29**.

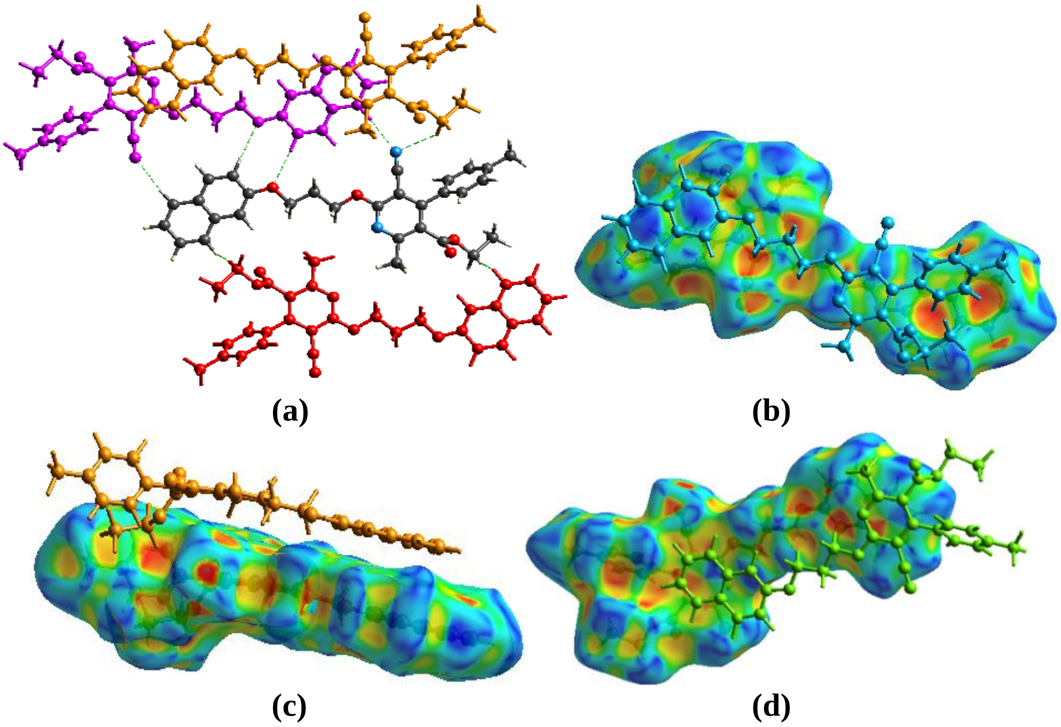

Figure 3.29: (a) C-H…O, C-H…N, and C-H…H interactions, (b) and (c) C-H…π interactions and (d) C-H…π and π…π interactions in compound **4.1E**

3.7.1.6. Crystal analysis of compound 4.1F

The compound **4.1F** was recrystallized in ethyl acetate at room temperature by slow evaporation of the solvent. The chiral asymmetric compound **4.1F** was analyzed using SC-XRD **(Figure 3.30)**. The compound crystallized with cell lengths **a** = 9.2109(5)Å, **b** = 10.3814(4)Å, **c** = 15.3885(8)Å, i.e., **a** ≠ **b** ≠ **c** and cell angles $\boldsymbol{\alpha}$ = 98.418(4)°, $\boldsymbol{\beta}$ = 90.090(5)°, $\boldsymbol{\gamma}$ = 116.208(5)°, i.e., $\boldsymbol{\alpha \neq \beta \neq \gamma \neq 90°}$ which indicate that the compound is exhibiting triclinic crystal system, with space group P-1 that contains two molecules per unit cell.

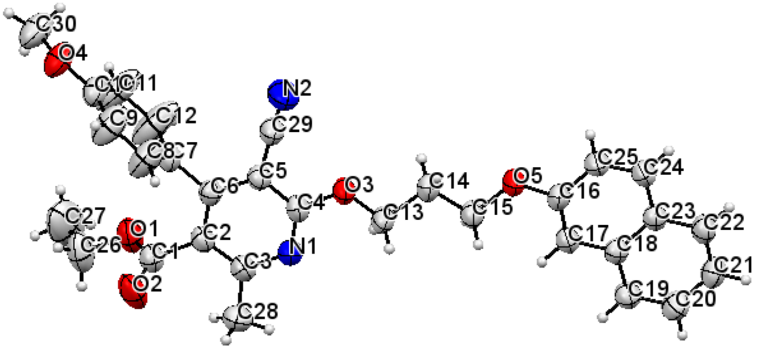

Figure 3.30: ORTEP diagram of compound **4.1F**

The chiral asymmetric compound **4.1F** crystal structure shows that the 6-membered benzenoid ring twisted away from the plane of the parent pyridine ring and with a dihedral angle of 82.86°. The 10-membered naphthalene ring also flips away from the parent pyridine ring plane at a dihedral angle of 9.59°. The nitrogen (N1) on the pyridine ring is also sp^2 hybridized, facilitating current ring delocalization within the ring. The crystallographic information is summarized in **Table 3.5**.

The supramolecular framework of compound 4.1F: The molecular association of compound **4.1F** involves C-H…O and C-H…N interactions that link the molecules horizontally along the plane of the aromatic rings to form a sheet. Among these interactions, the C-H…O interactions between the oxygen (O5) and the hydrogen (H25) of the naphthalene ring is the most dominant interaction having a distance of 2.585Å. This strong and dominant non-covalent C-H…O interactions also bring the two molecules close enough to have C-H…N interactions between the nitrogen (N2) of the cyano group and the hydrogen (H22) of the naphthalene ring with a distance of 2.681Å. Thus the interaction between the two molecules having C-H…O and C-H…N interactions results in the formation of $R_2^2(8)$ and $R_2^2(15)$ graph sets **(Figure 3.31 (b))**. Since the carbonyl oxygen (O2) of the ester moiety acts as a bifurcated acceptor, it forms two C-H…O bonds for both two other molecules, where one donor hydrogen comes from the naphthalene hydrogen (H19) and the other from the methoxy hydrogen (H30A) with an interaction distances 2.697Å and 2.703Å respectively. Thus the two C-H…O bonds having 2.697Å distance and the other two C-H…O bonds having 2.703Å distance also result in the formation of another graph sets notation of $R_2^2(32)$ and $R_2^2(22)$, respectively **(Figure 3.31 (c) and (d))**. The two crystals contained within the crystal packing are stabilized by two C-H…C bonds at a distance of 2.884Å and 2.861Å respectively. These interactions act as an interconnection that forms a linkage between different sheets. Since these two C-H…C interactions are formed between the naphthalene ring carbon and the 6-membered benzenoid hydrogen through the edge to face fashion, it also allows the same hydrogen that forms C-H…C bond and the adjacent hydrogen to have C-H…π interactions with the naphthalene p-orbital at an interaction distance of 2.574Å and 3.062Å respectively, to assist the crystal packing **(Figure 3.31 (e))**.

Furthermore, the supramolecular associations of compound **4.1F** also display another C-H…π interaction between the 6-membered benzenoid ring with the alkyl hydrogen from the tail of the ester moiety at a distance of 3.559Å. Beyond these, the pyridine ring also forms π…π stacking interactions with one naphthalene ring p-orbital at a distance of 3.748Å **(Figure 3.31 (f))**. Thus the overall structure is supported by C-H…O, C-H…N, C-H…C, C-H…π, and π…π stacking interactions in stabilizing and facilitating the supramolecular network. The non-covalent interactions are given in **Table 3.8**.

Table 3.8: Hydrogen bonds and other interactions in compound **4.1F**

Donor-H...Acceptor	**D – H, Å**	**H...A, Å**	**D...A, Å**	**D - H...A, º**
C8-H8…C17	0.930	2.884	3.664	142.30
C8-H8…C18	0.930	2.861	3.581	135.13
C19-H19…O2	0.930	2.697	3.592	161.87
C22-H22…N2	0.930	2.681	3.610	176.47
C25-H25…O5	0.930	2.585	3.515	177.95
C30-H30A…O2	0.959	2.703	3.654	171.20
C8-H8…π (C16-C18, C23-C25)	0.930	2.574	3.479	164.35
C9-H9…π (C18-C23)	0.930	3.062	3.808	138.34
C27-H27B…π (C7-C12)	0.960	3.559	4.295	135.32
Other contact				
π(C18-C23)…π(C2-C6, N1)		3.748		
Intramolecular				
C14-H14A…O3	0.970	2.529	2.357	68.70
C14-H14B…O3	0.970	2.537	2.357	68.25
C14-H14A…O5	0.970	2.488	2.345	70.26
C14-H14B…O5	0.970	2.565	2.345	66.02
C26-H26A…O2	0.970	2.618	2.655	81.56
C26-H26B…O2	0.970	2.655	2.655	79.47

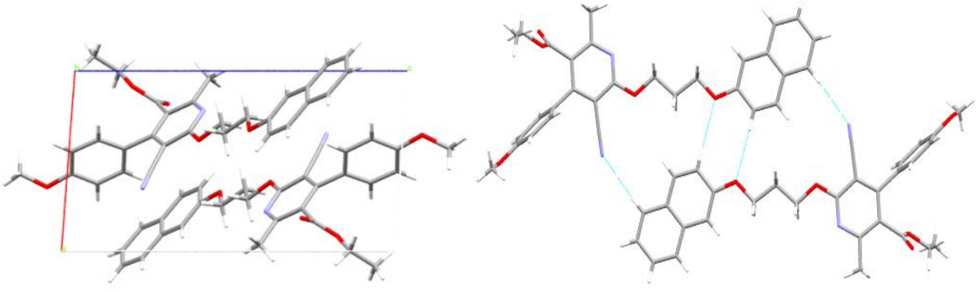
(a) **(b)**

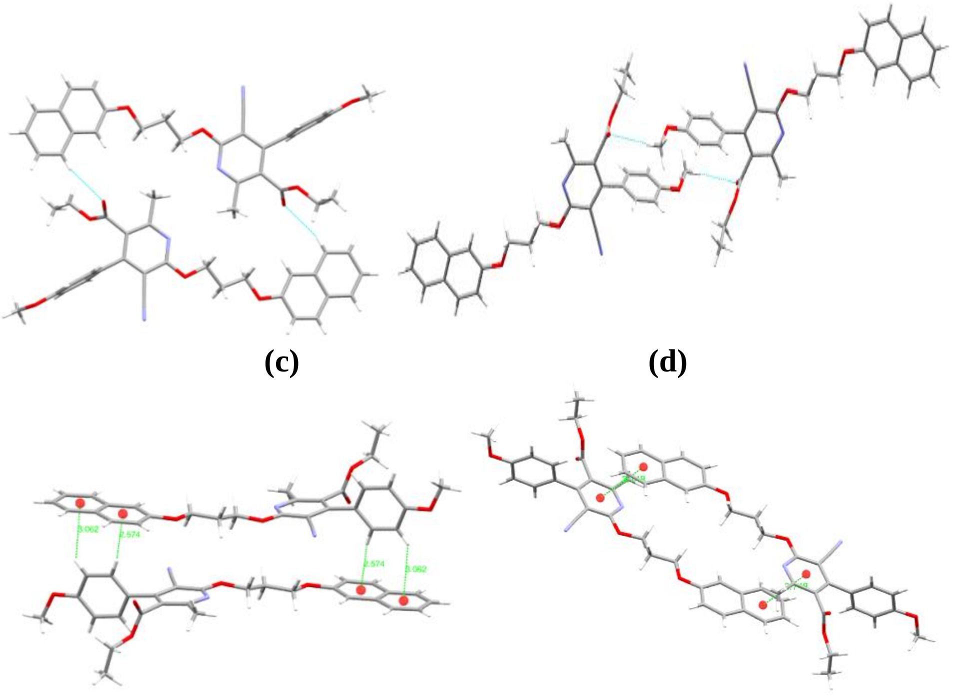

(c) (d)

(e) (f)

Figure 3.31: (a) Packing diagram of compound **4.1F**, (b), (c) and (d) graph sets, (e) H…π interactions and (f) π…π interaction, in compound **4.1F**

Hirshfeld surface analysis of compound 4.1F: The Hirshfeld surface mapped over the $_{\text{norm}}$ in the range of -0.12 to 1.79Å for compound **4.1F** is displayed in **Figure 3.32 (a) and (b)**. The region of bright red spots corresponds to shorter dominant contacts due to C-H…O and C-H…N interactions between the naphthalene hydrogen and the oxygen (O5) of the ester moiety and the nitrogen (N2) of the cyano group. The lighter dull red spots also arise due to weaker C-H…O and C-H…C contacts and have longer bond lengths.

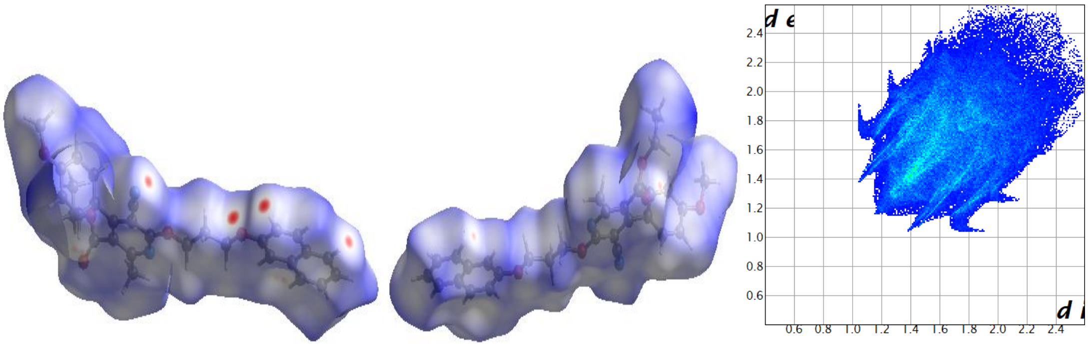

(a) (b) (c)

Figure 3.32: (a) and (b) d$_{\text{norm}}$ both side view, (c) 2-D fingerprint plot, of compound **4.1F**

The relative percentage contributions of non-covalent interaction to the Hirshfeld surface are summarized by the 2-D fingerprint plot of compound **4.1F (Figure 3.32 (c))**. Those are H…H (50.7%), C...H (20.8%), O…H (14.1%),N…H (9.7%), C…C (1.8%),C…O (1.7%),C…N (1.0%) and N…O (0.1%). The spoke-like pattern in the region of di + de = 2.4-3.0Å represents O…H interactions. Also, N…H interaction is also reflected around the spike in the region of di + de = 2.5-3.4Å. The C-H...π and C…H contacts appear as a hooks-like pattern on the 2-D fingerprint plot in the region of di + de = 2.6-3.8Å. The C…C contacts contribute 1.8%, indicating the presence of π...π stacking interactions within the rings.

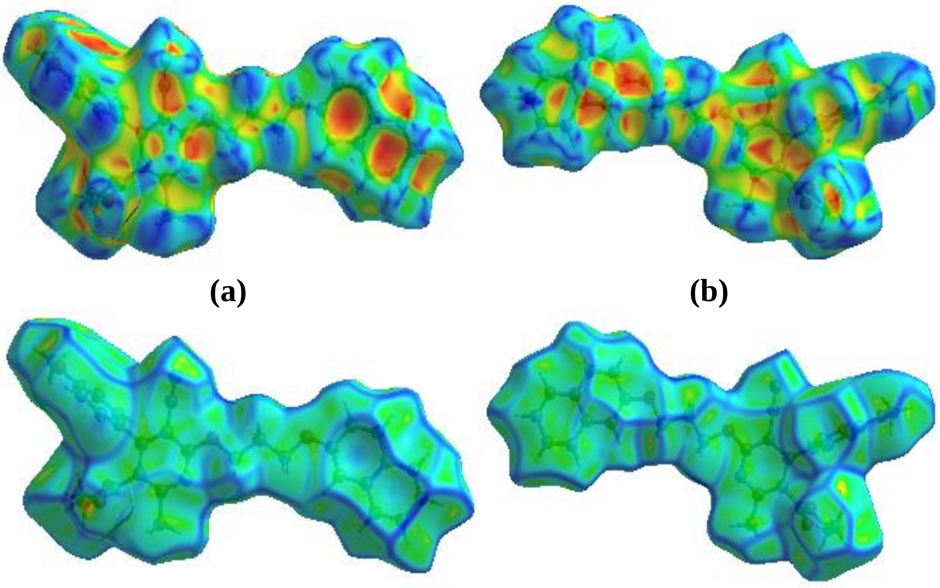

Figure 3.33: (a) and (b) Shape-index, (c) and (d) Curvedness, both side views of compound **4.1F**

The Hirshfeld surface mapped over the shape-index in a range of -1 to 1Å for compound **4.1F** shows the complementary pair of red and blue triangles around the aromatic ring surface, which indicate a significant presence of significant π...π stacking interactions between the aromatic rings **(Figure 3.33 (b))**. However, since the stacking interaction between the pyridine ring and one side of the naphthalene ring is in a staggered form, the blue and green triangles on the surface of the ring do not have sharp edges. The yellowish-red colored concave regions in the shape index around the surface of the naphthalene and benzenoid rings represent the acceptor region where C-H...πinteractions occur **(Figure 3.33 (a))**. The Hirshfeld surface mapped over the curvedness in a range of -4 to 0.4 Å for compound 4.1F also displays a flat green region around the aromatic ring surface, which indicates the presence of $\pi \ldots \pi$ stacking interaction between the aromatic rings **(Figure 3.33 (d))**.

The C-H…O, C-H…N, C-H…C, C-H…π, and $\pi \ldots \pi$ interactions are supported by the Hirshfeldcalculation of weak non-covalent intermolecular interactions in the crystal packing within the cluster of radius 3.8Å from a single crystals fragment is shown in **Figure 3.34**.

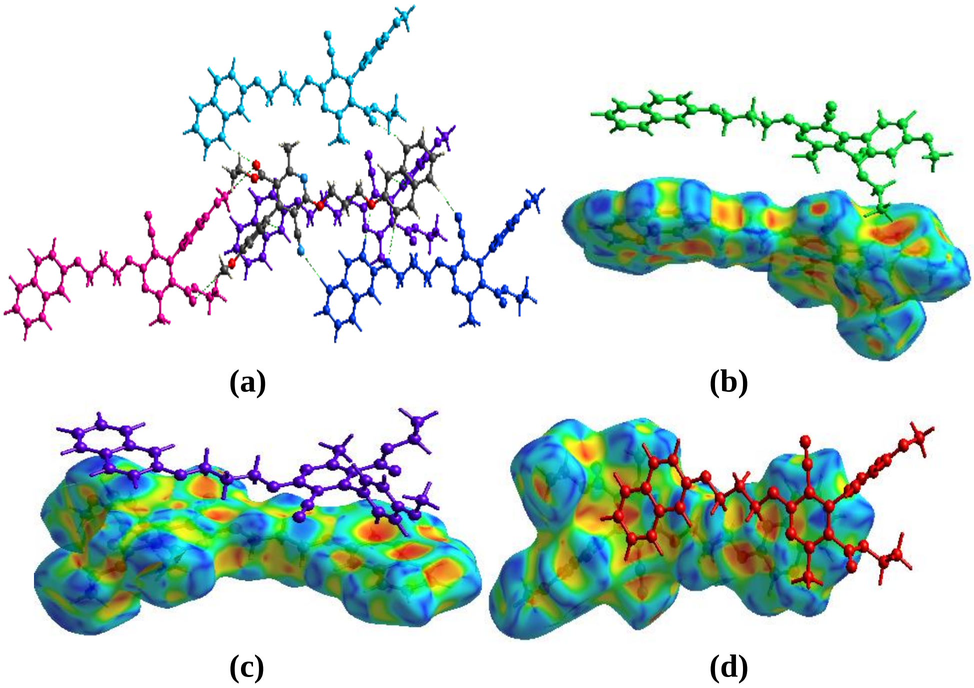
(a) **(b)**
(c) **(d)**

Figure 3.34: (a) C-H…O, C-H…N, and C-H…C interactions, (b) and (c) C-H…π interactions, (d) $\pi \ldots \pi$ interaction, in compound **4.1F**

3.7.1.7. Crystal analysis of compound 4.2A

The compound **4.2A** was recrystallized in ethyl acetate at room temperature by slow evaporation of the solvent. The chiral asymmetric compound **4.2A** was analyzed using SC-XRD **(Figure 3.35)**. The compound crystallized with cell lengths **a** = 9.2579(3)Å, **b** = 17.0772(5)Å, **c** = 16.4527(4)Å, i.e., $\mathbf{a} \neq \mathbf{b} \neq \mathbf{c}$ and cell angles $\boldsymbol{\alpha}$ = 90°, $\boldsymbol{\beta}$ = 100.754(3)°, $\boldsymbol{\gamma}$ = 90°, i.e., $\boldsymbol{\alpha = \gamma = 90°, \beta \neq 90°}$, which indicate that the compound is exhibiting monoclinic crystal system, with space group P2$_1$/n that contains four molecules per unit cell.

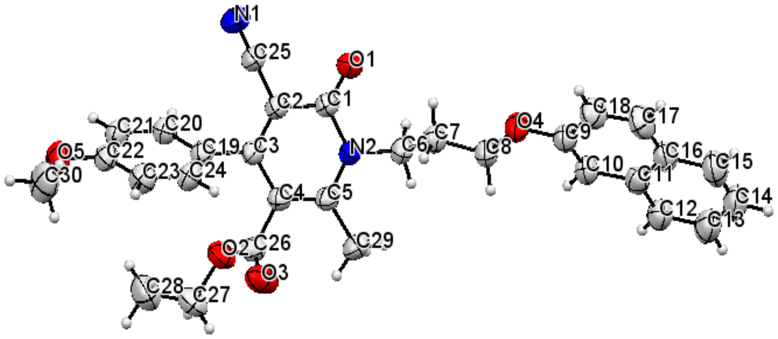

Figure 3.35: ORTEP diagram of compound **4.2A**

The chiral asymmetric compound **4.2A** crystal structure shows that the 6-membered benzenoid ring twisted away from the plane of the parent pyridone ring and with a dihedral angle of 56.49°. The 10-membered naphthalene ring also flips and twists away from the parent pyridone ring plane at a dihedral angle of 59.36°. The cyclic rings present in **4.2A** crystal are all planar and aromatic. The crystallographic information is summarized in **Table 3.9**.

Table 3.9: Crystal data on compound **4.2A**

Compound	**4.2A**
Identification code	2170458
Empirical formula	$C_{30}H_{28}N_2O_5$
Formula weight	496.54
Temperature(K)	293(2)
Crystal system	Monoclinic
Space group	$P2_1/n$
a(Å)	9.2579(3)
b(Å)	17.0772(5)
c(Å)	16.4527(4)
α(°)	90
β(°)	100.754(3)
γ(°)	90
Volume(Å^3)	2555.47(13)
Z	4
ρ (g/cm^3)	1.291
μ(mm^{-1})	0.088
F(000)	1048.0
Crystal size(mm^3)	0.32 × 0.3 × 0.26
Radiation	MoKα (λ = 0.71073)
2Θ range for data collection(°)	6.538 to 54.89
Index ranges	$-11 \leq h \leq 11$, $-21 \leq k \leq 21$, $-21 \leq l \leq 20$
Reflections collected	35165
Independent reflections	5541
Data/restraints/parameters	5541/0/337
Goodness-of-fit on F^2	1.083
Final R indexes [I>=2σ (I)]	$R_1 = 0.0475$, $wR_2 =$

	0.1207
Final R indexes [all data]	R_1 = 0.0778, wR_2 = 0.1351
Largest diff.peak/hole/e Å^{-3}	0.13/-0.20

The supramolecular framework of compound 4.2A: The molecular associations of the compound **4.2A** display a zig-zag pattern of symmetrically arranged molecules. C-H links the molecules together C-H…N interaction between the nitrogen (N1) of the cyano group and the polycyclic linker hydrogen (H6B) at a distance of 2.624Å to form a network of sheets. The sheets are interconnected through C-H…O and C-H…C interactions. The C-H…O interlayer connections between the bifurcated acceptor oxygen (O3) of the ester carbonyl group with the linker hydrogen (H7B) and the alkyl hydrogen (H29C) of the pyridone substituent at a distance of 2.495Å and 2.639Å respectively result in the formation of $R_2^1(8)$ and $R_2^2(12)$ graph sets **(Figure 3.36 (b))**. The hydrogen (H20) from the 6-membered benzenoid ring acts as bifurcated hydrogen and forms C-H…O and C-H…C interlayer connections with the oxygen (O4) and the naphthalene carbon (C9) at an interaction distance of 2.641Å and 2.857Å respectively. These C-H…O and C-H…C interactions, along with the C-H…C interaction found between the hydrogen (H29A) from the alkyl group of the pyridone ring substituent and the naphthalene ring carbon (C13) at a distance of 2.833Å, and another C-H…C interaction between the hydrogen (H8B) of the polycyclic linker with the carbon (C20) from the 6-membered benzenoid ring at a distance of 2.864Å, strengthens the interlayer interaction **(Figure 3.36 (c))**. Also, these C-H…O and C-H…C interactions assist in stabilizing the crystal packing with one additional C-H…O interaction between the carbonyl oxygen (O1) of the pyridone ring and the hydrogen (H27A) from the ester moiety at a distance of 2.529Å. There are also two C-H…π interactions that facilitate the crystal packing in the unit cell, which arises between the naphthalene ring and the two methoxy hydrogen (H30A and H30C) at a distance of 3.574Å and 3.532Å respectively **(Figure 3.36 (d))**. The supramolecular framework of compound **4.2A** also exhibits C-H…π interaction between the methoxy hydrogen (H30B) and the pyridone ring, having a bond distance of 3.294Å. π…π stacking interaction between the pyridone ring and the naphthalene ring at a distance of 3.898Å **(Figure 3.36 (e))**. The π…π stacking interaction occurs in such a way that the pyridone ring and the naphthalene ring overlap with the naphthalene ring and pyridone ring of another compound (i.e., for one single crystal π…π interaction involves two other crystal compounds) **(Figure 3.36 (f))**. Thus the overall supramolecular framework of compound **4.2A** exhibits C-H…O, C-H…C, C-H…N, C-H…π, and π…π stacking interactions within its zig-zag molecular arrangement. The weak non-covalent interactions are listed in **Table 3.10**.

Table 3.10: Hydrogen bonds and other interactions in compound **4.2A**

Donor-H...Acceptor	**D – H, Å**	**H...A, Å**	**D...A, Å**	**D - H...A, °**
C6-H6B…N1	0.970	2.624	3.532	155.89
C7-H7B…O3	0.970	2.495	3.450	168.33
C29-H29C…O3	0.960	2.639	3.301	126.47
C27-H27A…O1	0.970	2.529	3.413	151.54
C20-H20…O4	0.930	2.641	3.433	143.47
C8-H8B…C20	0.970	2.864	3.530	126.61
C20-H20…C9	0.930	2.857	3.675	147.39
C29-H29A…C13	0.960	2.833	3.666	145.64
C30-H30A…π(C11-C16)	0.960	3.574	4.003	109.83
C30-H30C…π(C9-C11,C16-C18)	0.960	3.532	4.415	153.94
C30-H30B…π(N2, C1-C5)	0.960	3.294	4.252	176.71
Other contact				
π(N2,C1-C6)…π(C9-C11,C16-C18)		3.898		
Intramolecular				
C7-H7A…O4	0.970	2.435	2.367	74.47
C7-H7B…O4	0.970	2.698	2.367	60.01
C29-H29B…O3	0.960	2.412	3.131	131.44
C27-H27B…O3	0.970	2.342	2.703	101.19
C28-H28B…π(C19-C24)	0.960	3.424	3.808	106.45
C28-H28c…π(C19-C24)	0.960	3.354	3.808	111.23

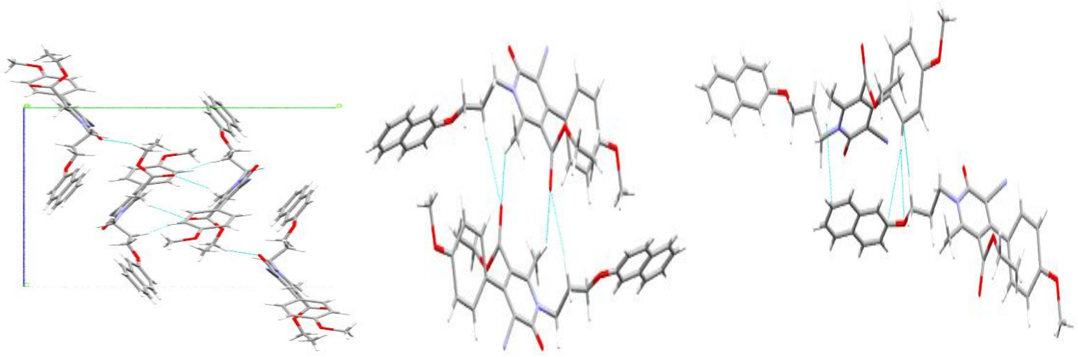

(a) **(b)** **(c)**

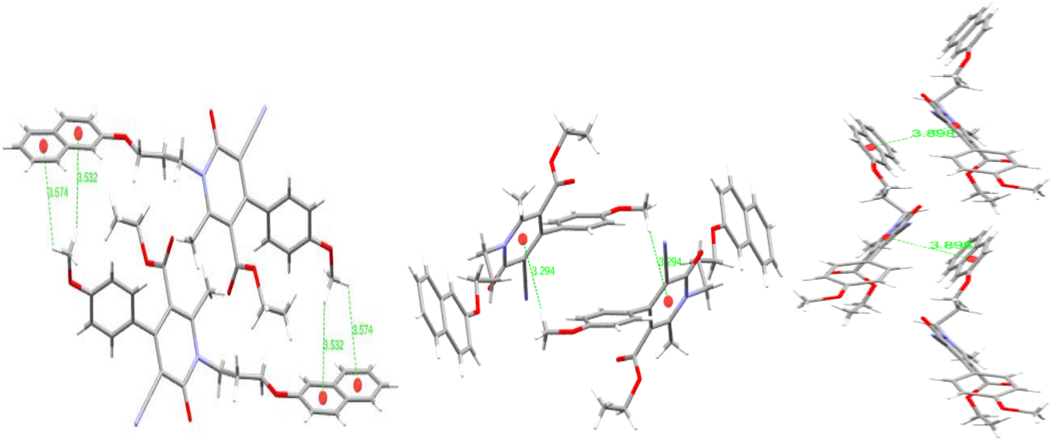

(d) (e) (f)

Figure 3.36: (a) Packing diagram of **4.2A**, (b) graph sets, (c) C-H…O and C-H…C, (d) and (e) C-H…π interactions, (f) π…π interaction, in compound **4.2A**

Hirshfeld surface analysis of compound 4.2A: The Hirshfeld surface mapped over the d_{norm} in the range of -0.16 to 1.41Å for compound **4.2A** is displayed in **Figure 3.37 (a) and (b)**. The region of bright red spots corresponds to a shorter bond length due to C-H…O contacts. The other lighter red color spots also arise from C-H…O, C-H…N, and C-H…C contacts that have a little longer bond length in the molecular self-assembly.

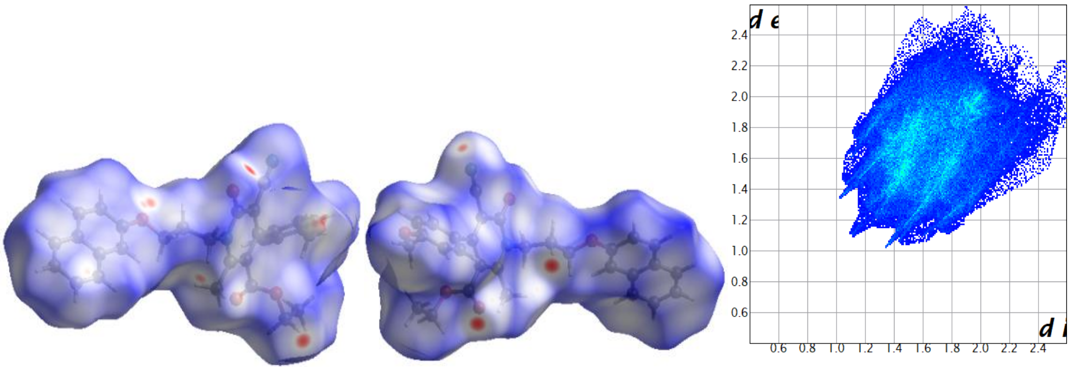

(a) (b) (c)

Figure 3.37: (a) and (b) d_{norm} both side view, (c) 2-D fingerprint plot, of compound **4.2A**

The 2-D fingerprint plot of the compound **4.2A** represents the relative percentage contributions of non-covalent interaction to the Hirshfeld surface **(Figure 3.37 (c))**. Those are H…H (47.4%), C...H (19.4%), O…H (18.6%), N…H (8.9%), C…C (4.1%), C…N (0.8%), C…O (0.7%) and O…O (0.3%). The spoke-like pattern in the region of di + de = 2.3-2.9Å represents O…H interactions. N…H interaction is also reflected around the basal foot of the spike in the region of di + de = 2.5-3.2Å. The presence of C-H...π is not distinguishable in the 2-D fingerprint plot. However, it decomposes within the C…H contacts in the region of di + de = 2.7-3.8Å that appears as a folded wings-like pattern. The C…C contacts which contribute 4.1%, also reflect the presence of π...π stacking interactions between the aromatic rings.

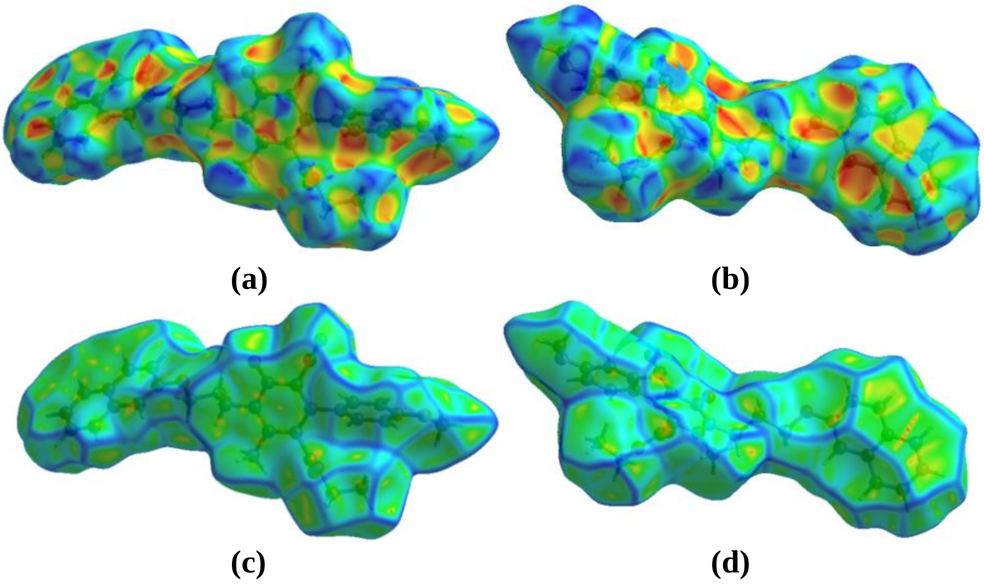

Figure 3.38: (a) and (b) Shape-index, (c) and (d) Curvedness, both side views of compound **4.2A.**

The shape-index red region indicates acceptor property, and the blue region indicates donor property. The Hirshfeld surface mapped over the shape-index in a range of -1 to 1Å for compounds **4.2A** shows the complementary pair of red and blue triangles having an edge-to-edge connection around the naphthalene ring and the pyridone ring surfaces which indicates the presence of π...π stacking interactions between the aromatic rings **(Figure 3.38 (a))**. The yellowish-red colored concave regions in the shape index around the surface of the naphthalene and pyridone rings represent the acceptor region of C-H...π interactions **(Figure 3.38 (b))**. In the curvedness plot, the yellow and red-yellow colored spots indicate weak and robust hydrogen bond interactions in the crystal.

Similarly, the Hirshfeld surface mapped over the curvedness in a range of -4 to 0.4 Å for compound **4.2A** displays the presence of a flat green region with a yellowish spot around the naphthalene ring and the pyridone ring surface. That indicates the presence of π…π stacking interaction between the aromatic rings **(Figure 3.38 (c))**.

The C-H…O, C-H…N, C-H…C, C-H…π, and π…π interactions found in the supramolecular framework are also supported by the Hirshfeld calculation within the cluster of 3.8Å radius from a single crystals fragment as shown in **Figure 3.39**.

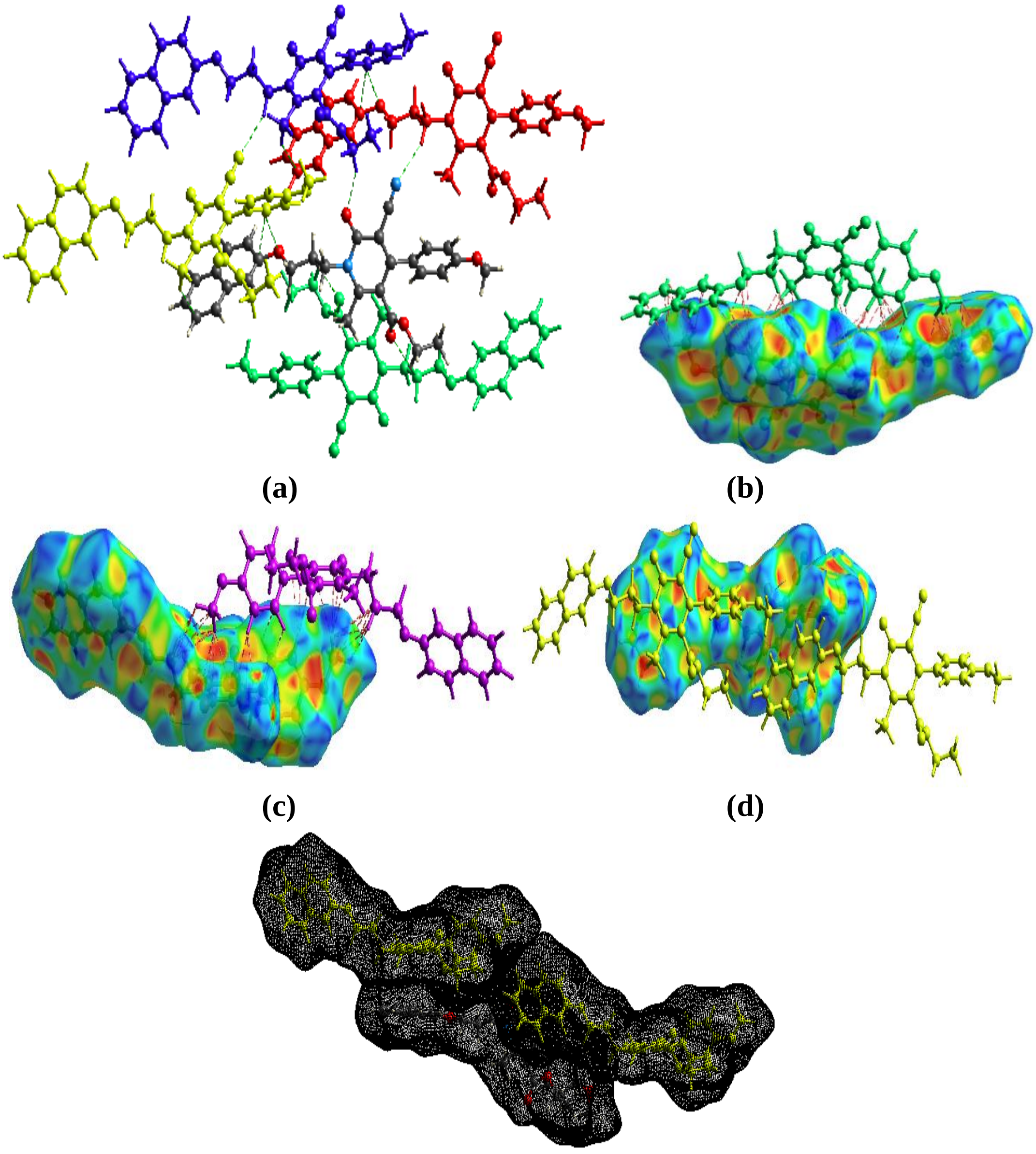

(a) **(b)**

(c) **(d)**

(e)

Figure 3.39: (a) C-H…O, C-H…C, and C-H…N interactions, (b) and (c) C-H…π interactions, (d) and (e) π…π interaction, in compound **4.2A**

3.8. Synthesis of polycyclic aromatic fleximers from 4,6-dimethyl-2-oxo-1,2-dihydropyridine-3-carbonitrile

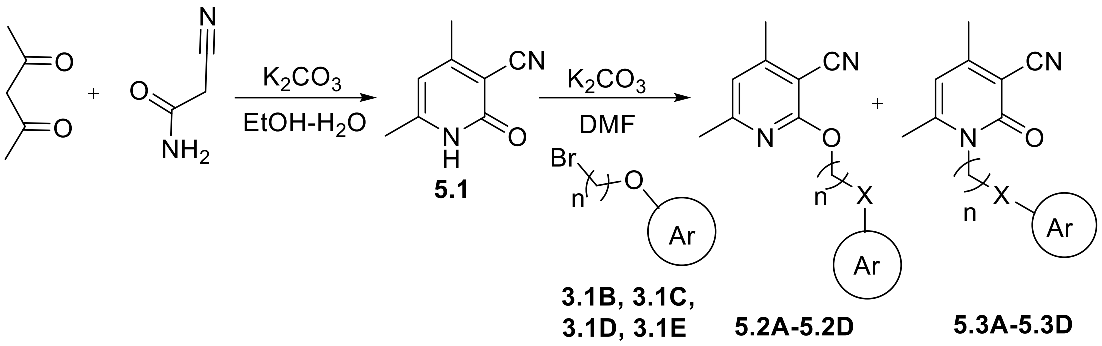

Scheme 5

In scheme 5, polycyclic aromatic fleximers **(Figure 3.40)** were synthesized by introducing compounds **(3.1B, 3.1C, 3.1D,** and **3.1E)** from Scheme 3 to 4,6-dimethyl-2-oxo-1,2-dihydropyridine-3-carbonitrile **(5.1)**. The reaction was done in the presence of potassium carbonate as a base and DMF as a solvent to form an alkylated product with flexible models having an increased surface area of aromatic rings.

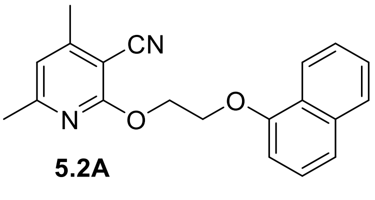

5.2A

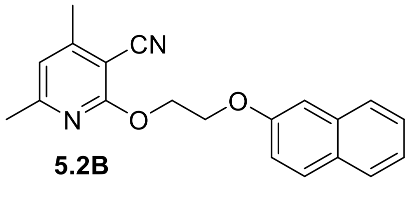

5.2B

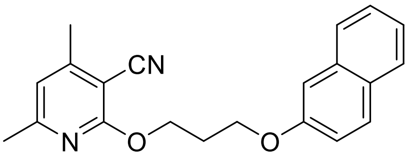

5.2C

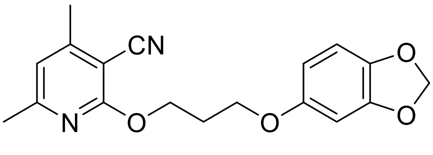

5.2D

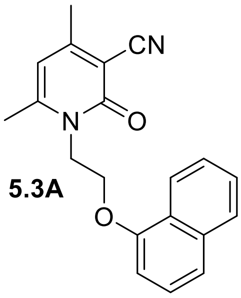

5.3A

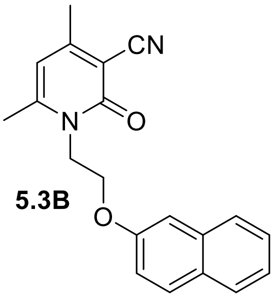

5.3B

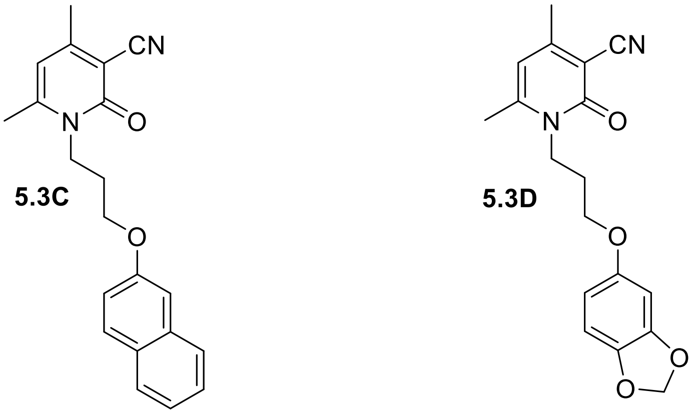

5.3C

5.3D

Figure 3.40: Structures of 4,6-dimethyl-2-oxo-1,2-dihydropyridine-3-carbonitrile derivative fleximers

3.9. Experimental

^{1}H NMR (300 MHz) and ^{13}C NMR (75 MHz) spectra were recorded on JEOL AL300 FTNMR spectrometer using TMS as an internal reference, and chemical shift values are expressed in δ, ppm units. Melting points of all the compounds were recorded on the electrically heated instrument and are uncorrected. All the reactions were monitored by thin-layer chromatography (TLC) on pre-coated aluminum sheets of Merck using an appropriate solvent system, and chromatograms were visualized under UV light.

3.9.1. Synthesis of 4,6-dimethyl-2oxo-1,2-dihydropyridine-3carbonitrile (5.1)

In a 100 mL round bottom flask, cyanoacetamide (4.2 g, 0.05 mol) was taken in ethanol. Potassium carbonate (2.0 g, 0.05 mol) dissolved in water was added to the reaction mixture and stirred. Acetyl acetone (5.0 g, 0.05 mol) was added slowly with stirring after 20 min. The reaction mixture was stirred for 2 h. The completion of the reaction was checked by TLC. Light yellow colored precipitate appeared, which was filtered and washed with cold ethanol. Pure white-colored 4,6-dimethyl-2-oxo-1,2-dihydropyridine-3-carbonitrile was then recrystallized with hot aqueous ethanol.

3.9.1.1. **4,6-dimethyl-2oxo-1,2-dihydropyridine-3carbonitrile (5.1):** Yield: 6.40 g, 87%, m.p. 127-129°C; **^{1}H NMR (300 MHz, CDCl$_3$):** δppm 2.409 (3H, s, CH3); 2.43 (3H, s, CH3); 6.07 (1H, s, Ar-H).

3.9.2. General procedure for the synthesis of 4,6-dimethyl-2-oxo-1,2-dihydropyridine-3-carbonitrile derivative fleximers (5.2A-5.2D and 5.3A-5.3D)

In a 100 mL round bottom flask, 4,6-dimethyl-2oxo-1,2-dihydropyridine3carbonitrile **(5.1)** (1 g, 0.0068 mol)and potassium carbonate (1 g, 0.0072 moles) were taken in DMF (20 mL) and stirred. After 20 min, compound **3.1B, 3.1C, 3.1D,** or **3.1E** (0.0068 mol) was added and stirred for 12 h. Completion of the reaction was checked by TLC (30% EtOAc& Hexane). After completing the reaction, DMF was removed under reduced pressure by a rotary evaporator, and the reaction mixture was extracted with CHCl3/ H2O (200/ 200 X 3 mL). The chloroform layer was dried with anhydrous sodium sulfate and filtered. Chloroform was removed, and the product was purified by flash column chromatography (silica gel 230-400 mesh). The first fraction **(5.2A-5.2D)** was collected at 10 % and the second fraction **(5.3A-5.3D)** at 25 % ethyl acetate-hexane.

3.9.2.1. 4,6-dimethyl-2-(2-(naphthalen-1-yloxy)ethoxy)nicotinonitrile (5.2A): Yellow solid, yield: 43%, m.p. 189-193°C; **^{1}H NMR (300 MHz, CDCl$_3$):** δppm 2.44 (6H, s, CH$_3$); 4.51 – 4.54 (2H, t, CH$_2$, *J* = 5.4 Hz); 4.90 – 4.94 (2H, t, CH$_2$, *J* = 5.4 Hz); 6.69 (1H, s, CH); 6.88 – 6.91 (1H, d, Ar-H, *J* = 7.5 Hz); 7.34 – 7.50 (4H, m, Ar-H); 7.76 – 7.78 (1H, d, Ar-H, *J* = 7.5 Hz); 8.23 – 8.25 (1H, d, Ar-H, *J* = 7.5 Hz); **^{13}C NMR (75 MHz, CDCl$_3$):** δppm 21.8, 23.4, 68.9, 69.5, 93.4, 107.3, 111.7, 113.1, 121.1, 123.5, 125.4, 126.2, 126.8, 127.6, 134.5, 134.7, 154.1, 156.1, 161.3, 164.5; **MS (m/z):** 318.14 (M+1).

3.9.2.2. 4,6-dimethyl-2-(2-(naphthalen-2-yloxy)ethoxy)nicotinonitrile (5.2B): White solid, yield: 53%, m.p. 197-201°C; **^{1}H NMR (300 MHz, CDCl$_3$):** δppm 2.44 (6H, s, CH$_3$); 4.44 – 4.48 (2H, t, CH$_2$, *J* = 5.4 Hz); 4.80 – 4.84 (2H, t, CH$_2$, *J* = 5.4 Hz); 6.68 (1H, s, CH); 7.16 (1H, s, Ar-H); 7.17 – 7.20 (1H, d, Ar-H, *J* = 8.1 Hz); 7.30 – 7.36 (1H, t, Ar-H, *J* = 7.2 Hz); 7.40 – 7.46 (1H, t, Ar-H, *J* = 7.2 Hz); 7.72 – 7.70 (3H, t, Ar-H, *J* = 7.2 Hz); **^{13}C NMR (75 MHz, CDCl$_3$):** δppm 21.8, 23.4, 68.9, 69.5, 93.4, 107.3, 111.7, 113.1, 121.1, 123.5, 125.4, 126.2, 126.8, 127.6, 134.5, 134.7, 154.1, 156.1, 161.3, 164.5; **MS (m/z):** 318.14 (M+1).

3.9.2.3. 4,6-dimethyl-2-(3-(naphthalen-2-yloxy)propoxy)nicotinonitrile (5.2C): White solid, yield: 59%, m.p. 211-213°C; **^{1}H NMR (300 MHz, $CDCl_3$):** δppm 2.30 – 2.38 (2H, m, CH_2); 2.40 (6H, s, CH_3); 4.26 – 4.30 (2H, t, CH_2, *J* = 6.0 Hz); 4.59 – 4.63 (2H, t, CH_2, *J* = 6.0 Hz); 6.63 (1H, s, CH); 7.12 (1H, s, Ar-H); 7.13 – 7.16 (1H, d, Ar-H, *J* = 8.7 Hz); 7.28 – 7.34 (1H, t, Ar-H, *J* = 8.1Hz); 7.39 – 7.49 (1H, t, Ar-H, *J* = 8.1 Hz); 7.70 – 7.76 (3H, t, Ar-H, *J* = 8.1 Hz); **^{13}C NMR (75 MHz, $CDCl_3$):** δppm 20.8, 24.3, 29.1, 65.0, 65.0, 93.8 107.2, 111.7, 113.2, 118.5, 124.0, 126.5, 126.9, 127.8, 129.4, 129.6, 129.9, 155.6, 156.3, 160.5, 163.4; **MS (m/z):** 332.15 (M+1).

3.9.2.4. 2-(3-(benzo[d][1,3]dioxol-5-yloxy)propoxy)-4,6-dimethylnicotinonitrile (5.2D): White solid, yield: 51%, m.p. 178-180°C; **^{1}H NMR (300 MHz, $CDCl_3$):** δppm 2.20 – 2.28 (2H, m, CH_2); 2.42 (6H, s, CH_3); 4.06 – 4.10 (2H, t, CH_2, *J* = 6.0 Hz); 4.53 – 4.57 (2H, t, CH_2, *J* = 6.0 Hz); 5.89 (2H, s, Ar-H); 6.32 – 6.36 (2H, dd, Ar-H); 6.49 – 6.50 (1H, d, Ar-H, *J* = 2.7 Hz); 6.66 – 6.68 (1H, d, Ar-H, *J* = 2.7 Hz); **^{13}C NMR (75 MHz, $CDCl_3$):** δppm 20.8, 24.7, 28.9, 64.0, 65.1, 93.8, 101.2, 101.5, 105.7, 108.4, 111.2, 114.7, 143.5, 149.7, 152.7, 155.2, 160.5, 163.1; **MS (m/z):** 326.13 (M+1).

3.9.2.5. 4,6-dimethyl-1-(2-(naphthalen-1-yloxy)ethyl)-2-oxo-1,2-dihydropyridine-3-carbonitrile (5.3A): Yellow solid, yield: 54%, m.p. 196-198°C; **^{1}H NMR (300 MHz, $CDCl_3$):** δppm 2.36 (3H, s, CH_3); 2.66 (3H, s, CH_3); 4.48 – 4.57 (4H, m, CH_2); 6.07 (1H, s, CH); 6.79 – 6.82 (1H, d, Ar-H, *J* = 7.5 Hz); 7.31 – 7.37 (1H, d, Ar-H, *J* = 7.5 Hz); 7.41 – 7.50 (3H, m, Ar-H); 7.77 – 7.80 (1H, d, Ar-H, *J* = 7.5 Hz); 7.99 – 8.02 (1H, d, Ar-H, *J* = 7.5 Hz); **^{13}C NMR (75 MHz, $CDCl_3$):** δppm 21.8, 23.4, 68.9, 69.5, 93.4, 107.3, 111.7, 113.1, 121.1, 123.5, 125.4, 126.2, 126.8, 127.6, 134.5, 134.7, 154.1, 156.1, 161.3, 164.5; **MS (m/z):** 318.14 (M+1).

3.9.2.6. 4,6-dimethyl-1-(2-(naphthalen-2-yloxy)ethyl)-2-oxo-1,2-dihydropyridine-3-carbonitrile (5.3B): White solid, yield: 44%, m.p. 212-215°C; **^{1}H NMR (300 MHz, $CDCl_3$):** δppm 2.33 (3H, s, CH_3); 2.59 (3H, s, CH_3); 4.40 – 4.47 (4H, m , CH_2); 6.02 (1H, s, CH); 7.00 – 7.04 (2H, dd, Ar-H); 7.07 (1H, s, Ar-H); 7.30 – 7.36 (1H, t, Ar-H, *J* = 7.2 Hz); 7.40 – 7.46 (1H, t, Ar-H, *J* = 7.2 Hz); 7.68 – 7.74 (2H, t, Ar-H, *J* = 7.2 Hz); **^{13}C NMR (75 MHz, CDCl$_3$):** δppm 21.8, 23.4, 68.9, 69.5, 93.4, 107.3, 111.7, 113.1, 121.1, 123.5, 125.4, 126.2, 126.8, 127.6, 134.5, 134.7, 154.1, 156.1, 161.3, 164.5; **MS (m/z):** 318.14 (M+1).

3.9.2.7. 4,6-dimethyl-1-(3-(naphthalen-2-yloxy)propyl)-2-oxo-1,2-dihydropyridine-3-carbonitrile (5.3C): Yellow solid, yield: 41%, m.p. 224-227°C; **^{1}H NMR (300 MHz, CDCl$_3$):** δppm 1.98 – 2.17(2H, m, CH$_2$); 2.21 (3H, s, CH$_3$); 2.26 (3H, s, CH$_3$); 4.20 – 4.24(2H, t, CH$_2$, *J* = 5.7 Hz); 4.53 – 4.57 (2H, t, CH$_2$, *J* = 5.7 Hz); 6.65 (1H, s, CH); 7.14 (1H, s, Ar-H); 7.15 – 7.18 (1H, d, Ar-H, *J* = 8.7 Hz); 7.30 – 7.336 (1H, t, Ar-H, *J* = 8.1Hz); 7.41 – 7.51 (1H, t, Ar-H, *J* = 8.1 Hz); 7.72 – 7.78 (3H, t, Ar-H, *J* = 8.1 Hz); **^{13}C NMR (75 MHz, CDCl$_3$):** δppm 20.8, 24.3, 29.1, 65.0, 65.0, 93.8 107.2, 111.7, 113.2, 118.5, 124.0, 126.5, 126.9, 127.8, 129.4, 129.6, 129.9, 155.6, 156.3, 160.5, 163.4; **MS (m/z):** 332.15 (M+1).

3.9.2.8. 1-(3-(benzo[d][1,3]dioxol-5-yloxy)propyl)-4,6-dimethyl-2-oxo-1,2-dihydropyridine-3-carbonitrile (5.3D): White solid, yield: 47%, m.p. 193-195°C; **^{1}H NMR (300 MHz, CDCl$_3$):** δppm 2.12 – 2.21 (2H, m, CH$_2$); 2.36 (3H, s, CH$_3$); 2.44 (3H, s, CH$_3$); 3.91 – 3.95 (2H, t, CH$_2$, *J* = 5.7 Hz); 4.18 – 4.23 (2H, t, CH$_2$, *J* = 5.7 Hz); 5.91 (2H, s, CH$_2$); 6.02 (1H, s, Ar-H); 6.26 – 6.30 (1H, m, Ar-H); 6.44 (1H, s, Ar-H); 6.68 – 6.70 (1H, d, Ar-H, *J* = 8.4 Hz); **^{13}C NMR (75 MHz, CDCl$_3$):** δppm 20.8, 24.7, 28.9, 64.0, 65.1, 93.8, 101.2, 101.5, 105.7, 108.4, 111.2, 114.7, 143.5, 149.7, 152.7, 155.2, 160.5, 163.1. **MS (m/z):** 326.13 (M+1).

3.10. Results and discussions

In scheme 5, a series of polycyclic fleximers **(5.2A-5.2D** and **5.3A-5.3D)** were synthesized compounds and from those polycyclic fleximers, compounds **5.2A, 5.2B, 5.2C, 5.2D, 5.3A, 5.3B** and **5.3D** gave a suitable crystal for the analysis. The product obtained from the reaction gives a good yield for both O-linked and N-linked fleximers. The crystal obtained was studied by single-crystal X-ray diffraction (SC-XRD) and Hirshfeld surface analysis.

3.10.1. X-Ray Crystallographic studies and Hirshfeld surface analysis of compounds 5.2A, 5.2B, 5.2C, 5.2D, 5.3A, 5.3B and 5.3D

3.10.1.1. Crystal analysis of compound 5.2A

The compound **5.2A** was recrystallized in ethyl acetate at room temperature by slow evaporation of the solvent. The chiral asymmetric compound **5.2A** was analyzed using SC-XRD **(Figure 3.41)**. The compound crystallized with cell lengths **a** = 7.68622(16)Å, **b** = 8.10494(19)Å, **c** = 13.7324(3)Å, i.e., **a ≠ b ≠ c** and cell angles $\boldsymbol{\alpha} =$ 92.6640(18)°, $\boldsymbol{\beta}$ = 95.0949(17)°, $\boldsymbol{\gamma}$ = 103.1516(19)°, i.e., $\boldsymbol{\alpha \neq \beta \neq \gamma \neq 90°}$. It indicates that the compound is exhibiting a triclinic crystal system, with space group P-1 containing two molecules per unit cell.

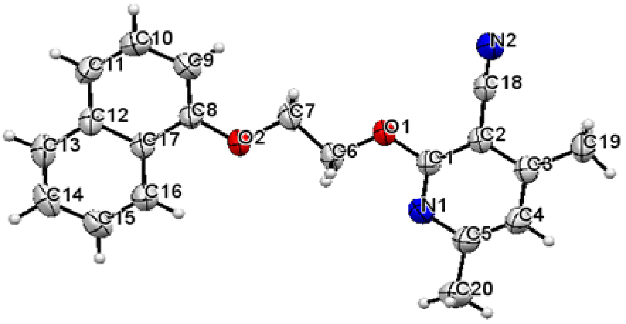

Figure 3.41: ORTEP diagram of compound **5.2A**

The crystal structure of compound **5.2A** shows that both the pyridine and the naphthalene ring are planar and aromatic. The naphthalene ring and the pyridine ring almost lie in the same plane, and the dihedral angle between the two planes is only 2.52°. The crystallographic information is in **Table 3.11**.

Table 3.11: Crystal data compounds **5.2A**, **5.2B** and **5.2C**

Compound	5.2A	5.2B	5.2C
Identification code	2170478	2170482	2170480
Empirical formula	C20H18N2O2	C20H18N2O2	C21H20N2O2
Formula weight	318.36	318.36	332.39
Temperature(K)	293(2)	293(2)	293(2)
Crystal system	Triclinic	Monoclinic	Triclinic
Space group	P-1	C2/c	P-1
a(Å)	7.68622(16)	13.2682(5)	8.4985(2)
b(Å)	8.10494(19)	12.6180(5)	8.5046(3)
c(Å)	13.7324(3)	20.5116(8)	13.8343(3)
α(°)	92.6640(18)	90	77.856(2)
β(°)	95.0949(17)	102.579(4)	75.183(2)
γ(°)	103.1516(19)	90	66.165(3)
Volume(Å^3)	827.79(3)	3351.6(2)	877.70(5)
Z	2	8	2
ρ (g/cm^3)	1.277	1.262	1.258
μ(mm^{-1})	0.083	0.082	0.082
F(000)	336.0	1344.0	352.0

Crystal size(mm^3)	0.2 × 0.18 × 0.16	0.3 × 0.29 × 0.23	0.32 × 0.3 × 0.28
Radiation	MoKα (λ = 0.71073)	MoKα (λ = 0.71073)	MoKα (λ = 0.71073)
2Θ range for data collection(°)	6.496 to 54.906	6.458 to 54.806	6.416 to 54.714
Index ranges	-9 ≤ h ≤ 9, -10 ≤ k ≤ 10, -17 ≤ l ≤ 17	-17 ≤ h ≤ 17, -15 ≤ k ≤ 16, -26 ≤ l ≤ 25	-10 ≤ h ≤ 10, -10 ≤ k ≤ 10, -17 ≤ l ≤ 16
Reflections collected	10950	12243	12401
Independent reflections	3534	3550	3757
Data/restraints/parameters	3534/0/219	3550/0/219	3757/0/228
Goodness-of-fit on F^2	1.087	1.054	1.086
Final R indexes [I>=2σ (I)]	R_1 = 0.0494, wR_2 = 0.1282	R_1 = 0.0425, wR_2 = 0.1146	R_1 = 0.0501, wR_2 = 0.1363
Final R indexes [all data]	R_1 = 0.0753, wR_2 = 0.1479	R_1 = 0.0651, wR_2 = 0.1281	R_1 = 0.0764, wR_2 = 0.1532
Largest diff.peak/hole/e Å^{-3}	0.17/-0.20	0.13/-0.15	0.19/-0.16

The supramolecular framework compound 5.2A: The molecular association of compound **5.2A** involves C-H…N and C-H…H interactions along the ring plane. The nitrogen (N2) of the cyano group acts as a bifurcated acceptor and forms two C-H…N bonds with the two naphthalene ring hydrogen (H11) and (H14) at a distance of 2.638Å and 2.655Å respectively. The hydrogen (H9) from the naphthalene ring also interacts with the same intermolecular atom (H9), forming a C-H…H interaction at a distance of 2.369Å. Thus, the two C-H...N interactions and the C-H…H interaction result in forming a polymeric layer of sheets. It also established the formation of $R_2^2(16)$ and $R_4^2(14)$ graph set notations **(Figure 3.42 (b))**. The C-H…C interactions between the linker hydrogen (H6A) and the naphthalene ring carbon (C8), which have an interaction distance of 2.813Å, act as interlayer connectivity between the sheets **(Figure 3.42 (c))**. C-H…π interactions between the alkyl hydrogen (H19A) of the pyridine ring substituent and the naphthalene p-orbital at a distance of 2.832Å stabilizes the crystal packing within the unit cell **(Figure 3.42 (d))**. In addition, π…π parallel displaced stacking interaction at a distance of 3.858Å between the pyridine ring and the naphthalene ring also stabilizes the crystal packing **(Figure 3.42 (d))**. The supramolecular arrangement of compound **5.2A** also displays another π…π stacking interaction between the pyridine ring and the naphthalene ring on the other face of the aromatic ring at a distance of 3.840Å **(Figure 3.42 (e))**. The non-covalent interactions found for compound **5.2A** are given in **Table 3.12**.

Table 3.12: Hydrogen bonds and other interactions in compound **5.2A**

Donor-H...Acceptor	**D–H, Å**	**H...A, Å**	**D...A, Å**	**D -H...A, ^{o}**
C14-H14…N2	0.930	2.655	3.534	157.79
C6-H6A…C8	0.970	2.813	3.667	147.35
C11-H11…N2	0.930	2.638	3.455	147.10
C9-H9…H9	0.930	2.369	3.175	144.93
C19-H19A…π(C12-C17)	0.960	2.832	3.644	142.91
Other contacts				
π(C1-C5, N1)… π(C8-C12, C17)		3.858		
π(C1-C5, N1)… π(C12,-C17)		3.840		
Intramolecular				
C6-H6A…O2	0.970	2.528	2.302	65.54
C6-H6B…O2	0.970	2.468	2.302	68.77
C7-H7A…O1	0.970	2.588	2.349	65.00
C7-H7B…O1	0.970	2.530	2.349	68.18

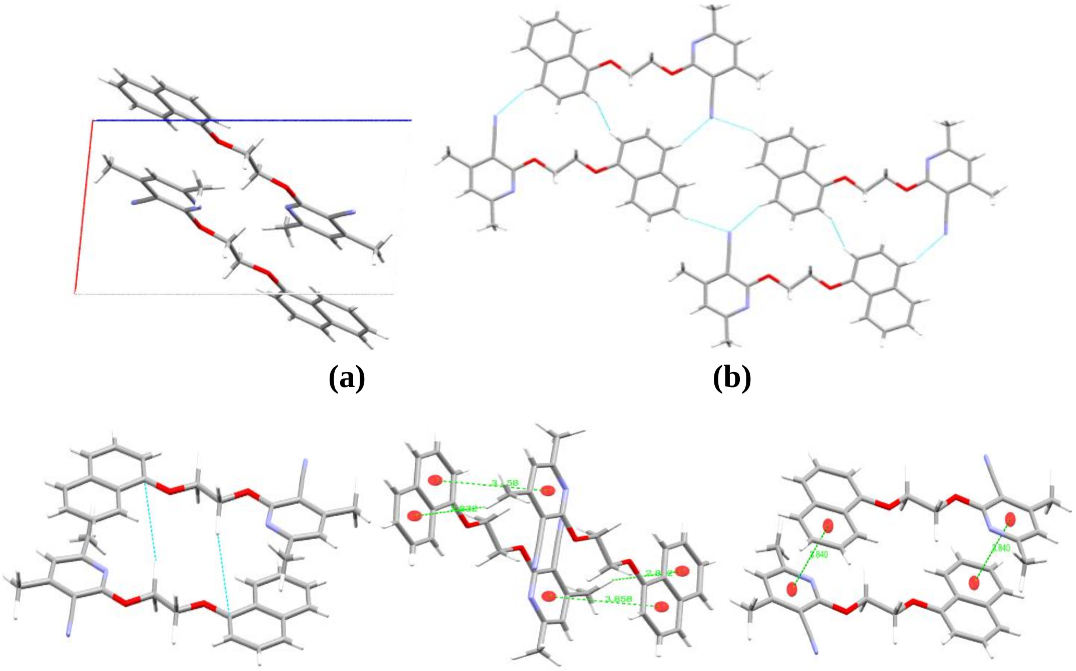
(a) **(b)**

(c) **(d)** **(e)**

Figure 3.42: (a) Packing diagram of compound **5.2A**, (b) graph set, (c) C-H…C, (d) C-H…π and (e) π…π interactions, in compound **5.2A**

Hirshfeld surface analysis of compound 5.2A: The Hirshfeld surface mapped over the d_{norm} in the range of -0.09 to 1.39Å for compound **5.2A** is displayed in **Figure 3.43 (a) and (b)**. The region of bright red spots corresponds to a shorter bond length due to C-H…N, C-H…C, and C-H…H contacts. The intensity of the red color and the size of the spots depend on interaction distance. The more dominant the interaction, the more intense the red color and the larger the size of the spots and vice versa.

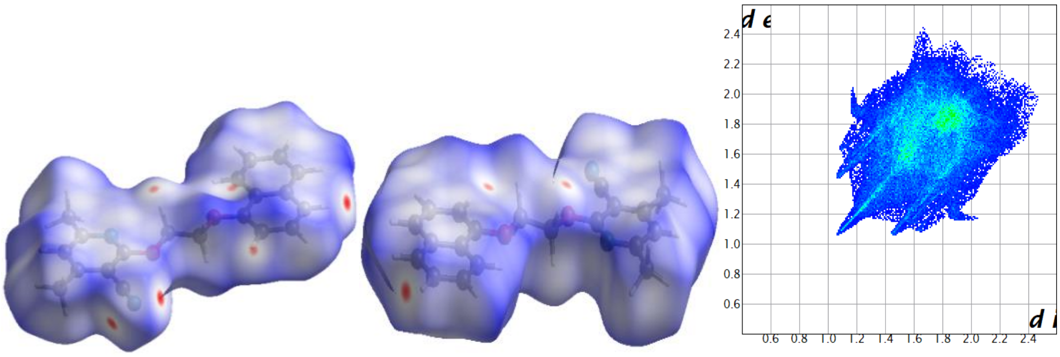

(a) **(b)** **(c)**

Figure 3.43: (a) and (b) d_{norm} both side view, (c) 2-D fingerprint plot, of compound **5.2A**

The relative percentage contributions of non-covalent interaction to the Hirshfeld surface are summarized by the 2-D fingerprint plot of compound **5.2A (Figure 3.43 (c))**. Those are H…H (53.7%), C...H (14.8%), N…H (14.2%), C…C (9.0%), O…H (4.6%),C…O (2.2%) and C…N (1.4%). The sting-like pattern in the 2-D fingerprint plot in the region of di + de = 2.1-2.8Å represents H…H interactions. N…H interaction also appears as a pair of tiny spikes in the region of di + de = 2.5-3.2Å. C-H...π merged within the C…H contacts and appears in the region of di + de = 2.7-3.4Å. It also appears as a characteristic hook-like pattern. The C…C contacts which contribute 9.0%, also represent the presence of π...π stacking interactions between the aromatic rings.

The Hirshfeld shape-index in a range of -1 to 1Å for compound **5.2A** shows yellowish-red colored concave regions around the surface of the naphthalene ring, which represents the acceptor region where C-H...π interactions occur **(Figure 3.44 (a))**. The complementary pair of red and blue triangles around the surface of the naphthalene and pyridine ring indicates the presence of π...π stacking interaction between the aromatic rings **(Figure 3.44 (a) and (b))**. The Hirshfeld curvedness in a range of -4 to 0.4 Å for compound **5.2A** also displays a flat green region with a yellowish spot around the naphthalene and the pyridone ring surfaces. It again indicates the presence of π…π stacking interaction **(Figure 3.44 (c) and (d))**.

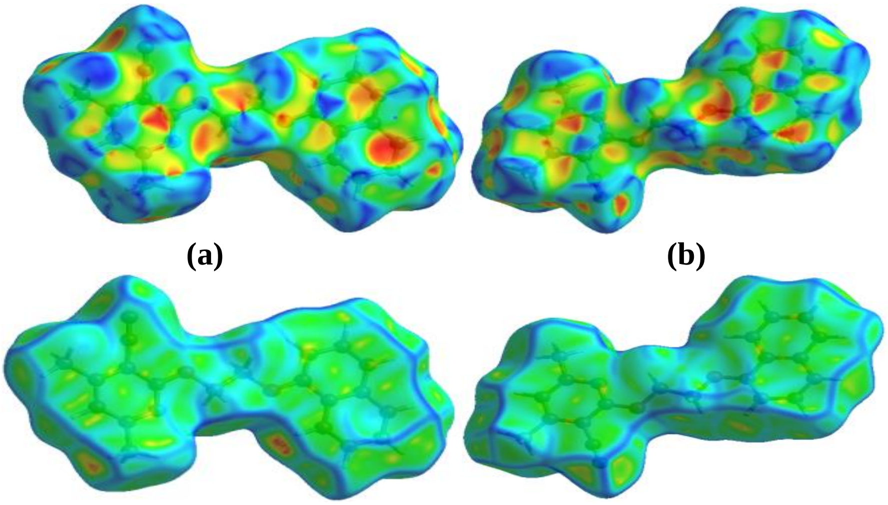

(a) (b)

(c) (d)

Figure 3.44: (a) and (b) Shape-index, (c) and (d) Curvedness, both side views of compound **5.2A**

The C-H…N, C-H…C, C-H…H, C-H…π, and π…π stacking interactions found in the supramolecular framework are also supported by the Hirshfeld calculation within the cluster of 3.8Å radius from a single crystals fragment as shown in **Figure 3.45**.

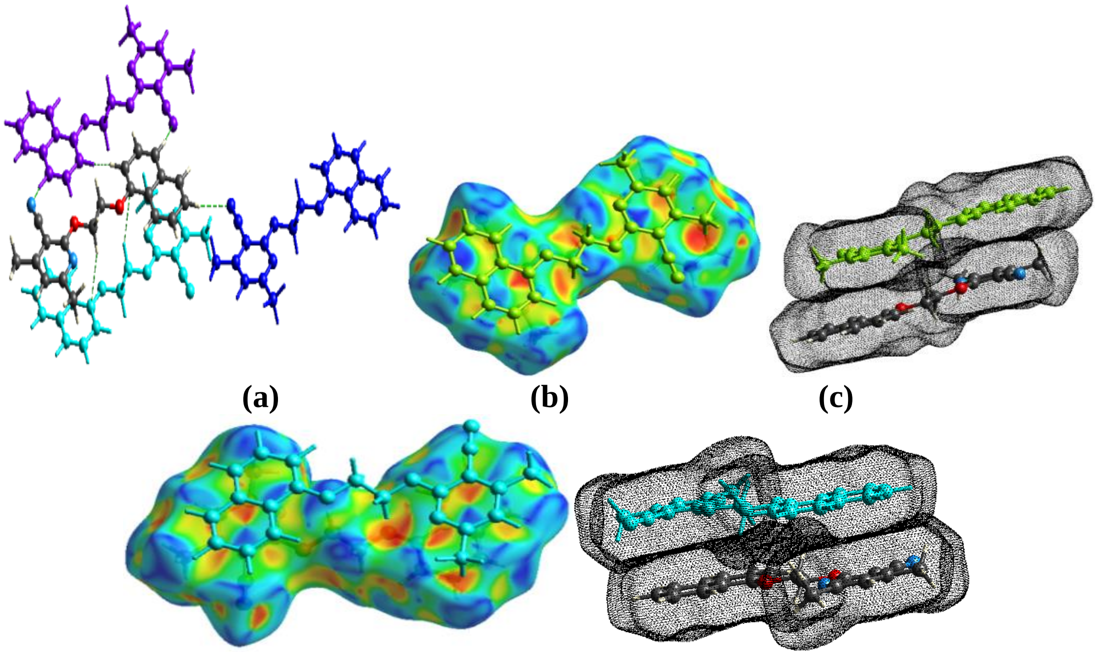

(a) (b) (c)

(d) (e)

Figure 3.45: (a) C-H…N, C-H…C, and C-H…H interactions, (b), (c), (d), and (e) π…π interactions in compound **5.2A**

3.10.1.2. Crystal analysis of compound 5.2B

The compound **5.2B** was recrystallized in ethyl acetate at room temperature by slow evaporation of the solvent. The chiral asymmetric compound **5.2B** was analyzed using SC-XRD **(Figure 3.46)**. The compound crystallized with cell lengths **a** = 13.2682(5)Å, **b** = 12.6180(5)Å, **c** = 20.5116(8)Å, i.e., $\mathbf{a} \neq \mathbf{b} \neq \mathbf{c}$ and cell angles $\boldsymbol{\alpha}$ = 90°, $\boldsymbol{\beta}$= 102.579(4)°, $\boldsymbol{\gamma}$= 90°, i.e., $\boldsymbol{\alpha = \gamma = 90°}$, $\boldsymbol{\beta \neq 90°}$, which indicate that the compound is exhibiting monoclinic crystal system, with space group C2/c that contains eight molecules per unit cell.

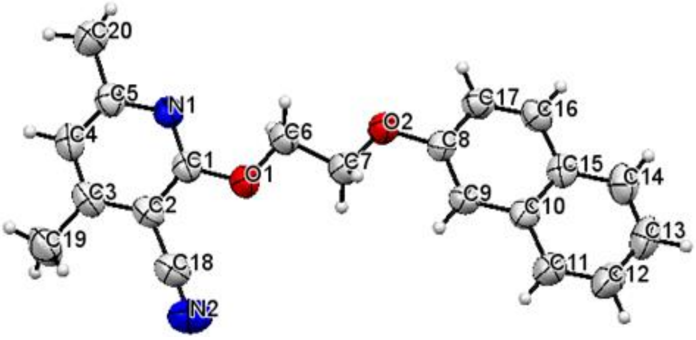

Figure 3.46: ORTEP diagram of compound **5.2B**

The crystal structure of compound **5.2B** shows that both the pyridine and the naphthalene ring are planar and aromatic. The naphthalene ring and the pyridine ring almost lie in the same plane. The angle of deviation between the two planes is only 6.01°. The crystallographic information is in **Table 3.11**.

The supramolecular framework of compound 5.2B: The crystal of compound **5.2B** displays C-H…O interactions between the hydrogen (H12) from the naphthalene ring and the oxygen (O2) along the plane rings at a distance of 2.652Å that forms a polymeric chain of sheets. A layer of sheets is interconnected by C-H…C interactions between the alkyl hydrogen (H20A) and carbon (C18) of the cyano group at a distance of 2.798Å. It gives a graph set of $R_2^2(14)$ **(Figure 3.47 (b))**. A different layer of sheets runs diagonally to the plane of another layer of sheets. Those having different orientations are interconnected by C-H…C interactions between the hydrogen (H13) and carbon (C17) of the naphthalene ring at a distance of 2.785Å. The repetitive C-H…C interaction between the different orientations of sheets over other sheets adopts the arrangement of the crystal to have an appearance in a zig-zag fashion. This C-H…C interaction assists in stabilizing the crystal packing within the unit cell, and it forms $R_4^4(14)$ graph set notation together with the C-H...O interaction **(Figure 3.47 (c))**. The supramolecular structure of compound **5.2B** also displays C-H…π interaction between the naphthalene p-orbital and the hydrogen (H19A) and (H19B) from the alkyl substituent of the pyridine ring, having an interaction distance of 3.417Å and 2.860Å respectively **(Figure 3.47 (d))**. The crystal packing of compound **5.2B** is also stabilized by π…π interactions between the pyridine and the naphthalene ring at a distance of 3.675Å **(Figure 3.47 (e))**. In addition to these, π…π stacking interactions having a distance of 3.775Å are found between the pyridine rings **(Figure 3.47 (f))**. The weak interactions are given in **Table 3.13**.

Table 3.13: Hydrogen bonds and other interactions in compound **5.2B**

Donor-H...Acceptor	**D – H, Å**	**H...A, Å**	**D...A, Å**	**D - H...A, º**
C12-H12…O2	0.930	2.652	3.564	166.74
C13-H13…C17	0.930	2.785	3.694	166.15
C20-H20A…C18	0.960	2.798	3.711	159.15
C19-H19A…π(C8-C10, C15-C17)	0.960	3.417	3.950	117.25
C19-H19B…π(C10- C15)	0.960	2.860	3.588	133.35
Other contacts				
π(C1- C5, N1)… π(C10- C15)		3.675		
π(C1- C5, N1)… π(C1- C5, N1)		3.775		
Intramolecular				
C6-H6A…O2	0.970	2.581	2.336	64.63
C6-H6B…O2	0.970	2.512	2.336	68.40
C7-H7A…O1	0.970	2.548	2.316	65.21
C7-H7B…O1	0.970	2.478	2.316	69.05

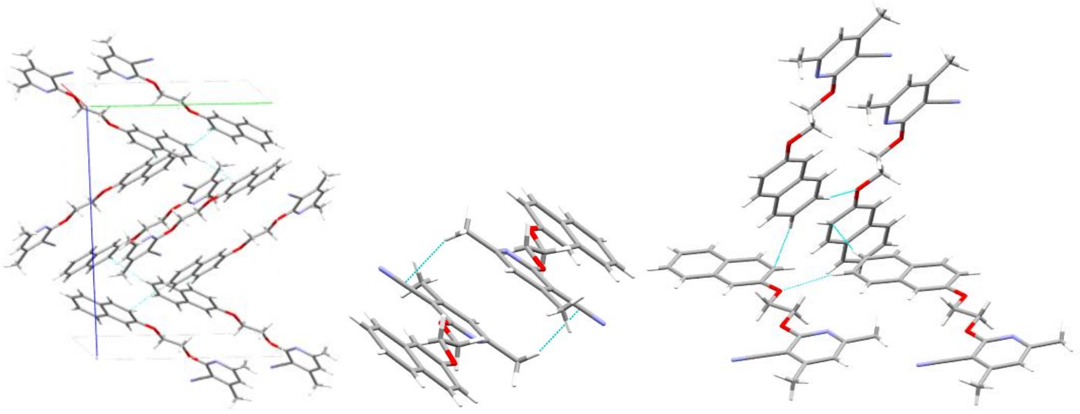

(a) **(b)** **(c)**

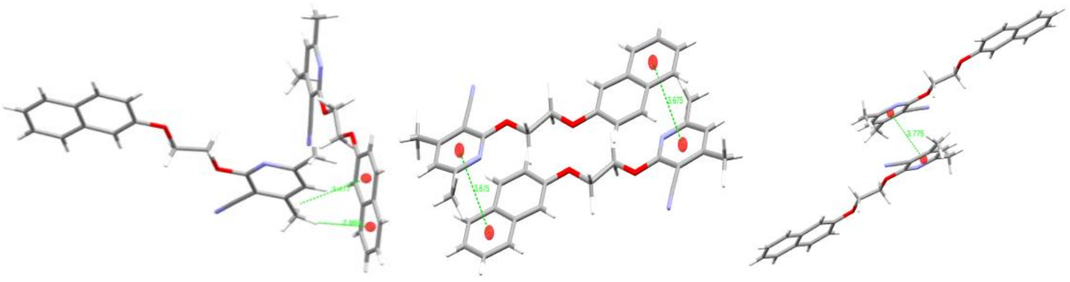

(d) (e) (f)

Figure 3.47: (a) Packing diagram of compound **5.2B**, (b) and (c) graph sets, (d) C-H…π interactions, (e) and (f) π…π interactions, in compound **5.2B**

Hirshfeld surface analysis of compound 5.2B: The Hirshfeld surface mapped over the d$_{norm}$ in the range of -0.1 to 1.29Å for compound **5.2B** is displayed in **Figure 3.48 (a) and (b)**. The region of bright red spots corresponds to a shorter bond length due to C-H…O and C-H…C contacts. The relative percentage contributions of non-covalent interaction to the Hirshfeld surface are summarized by the 2-D fingerprint plot of compound 5.2B **(Figure 3.48 (c))**. Those are H…H (50.9%), C...H (19.9%), N…H (13.0%), O…H (6.0%), C…C (5.6%), C…N (2.8%), C…O (1.8%) and N…N (0.1%). The C-H...π and C…H contacts appear as a pair of wing-like patterns in the region of di + de = 2.7-3.0Å. O…H contacts also appear as a short spike in between the H…H and C…H/C-H…π contacts in a region of di + de = 2.5-2.8Å. The C…C contacts which contribute 5.6%, indicates the existence of π...π stacking interactions.

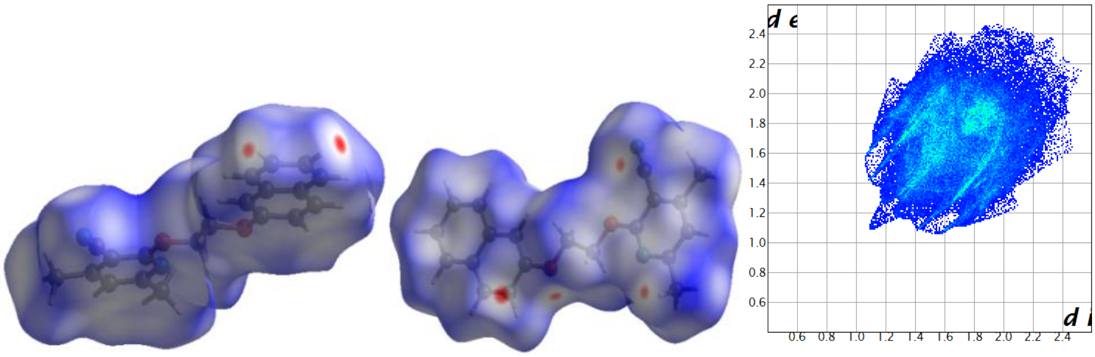

(a) (b) (c)

Figure 3.48: (a) and (b) d$_{norm}$ both side view, (c) 2-D fingerprint plot, of compound **5.2B**

The Hirshfeld surface mapped over the shape-index in a range of -1 to 1Å for compound **5.2B** shows yellowish-red colored concave regions around the surface of the naphthalene ring, which represents the acceptor region for C-H...π interactions **(Figure3.49 (a))**.

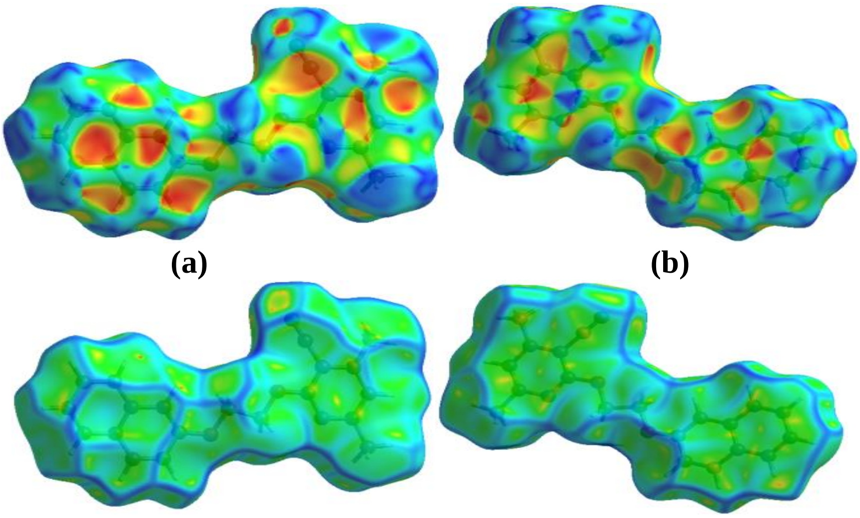

(a) (b)

(c) (d)

Figure 3.49: (a) and (b) Shape-index, (c) and (d) Curvedness, both side views of compound **5.2B**

Red and blue triangles also appear on the surface of the naphthalene and the pyridine ring, which indicate the presence of π…π stacking interactions **(Figure 3.49 (a) and (b))**. Similarly, the Hirshfeld surface mapped over the curvedness in a range of -4 to 0.4 Å displays a flat green region with a yellowish spot around the naphthalene ring and the pyridine ring surfaces, which again confirm the presence of π…πstacking interaction **(Figure 3.49 (c) and (d))**.

The Hirshfeld calculation of weak interactions within the cluster of 3.8Å radius from a single crystals fragment also supports the different types of interactions found within the supramolecular framework, as shown in **Figure 3.50**.

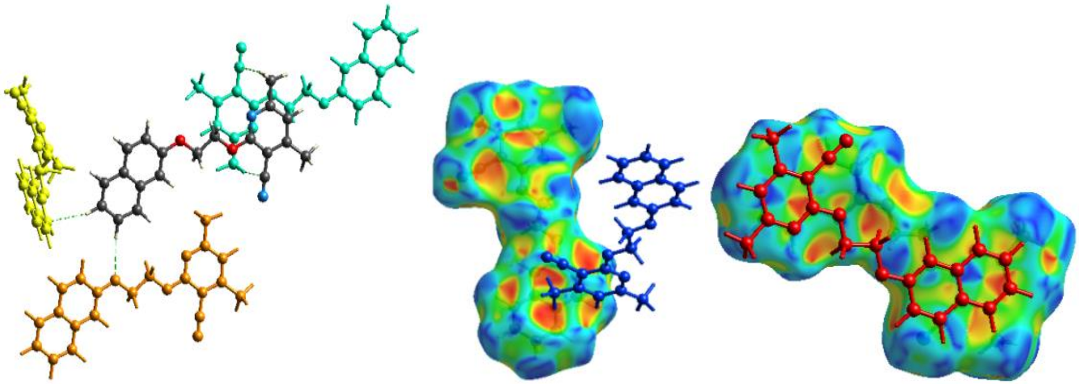

(a) (b) (c)

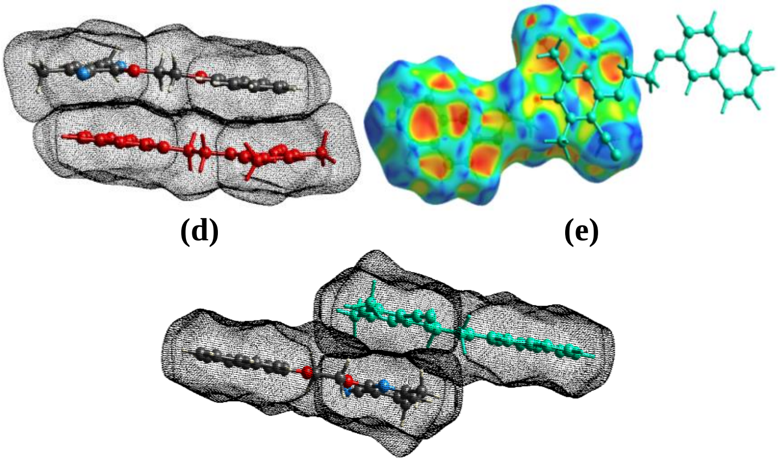
(d) (e)

(f)

Figure 3.50: (a) C-H…O and C-H…C interactions, (b) C-H…π interactions, (c), (d), (e) and (f) π…π interactions, in compound **5.2B**

3.10.1.3. Crystal analysis of compound 5.2C

The compound **5.2C** was recrystallized in ethyl acetate at room temperature by slow evaporation of the solvent. The chiral asymmetric compound **5.2C** was analyzed using SC-XRD **(Figure 3.51)**. The compound crystallized with cell lengths **a** = 8.4985(2)Å, **b** = 8.5046(3)Å, **c** = 13.8343(3)Å, i.e., **a** ≠ **b** ≠ **c**, and cell angles $\boldsymbol{\alpha}$ = 77.856(2)°, $\boldsymbol{\beta}$ = 75.183(2)°, $\boldsymbol{\gamma}$ = 66.165(3)°, i.e., $\boldsymbol{\alpha \neq \beta \neq \gamma \neq 90°}$. It indicates that the compound exhibits a triclinic crystal system, with space group P-1 that contains two molecules per unit cell.

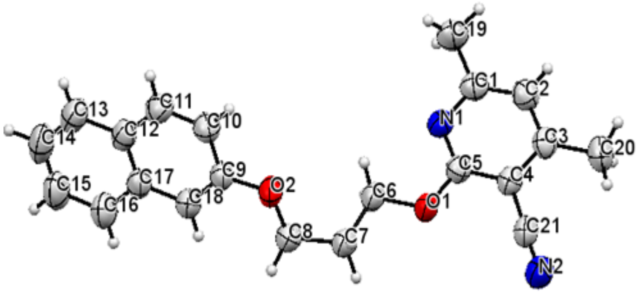

Figure 3.51: ORTEP diagram of compound **5.2C**

The crystal structure of compound **5.2C** shows that both the pyridine and the naphthalene ring are planar and aromatic. The pyridine ring and the atoms O1, C6, and C7 lie in one plane. Also, the naphthalene ring and the atom O2 lie on the same plane. The naphthalene ring twisted away from the plane of the pyridine ring and flipped towards the parent pyridine ring. The dihedral angle between the two planes is 61.25°. The flexibility of the ring is achieved through carbon atoms (C8). The crystallographic information is in **Table 3.11**.

The supramolecular framework of compound 5.2C: The nitrogen (N2) of the cyano group act as a bifurcated acceptor and forms C-H…N interactions with the hydrogen (H15) of the naphthalene ring and with hydrogen (H19B) of the alkyl substituent of the pyridine ring with an interaction distance of 2.725Å and 2.618Å respectively. An extensive C-H…N intermolecular interaction results in forming a layer of the sheet. The analysis of the molecular association of compound **5.2C** involves C-H…C interactions at a distance of 2.852Å between the linker hydrogen (H8B) and the carbon (C16) from the naphthalene ring, which forms the $R_2^2(14)$ graph set **(Figure 3.52 (b))**. The linker hydrogen (H8A) acts as bifurcated hydrogen. It forms C-H…C interactions with the pyridine carbon (C4) and the carbon (C21) from the cyano group at an interaction distance of 2.886Å and 2.796Å, respectively. This C-H…C interactions formed by the bifurcated hydrogen also forms a graph set notation of $R_2^2(14)$ and $R_2^2(16)$ **(Figure 3.52 (c))**. The hydrogen (H20B) from the alkyl substituent of the pyridine ring forms C-H…O interaction with the oxygen (O2) at a distance of 2.565Å and also forms the $R_2^2(20)$ graph set **(Figure 3.52 (d))**.

The crystal packing within the unit cell is stabilized by the C-H…C interactions formed by the bifurcated hydrogen and the C-H…π interactions between the linker hydrogen (H7B) and the pyridine ring at a distance of 3.221Å **(Figure 3.52 (e))**. Beyond these interactions, the supramolecular structure of compound **5.2C** display C-H…π interactions between the linker hydrogen (H8B) and the naphthalene ring, having an interaction distance of 2.883Å. Also, the hydrogen (H20C) from the alkyl substituent of the pyridine ring interacts with the naphthalene p-orbital and forms a C-H…π interaction with a distance of 3.165Å **(Figure 3.52 (f))**. Furthermore, π…π stacking interactions between the pyridine rings at a distance of 3.999Å and between the naphthalene rings at a distance of 3.900Å also involved in assisting the overall structure of compound **5.2C (Figure 3.52 (g) and (h))**. The non-covalent interactions found in the crystal structure of compound **5.2C** are given in **Table 3.14**.

Table 3.14: Hydrogen bonds and other interactions in compound **5.2C**

Donor-H...Acceptor	**D–H, Å**	**H...A, Å**	**D...A, Å**	**D -H...A, °**
C19-H19B…N2	0.960	2.618	3.566	169.13
C15-H15…N2	0.930	2.725	3.552	148.58
C8-H8B…C16	0.970	2.852	3.631	138.08
C8-H8A…C4	0.970	2.886	3.562	127.57
C8-H8A…C21	0.970	2.796	3.703	156.06
C20-H20B…O2	0.960	2.565	3.481	159.52
C7-H7B…π(C1-C5, N1)	0.970	3.221	3.965	134.94
C8-H8B…π(C12-C17)	0.970	2.883	3.812	160.72
C20-H20C…π(C9-C12, C17, C18)	0.960	3.165	4.033	151.15
Other Contact				
π(C9-C18)… π(C9-C18)		3.999		
π(C1-C5, N1)… π(C1-C5, N1)		3.900		
Intramolecular				
C7-H7A…O1	0.970	2.589	2.337	66.63
C7-H7B…O1	0.970	2.526	2.337	70.10
C6-H6B…O2	0.970	2.681	2.954	96.58

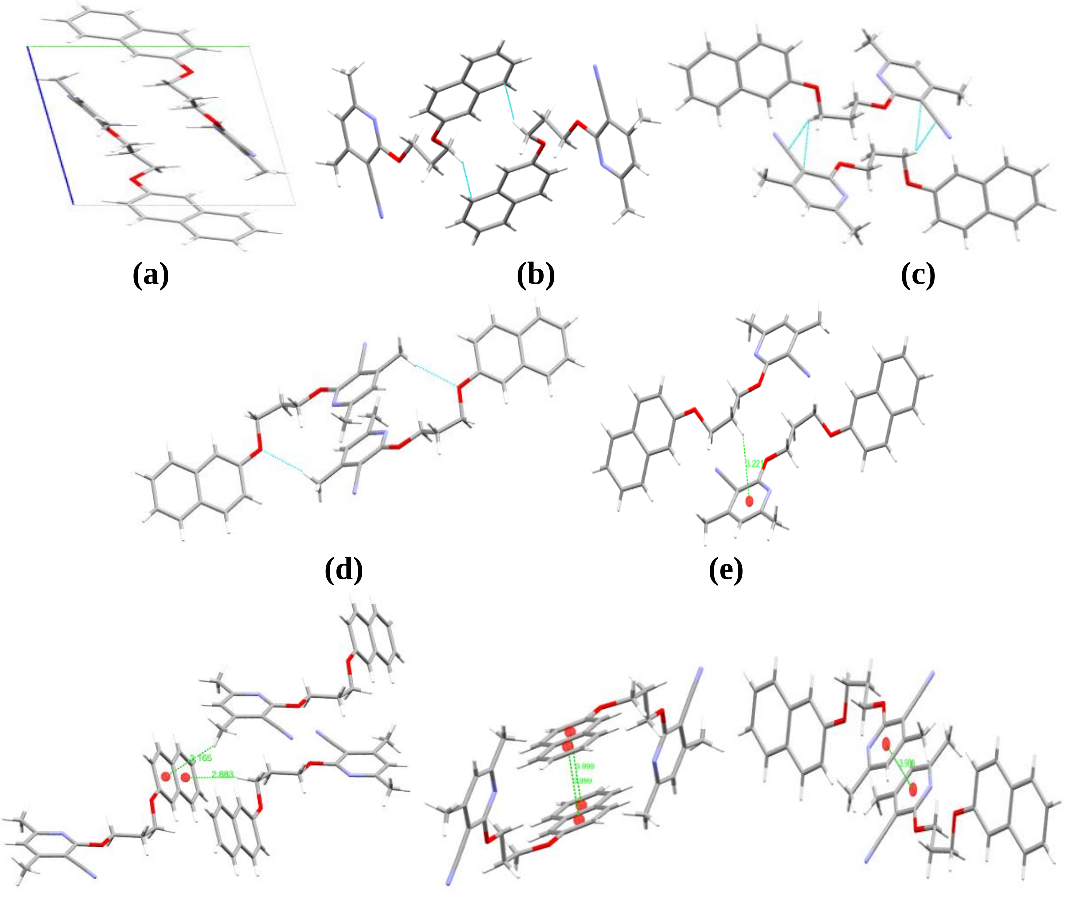

(a) (b) (c)

(d) (e)

(f) (g) (h)

Figure 3.52: (a) Packing diagram of compound **5.2C**, (b), (c) and (d) graph sets, (e) and (f) C-H…π interactions, (g) and (h) π…π interactions, in compound **5.2C**

Hirshfeld surface analysis of compound 5.2C: The Hirshfeld surface mapped over the d_{norm} in the range of -0.11 to 1.36Å for compound **5.2C** is displayed in **Figure 3.53 (a) and (b)**. The region of red spots corresponds to shorter contacts due to C-H…O, C-H…N, and C-H…C interactions. The intensity of the red color and the size of the spots depend on interaction distance. The more dominant the interaction, the more intense the red color and the larger the size of the spots and vice versa.

The 2-D fingerprint plot of compound **5.2C** represents the relative percentage contributions of non-covalent interaction to the Hirshfeld surface **(Figure 3.53 (c))**. Those are H…H (51.9%), C…H (21.8%), N…H (13.0%), O...H (5.8%), C…C (4.5%), O…C (1.8%) and C…N (1.2%).

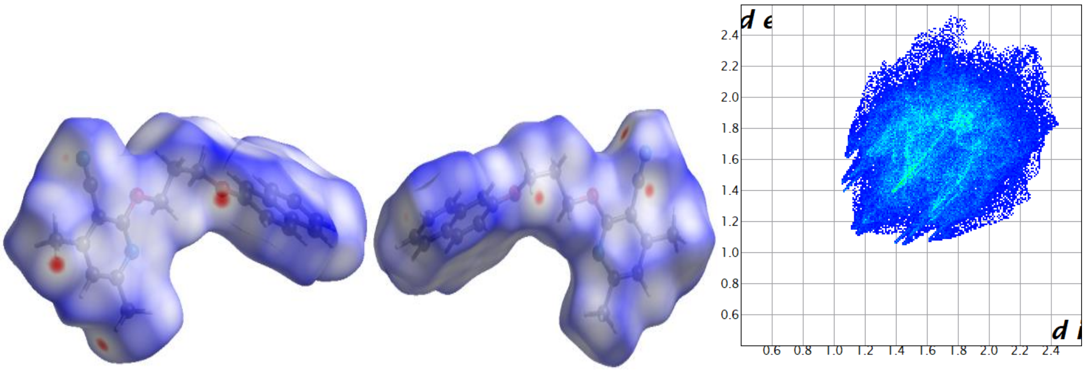

(a) **(b)** **(c)**

Figure 3.53: (a) and (b) d_{norm} both side view, (c) 2-D fingerprint plot, of compound **5.2C**

In the 2-D fingerprint plot, a pair of thinner spoke-like patterns in the region of di + de = 2.5-2.8Å represents O…H interactions. The other pair of thicker spoke-like patterns in the region of di + de = 2.6-3.0Å also represents N…H interaction. The C-H...π and C…H contacts come in the same region in the 2-D fingerprint, which appears as a characteristic wing-like pattern in the region of di + de = 2.7-3.4Å. The C…C contacts which account for 4.5%, indicate the presence of π...π stacking interactions between the aromatic rings.

The Hirshfeld shape-index in a range of -1 to 1Å for compound **5.2C** shows the presence of complementary pair of red and blue triangles having an edge to edge connection at the surface of the naphthalene and the pyridine rings, which indicates the presence of π...π stacking interactions between the rings **(Figure 3.54 (a) and (b))**. The yellowish-red colored concave regions around the surface of the naphthalene and the pyridine rings represent the acceptor region where C-H...π occur **(Figure 3.54 (a) and (b))**. Moreover, the Hirshfeld curvedness surface in a range of -4 to 0.4 Å for compound **5.2C** also displays a flat green region with a yellowish spot around the surface of the naphthalene and the pyridine rings, which indicates the presence of π…π stacking interaction between the rings **(Figure 3.54 (c) and (d))**.

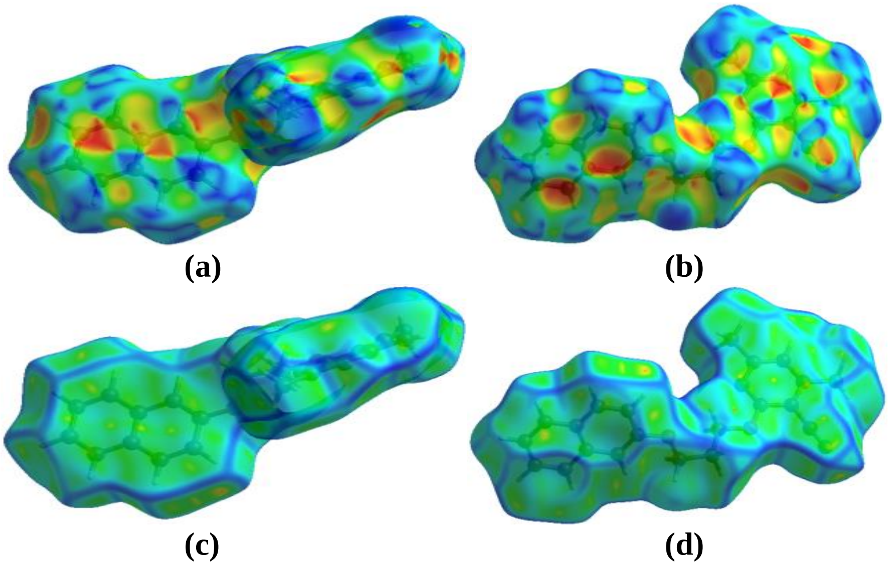
(a) **(b)**

(c) **(d)**

Figure 3.54: (a) and (b) Shape-index, (c) and (d) Curvedness, both side views of compound **5.2C**

The C-H…O, C-H…N, C-H…C, C-H…π, and π…π stacking interactions found within the supramolecular association of compound **5.2C** is also supported by the Hirshfeld calculation within the cluster of radius 3.8Å is shown in **Figure 3.55**.

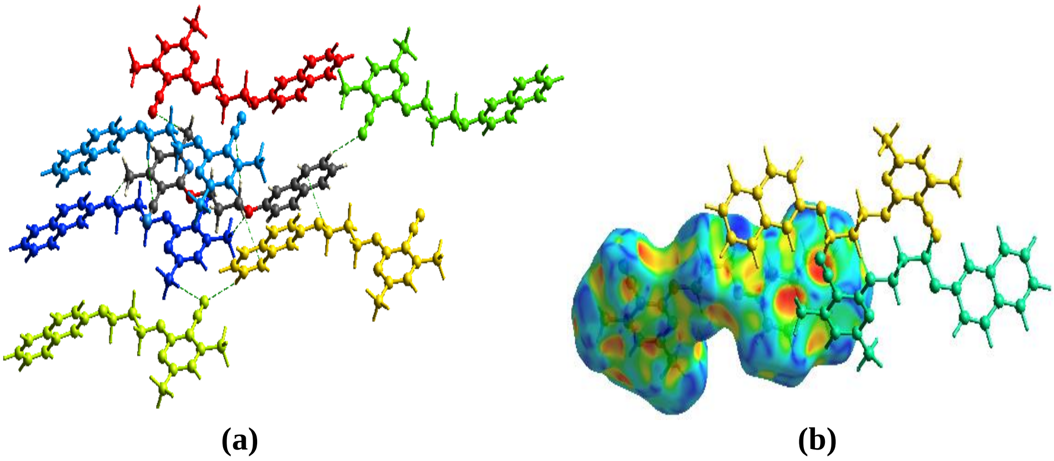
(a) **(b)**

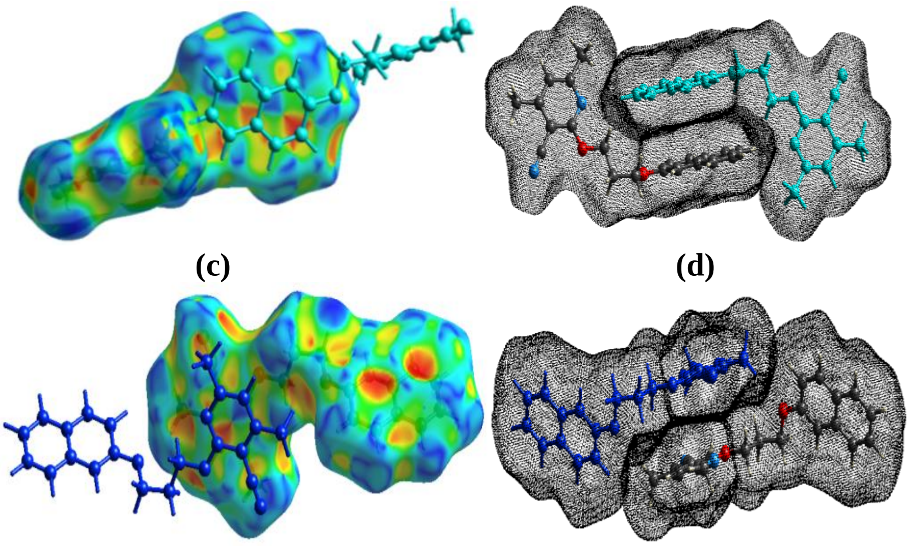

(c) (d)

(e) (f)

Figure 3.55: (a) C-H…O, C-H…N, and C-H…C interactions, (b) C-H…π interactions, (c), (d), (e) and (f) π…π interactions in compound **5.2C**

3.10.1.4. Crystal analysis of compound 5.2D

The compound **5.2D** was recrystallized in ethyl acetate at room temperature by slow evaporation of the solvent. The chiral asymmetric compound **5.2D** was analyzed by SC-XRD **(Figure 3.56)**. The compound crystallized with cell lengths **a** = 7.7552(3)Å, **b** = 8.8292(3)Å, **c** = 13.3083(4)Å, i.e., $\mathbf{a} \neq \mathbf{b} \neq \mathbf{c}$ and cell angles $\boldsymbol{\alpha}$ = 77.264(3)°, $\boldsymbol{\beta}$ = 82.079(3)°, $\boldsymbol{\gamma}$ = 65.755(4)°, i.e., $\boldsymbol{\alpha} \neq \boldsymbol{\gamma} \neq \boldsymbol{\beta} \neq \mathbf{90°}$. It indicates that the compound exhibits a triclinic crystal system, with space group P-1 that contains two molecules per unit cell.

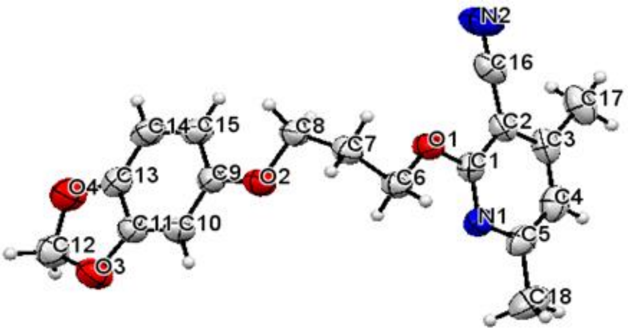

Figure 3.56: ORTEP diagram of compound **5.2D**

The crystal structure of compound **5.2D** shows that both the pyridine and benzodioxole rings are planar and aromatic. The benzodioxole ring flips toward the pyridine ring almost perpendicular to the plane of the pyridine ring, where maximum flexibility is achieved through the carbon (C7) atom. The dihedral angle between the planes of the two rings is 87.79°. The crystallographic information is in **Table 3.15**.

Table 3.15: Crystal data on compounds **5.2D**, **5.3A**, **5.3B**

Compound	5.2D	5.3A	5.3B
Identification code	2170470	2062948	2170481
Empirical formula	$C_{18}H_{18}N_2O_4$	$C_{20}H_{18}N_2O_2$	$C_{20}H_{18}N_2O_2$
Formula weight	326.34	318.36	318.36
Temperature(K)	293(2)	296.15	293(2)
Crystal system	Triclinic	Orthorhombic	Monoclinic
Space group	P-1	$Pca2_1$	$P2_1/c$
a(Å)	7.7552(3)	8.911(3)	15.0512(4)
b(Å)	8.8292(3)	7.340(2)	12.6307(4)
c(Å)	13.3083(4)	25.204(7)	8.5290(3)
α(°)	77.264(3)	90	90
β(°)	82.079(3)	90	91.810(2)
γ(°)	65.755(4)	90	90
Volume($Å^3$)	809.29(5)	1648.6(8)	1620.62(9)
Z	2	4	4
ρ (g/cm^3)	1.339	1.283	1.305
μ(mm^{-1})	0.096	0.084	0.085
F(000)	344.0	672.0	672.0
Crystal size(mm^3)	0.2 × 0.18 × 0.17	0.23 × 0.17 × 0.13	0.26 × 0.24 × 0.22
Radiation	MoKα (λ = 0.71073)	MoKα (λ =0.71073)	MoKα (λ = 0.71073)
2Θ range for data collection(°)	6.498 to 54.816	5.55 to 54.58	6.304 to 54.836
Index ranges	$-9 \leq h \leq 9$, $-11 \leq k \leq 11$, $-16 \leq l \leq 16$	$-11 \leq h \leq 11$, $-9 \leq k \leq 9$, $-32 \leq l \leq 32$	$-19 \leq h \leq 18$, $-15 \leq k \leq 16$, $-10 \leq l \leq 10$
Reflections collected	9382	25527	13237
Independent reflections	3427	3696	3444
Data/restraints/parameters	3427/0/219	3696/1/219	3444/0/219
Goodness-of-fit on F^2	1.073	0.991	1.093
Final R indexes [I>=2σ (I)]	$R_1 = 0.0525$, $wR_2 = 0.1346$	R1 = 0.0513, $wR_2 = 0.1170$	$R_1 = 0.0460$, $wR_2 = 0.1191$
Final R indexes [all data]	$R_1 = 0.0730$, $wR_2 = 0.1512$	R1 = 0.0674, $wR_2 = 0.1258$	$R_1 = 0.0636$, $wR_2 = 0.1311$
Largest diff.peak/hole/e $Å^{-3}$	0.19/-0.27	0.23/-0.26	0.18/-0.19

The supramolecular framework of compound 5.2D: The analysis of the molecular assembly of compound **5.2D** crystal involves C-H…O interaction between the benzodioxole ring hydrogen (H10) and the oxygen (O2) along the plane of the ring at a distance of 2.714Å that result in the formation of the unsymmetrical dimer. This C-H…O interaction between the two molecules also forms $R_2^2(8)$ graph set notation **(Figure 3.57 (b))**. The benzodioxole ring hydrogen (H15) also interacts with the nitrogen (N2) of the cyano group having an interaction distance of 2.571Å along the plane of the ring, which also gives the $R_2^2(24)$ graph set **(Figure 3.57 (c))**. The molecules are stacked one over another, and C-H...H interaction interconnects them between linker hydrogen (H6A) and the alkyl hydrogen (H17C) at a distance of 2.297Å and C-H...C interaction between the alkyl hydrogen (H17B) and the benzodioxole ring atom (C9) at an interaction distance of 2.692Å. The linker hydrogen (H8A) also interacts with the oxygen (O4) from the benzodioxole ring and forms C-H…O interactions at a distance of 2.716Å **(Figure 3.57 (d))**. The C-H…C interactions having 2.692Å interaction distance also stabilizes the crystal packing within the unit cell **(Figure 3.57 (a))**. In addition to this, π…π stacking interaction between the pyridine rings at a distance of 3.606Å also stabilizes the crystal packing **(Figure 3.57 (e))**.

The molecular association of compound **5.2D** also exhibits dipole-dipole intermolecular interaction along the ring plane between the oxygen (O4) and the carbon (C12) within the benzodioxole ring. The network of compounds within the supramolecular assembly also displays π…π stacking interaction between the benzodioxole rings at a distance of 3.943Å and one additional π…π parallel displaced stacking interaction between the pyridine rings at a distance of 5.190Å **(Figure 3.57 (f) and (g))**. The weak interactions are listed in **Table 3.16**.

Table 3.16: Hydrogen bonds and other interactions in compound **5.2D**

Donor-H...Acceptor	**D – H, Å**	**H...A, Å**	**D...A, Å**	**D - H...A, º**
C8-H8A…O4	0.970	2.716	3.449	132.77
C17-H17B…C9	0.960	2.692	3.631	165.77
C10-H10…O2	0.930	2.714	3.639	173.36
C15-H15…N2	0.930	2.571	3.466	161.56
C6-H6A…H17C	0.970	2.297	2.999	128.58
Other contacts				
O4…C12		3.160		
π(C9-C11,C13-C15)… π(C9-C11,C13-C15)		3.943		
π(C1-C5,N1)… π(C1-C5,N1)		3.606		
π(C1-C5,N1)… π(C1-C5,N1)		5.190		
Intramolecular				
C6-H6B…O2	0.970	2.646	2.980	100.53
C7-H7A…O2	0.970	2.464	2.354	72.06
C8-H8B…O1	0.970	2.624	2.967	101.06

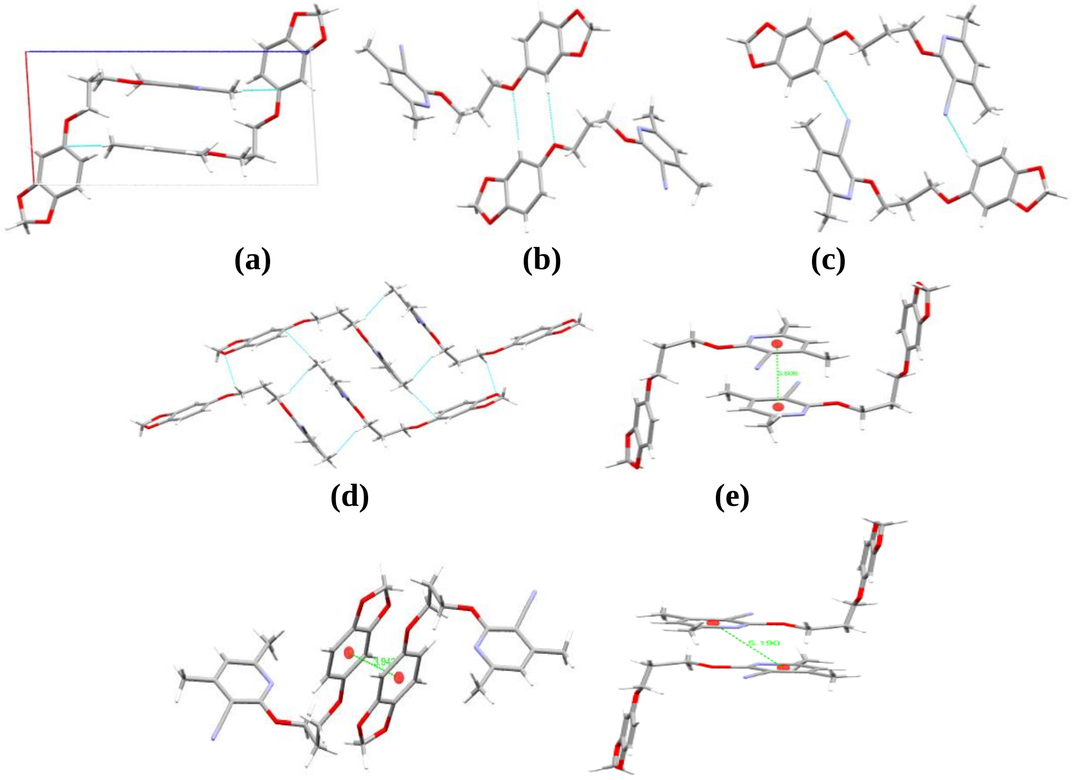

(a) **(b)** **(c)**

(d) **(e)**

(f) **(g)**

Figure 3.57: (a) Packing diagram of compound **5.2D**, (b) and (c) graph sets, (d) C-H…H and C-H…C interactions, (e), (f) and (g) π…π interactions, in compound **5.2D**

Hirshfeld surface analysis of compound 5.2D: The Hirshfeld surface mapped over the d_{norm} in the range of -0.51 to 1.44Å for compound **5.2D** is displayed in **Figure 3.58 (a) and (b)**. The region of red spots corresponds to a shorter bond length due to C-H…O, C-H…C, C-H…N, and C-H…H contacts. The intensity and size of the red color spots increase for those interactions which are more dominant and vice versa.

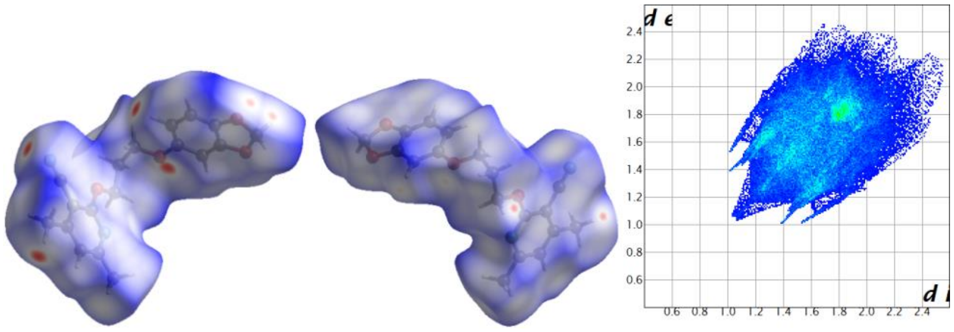

(a) **(b)** **(c)**

Figure 3.58: (a) and (b) d_{norm} both side view, (c) 2-D fingerprint plot, of compound **5.2D**

The 2-D fingerprint plot of the compound **5.2D** gives the relative percentage contributions of different non-covalent interactions to the Hirshfeld surface **(Figure 3.58 (c))**. Those interactions are H…H (48.6%), O…H (14.7%), N…H (14.1%), C...H (12.3%), C…C (5.8%), C…O (2.9%), O…O (0.4%),N…N (1.2%)and C…N (0.2%). N…H interactions appear as a pair of spoke-like patterns in the region of di + de = 2.4-2.8Å. Also, O…H interactions appear around the N…H spoke as a tiny outgrowth of spikes in the region of di + de = 2.5-2.8Å. The other pair of a spoke-like pattern at the outer region of the 2-D fingerprint plot in the region of di + de = 2.5-3.0Å corresponds to C…H contacts. The C…C contacts which contribute 5.8%, indicate the existence of $\pi...\pi$ stacking interactions.

The Hirshfeld surface mapped over the shape-index in a range of -1 to 1Å for compounds **5.2D** shows complementary red and blue triangles on the surface of the pyridine and benzodioxole rings, which indicate the presence of π…π stacking interactions **(Figure 3.59 (a) and (b))**. However, there is no evidence of yellowish-red bins on the surface of the aromatic rings. Similarly, the Hirshfeld surface mapped over the curvedness in a range of -4 to 0.4 Å for compound **5.2D** displays a flat green region with a yellowish spot around the surface of the benzodioxole and the pyridine rings, which again validates the presence of $\pi…\pi$stacking interaction **(Figure 3.59 (c) and (d))**.

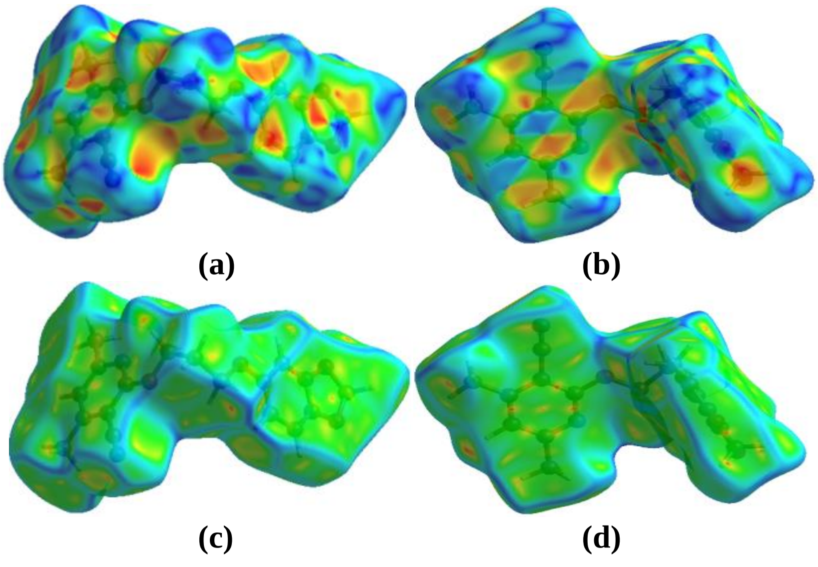

Figure 3.59: (a) and (b) Shape-index, (c) and (d) Curvedness, both side views of compound **5.2D.**

The different types of interactions found within the supramolecular framework are also found by the Hirshfeld calculations of weak interaction within a radius of 3.8Å from the single crystal fragments, as shown in **Figure 3.60**.

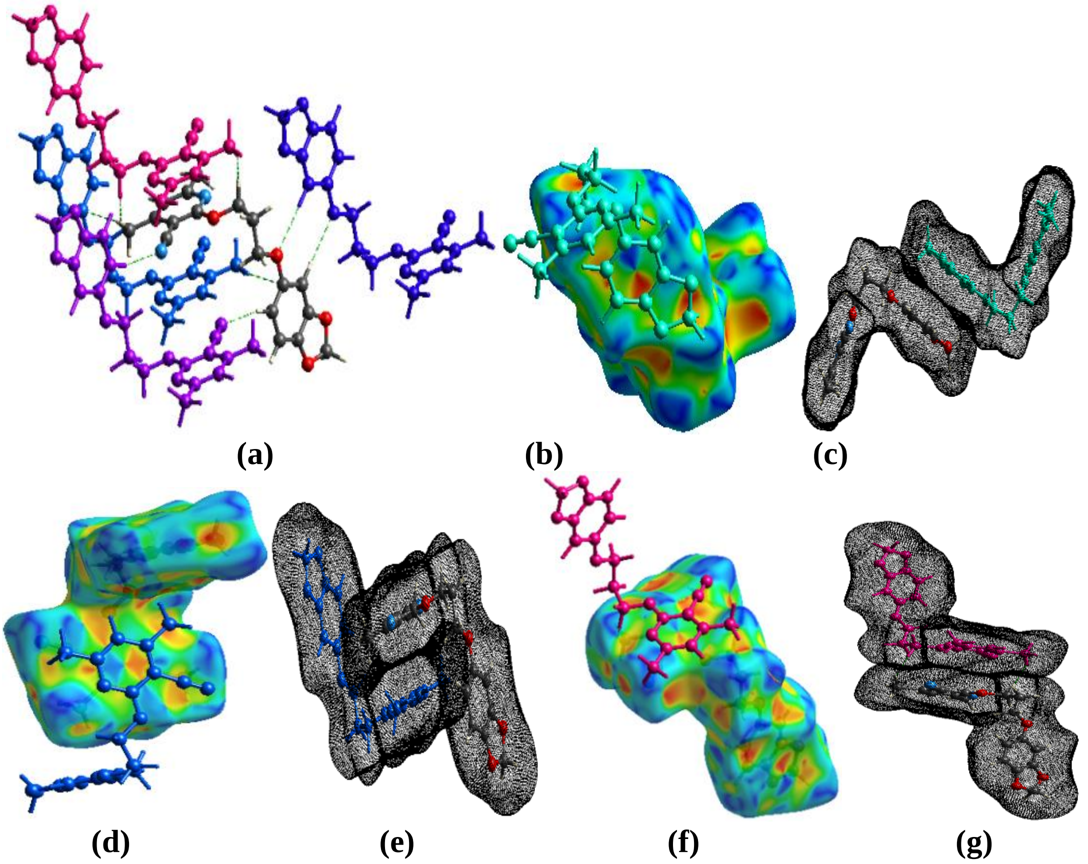
(a) (b) (c)

(d) (e) (f) (g)

Figure 3.60: (a) C-H…O, C-H…C and C-H…N interactions, (b), (c), (d), (e), (f) and (g) π…π interactions, in compound **5.2D**

3.10.1.5. Crystal analysis of compound 5.3A

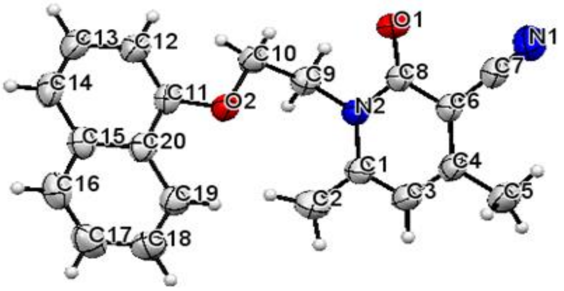

Figure 3.61: ORTEP diagram of compound **5.3A**

The compound **5.3A** was recrystallized in ethyl acetate at room temperature by slow evaporation of the solvent. The chiral asymmetric compound **5.3A** was analyzed using SC-XRD **(Figure 3.61)**. The compound crystallized with cell lengths

a = 8.911(3)Å, **b** = 7.340(2)Å, **c** = 25.204(7)Å, i.e., **a ≠ b ≠ c**, and cell angles $\boldsymbol{\alpha}$ = 90°, $\boldsymbol{\beta}$ = 90°, $\boldsymbol{\gamma}$ = 90°, i.e., $\boldsymbol{\alpha = \beta = \gamma = 90°}$. It indicates that the compound exhibits an orthorhombic crystal system, with space group $Pca2_1$ that contains four molecules per unit cell.

The crystal structure of compound **5.3A** shows that both the pyridone and the naphthalene ring are planar and aromatic. The naphthalene ring is twisted away from the plane of the pyridone ring, and it also flips in a vertical position towards the pyridone plane. The dihedral angle between the two planes is 63.95°. The crystallographic information is in **Table 3.15**.

The supramolecular framework of compound 5.3A: The crystal association of compound **5.3A** involves a strong C-H…O between the carbonyl oxygen (O1) and the alkyl hydrogen (H2B) from the pyridone ring substituents at a distance of 2.365Å. Since the carbonyl oxygen (O1) from the pyridone moiety is a bifurcated acceptor, it forms another weaker intermolecular C-H…O bond with the pyridone hydrogen (H3) at a distance of 2.668. These two C-H…O repeatedly form a network horizontally along the plane of the pyridone ring, which results in the formation of a layer of sheets. The two C-H…O interactions found for this bifurcated acceptor (O2) also give the $R_2^1(6)$ graph set **(Figure 3.62 (b))**. The methylene linker's hydrogen H9B and H10B interact with the pyridone ring carbon (C8) and the naphthalene ring carbon (C20) to form C-H…C non-covalent interaction at a distance of 2.894Å and 2.842Å respectively. This two C-H…C interactions act as interlayer connectivity between the sheets and the stabilizing forces within the crystal packing, and the molecules are piled up over one another in ABAB orientation **(Figure 3.62 (c))**. Due to these C-H…C interactions, the two hydrogen's H9B and H10B have sufficient distance to interact with the pyridone ring and the naphthalene ring having an interaction distance of 2.839Å and 3.309Å, respectively. In addition to these, the hydrogen (H12) from the naphthalene ring also forms C-H…π intermolecular interaction with the naphthalene ring at a distance of 3.041Å, which facilitate in stabilizing the crystal packing. The supramolecular structure of **5.3A** also displays C-H…π intermolecular interaction between the hydrogen (H17) of the naphthalene ring with the other side of the naphthalene ring plane at a distance of

3.033Å **Figure 3.62 (d)**. Similarly, nitrogen (N1) of the cyano group also forms intermolecular lone pair…π interaction on the other side of the pyridone ring plane where C-H…π interaction is found (**Figure 3.62 (d))**. Thus, the overall molecular association of compound **5.3A** displays intermolecular C-H…O, C-H…C, C-H…π, and N…π (lone pair…π) interactions within its zig-zag pattern of molecular arrangement. The interactions are given in **Table 3.17**.

Table 3.17: Hydrogen bonds and other interactions in compound **5.3A**

Donor-H...Acceptor	**D–H, Å**	**H...A, Å**	**D...A, Å**	**D -H...A, °**
C2-H2B…O1	0.960	2.365	3.307	167.04
C3-H3…O1	0.930	2.668	3.494	148.40
C9-H9B…C8	0.970	2.894	3.378	111.91
C10-H10B…C20	0.970	2.842	3.806	172.66
C9-H9B…π(N2,C1,C3,C4,C6,C8)	0.970	2.839	3.639	140.33
C10-H10B…π(C11-C15,C20)	0.970	3.309	4.242	162.01
C12-H12…π(C15-C20)	0.930	3.041	3.821	142.56
C17-H17…π(C11-C15,C20)	0.930	3.033	3.817	143.04
Other contact				
N1…π(N2,C1,C3,C4,C6,C8)		3.372		
Intramolecular				
C2-H2A…O2	0.960	2.628	3.351	132.36
C9-H9A…O2	0.970	2.593	2.385	66.90
C10-H10A…O1	0.970	2.627	3.114	111.31
C9-H9B…O1	0.970	2.412	2.655	93.55

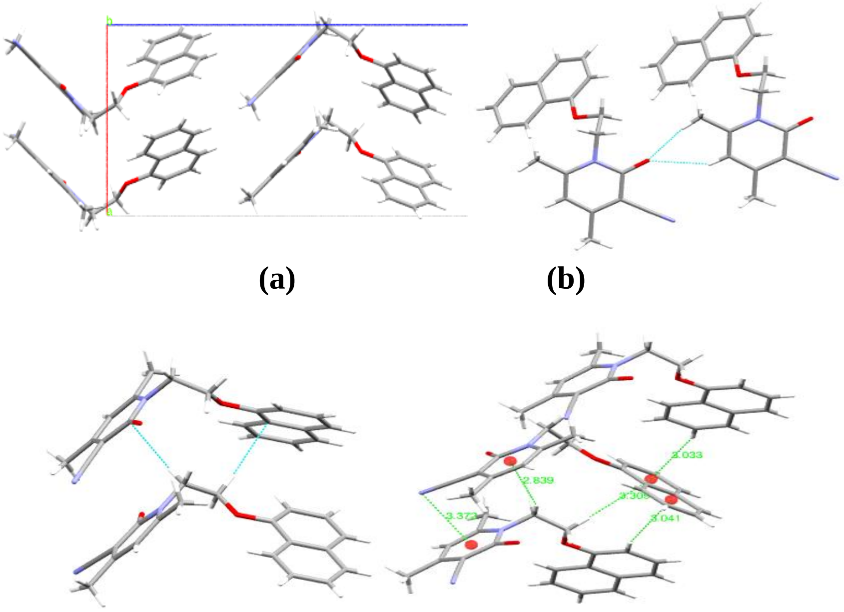

Figure 3.62: (a) Packing diagram of **5.3A**, (b) graph set in **5.3A**, (c) C-H…C interactions, and (d) Lone pair…π and C-H…π interactions

Hirshfeld surface analysis of compound 5.3A: The Hirshfeld surface mapped over the d_{norm} in the range of -0.27 to 1.37Å for compound **5.3A** is displayed in **Figure 3.63 (a) and (b)**. The region of bright red spots corresponds to a shorter bond length due to C-H…O contact. The other non-covalent intermolecular C-H…O and C-H…C interactions with longer bond lengths also appear as lighter red color spots.

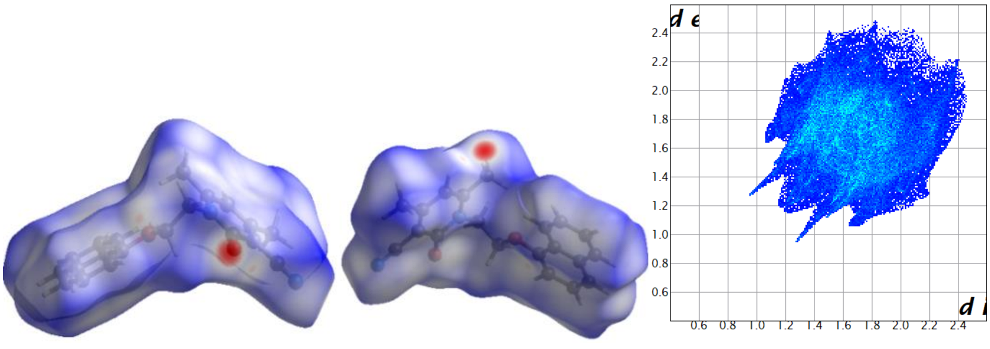

(a) **(b)** **(c)**

Figure 3.63: (a) and (b) d_{norm} both side view, (c) 2-D fingerprint plot, of compound **5.3A**

The relative percentage contributions of non-covalent interaction to the Hirshfeld surface are summarized by the 2-D fingerprint plot of compound **5.3A (Figure 3.63 (c))**. Those are H…H (43.8%), C...H (28.7%), N…H (11.4%), O…H (10.1%), C…N (3.4%), C…C (2.5%) and C…O (0.1%). The spoke-like pattern in the region of di + de = 2.2-2.8Å represents O…H interactions. N…H interaction also appears as a tiny spike in the region of di + de = 2.6-3.2Å. The presence of C-H...π merge within the C…H contacts in the region of di + de = 2.7-3.6Å also appears as a characteristic wing-like pattern. The C…N contacts which contribute 3.4%, also represent the lone pair…π interaction between the nitrogen (N1) of the cyano group with the pyridone ring.

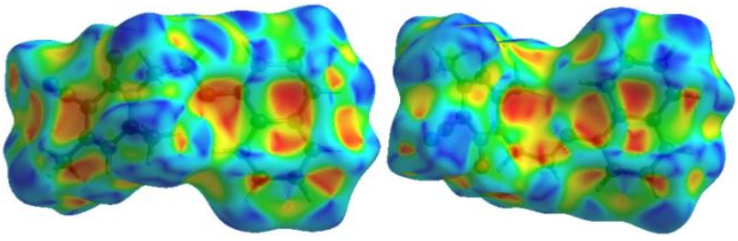

(a) **(b)**

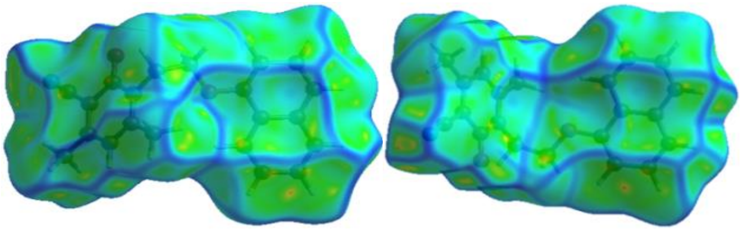
(c) (d)

Figure 3.64: (a) and (b) Shape-index, (c) and (d) Curvedness, both side views of compound **5.3A**

The red and blue color in the shape-index indicates the acceptor and donor property, respectively. The Hirshfeld surface mapped over the shape-index in a range of -1 to 1Å for compound **5.3A** shows yellowish-red colored concave regions around the surface of the naphthalene and pyridone rings represent the acceptor region. It represents C-H...π interactions **(Figure 3.64 (a) and (b))**. The absence of a complementary pair of red and blue triangles around the two aromatic ring surfaces signifies the lack of significant π...π stacking interaction between the aromatic rings. Similarly, the Hirshfeld surface mapped over the curvedness in a range of -4 to 0.4 Å for compound **5.3A** have no flat green region with a yellowish spot around the naphthalene and the pyridone ring surfaces. It indicates the absence of π…π stacking interaction **(Figure 3.64 (c) and (d))**.

The weak non-covalent interactions found in the supramolecular framework of compound **5.3A** are also supported by the Hirshfeld calculation of weak interactions within the cluster of 3.8Å radius from a single crystals fragment. However, C-H…N intermolecular interactions from the Hirshfeld interactions as shown in **Figure 3.65**.

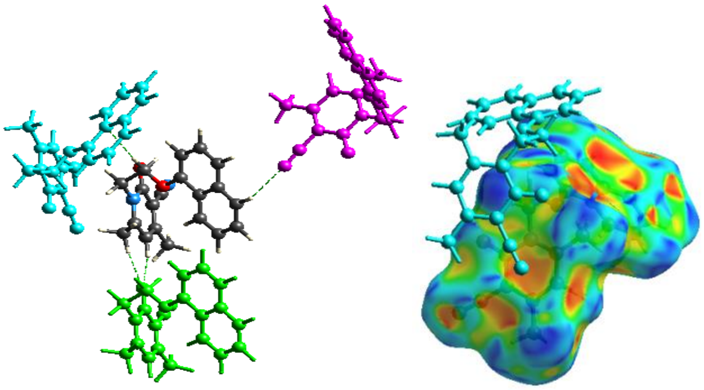
(a) (b)

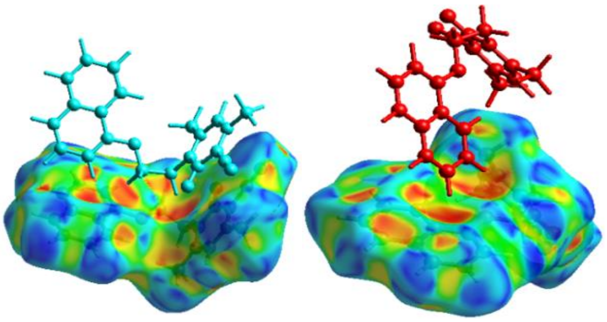

(c) **(d)**

Figure 3.65: (a) C-H…O, C-H…C and C-H…N interactions, (b) Lone pair…π and C-H…π interactions, (c) and (d) C-H…π interactions, in compound **5.3A**

3.10.1.6. Crystal analysis of compound 5.3B

The compound **5.3B** was recrystallized in ethyl acetate at room temperature by slow evaporation of the solvent. The chiral asymmetric compound **5.3B** was analyzed using SC-XRD **(Figure 3.66)**. The compound crystallized with cell lengths **a** = 15.0512(4)Å, **b** = 12.6307(4)Å, **c** = 8.5290(3)Å, i.e. $\mathbf{a} \neq \mathbf{b} \neq \mathbf{c}$ and cell angles $\boldsymbol{\alpha}$ = 90°, $\boldsymbol{\beta}$ = 91.810(2)°, $\boldsymbol{\gamma}$ = 90°, i.e. $\boldsymbol{\alpha = \gamma = 90°}$, $\boldsymbol{\beta \neq 90°}$. It indicates that the compound exhibits a monoclinic crystal system, with space group P 2_1/c that contains four molecules per unit cell.

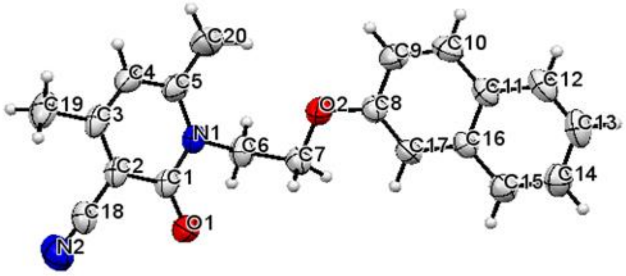

Figure 3.66: ORTEP diagram of compound **5.3B**

The crystal structure of compound **5.3B** shows that both the pyridone and the naphthalene ring are planar and aromatic. The naphthalene ring flips towards the parent pyridine ring, and the dihedral angle between the two planes is 55.70°. The crystallographic information is in **Table 3.15**.

The supramolecular framework of compound 5.3B: The study of the molecular association of compound **5.3B** shows the existence of C-H…O and C-H…N intermolecular interactions that have an interaction distance of 2.696Å and 2.708Å respectively. The C-H…O interaction arises between the hydrogen (H12) from the naphthalene ring and the oxygen (O1) from the pyridone ring. Also, the C-H…N interaction arises between the hydrogen (H19B) from the alkyl substituent of the pyridone ring and the nitrogen (N2) of the cyano group. An extensive network of C-H…O and C-H…N intermolecular interactions also lead to the formation of a layer of sheets that appear as a zig-zag pattern which also establishes a graph set notation of R_4^4(38) (**Figure 3.67 (b))**. The hydrogen (H6A) interacts with the carbon (C15) and (C16) of the naphthalene ring. It forms C-H…C interactions at a distance of 2.810Å and 2.893Å, respectively, which serve as interconnectivity between different layers of sheets **(Figure 3.67 (c))**. These C-H…C and C-H…O interactions stabilizes the crystal packing within the unit cell

Moreover, the packing diagram of compound **5.3B** also shows C-H…π interactions on both sides of the naphthalene ring surface where the linker hydrogen (H6A) and (H6B) interacts with the naphthalene ring p-orbital from the same side at a distance of 2.719Å and 2.791Å respectively. The naphthalene hydrogen (H9) and (H10) interact with the naphthalene p-orbital on the other side at a distance of 3.248Å and 2.802Å, respectively. Beyond these interactions, the C-H…π intermolecular interactions between the hydrogen (H20B) from the alkyl substituent of the pyridone ring and the pyridone ring p-orbitals at an interaction distance of 2.969Å also strengthen the stability of the packing **(Figure 3.67 (d) and (e))**. Since the carbon (C18) is partially positive according to the Lewis acidity concept, it also forms cation…π interaction with the pyridone ring, which has an interaction distance of 3.459Å **(Figure 3.67 (f))**. The non-covalent hydrogen bonding and other interactions are given in **Table 3.18**.

Table 3.18: Hydrogen bonds and other interactions in compound **5.3B**

Donor-H...Acceptor	**D – H, Å**	**H...A, Å**	**D...A, Å**	**D - H...A, º**
C19-H19B…N2	0.960	2.708	3.590	153.01
C12-H12…O1	0.930	2.696	3.595	162.79
C6-H6A…C15	0.970	2.810	3.687	150.76
C6-H6A…C16	0.970	2.893	3.520	123.24
C6-H6A…π(C11-C16)	0.970	2.719	3.380	125.85
C7-H7B…π(C8-C11, C16, C17)	0.970	2.791	3.604	141.91
C9-H9…π(C8-C11, C16, C17)	0.930	3.248	3.887	127.63
C10-H10…π(C11-C16)	0.930	2.802	3.528	135.73
C20-H20B…π(C1-C5, N1)	0.960	2.969	3.702	134.14

Other contacts				
C18…π(C1-C5, N1)		3.459		
Intramolecular				
C6-H6A…O2	0.970	2.483	2.370	71.95
C6-H6B…O1	0.970	2.360	2.646	96.15
C7-H7A…O1	0.970	2.714	3.160	108.61
C20-H20A…O2	0.960	2.413	3.196	138.56

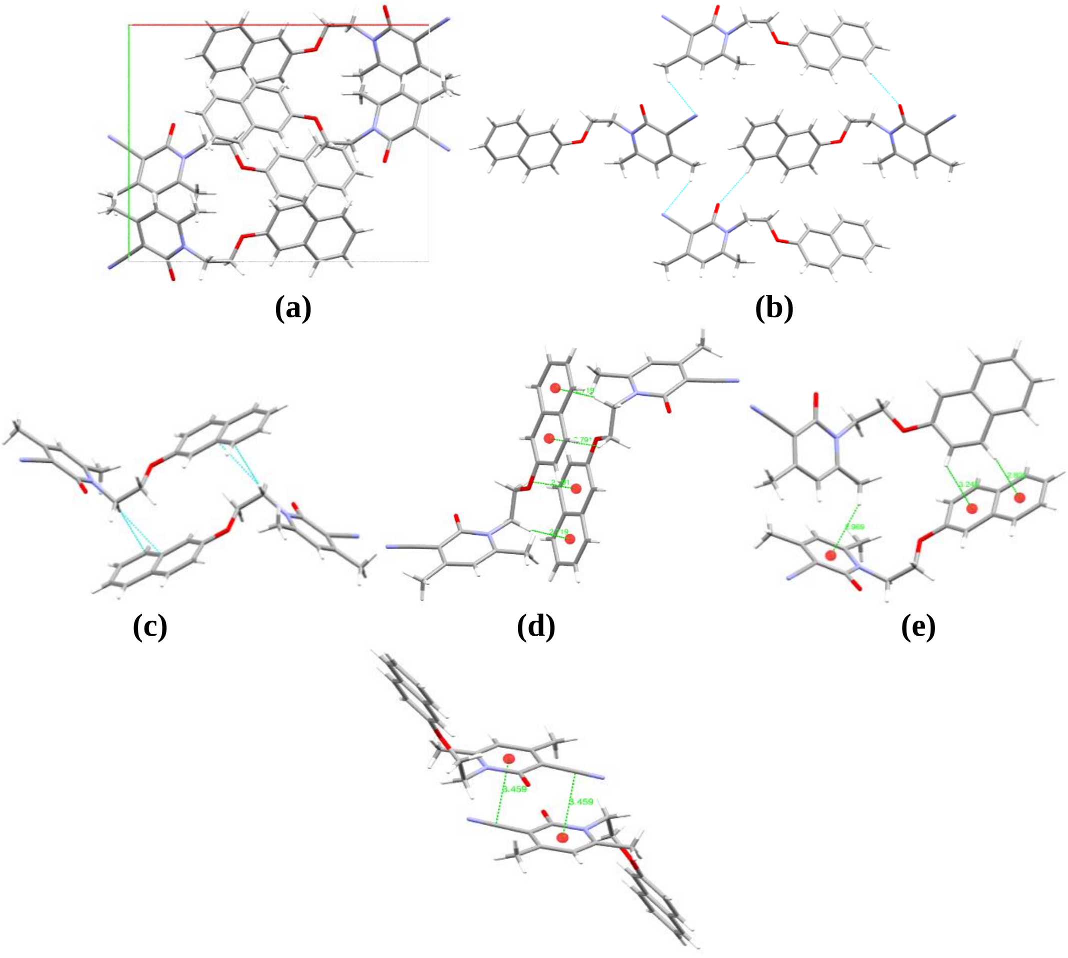

(a) (b)

(c) (d) (e)

(f)

Figure 3.67: (a) Packing diagram of compound **5.3B**, (b) graph set, (c) C-H…C, (d) and (e) C-H…π interactions and (f) Cation…π interaction, in compound **5.3B**

Hirshfeld surface analysis of compound 5.3B: The Hirshfeld surface mapped over the d_{norm} in the range of -0.05 to 1.20Å for compound **5.3B**is displayed in **Figure 3.68 (a) and (b)**. The region of bright red spots corresponds to a shorter bond length due to C-H…N, C-H…O, and C-H…C contacts. The intensity of the red color and the size of the spots depends on interaction distance. The more dominant the interaction, the more intense red color and the larger the size of the spots.

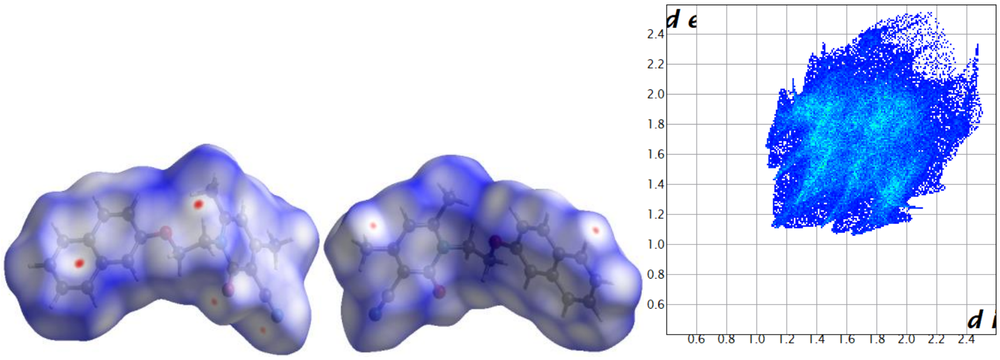

(a) **(b)** **(c)**

Figure 3.68: (a) and (b) d_{norm} both side view, (c) 2-D fingerprint plot, of compound **5.3B**

The relative percentage contributions of non-covalent interaction to the Hirshfeld surface are summarized by the 2-D fingerprint plot of compound **5.3B (Figure 3.68 (c))**. Those are H…H (42.6%), C...H (30.0%), N…H (10.6%), O…H (10.5%), C…C (2.4%),C…N (2.4%),N…N (1.0%) and C…O (0.4%) . The O…H interactions appear as a tiny spindle shape pattern in the region of di + de = 2.5-2.8Å. N…H interaction also appears as a pair of a tiny thick spike in the region of di + de = 2.6-3.2Å. The C-H...π and C…H contacts also appear as two pairs of hook-like patterns in the region of di + de = 2.7-3.6Å. The C…C contacts contributing 2.4%, does not reflect any π...π stacking interactions. However, it indicates the cation…π interaction between the nitrile carbon and the pyridine ring.

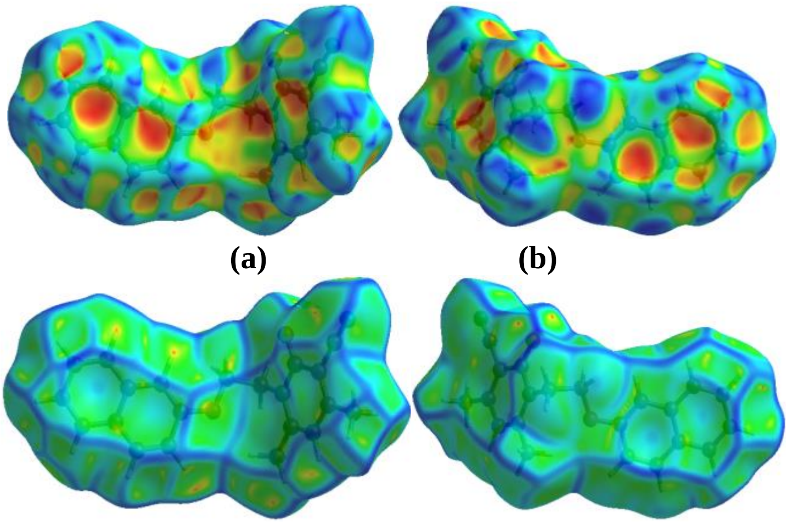

(a) **(b)**

(c) **(d)**

Figure 3.69: (a) and (b) Shape-index, (c) and (d) Curvedness, both side views of compound **5.3B**

The Hirshfeld shape-index in a range of -1 to 1Å for compound **5.3B** shows yellowish-red colored concave regions around the surface of the naphthalene and the pyridine rings, which represents the acceptor region where C-H...π interactions occur **(Figure 3.69 (a) and (b))**. Similarly, the pyridine ring also displays an additional yellowish-red concave region on its surface, reflecting the cation…π interaction **(Figure 3.69 (b))**. The absence of blue and red triangles around the surface of the aromatic rings indicates the absence of π…π stacking interaction. Similarly, the Hirshfeld surface mapped over the curvedness in a range of -4 to 0.4 Å for compound **5.3B** does not have a flat green region with a yellowish spot around the naphthalene ring and the pyridone ring surfaces. It reveals the absence of π…π stacking interaction **(Figure 3.69 (c) and (d))**.

The C-H…N, C-H…O, C-H…C, C-H…π and cation…π interactions found in the supramolecular framework of compound **5.3B** are supported by the Hirshfeld calculation of weak interactions within the cluster of 3.8Å radius from a single crystals fragment as shown in **Figure 3.70**.

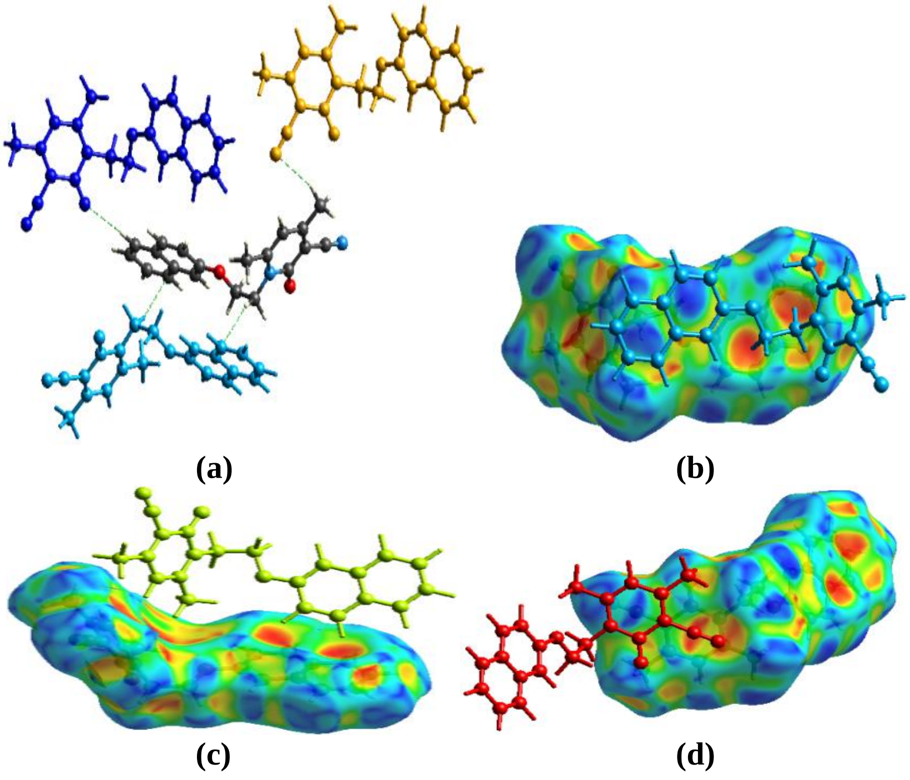
(a) **(b)**

(c) **(d)**

Figure 3.70: (a) C-H…N, C-H…O, and C-H…C interactions, (b) and (c) C-H…π interactions, and (d) Cation…π interaction in compound **5.3B**

3.10.1.7. Crystal analysis of compound 5.3D

The compound **5.3D** was recrystallized in ethyl acetate at room temperature by slow evaporation of the solvent. The chiral asymmetric compound **5.3D** was analyzed using SC-XRD **(Figure 3.71)**. The compound crystallized with cell lengths **a** = 6.9770(2)Å, **b** = 30.8178(10)Å, **c** = 7.6575(3)Å, i.e., $\mathbf{a} \neq \mathbf{b} \neq \mathbf{c}$ and cell angles $\boldsymbol{\alpha}$ = 90°, $\boldsymbol{\beta}$ = 101.449(3)°, $\boldsymbol{\gamma}$ = 90°, i.e., $\boldsymbol{\alpha = \gamma = 90°}$, $\boldsymbol{\beta \neq 90°}$. It indicates that the compound exhibits a monoclinic crystal system, with space group P 2_1/c containing four molecules per unit cell.

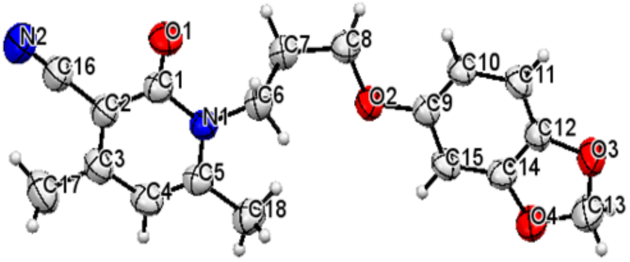

Figure 3.71: ORTEP diagram of compound**5.3D**

The crystal structure of compound **5.3D** shows that both the pyridone and the benzodioxole rings are planar and aromatic. The benzodioxole ring and the linker atoms (O2), (C8) and (C7) lie on the same plane, and also the pyridone ring and the linker atom (C6) also lie on the same plane. Maximum flexibility of the compound is achieved through the linker carbon (C6) and (C7) atoms. The dihedral angle between the planes of the two rings is 2.98°. The crystallographic information is in **Table 3.19**.

Table 3.19: Crystal data on compound **5.3D**

Compound	5.3D
Identification code	2170477
Empirical formula	$C_{18}H_{18}N_2O_4$
Formula weight	326.34
Temperature(K)	293(2)
Crystal system	Monoclinic
Space group	$P2_1/c$
a(Å)	6.9770(2)
b(Å)	30.8178(10)
c(Å)	7.6575(3)
α(°)	90
β(°)	101.449(3)
γ(°)	90
Volume(Å^3)	1613.71(10)
Z	4

ρ (g/cm^3)	1.343
μ(mm^{-1})	0.096
F(000)	688.0
Crystal size(mm^3)	0.24 × 0.23 × 0.21
Radiation	MoKα (λ = 0.71073)
2Θ range for data collection(°)	6.518 to 54.784
Index ranges	$-8 \leq h \leq 8$, $-30 \leq k \leq 39$, $-9 \leq l \leq 9$
Reflections collected	12724
Independent reflections	3424
Data/restraints/parameters	3424/0/219
Goodness-of-fit on F^2	1.095
Final R indexes [I>=2σ (I)]	R_1 = 0.0470, wR_2 = 0.1192
Final R indexes [all data]	R_1 = 0.0674, wR_2 = 0.1306
Largest diff. peak/hole / e Å^{-3}	0.16/-0.20

The supramolecular framework of compound 5.3D: The molecular association of compound **5.3D** involves C-H…O interactions between the molecules. The oxygen (O1) from the pyridone ring acts as a trifurcated acceptor. It interacts with the linker hydrogen (H8B) and the benzodioxole ring hydrogen (H10) with an interaction distance of 2.626Å and 2.424Å respectively, giving $R_2^1(7)$ and $R_2^2(14)$ graph sets **(Figure 3.72 (b))**. The oxygen (O4) from the benzodioxole ring and the hydrogen (H4) from the pyridone ring forms C-H…O interactions at a distance of 2.623Å which results in the formation of the $R_2^2(24)$ graph set **(Figure 3.72 (b))**. Also, the oxygen (O3) from the benzodioxole ring interacts with the alkyl hydrogen (H17C) and forms C-H…O interaction at a distance of 2.579Å. This C-H…O interaction, along with the other C-H…O interactions which have an interaction distance of 2.424Å and 2.623Å involving four molecules of compound **5.3D**, also forms a graph set notation of $R_4^4(19)$ **(Figure 3.72 (b))**. The extensive network of compounds through these C-H…O interactions also forms a polymeric layer of sheets. The different layers of sheets are interconnected by the C-H…O interaction between the alkyl hydrogen (H18C) and the trifurcated acceptor (O1) at a distance of 2.612Å. C-H…O interaction having a distance of 2.579Å, and π...π stacking interaction between the pyridone ring and the benzodioxole ring at a distance of 3.888Å, stabilizes the packing of the crystal within the unit cell **(Figure 3.72 (c))**. The molecular aggregations of compound **5.3D** also exhibit one more π…π stacking interaction at the other side of the plane between the pyridone ring and the benzodioxole ring at a distance of 3.781Å **(Figure 3.72 (d))**. The weak interactions found within the supramolecular framework are given in **Table 3.20**.

Table 3.20: Hydrogen bonds and other interactions in compound **5.3D**

Donor-H...Acceptor	**D – H, Å**	**H...A, Å**	**D...A, Å**	**D - H...A, º**
C8-H8B…O1	0.970	2.626	3.342	130.88
C10-H10…O1	0.930	2.424	3.333	165.52
C4-H4…O4	0.930	2.623	3.488	154.95
C17-H17C…O3	0.960	2.579	3.263	128.30
C18-H18C…O1	0.960	2.612	3.281	127.02
Other contacts				
π(C9-C12,C14,C15)… π(C1-C5,N1)		3.888		
π(C9-C12,C14,C15)… π(C1-C5,N1)		3.781		
Intramolecular				
C6-H6B…O1	0.970	2.359	2.662	97.31
C6-H6A…O2	0.970	2.577	2.965	103.96
C7-H7B…O1	0.970	2.839	3.237	105.51
C7-H7A…O2	0.970	2.448	2.345	72.38
C18-H18A…O2	0.960	2.933	3.743	142.80

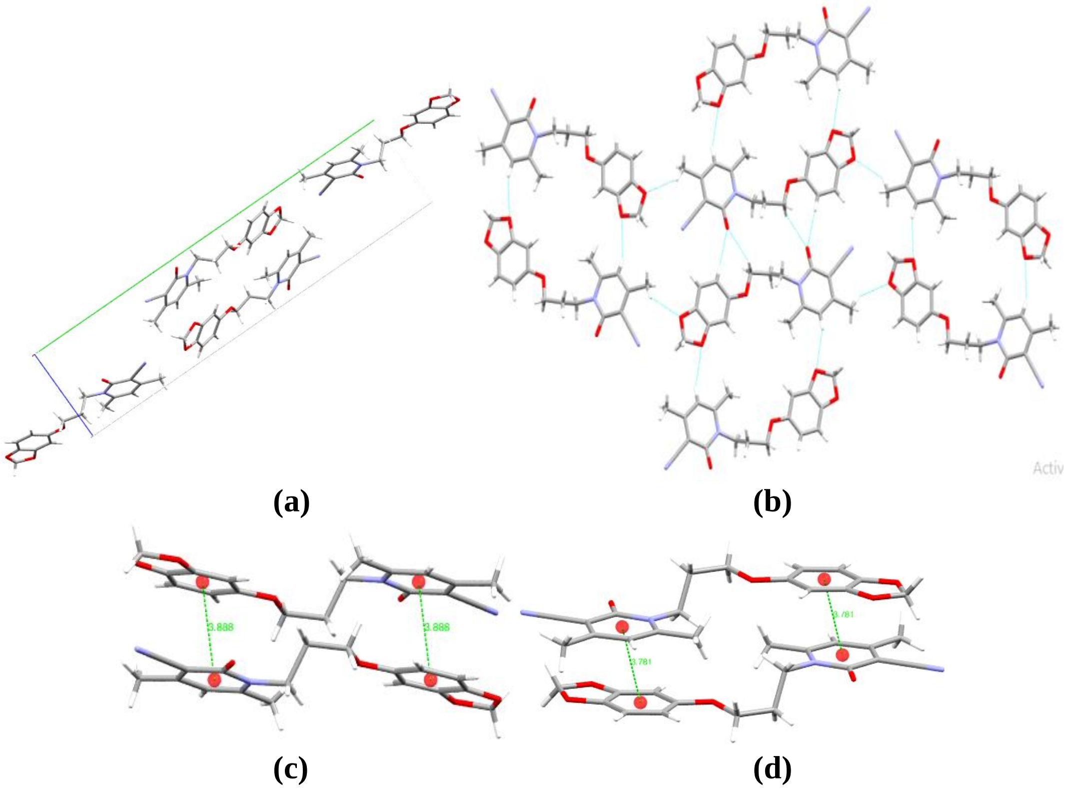

(a) **(b)**

(c) **(d)**

Figure 3.72: (a) Packing diagram of compound **5.3D**, (b) graph sets, (c) and (d) π…π interactions, in compound **5.3D**

Hirshfeld surface analysis of compound 5.3D: The Hirshfeld surface mapped over the d_{norm} in the range of -0.51 to 1.44Å for compound **5.3D** is displayed in **Figure 3.73 (a) and (b)**. The region of red spots corresponds to a shorter bond length due to C-H…O contacts. The intensity and size of the red color spots increase for those interactions which are more dominant and vice versa.

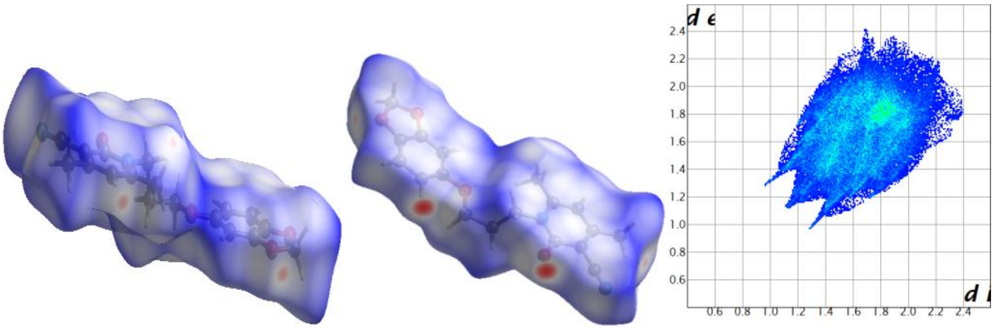

(a) **(b)** **(c)**

Figure 3.73: (a) and (b) d_{norm} both side view, (c) 2-D fingerprint plot, of compound **5.3D**

The 2-D fingerprint plot of the compound **5.3D** gives the relative percentage contributions of different non-covalent interactions to the Hirshfeld surface **(Figure 3.73 (c))**. Those interactions are H…H (44.0%), O…H (19.6%), N…H (13.8%), C...H (11.1%), C…C (6.3%), C…O (3.6%), C…N (1.2%), O…O (0.2%) and O…N (0.2%). A pair of spoke-like patterns in the region of di + de = 2.3-2.8Å corresponds to O…H interactions. The C…C contacts which account for 6.3%, indicate the presence of π...π stacking interactions.

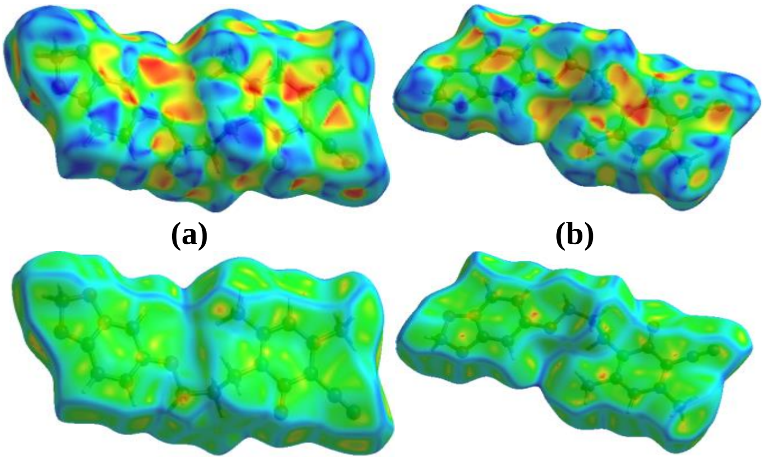

(a) **(b)**

(c) **(d)**

Figure 3.74: (a) and (b) Shape-index, (c) and (d) Curvedness, both side views of compound **5.3D**

The Hirshfeld surface mapped over the shape-index in a range of -1 to 1Å for compound **5.3D** shows complementary red and blue triangles on the surface of the pyridone and benzodioxole rings. It indicates the presence of π…π stacking interactions **(Figure 3.74 (a) and (b))**. However, there is no evidence of yellowish-red bins on the surface of the aromatic rings. Similarly, the Hirshfeld surface mapped over the curvedness in a range of -4 to 0.4 Å for compound **5.3D** displays a flat green region with a yellowish spot around the surface of the benzodioxole and the pyridone rings. It confirms the presence of π…π stacking interaction **(Figure 3.74 (c) and (d))**.

The different types of interactions found within the supramolecular framework are also found by the Hirshfeld calculations of weak interaction within a radius of 3.8Å from the single crystal fragments, as shown in **Figure 3.75**.

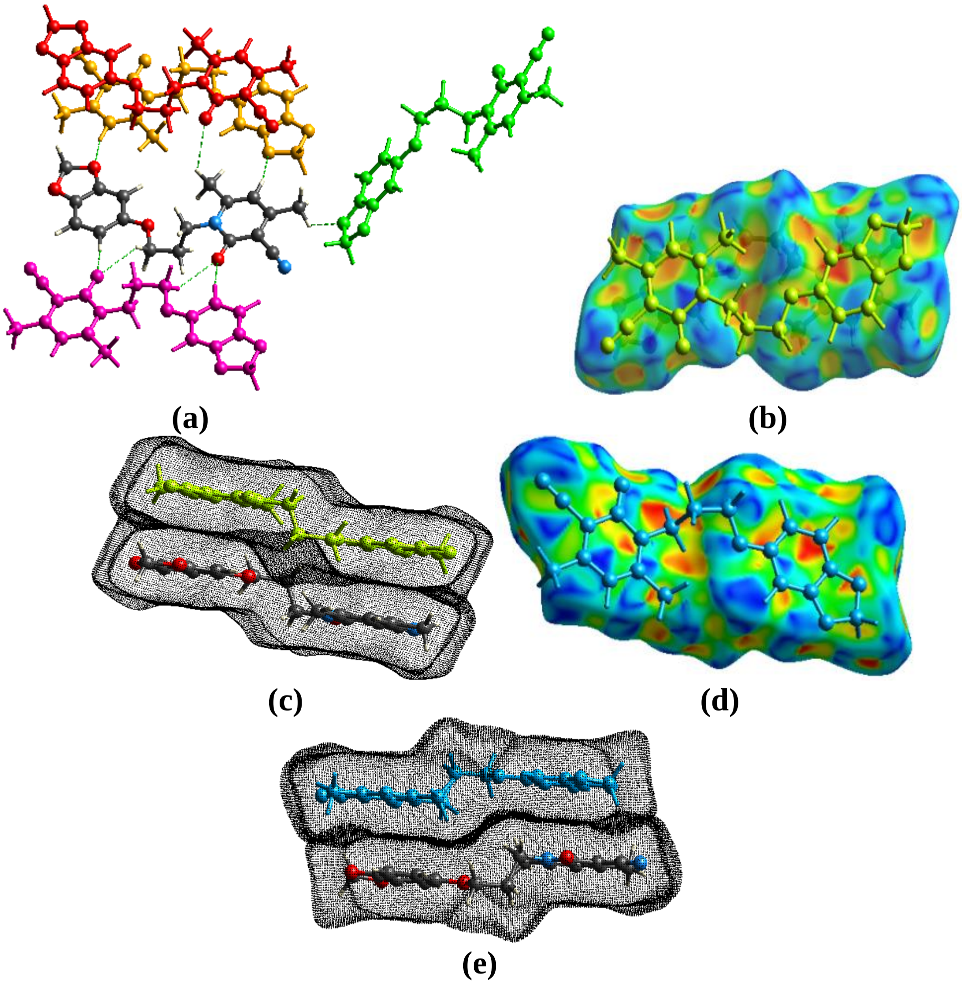

Figure 3.75: (a) C-H…O interactions, (b), (c), (d) and (e) π…π interactions, in compound **5.3D**

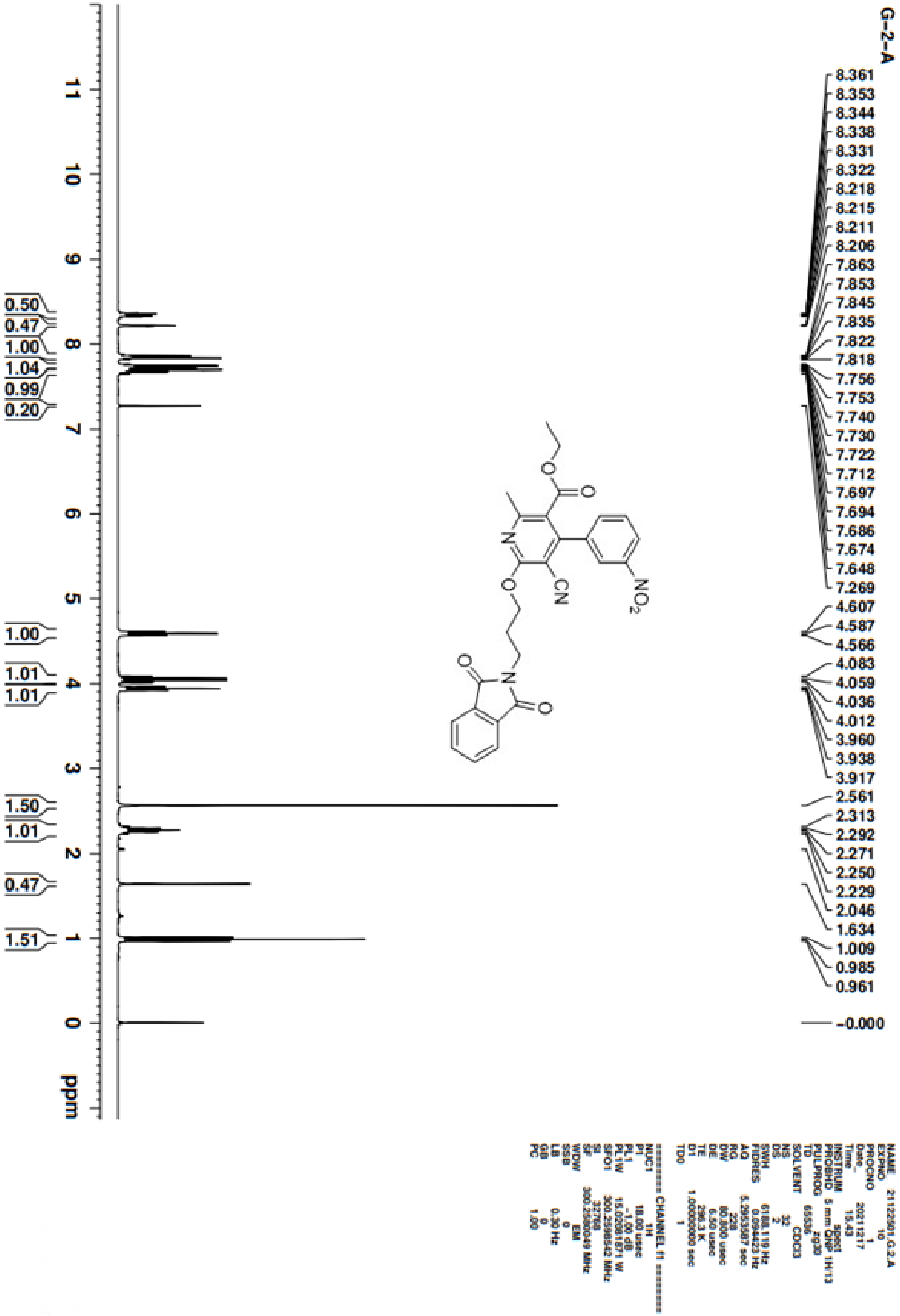

Figure 3.76: ^{1}H NMR spectra of compound **4.1A**

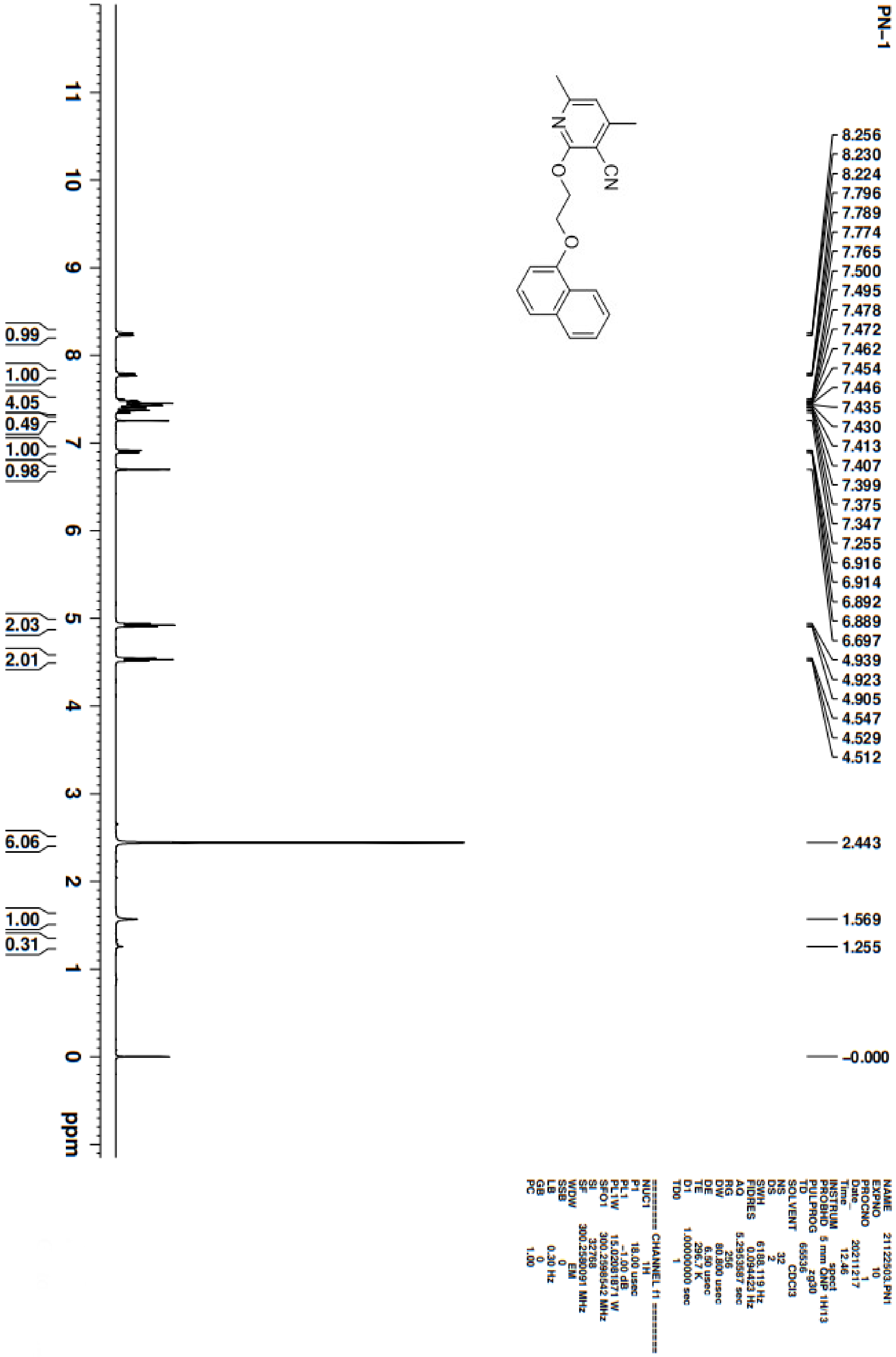

Figure 3.77: ^{1}H NMR spectra of compound **5.2A**

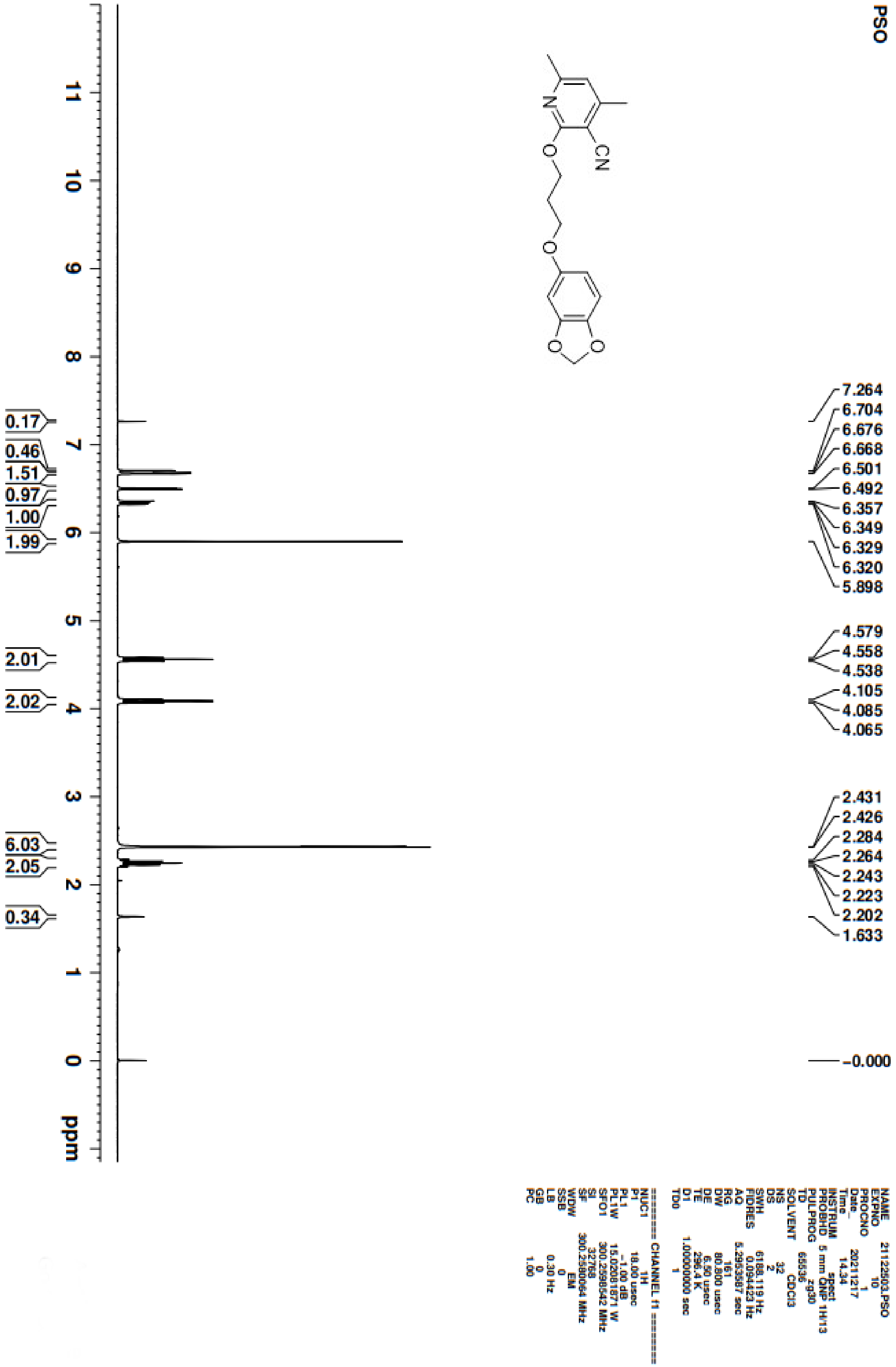

Figure 3.78: ^{1}H NMR spectra of compound **5.2D**

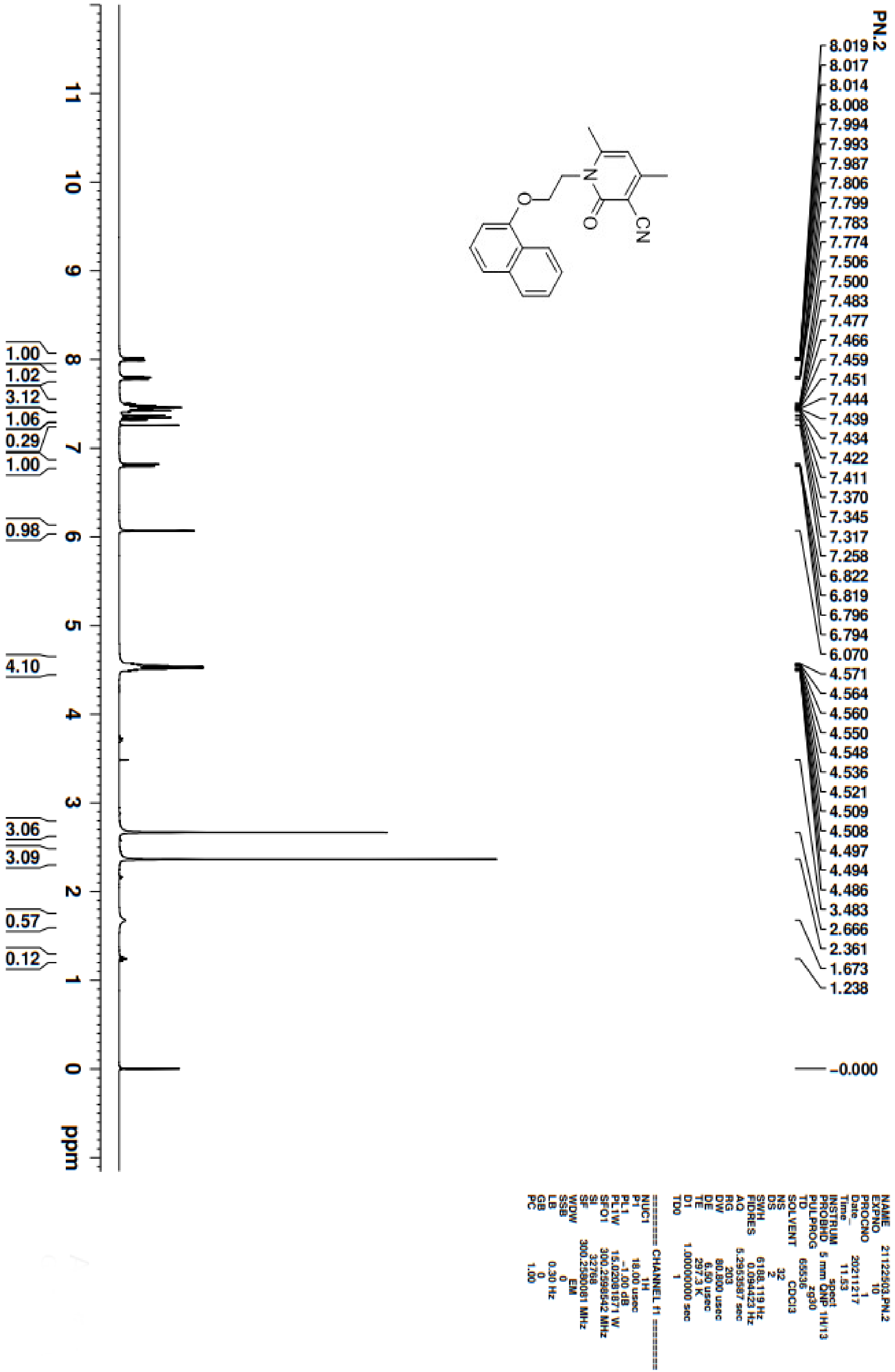

Figure 3.79: ^{1}H NMR spectra of compound **5.3A**

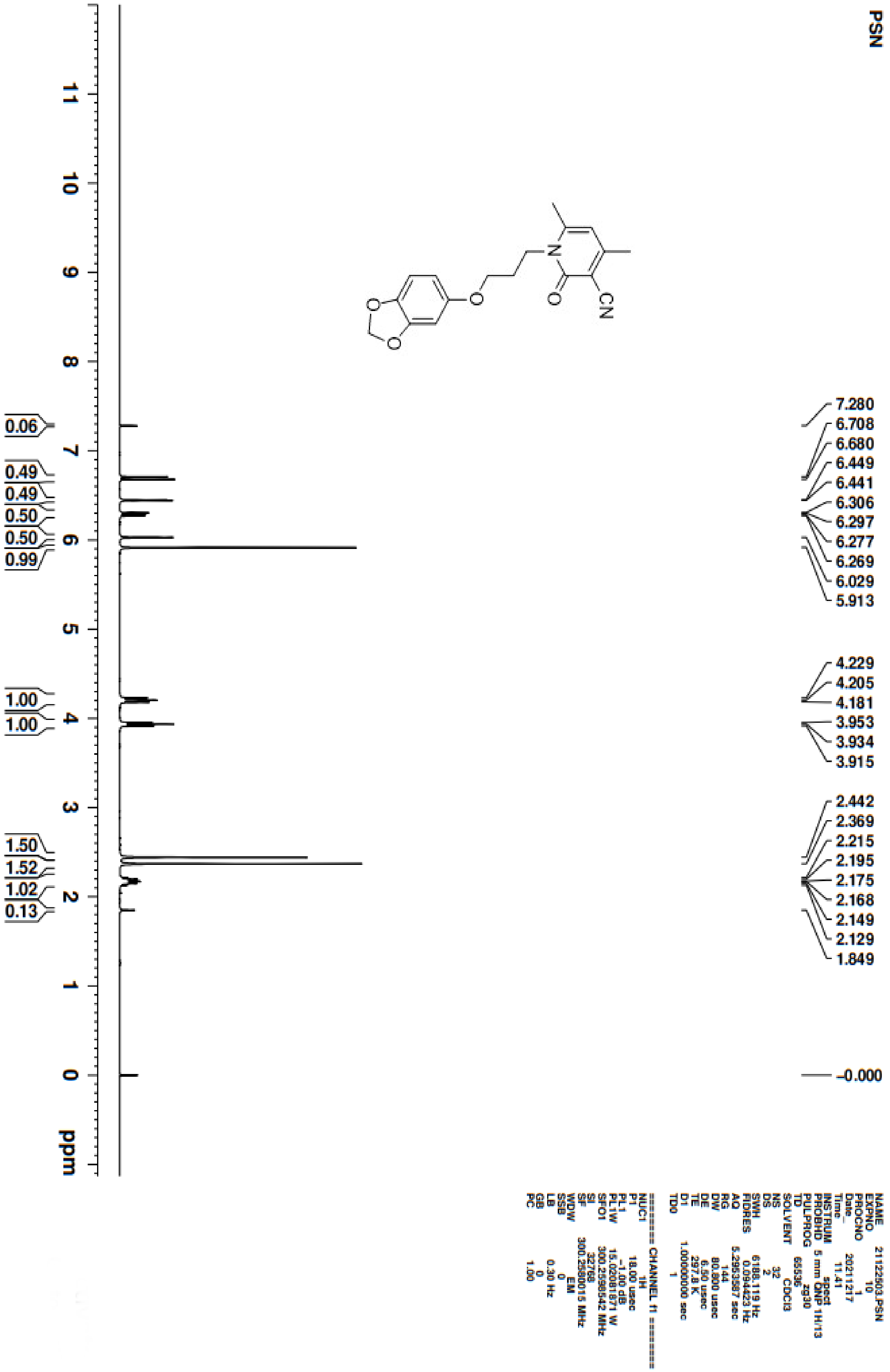

Figure 3.80: ^{1}H NMR spectra of compound **5.3D**

CHAPTER 4

BIOLOGICAL STUDY OF HETERO-POLYCYCLIC/POLYCYCLIC AROMATIC SYSTEMS BY *IN SILICO* ANALYSIS

4.1. Introduction

Cancer is the second leading cause of death worldwide, accounting for nearly 10 million deaths in 2020. The American Institute for Cancer Research reported an estimated number of 18.1 million cancer cases around the world in 2020. India ranks third among nations with the highest number of cancers (Coelho, 2012). As per the National Cancer Registry Program report, over 13 lakh people in India suffer from cancers every year. Sedentary lifestyles increase urban pollution. In addition to the rise in obesity, tobacco and alcohol consumption are the reasons behind the rise. The Indian Council of Medical Research (ICMR) estimates that there will be a 12 percent rise in cancer cases in India in the next five years. The most common forms of cancer affecting the people of India are breast cancer, cervical cancer, and oral cancer.

Cancer is a disease in which some of the body's cells grow uncontrollably and spread to other parts of the body. Cancer-causing natural exposures incorporate substances, for example, the synthetic concoctions in tobacco smoke, and radiation, for example, UV Rays from the sun, all cell development with the possibility to attack or spread to different parts of the body (Orlando et al., 2014). Cancer is caused by changes (mutations) to the DNA within cells. The DNA inside a cell is packaged into a large number of individual genes, each of which contains a set of instructions telling the cell what functions to perform and how to grow and divide. Errors in the instructions can cause the cell to stop its normal function and may allow a cell to become cancerous. Treatment differs as indicated by the sort and phase of the tumor. Most treatments are intended to fit the individual patient's illness. Be that as it may, most medications incorporate no less than one of the accompanying and may incorporate all: medical procedure, chemotherapy, and radiation treatment.

4.2. Role of enzymes in inducing cancer

Scientists have discovered a previously unknown ability in some enzymes that can cause cancer to spread if they are unbalanced. The discovery of this function may be crucial to more effective treatment. Enzymes that can contribute to the spread of cancer are more advanced than we used to think. Cancer is currently being treated based on the assumption that the enzymes should be prevented from cleaving the next substance in a chain. It is done to prevent a chain reaction that would trigger cancer to spread.

4.2.1. COX-2: COX-2 is an enzyme that speeds up the formation of substances that cause inflammation and pain. It may also cause tumor cells to grow. Some tumors have high levels of COX-2, and blocking its activity may reduce tumor growth. COX-2 is often expressed in many types of cancers, exerting a pleiotropic and multifaceted role in the genesis or boosting carcinogenesis and cancer cell resistance to chemo- and radiotherapy. COX-2 is released by cancer-associated fibroblasts (CAFs), macrophage type 2 (M2) cells, and cancer cells to the tumor microenvironment (TME). COX-2 induces cancer stem cell-like activity and promotes apoptotic resistance, proliferation, angiogenesis, inflammation, invasion, and metastasis of cancer cells (Hashemi Goradel et al., 2019). Inflammation is an inducer of carcinogenesis in which an inflammatory microenvironment is considered a promoter of cancer development and invasiveness (Echizen et al., 2018). COX-2 is a pro-inflammatory enzyme overexpressed at the inflammatory site of cancer (Raj et al., 2019). COX-2 is related to apoptosis suppression in many cancers. COX-2 causes apoptosis resistance in cancer cells by delaying the G1 phase (Gungor et al., 2018). In some and limited situations, COX-2 may act as an antitumor enzyme. Multiple signals are contributed to the functions of COX-2 on cancer cells or its regulation. Mitogen-activated protein kinase (MAPK) family members, epidermal growth factor receptor (EGFR), and nuclear factor-κβ are the main upstream modulators for COX-2 in cancer cells. COX-2 also interacts with several hormones within the body (Hashemi Goradel et al., 2019). Inhibition of COX-2 provides a high possibility of exerting therapeutic outcomes in cancer (Shi et al., 2018). Administration of COX-2 inhibitors for organs like lung, breast, colon, and prostate has been attested to cause a reduction of cancer risk by about 68% (Brizzolara et al., 2017). COX-2 inhibition also sensitizes cancer cells to treatments like radio- and chemotherapy.

4.2.2. Chk1: Chk1 has a central role in coordinating the DNA damage response and therefore is an area of great interest in oncology and the development of cancer therapeutics (Goto et al., 2012). Initially, Chk1 was thought to function as a tumor suppressor due to the regulatory role amongst cells with DNA damage. However, there has been no evidence of homozygous loss of function mutants for Chk1 in human tumors. Instead, Chk1 is overexpressed in numerous tumors, including breast, colon, liver, gastric and nasopharyngeal carcinoma. A positive correlation between Chk1 expression and tumor grade and disease recurrence suggests Chk1 may promote tumor growth (Zhang & Hunter, 2014). Chk1 is essential for cell survival, and through high levels of expression in tumors, the function may be inducing tumor cell proliferation. Further, a study has demonstrated that targeting Chk1 reactivates the tumor-suppressive activity of the protein phosphatase 2A (PP2A) complex in cancer cells (Khanna et al., 2013). Due to the possibility of Chk1 involvement in tumor promotion, the kinase and related signaling molecules may be potentially effective therapeutic targets. Tumor cells with increased levels of Chk1 acquire survival advantages due to the ability to tolerate a higher level of DNA damage. Therefore, Chk1 may contribute to chemotherapy resistance (Liang et al., 2009). In order to optimize chemotherapies, Chk1 must be inhibited to reduce the survival advantage (McNeely et al., 2014). By inhibiting Chk1, cancer cells lose the ability to repair damaged DNA, which allows chemotherapeutic agents to work more effectively. Combining DNA damaging therapies such as chemotherapy or radiation with Chk1 inhibition enhances targeted cell death and provides synthetic lethality (L. I. Toledo et al., 2011).

4.2.3. 5-LOX: Increasing evidence in literature implicates 5-LOX in the growth of several tumor types, including pancreatic, colorectal, prostate, and breast cancer. Numerous studies demonstrated the overexpression of 5-LOX in tissue samples of primary tumor cells and established cancer cell lines (Chen et al., 2006). Adding 5-LOX products to cultured tumor cells led to increased cell proliferation and activation of anti-apoptotic signaling pathways (Tong et al., 2005). 5-LOX antisense technology approaches impaired tumor cell growth by reducing 5-LOX expression (Sveinbjörnsson et al., 2008). Finally, pharmacological inhibition of 5-LOX has been shown to suppress tumor cell growth by inducing cell cycle arrest and triggering cell death via the intrinsic apoptotic pathway (Ding et al., 1999). Based on these findings, anti-leukotriene drugs were considered a promising and novel pharmacological strategy for cancer prevention and therapy.

4.2.4. Eg5: Eg5 mutations have been widely described in cancer, and many trials with Eg5 inhibitors are ongoing. Eg5 mainly relates to chromosome localization, centrosome separation, and the formation and separation of a bipolar spindle. The increasing high expression of Eg5 disturbs the normal assembly of the spindle and the balance of power associated with its function, which eventually leads to the loss of spindle, genomic instability, and tumor. Eg5 has been implicated in tumorigenesis because it is overexpressed and activated in leukemia (Kaiser et al., 1999; Nowicki et al., 2003). Hayashi et al. reported that Eg5 expression levels were proportional to the mitotic population in prostate cell lines (Hayashi et al., 2008). Eg5 expression could be detected in all head and neck squamous cell carcinoma cases, and the Eg5 expression level is correlated with cancer cell proliferative activity (Tang et al., 2008). Several Eg5 inhibitors decrease cancer growth and cause tumor regression (Exertier et al., 2013; Marquis et al., 2012; L. Yang et al., 2008), such as Eg5 small molecule inhibitors can prevent pancreatic cancer cells from mitosis to stop pancreatic cancer cells and induce apoptosis.

4.3. Importance of enzyme inhibitors

Enzyme inhibitors can be defined as molecules that bind to the enzymes and decrease their activity. Binding takes place at the active site of enzymes. It decreases their compatibility with substrates which causes the inhibition of the Enzyme-Substrate complexes formation, consequently preventing the production of unwanted products by decreasing the enzyme activity. The activity of the enzyme or the product produced is inversely proportional to the concentration of the inhibitors. As the concentration of inhibitors increases, the enzyme activity decreases. Many drugs act as inhibitors because by blocking the activity of enzymes, pathogens can be killed, or metabolic imbalances can be corrected (Ramsay & Tipton, 2017). Inhibitors work in two ways- they either stop the substrate from getting to the enzyme’s active site or prevent the enzyme from catalyzing the reaction.

The first step to new drug development is the discovery of new inhibitors. One way to do this is through trial and error, i.e., by screening extensive libraries of compounds against a chosen enzyme to achieve successful leads. The alternative method is the rational drug design method. It uses the 3-D structure of the active site to postulate which molecules could be potential inhibitors. The hypothesis is tested to determine which is the new inhibitor. The enzyme's structure is determined through the new inhibitor in an inhibitor-enzyme complex to portray the change made to the enzyme so that the inhibitor can be modified to maximize binding. Testing and improvement are repeated until an adequately potent inhibitor is made.

This is the most common use for enzyme inhibitors is to treat disease because they target human enzymes and try to correct a pathological condition. Inhibitors are also often used in chemotherapy for cancer. For example, methotrexate blocks the action of dihydrofolate reductase, an enzyme implicated in the production of nucleotides. Blocking the biosynthesis of nucleotides is toxic to rapidly growing cells but not toxic to non-dividing cells. This is because the rapidly growing cell has to replicate DNA, which is why methotrexate is used in chemotherapy (Raimondi et al., 2019).

4.4. *In silico* molecular docking

The hunt for a lead molecule is a long and tedious process, and one is often demoralized by the endless possibilities one has to search through. Fortunately, computational tools have come to the rescue and have undoubtedly played a pivotal role in rationalizing the path to drug discovery (Sethi et al., 2020). Molecular docking is a fascinating scaffold to understand biomolecular drug interactions for the rational drug design and discovery, as well as in the mechanistic study by placing a molecule (ligand) into the preferred binding site of the target-specific region of the DNA/protein (receptor) mainly in a non-covalent fashion to form a stable complex of potential efficacy and more specificity (Guedes et al., 2014; Rohs, 2005). The information obtained from the docking technique can suggest the binding energy, free energy, and stability of complexes. The docking technique is currently utilized to predict the tentative binding parameters of the ligand-receptor complex.

The practical application of molecular docking requires a data bank to search targets with a proper PDB format and a methodology to prepare ligand as a PDB file. Various software (Discovery studio, etc.) is available where the ligand can be made in PDB format. These tools provide the organization with ligands based on their ability to interact with target proteins/DNA. Molecular docking of small molecules to a target includes a pre-defined sampling of possible conformation of ligand in the particular groove of the target to establish the optimized conformation of the complex. It can be made possible using the scoring function of the software (Rauf et al., 2015).

4.5. Present Studies

The present studies aim to understand the importance of non-covalent interactions between the synthesized compounds and enzyme targets. This understanding can help predict and identify the synthesized compounds' potential anti-cancer and anti-inflammatory activities. Therefore, we reported the molecular docking studies of the synthesized compounds with Chk1, Eg5, 5-LOX, and COX-2 receptors.

Monastrol is a protagonist Eg5 inhibitors and it contains phenyl, methyl and ester group as its ring substituents. The 2-Pyridone derivatives synthesized is a bioisostere possessing a similar monastrol ring substituents and standard drug milrinone heterocyclic ring scaffolds as its core structures. Similarly the 2-pyridone derivatives have also shown anti-inflammatory activity towards COX-2 enzyme. Since some COX-2 inhibitor show dual inhibitory activity towards 5-LOX enzymes, the 2-pyridone and its derivatives also attracted the intuitions of the medicinal chemist towards their biological potency. Moreover, microtublulin inhibitor Crolibulin and pyranopyrazoles the Chk1 inhibitor contains pyran heterocyclic ring moiety. According to the structure-activity relationship (SAR) concept, the synthesized compounds have an analog of compounds which are biologically active and they are also predicted to have the similar kind of entities related to the biological activity.

4.6. Methodology

A molecular docking investigation was carried out using the AutoDockVina (Trott& Olson, 2009). The crystal structures of the Chk1, mitotic kinesin Eg5, 5-LOX, and COX-2 enzymes were retrieved from the RCSB protein data bank (PDB id: 6FC8, 1X88, 6NCF, and 5KIR, respectively). The enzyme preparation was done by removing co-crystallized ligands, cofactors, and embedded water molecules. Subsequently, polar hydrogens and Kollman charges were added to the enzymes in Autodock tools software, and the file was saved in pdbqt format. The CIF file of the titled compounds is converted to PDB format in Mercury software. The grid parameters for the binding cavity in the target enzyme were determined based on the native ligands, ensuring all the residues of the binding cavity are encompassed. For Chk1 the grid parameters are centered at x= 2.409, y= -2.864, z = 41.899; 15 Å × 15 Å × 21.82 Å. For Eg5 the grid parameters are centered at x= 18.06, y= 24.56, z = 49.31; 18.46 Å × 21.52 Å × 21.82 Å. The grid parameters employed for docking in 5-Lox are centered at x = 11.277, y = -21.891, z = -18.408; 20 Å × 20 Å × 20 Å, while for docking in Cox-2 are centered at x = 23.287, y = 0.587, z = 34.435; 20 Å ×2 0 Å × 20 Å. The exhaustiveness parameter for analyzing the binding affinity was set to 8 modes, and the crystal compounds were subjected to molecular docking with the target enzymes. The docking results are validated by re-docking. Further, validation of docking parameters was done by analyzing the docking of the embedded native ligands to their respective enzyme and then superimposing it with the undocked native ligand. Lastly, discovery studio and pymol were used to visualize and analyze the docking poses.

4.7. Interaction of Scheme 1 compounds (1.3A-1.3F) in the binding cavity of Eg5

The common trend in the binding interactions of compounds **(1.3A-1.3F)** and the standard compound monastrol in the cavity of Eg5 is that the ester group protrudes outside the cavity. Compound **1.3F** exhibited the highest binding affinity among these compounds having -7.3 kcal/mol. The docking analysis also showed that all the compounds **(1.3A-1.3F)** occupy the same position in the binding cavity of Eg5. **Figure 4.1 (c)** depicts the overlay diagram of the structure of these compounds in the binding cavity of Eg5. However, only compound **1.3F** showed hydrogen bonding interaction with the residue Arg221 **(Figure 4.1 (a) and (b))**.

Table 4.1: Binding affinity and the residues involved in the interactions of **Scheme 1** compounds with Eg5 enzyme

Compounds	**Docking score (kcal/mol)**	**Residues involved in H-bond**	**Residues involved in other interactions (π…anion and π…alkyl)**
1.3A	-5.9	--	Glu116, Ala218, Ala133, Pro137
1.3B	-6.8	--	Glu116, Ala218, Ala133, Pro137
1.3C	-6.4	--	Glu116, Ala218, Ala133, Pro137
1.3D	-6.4	--	Ala218, Ala133, Pro137, Leu214, Tyr211, Trp127
1.3E	-6.9	--	Glu116, Ala218, Ala133, Pro137
1.3F	-7.3	Arg221	Glu116, Ala218, Ala133, Pro137

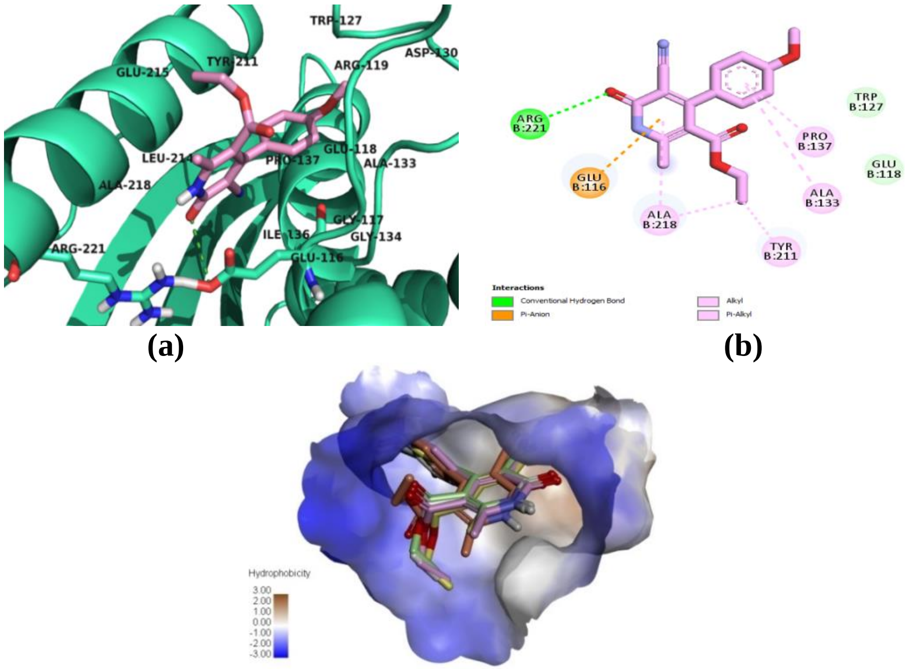

(a) **(b)**

(c)

Figure 4.1: (a) and (b) binding mode of **1.3F** in the binding cavity of Eg5, (c) Overlay diagram: **1.3A** (yellow), **1.3B** (orange), **1.3C** (white), **1.3D** (orange), **1.3E** (light green), **1.3F** (pink)

Except for compound **1.3D**, all the compounds exhibited π…anion interaction between the pyridone ring and Glu116 residue. Further, all the compounds are oriented so that the residues Ala218, Ala133, and Pro137 facilitate hydrophobic alkyl and π…alkyl interactions in the binding cavity of Eg5 except in **1.3D**, where it had additional interactions with the residues Leu214, Tyr211, and Trp127. **Table 4.1** shows the docking scores as well as the residue involved in hydrogen bonding and in other non-covalent interactions.

4.8. Interaction of Scheme 2 compounds (2.2A-2.2C) in the ATP binding site of Chk1

Compounds **2.2A** and **2.2C** involved the hydrogen bond interactions with Cys87 located at a highly conserved backbone kinase motif. Compound **2.2A** formed two hydrogen bond interactions between the carbonyl group and Cys87, and the other between m-hydroxy of the phenyl moiety and Glu134 **(Figure 4.2 (a) and (b))**. Compound **2.2C** exhibited one hydrogen bond interaction between the only carbonyl group and Cys87 **(Figure 4.2 (c) and (d))**. Moreover, π…alkyl interaction with the residues Leu15, Val23, and Leu137 provided additional stability to compounds **2.2A** and **2.2C** in the ATP binding cavity of Chk1. However, compound **2.2B** showed no hydrogen bond interaction in the active site. It is stabilized in the binding cavity mainly by π…σ interaction with Leu15 and π…alkyl interactions with Leu15, Val23, and Leu137 residues. Docking scores and interactions are given in **Table 4.2**.

Table 4.2: Binding affinity and the residues involved in the interactions of **Scheme 2** compounds with the Chk1 enzyme

Compounds	**Docking score (kcal/mol)**	**Residues involved in H-bond**	**Residues involved in other interactions (π…anion, π…Sulphur, π…σ, π…π, π…alkyl, and alkyl)**
2.2A	-9.8	Cys87, Glu134	Glu91, Val23, Leu15
2.2B	-8.0	--	Leu15, Val23, Leu137
2.2C	-8.6	Cys87	Glu91, Leu15, Val23, Leu137

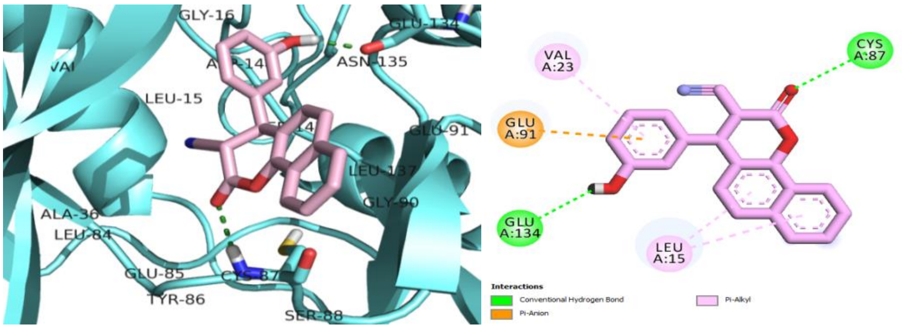

(a) **(b)**

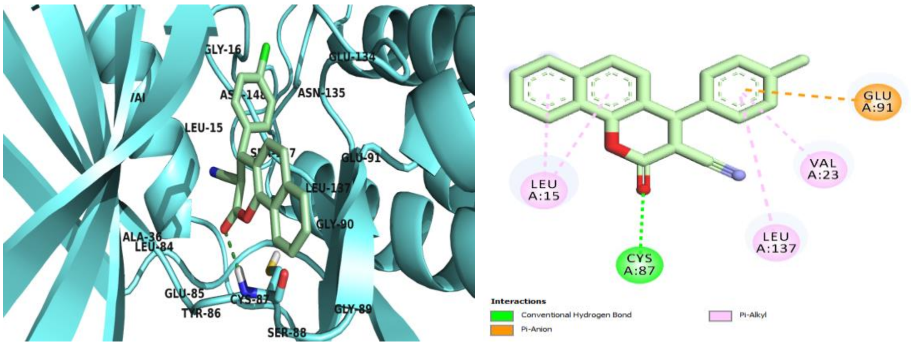

(c) **(d)**

Figure 4.2: Binding mode of compounds in the ATP binding cavity of Chk1. (a) and (b) **2.2A**, (b) and (c) **2.2C**

4.9. Interaction of Scheme 4 compounds (4.1A-4.1F and 4.2A) in the active sites of 5-LOX and COX-2

The docking experiment of Scheme 4 compounds in the active site of 5-LOX showed that **4.1A**, **4.1B**, **4.1E**, and **4.2A** have high binding affinities toward 5-LOX. Their binding energies are -8.8, -8.7, -8.5, and -8.7 kcal/mol. The orientation of the least energy conformation of these compounds in the active site is almost similar **(Figure 4.3 (e))**. Compound **4.1A** exhibited two hydrogen bonds between one of the imide carbonyl and the residues Arg68, and the other between the nitro group and Arg101 **(Figure 4.3 (a) and (b))**.

In compound **4.1B**, the carbonyl group of imide established hydrogen bond interactions with Arg68 and His130 residues. While the carbonyl group of ester moiety of compounds **4.1E** and **4.2A** established hydrogen bond interactions with Arg101. Further, compound **4.2A** has additional hydrogen bond interactions between the oxygen atom attached to the naphthyl ring and His130 **(Figure 4.3 (c) and (d))**. The phenyl ring of compounds **4.1A**, **4.1B**, **4.1E**, and **4.1F** formed π…σ interaction with Val107 residue. Further, the pyridine ring of **4.1A** and **4.1F** formed π…cation and π…σ interactions with Arg101 and Thr137 residues, respectively. Moreover, the naphthyl rings of **4.1E** and **4.1F** exhibited π…cation and π…σ with His130 and Ile126 residues, respectively. The naphthyl ring also formed π…π stacking with His130 in compound **4.1E**. Further, these compounds are stabilized in the active site of 5-LOX by π…alkyl interaction with Leu66, Val107, His130, Val29, Val110, and His130. Docking scores and interactions are given in **Table 4.2**.

Table 4.3: Binding affinity and the residues involved in the interactions of **Scheme 4** compounds with 5-LOX and COX-2 enzymes

Compounds	Docking score (kcal/mol)	Residues involved in H-bond	Residues involved in other interactions (π-anion, π…cation, π…σ, π…π, π…alkyl, and alkyl)
		5-LOX	
4.1A	-8.8	Arg68, Arg101	Arg101, Val107, His130, Leu66, Val29, Val110
4.1B	-8.7	Arg68, His130	Val107, His130, Leu66, Val110
4.1C	-8.4	Arg68, His130	Val107, His130, Leu66, Val110
4.1D	-7.6	Arg101, Arg138, Thr137, Gln141	Arg101, Val107, Lys133, Val110
4.1E	-8.5	Arg101	Val107, Thr137, His130, Leu66, Val29, Val110
4.1F	-8.3	Arg101	Val107, Thr137, His130, Leu66, Val29, Val110, Ile126
4.2A	-8.7	Arg101, His130	Val107, Thr137, His130, Leu66, Val29, Val110, Ile126
		COX-2	
4.1A	-8.6	Arg120, Ser530	Leu352, Leu93, Val116, Ala527, Val349, Val523
4.1B	-8.1	Arg120	Leu93, Val116, Ala527, Val349, Val523, Tyr385, Trp387, Leu352, Tyr355
4.1C	-8.4	Arg120, Tyr385	Tyr385, Leu93, Val116,Val523, Tyr385,Ala527, Val349,
4.1D	-9.5	Arg120	Val116, Leu93, Ala527, Leu352, Phe518, Tyr355, Val349, Val523
4.1E	-8.7	Arg120	Val116, Leu93,Ala527, Leu352, Tyr355, Val349, Val523, Leu384, Tyr385, Trp387
4.1F	-8.5	Arg120, Tyr385	Val116, Leu93,Ala527,Tyr355, Val523, Leu352, Val349,
4.2A	-5.2	--	Ala527, Leu534, Val344, Gly526, Val349, Val523, Phe518, Leu359, Leu531, Phe205

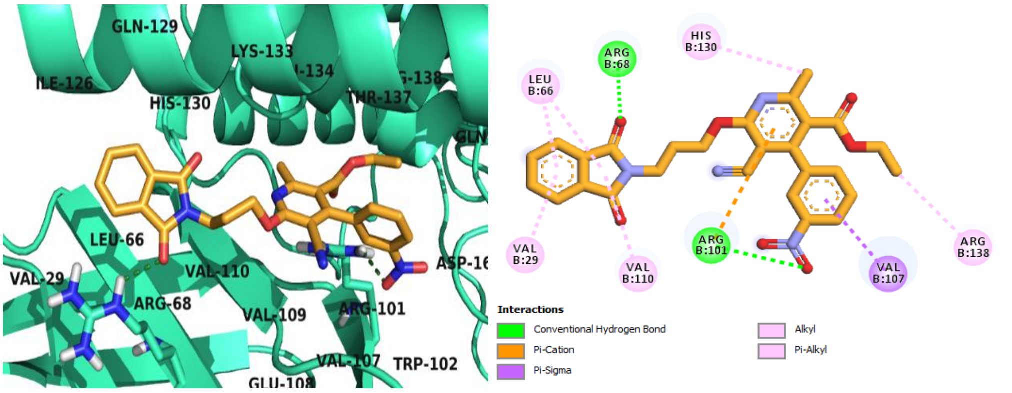

(a) **(b)**

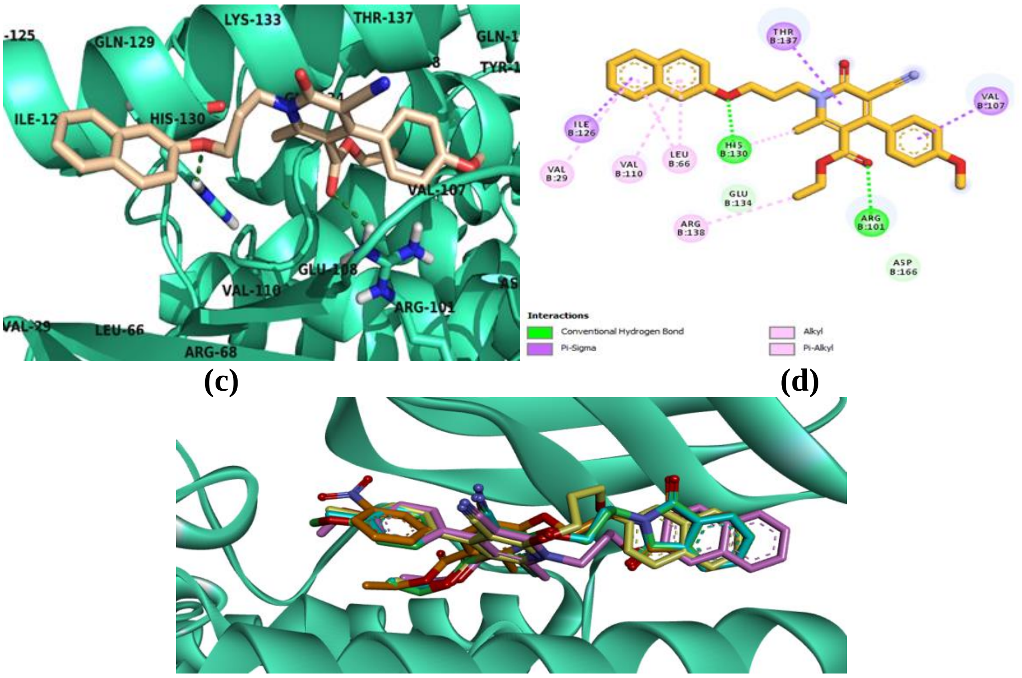

(c) (d)

(e)

Figure 4.3: Binding mode of compounds in the active site of 5-LOX (a) and (b) **4.1A**, (c) and (d) **4.2A**, (e) overlay diagram: **4.1A** (orange), **4.1B** (blue), **4.1E** (yellow), 5.2A (pink), **4.1C** (green)

The molecular docking study of Scheme 4 compounds indicated that the **4.1A, 4.1D**, and **4.1E** exhibited a high binding affinities towards COX-2. Their binding affinities are -8.6, -9.5, and -8.7 kcal/mol, respectively. The orientation of these compounds in the active site is similar, and all of them had a hydrogen bond interaction with the residue Arg120 **(Figure 4.4 (c))**. In compounds **4.1D** and **4.1E**, the electrostatic interaction between the oxygen atom attached to the naphthyl ring and the residue Arg120 resulted in hydrogen bond formation **(Figure 4.4 (a) and (b))**. In compound **4.1A**, one of the carbonyl oxygen of the phthalimide ring acts as a bifurcated acceptor and facilitates two hydrogen bond interactions with the residue Arg120. Moreover, compound **4.1A** has additional hydrogen bond interactions between the oxygen atom of the nitro group and the residue Ser530. Apart from that, the naphthyl group in **4.1D** and **4.1E** and the pyridone rings in **4.1A** exhibited π…σ interaction with Leu93 and Val116. Further, the pyridone and phenyl rings formed a π…σ interaction with the residues Ala527 and Leu352, respectively, in compounds **4.1D** and **4.1A**. The extra stability of these compounds in the active site is also reinforced by the extensive hydrophobic π…alkyl and alkyl interactions. Compound **4.1D** formed π…alkyl and alkyl interactions with the residues Leu93, Val116, Tyr355, Val523, Val349, and Phe518 **(Figure 4.4 (a) and (b))**. Compound **4.1E** formed π…alkyl and alkyl interactions with the residues Val116, Val523, Val349, Tyr355, Leu384, Leu352, Trp387, Tyr385, and Ala527. At the same time, compound **4.1A** exhibited π…alkyl and alkyl interactions with the residues Val349, Val523, Tyr355, and Val116.

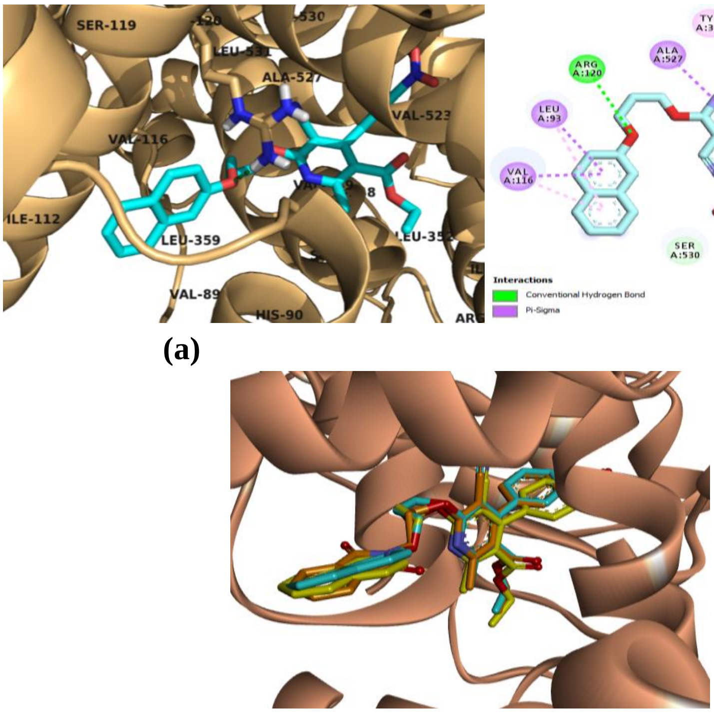

(a) **(b)**

(c)

Figure 4.4: (a) and (b) binding mode of compound **4.1D** in the active site of COX-2, (c) overlay diagram of **4.1A** (orange), compound **4.1D** (blue), and **4.1E** (yellow)

4.10. Interaction of Scheme 5 compounds (5.2A-5.2D and 5.3A-5.3D) in the active sites of 5-LOX and COX-2

The compounds exhibited good binding affinity in the active site of 5-LOX. The binding affinities of the compounds **5.2A**, **5.2B**, **5.2C**, **5.2D**, **5.3A**, **5.3B**, **5.3C** and **5.3D** are -7.9, -8.0, -8.5, -7.8, -8.2, -8.6, -8.1 and -7.8 respectively. In all the compounds, the nitrogen atom of the cyano group acts as a bifurcated acceptor and exhibits hydrogen bond interactions in the active site of the 5-LOX enzyme.

Table 4.4: Binding affinity and the residues involved in the interactions of **Scheme 5** compounds with 5-LOX and COX-2 enzymes

		5-LOX	
Compounds	**Docking score (kcal/mol)**	**Residues involved in H-bond**	**Residues involved in other interactions (π…anion, π…σ, π…π, π…alkyl, and alkyl)**
5.2A	-7.9	Arg138, Arg101	His130, Arg101, Val107, Lys133, Val110, Tyr142, Arg138
5.2B	-8.0	Arg101	His130, Val107, Val110, Lys133
5.2C	-8.5	Arg138, Arg101	His130, Arg101, Val107, Lys133, Val110, Tyr142, Arg138
5.2D	-7.8	Arg138, Arg101	His130, Arg101, Val107, Lys133, Val110, Tyr142, Arg138
5.3A	-8.2	Arg138, Arg101	Arg101, Val107, Val110, Lys133, Tyr142, Arg138
5.3B	-8.6	Arg101	Thr137, His130, Leu66, Val107, Val110, Lys133, Val29
5.3C	-8.1	Arg138	Leu66, Val29, Val110, His130, Arg101
5.3D	-7.8	Arg138, Arg68	Arg101, Leu66, Val110, Val29
		COX-2	
5.2A	-8.4	Arg120	Val116, Leu93, Val349 and Ala527, Val523, Leu352, Leu531, Leu359, Tyr355, Phe357, Val89. Val349, Ala527, Val116, Leu93.
5.2B	-8.7	--	Val523, Ser353, Leu352, Ala516, Leu384, Tyr385, Val349, Trp387, Tyr348.
5.2C	-8.6	--	Val523, Leu352, Ala516, Leu384, Tyr385, Val349, Trp387, Tyr348.
5.2D	-8.3	His90, Tyr355, Arg120	Leu93, Val116, Val523, Leu352, Ala527, Val349, Phe518
5.3A	-7.7	Tyr385	Val523, Ser353, Leu352, Ala516, Phe518, Phe381, Leu384, Val349, Trp387.
5.3B	-8.5	--	Val523, Ser353, Leu352, Ala516, Val349, Trp387, Tyr385, Leu531, Ala527.
5.3C	-8.2	Arg120	Leu352, Phe518, Val349, Val523, Leu531, Ala527, Ile112 and Val116, Phe357, Leu93
5.3D	-8.1	Arg120	Leu93, Val116, Val349, Val523, Leu352, Leu351, Ala527, Phe518, Val89

The pyridine ring of O-linked fleximers, i.e., compounds **5.2A, 5.2B**, **5.2C**, and **5.2D**, have almost the same orientation in the active site of 5-LOX and thus have a similar hydrogen bond interaction pattern. The nitrogen from the cyano group acts as a bifurcated acceptor. It forms two hydrogen bond interactions with the residue Arg138, while the oxygen atom attached to the pyridine ring forms another hydrogen bond interaction with the residue Arg101 **(Figure 4.5 (a) and (b))**. The O-linked compounds also exhibited π…cation interaction between the pyridine ring and the residue Arg101. Moreover, the naphthyl ring in compounds **5.2B**, **5.2C**, and benzodioxole in compound **5.2D** have π…cation interaction with the residue His130, except with the naphthyl rings of compound **5.2A**. However, **5.2B** has only two hydrogen bonds between the pyridine ring nitrogen and Arg101, and the other between oxygen attached to the pyridine ring and the Arg101. The π…alkyl and alkyl interactions between the O-linked compounds and the residues Val107, Lys133, Val110, Tyr142, and Arg138 further gave the additional stability.

Among the N-linked fleximers, i.e., compounds **5.3A**, **5.3B**, **5.3C** and **5.3D**, the orientation of **5.3A** resembles the O-linked fleximers. Three hydrogen bonds stabilize it in the active site of 5-LOX. The nitrogen atom of the cyano group formed bifurcated hydrogen bond interactions with the residue Arg138, whereas the oxygen atom of the pyridone ring formed hydrogen bond interactions with the residue Arg101. It also exhibited π…cation interaction between the pyridine ring and the residue Arg101. The fused rings in the other end do not show π…cation interaction, unlike in O-linked compounds. The π…alkyl and alkyl interactions that stabilized **5.3A** are residues Val107, Val110, Lys133, Tyr142, and Arg138. In contrast, the orientation of the **5.3B** compound is also almost similar to the other O-linked compounds. It exhibited bifurcated hydrogen bond interactions between the nitrogen of the cyano group and Arg101. The pyridone ring formed π…σ interaction with the residue Thr137, and the fused rings of naphthyl formed π…σ and π…cation interactions with the residues Leu66 and His130 respectively. In addition, π…alkyl and alkyl interactions with the residues Val107, Val110, Lys133, and Val29 were also observed **(Figure 4.5 (c) and (d))**. The compound **5.3D** has four hydrogen bonds due to two bifurcated interactions out of two interactions: one between the nitrogen of the cyano group and the residue Arg138 and the other between the oxygen atom attached benzodioxole ring and the residue Arg68. The pyridone ring exhibited π…cation interaction with the residue Arg101, and the five-membered ring part of benzodioxole showed π…σ interaction with the residue Leu66. Moreover, it is stabilized by the π…alkyl interactions with the residues Val110 and Val29.

Compound **5.3C** exhibited one hydrogen bond interaction with the residue Arg138. The pyridone and the naphthyl ring formed π…cation interaction with the residue His130 and Arg101. Further, **5.3C** is provided extra stability by π…alkyl interactions with the residues Leu66, Val29, and Val110.

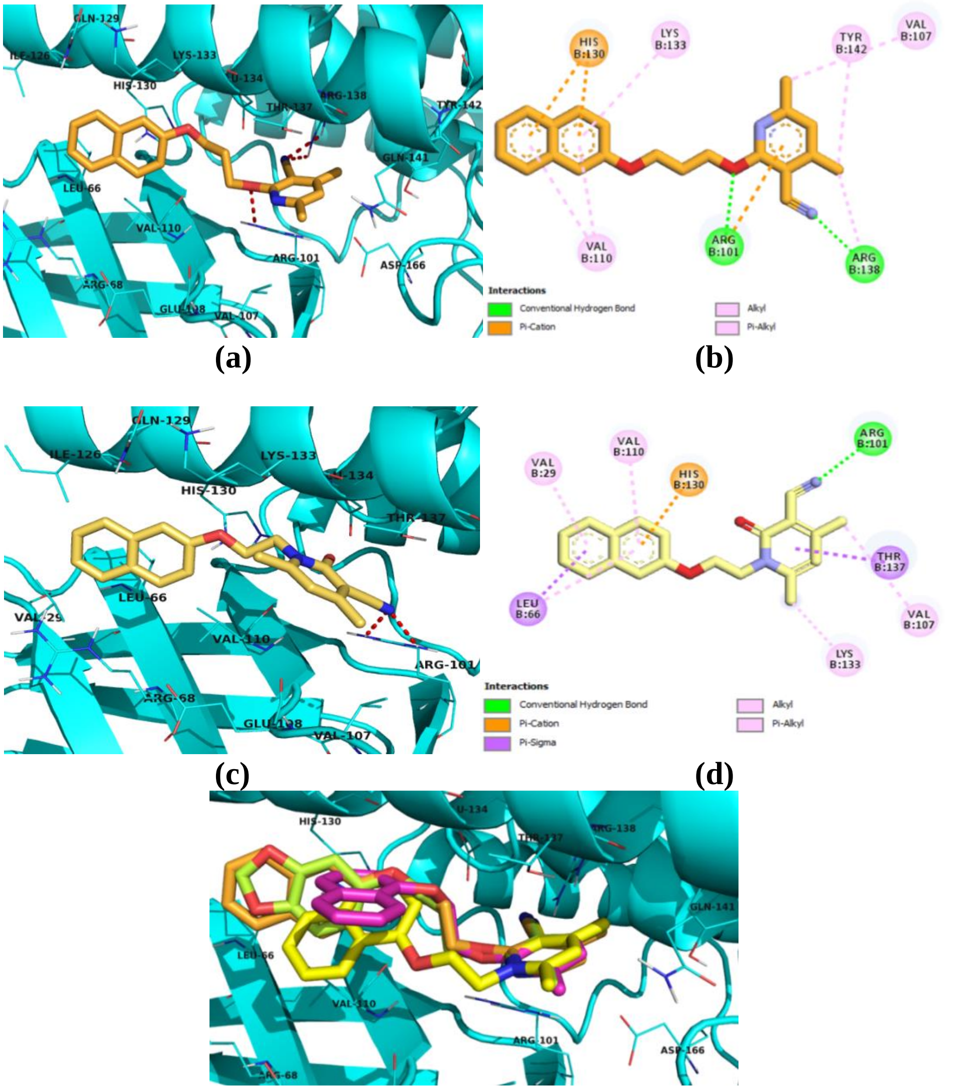

(a) **(b)**

(c) **(d)**

(e)

Figure 4.5: Binding mode of compounds in the active site of 5-LOX. (a) and (b) **5.2C**, (c) and (d) **5.3B**, (e) overlay diagram: **5.2C** (orange), **5.3A** (yellow), **5.2D** (green)

The compounds exhibited good binding affinity in the active site of COX-2. The binding affinities of the compounds **5.2A**, **5.2B**, **5.2C**, **5.2D**, **5.3A**, **5.3B**, **5.3C** and **5.3D** are -8.4, -8.7, -8.6, -8.3, -7.7, -8.5. -8.2 and -8.1, respectively. The docking experiment revealed that the main interactions between the titled compounds and the

COX-2 in the active site involved His90, Tyr355, Arg120, Val116, Leu93, Val349, Ala527, Val523, Leu352, Leu531, Leu359, Tyr355, Phe357, Val89, Val349, Ala527, Val116, Leu93, Phe518, and Tyr348 residues. The hydrogen bond interactions of the titled compounds in the active site of COX-2 are mainly mediated by the cyano group and the oxygen atoms.

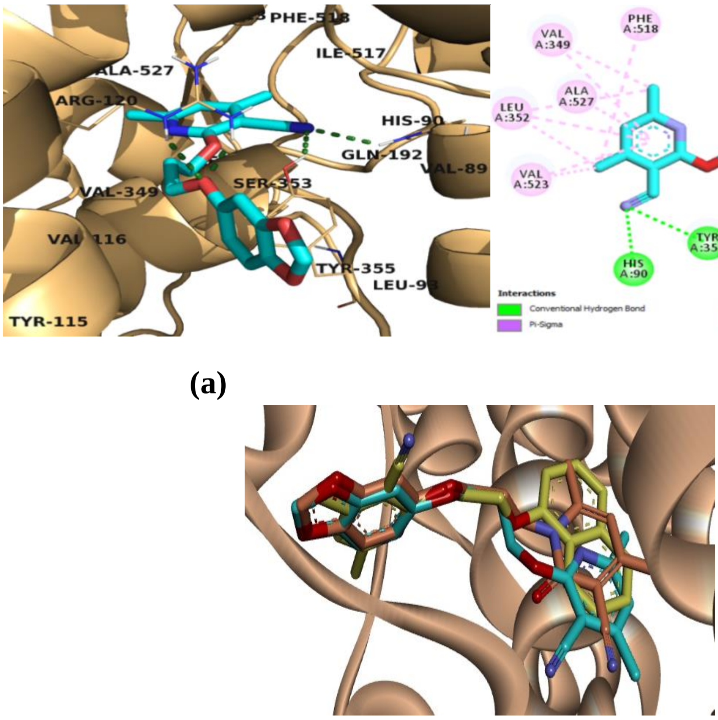

(a) **(b)**

(c)

Figure 4.6: (a) and (b) binding mode of **5.2D** in the active site of COX-2, (c) overlay diagram: **5.3D** (orange), **5.2A** (yellow), **5.2D** (blue)

Compound **5.2D** is stabilized by two bifurcated hydrogen bond interactions in the binding cavity of COX-2. The nitrogen atom of the cyano group established two hydrogen bond interactions with the residues His90 and Tyr355. The oxygen atom attached to the benzodioxole ring also established two hydrogen bond interactions with Arg120. Further, both the fused rings of benzodioxole exhibited π…σ interactions with Leu93 and Val116 residues. It is further stabilized by π…alkyl and alkyl interaction with the residues Val523, Leu352, Ala527, Val349, and Phe518 **(Figure 4.6 (a) and (b))**. In compounds **5.2A** and **5.3D**, oxygen atoms attached to the pyridine ring act as a bifurcated acceptor and established two hydrogen bond interactions with the residue Arg120. At the same time, the nitrogen atom of the cyano group in compound **5.3A** established one hydrogen bond interaction with Tyr385. Moreover, the pyridine ring of compounds **5.2A** formed π…σ interactions with Val116, Leu93, and Val349. Further, **5.2A** and **5.3D** exhibited π…alkyl and alkyl interactions with Val523, Leu352, Leu531, Leu359, Tyr355, Phe357, and Val89. Val349, Ala527, Val116, Leu93 residues. The compound **5.3C** exhibited hydrogen bond interaction between the oxygen atom attached to the naphthyl ring and the residue Arg120. Moreover, one of the naphthyl rings of **5.3C** formed π…π interaction with the residue Phe357. The naphthyl rings also formed π…σ interaction with the residues Val116 and Leu93. While, the pyridone ring also formπ…σ interactions with the residues Val349 and Ala527.Although the electrostatic hydrogen bond interactions do not bind compounds 5.2B, 5.2C, and 5.3B, they are extensively stabilized by π…σ interaction with Val523 and Ser353, amide…π stacking with Leu352, π…alkyl, and alkyl interactions with the residues Val523, Leu352, Leu531, Leu359, Tyr355, Phe357, Val89. Val349, Ala527, Val116, Leu93, Tyr348. **Figure 4.6 (c)** shows the overlay orientation of compounds **5.3D, 52A**, and **5.2D**.

CHAPTER 5

SUMMARY AND CONCLUSION

Chapter 1 deals with the general introduction to polycyclic aromatic compounds. It also contains an introduction to heterocyclic compounds and their importance in the biological systems and the pharmaceutical industries with some of its applications in medicine.

The importance of non-covalent interactions and different types of non-covalent interactions are highlighted by explaining the factors responsible for such interactions. Relevant examples concerning the biological phenomenon are also included. These non-covalent interactions are inseparable from the biological factor as they are the key to molecular recognition and supramolecular chemistry.

The general information on drug design was also included in **Chapter 1**. The idea of drug design also relies on the knowledge of molecular recognition, which is based on the concept of enzyme-substrate specificity, the "lock and key" model.

In **Chapter 2**, compounds containing pyran scaffolds were synthesized and further employed to synthesize hetero-polycyclic aromatic systems.

Scheme 1 covers the conversion of 4H-pyrans **(1.1A-1.1F)** into polycyclic 3,4-dihydropyridones **(1.2A-1.2F)**, which is further oxidized to form polycyclic 2-pyridone derivatives **(1.3A-1.3F)**. We also have reported for the first time the ring rearrangement of 4H-pyrans **(1.1A-1.1F)** into 3,4-dihydropyridones **(1.2A-1.2F)** by using either any iodine or formic acid as a catalyst. Both the reactions are very efficient, but the formic acid-catalyzed reaction was preferred due to the higher yield and the ability to recover the formic acid. The oxidation of 3,4-dihydropyridones **(1.2A-1.2F)** into 2-pyridones **(1.3A-1.3F)** was done using DDQ as an oxidizing agent under microwave and thermal conditions. Both microwave and thermal-assisted reactions give the same yield. However, microwave-assisted reactions require less time than thermal conditions. We have also observed that the powdered form of 3,4-dihypyridones **(1.2A-1.2F)** undergoes auto-oxidation in minor quantities.

The compounds which gave a suitable crystal in **Scheme 1**, except for compound **1.2B**, **1.2D**, and **1.3B** which does not give a suitable crystal, were studied by SC-XRD and Hishfeld surface analysis. Those 3,4-dihydro-2-pyridones **(1.2A-1.2F)** and 2-pyridones **(1.3A-1.3F)** supramolecular framework shows that N-H…O interactions are the most dominant non-covalent intermolecular interactions and are the main driving forces between the molecules to form an unsymmetrical dimer. None of the 3,4-dihydro-2-pyridones **(1.2A-1.2F)** crystals show π…π interactions between their aromatic rings. Among the 2-pyridone **(1.3A-1.3F)**, three compounds, i.e., **1.3C, 1.3E**, and **1.3F,** show π…π interactions between the aromatic rings. From the crystal analysis of **Scheme 1** compounds, the aromatic rings are also involved in C-H…π interactions and, in a rare case, lone pair…π interaction.

The conversion of 2-amino-4H-benzo[h]chromenes**(2.1A-2.1C)** into 2-oxo-3,4-dihydro-2H-benzo[h]chromene derivatives **(2.2A-2.2C)** was reported in **Scheme 2**, where amino group was replaced by a carbonyl group. Thus giving analogs of bothbenzo[h]chromene and dihydrocoumarin structural moieties. The synthesis of 2-amino-4H-benzo[h]chromenes **(2.1A-2.1C)** was done separately using piperidine and sodium carbonate, and we have observed better yield by using piperidine as a base. We have observed the role of formic acid as a catalyst in **Scheme 1**; however, in **Scheme 2**, we have seen that it was consumed within the reaction.

The crystal analysis of 2-oxo-3,4-dihydro-2H-benzo[h]chromene derivatives **(2.2A-2.2C)** of **Scheme 2** shows that compound **2.2A** supramolecular framework exhibit π…π interactions on all the aromatic rings. Compound **2.2B** also forms π…π interactions between the naphthalene ring moiety. While in compound **3.2C,** no evidence of stacking interaction was observed but shows lone pair…π and cation…π interaction with the aromatic ring surfaces. Beyond the different types of non-covalent hydrogen bonding observed in the molecular association of the three compounds, compound **2.2A** also shows dipole…dipole interaction between the atoms.

Chapter 3 consists of the synthesis of the designed polycyclic aromatic systems having flexible models. Firstly in **Scheme 3**, a series of the aromatic ring were linked with bromoalkanes, and the products **(3.1A-3.1E)** obtained were then employed in further schemes.

In **Scheme 4**, the 2-pyridone derivatives **(1.3A, 1.3E, 1.3F)** from **Scheme 1** were reacted with any methylene-linked aromatic ring with bromide **(3.1A, 3.1B)** from **Scheme 3** to gives polycyclic aromatic fleximers **(4.1A-4.1F)**. Polycyclic aromatic fleximers **(5.2A-5.2D** and **5.3A-5.3D)** were also synthesized from 4,6-dimethyl-2-oxo-1,2-dihydropyridine-3-carbonitrile in **Scheme 5** by reacting with compounds **(3.1B, 3.1C, 3.1D, 3.1E)** from **Scheme 3**. In both **Schemes 4** and **5**, potassium carbonate was used as a base. However, it was observed that O-alkylation was selective in **Scheme 4** except for compound **1.3F**, which gives both O-alkylated and N-alkylated products. However, in **Scheme 5**, O-alkylation and N-alkylation occur at a very close ratio for every reaction.

The crystal analysis of compounds **(4.1A-4.1F** and **4.2A)** from **Scheme 4** reveals that all the supramolecular frameworks display aromatic $\pi\ldots\pi$ stacking interactions. Also, all the fleximers that are the products of O-alkylation **(5.2A-5.2D)** from **Scheme 5** show $\pi\ldots\pi$ stacking interactions between the aromatic rings. Excluding compound **5.3C,** which does not give a suitable crystal, among the N-alkylated fleximers **(5.3A-5.3D)**, only compound **5.3D** shows $\pi\ldots\pi$ stacking interactions, and compounds **5.3A** and **5.3B** display lone pair…π and cation…π interactions respectively in their supramolecular framework. Different non-covalent interactions are observed in the crystal analysis from both **Schemes 5** and **6** products.

From all the crystal analyses of compounds from **Chapters 2** and **3,** we have observed that the increase in the number of the aromatic ring leads to the increase in percentage contribution of C…C contacts in the 2-D fingerprint plot. The $\pi\ldots\pi$ stacking interactions between aromatic rings that have different electronic distributions and slightly tilted stacking and aromatic stacking between the rings in a staggered fashion shows a small degree of deformities in the blue and red triangles around the aromatic ring surfaces in the Hirshfeld shape-index.

In **Chapter 4**, *In silico* analysis of the synthesized compounds was carried out using AutoDockVina by performing molecular docking of the compounds with selected enzymes, promoting the development of cancer cells.

Molecular recognition properties of **Scheme 1** compounds were carried out by docking it with the Eg5 enzyme. Compound **1.3F** gives the best docking score results of -7.3 kcal/mol. Compound **1.3F** is also the only compound which gives hydrogen bonding with amino acid residue (Arg221). The docking analysis shows that the compounds **(1.3A-1.3F)** occupy the same position in the binding cavity of the Eg5 enzyme. The ester group protrudes outside the binding cavity, also observed in the standard compound monastrol.

Scheme 2 compounds were docked with the Chk1 enzyme at the ATP binding site. Compounds from **Scheme 2** also exhibit an excellent binding affinity with the receptor Chk1 enzyme with a docking score of above -8.0 kcal/mol for all the compounds. Compound **2.2A** has the best docking score giving -9.8 kcal/mol. Cys87 and Glu134 are the residues involved in hydrogen bonding with compound **2.2A** and Cys87 is the residue involved in hydrogen bonding with compound **2.2C**. At the same time, compound **2.2B** hydrogen bonding was not observed with the amino acid residue.

Both **Scheme 4** and **5** compounds were docked with 5-LOX and COX-2 enzymes. Compounds **4.1A**, **4.1B**, **4.1E**, and **4.2A** from **Scheme 4** have high binding affinities towards the 5-LOX enzyme with a docking score of -8.8, -8.7, -8.5, and -8.7 kcal/mol, respectively. They also display a similar orientation in the region of the active site. Arg68, Arg101, Arg138, Thr137, His130, and Gln141 are the different residues observed in the formation of hydrogen bonding. The docking analysis of **Scheme 4** compounds **(4.1A-4.1F** and **4.2A)** in the active site of COX-2 also shows that compounds **4.1A**,**4.1D, 4.1E,** and **4.1F** exhibited a high binding score of 8.6, -9.5, -8.7 and-8.5 kcal/mol respectively with similar orientation in the active site. Arg120, Ser530, and Tyr385 are the residue involved in forming a hydrogen bond with the compounds, except compound **4.2A**, which do not show any hydrogen bonding with the amino acid residue.

Compounds **5.2C** from O-linked fleximers **(5.2A-5.2D)** and **5.3B** from N-linked fleximers **(5.3A-5.3D)** of **Scheme 5** have the highest binding affinities towards 5-LOX enzyme with a scoring of -8.5 and -8.6 kcal/mol respectively. Both O-linked and N-linked fleximer have the same orientation in the active site of the 5-LOX enzyme. Arg68, Arg138, and Arg101 are the residues involved in hydrogen bond formation. The docking analysis of **Scheme 5** compounds **(5.2A-5.2D** and **5.3A-5.3D)** with COX-2 enzyme reveals that compound **5.2B** from O-linked fleximers and **5.3B** from N-linked fleximers have the highest binding affinities with a score of -8.7 and -8.5 kcal/mol respectively. Arg120, His90, Tyr355, and Tyr385 are the residue involved in hydrogen bond formation with the compounds. Compound **5.2C,** in addition to compounds **5.2B** and **5.3B,** which gave the highest docking score does not display hydrogen bond formation with the residue amino acid of the COX-2 enzyme.

The aromatic rings present in the structure of the different synthesized compounds also play an important role in strengthening and stabilizing the ligand-receptor complex through non-covalent interactions such as π…anion and π…alkyl, π…Sulphur, π…σ, π…π and π…cation with the residues. Whereas the functional groups of the compounds were important in forming a hydrogen bond with the residue amino acid of the target enzyme. Compounds with a high docking score also give a theoretical lead compound which might be a potent inhibitor of the target enzymes.

LIST OF PUBLICATIONS

1. Ved Prakash Singh, Jayanta Dowarah, **Lalhruaizela**, and David K. Geiger. 2020. “Structural and Non-Covalent Interactions Study of 2-Pyridone Based Flexible Unsymmetrical Dimer.” *Crystal Research and Technology* 55(1):1900136. doi: 10.1002/crat.201900136.

2. Jayanta Dowarah, Brilliant N. Marak, **Lalhruaizela**, Balkaran S. Sran, and Ved Prakash Singh. 2020. “Design, Synthesis, In Silico Analysis, and Structural Study of 4,6-Dimethyl-2-(3-(*p*-Tolyloxy)Propoxy)Nicotinonitrile Fleximer.” *Crystal Research and Technology* 2000100. doi: 10.1002/crat.202000100.

3. **Lalhruaizela**, Brilliant N. Marak, Dipanta Gogoi, Jayanta Dowarah, Balkaran S. Sran, Zodinpuia Pachuau, and Ved Prakash Singh. 2021. “Study of Supramolecular Self-Assembly of Pyridone and Dihydropyridone Co-Crystal: Synthesis, Crystal Structure, Hirshfeld Surface, DFT and Molecular Docking Studies.” *Journal of Molecular Structure* 1235:130214. doi: 10.1016/j.molstruc.2021.130214.

4. **Lalhruaizela**, Brilliant N. Marak, Balkaran S. Sran, and Ved Prakash Singh. 2021. “Multicomponent Synthesis, Crystal Structure, Hirshfeld Surface Analysis, and Molecular Docking of 4H-Pyrans.” *Chemistry Select* 6(41):11249–60. doi: 10.1002/slct.202103182.

5. **Lalhruaizela**, Devanshi Patel, Brilliant N. Marak, Jayanta Dowarah, Balkaran Singh Sran, Umesh Chand Singh Yadav, and Ved Prakash Singh. 2022. “Supramolecular Architectures in Dihydropyridones: Synthesis, Crystal Structure, Hirshfeld Analysis, Cytotoxicity and in Silico Studies.” *Journal of Molecular Structure* 1250:131671. doi: 10.1016/j.molstruc.2021.131671.

CONFERENCES AND SEMINAR

1. Presented poster entitled, **“Design, Synthesis and Study of Novel Polycyclic Aromatic Systems”** at International Conference on Chemistry & Environmental Sustainability (ICCES-2019), held on 19th to 22nd February2019, organized by Department of Chemistry, Mizoram university Aizawl, Mizoram, India.

2. Presented paper entitled, **“Design, Synthesis and Studies of 3cyano-2-pyridone Analogues”** at National Conferences on Functional Materials and Applications (NCFMA- 2019), held on 22nd to 23rd November 2019, organized by Department of BS&HSS (Physics), National Institute of Technology, Aizawl, Mizoram, India.

3. Presented paper entitled, **“Synthesis Of 2-pyridone Derivatives And Studies Of Molecular Docking Interactions With CDK2 And COX2 Proteins”** at International Conference on Emerging Trends in Chemical Sciences (ETCS-2020), held on 13th to 15th February 2020, organized by Department of Chemistry, Guwahati University, Guwahati, Assam, India.

4. Presented paper entitled, “**Synthesis and study of 2-pyridone based supramolecular system**” at 2 nd Annual Convention of North East (India) Academy of Science and Technology (NEAST) & International Seminar on Recent Advances in Science and Technology (ISRAST), held on 16th -18th November 2020, Organized by NEAST, Mizoram University, Aizawl, Mizoram, India.

Journal of Molecular Structure 1250 (2022) 131671

Contents lists available at ScienceDirect

Journal of Molecular Structure

journal homepage: www.elsevier.com/locate/molstr

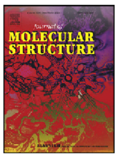

Supramolecular architectures in dihydropyridones: Synthesis, crystal structure, Hirshfeld analysis, cytotoxicity and *in silico* studies

Lalhruaizela[a], Devanshi Patel[b], Brilliant N. Marak[a], Jayanta Dowarah[a], Balkaran Singh Sran[c], Umesh Chand Singh Yadav[d], Ved Prakash Singh[a,e,*]

[a] *Department of Chemistry, School of Physical Sciences, Mizoram University, Aizawl 796004, Mizoram, India*
[b] *School of Life Sciences, Central University of Gujarat, Gandhinagar, Gujarat, 382030, India*
[c] *Department of Chemistry, Guru Nanak Dev University, Amritsar 143 005, India*
[d] *Special Centre for Molecular Medicine, Jawaharlal Nehru University, New Delhi 110067, India*
[e] *Department of Industrial Chemistry, School of Physical Sciences, Mizoram University, Aizawl 796004, Mizoram, India*

ARTICLE INFO

Article history:
Received 26 July 2021
Revised 4 October 2021
Accepted 5 October 2021
Available online 8 October 2021

Keywords:
Dihydropyridones
Non-covalent interactions
Hirshfeld surface analysis
Molecular docking
Cytotoxicity
Supramolecular chemistry

ABSTRACT

In this study, a series of five non-aromatic dihydropyridones were synthesized, crystallized, and single-crystal X-ray diffraction was used to obtain their molecular geometries. The supramolecular assembly of the molecules through non-covalent interactions was then studied and demonstrated. The weak intermolecular interactions in the molecular packing of compounds were further validated through Hirshfeld surface analysis. The synthesized compounds were screened *in vitro* using lung adenocarcinoma (A549) cells to assess their cytotoxic effects. A molecular docking study has also been employed to gain insight into the binding mode of the synthesized compounds in the allosteric binding pocket of the Eg5 motor domain and survivin protein. The results showed that the title compounds have mild to moderate cytotoxic effects in these cells. Ethyl-5-cyano-4-(2,5-dimethoxyphenyl)-2-methyl-6-oxo-1,4,5,6-tetrahydropyridine-3-carb-oxylate has shown more significant cytotoxicity among all the synthesized compounds. This study has further demonstrated the importance of non-covalent intermolecular interactions of dihydropyridones for exhibiting diverse supramolecular architectures as well as for having a significant binding affinity towards the receptor.

1. Introduction

The study of intermolecular interactions is crucial for understanding molecular recognition in biological systems as well as for creating solid-state materials with desired properties in supramolecular chemistry and crystal engineering [1–4]. Several non-covalent interactions such as conventional hydrogen bonding, $\pi\cdots\pi$ stacking, C–H···N, lone pair···π, C–H···O, C–H···N, etc. are crucial cohesive and adhesive forces in the supramolecular self-assembly of the molecules. These same interactions certainly play a significant role in supplementing the binding affinity and provide stability to the drugs in the binding cavity of the receptor.

The fascinating biological properties of dihydropyrimidinone (DHPM) derivatives have attracted the attention of organic chemists to synthesize novel congeners. The pyridine nucleus and its derivatives act as an attractive scaffold to design and develop new drugs due to its crucial interaction in biological systems [5]. Indeed, pyridine derivatives are one of the prominent N-heterocycles incorporated into the structure of many pharmacologically and biologically active compounds. For instance, pyridine derivatives such as cyanopyridine with different aryl and alkyl moieties have antihypertensive [6,7], antipyretic [8], anti-inflammatory [8–10], analgesic [8], antimicrobial [11], and cardiotonic properties [12]. Milrinone, a derivative of 3-cyano-2-pyridone is the phosphodiesterase-III inhibitor drug that is being used for the treatment of acute decompensated heart failure [13]. Moreover, they are interesting due to their anticancer activity as they can bind with different types of biological targets such as Eg5 motor domain, PIM1 Kinase, PDE3, and survivin protein, and inhibit their functions which consequently promote anticancer activity [14]. Some of the bioactivities of cyanopyridines are illustrated in Fig. 1. Further, a δ-lactam ring is incorporated in many antitumor compounds such as tyrosine kinase [15] and topoisomerase I inhibitors [16]. A δ-lactam ring is also present in the structure of antiangiogenic agents and immunoregulators [17,18].

In continuation of our previous work on chemistry and pharmaceutical activity on cyanopyridine-based dihydropyridone derivatives [19], we aimed to establish the supramolecular architectures

---

[*] Corresponding author.
E-mail address: vedsinghbhu@gmail.com (V.P. Singh).

https://doi.org/10.1016/j.molstruc.2021.131671

Journal of Molecular Structure 1235 (2021) 130214

Contents lists available at ScienceDirect

Journal of Molecular Structure

journal homepage: www.elsevier.com/locate/molstr

Study of supramolecular self-assembly of pyridone and dihydropyridone co-crystal: Synthesis, crystal structure, Hirshfeld surface, DFT and molecular docking studies

Lalhruaizela[a], Brilliant N. Marak[a], Dipanta Gogoi[a], Jayanta Dowarah[a], Balkaran S. Sran[b], Zodinpuia Pachuau[a], Ved Prakash Singh[a,*]

[a] *Department of Chemistry, School of Physical Sciences, Mizoram University, Aizawl-796004, Mizoram, India*
[b] *Department of Chemistry, Guru Nanak Dev University, Amritsar, Punjab 143005, India*

ARTICLE INFO

Article history:
Received 29 November 2020
Revised 25 February 2021
Accepted 25 February 2021
Available online 5 March 2021

Keywords:
Non-covalent interactions
Docking
Intra-molecular
Intermolecular
DFT
Hirshfeld
Crystal

ABSTRACT

Dihydropyridone is synthesized by the multicomponent condensation reactions (MCRs), followed by three different oxidation methods to synthesize pyridone. The 3-D self-assemblies of both the compounds were determined using the single-crystal X-ray diffraction method. Dihydropyridone products are found as a racemic mixture in synthesis and crystalized as co-crystal. Similar structural conformations are observed in both the compounds but stabilized with different non-covalent interactions. Hirshfeld surface analysis is done to analyze the various intermolecular interactions in both the structure. This study gives the clue of driving force in the self-assembly of molecules in crystal lattices. The propensity of inter-molecular contacts to construct the supramolecular assembly was further studied using DFT. The geometrical optimizations of both the compounds were done by the electronic structure method using density functional theory (DFT) to identify the active sites and explore the molecules' chemically reactive parameters. Further, both compounds were docked with Survivin Protein and Kinesin Eg5 protein to analyze the binding affinity with targeted protein.

Introduction

Dihydropyrimidinones (DHPM's) and their derivatives are heterocyclic compounds synthesized by multicomponent reactions [1,2]. This class of compounds are structural analogs of monastrol became important to the field of medicinal chemistry because monastrol is a very important bio-molecule having many biological activities [3]. Other DHPMs analogs have been synthesized since then, revealing several other pharmacological properties [4]. Monastrol is the protagonist of the DHPMs class. Several studies have revealed that its inhibitory action on human kinesin Eg5 leads to mitotic arrest and, consequently, to apoptosis [5]. At first, this was the main action described for this class of compounds, but some studies have shown other possible targets for these molecules, such as centrin [6], calcium channels [7] and topoisomerase I [8].

2-pyridones are a particular class of compounds with unique pharmacophores that exhibit several biological activities such as analgesic [9], antimalarial [10], antitumoral [11], anti-HIV [12], and anti-inflammatory [13]. Cyanopyridines are important intermediates for synthesizing many biological important analogs like nicotinamide, nicotinic acid, and isonicotinic acid. 3-cyano-2-pyridone are very significant frameworks in the past few decades. These are the structural basis of the alkaloid ricinine, the first known cyano group-containing alkaloid. Milrinone is also a 3- cyano-2-pyridone derivative used for the treatment of congestive heart failure [14,15]. Some derivative of 3-cyano2-pyridone has shown anticancer activity [16–18]. 3-cyano-4,6-diaryl-2-pyridone derivatives I and IV (Fig. 1) possess anticancer activity due to their ability to act as survivin inhibitors [19]. Undoubtedly, the need to bridge the gap between minimizing side effects and the mode of action of antimitotic drugs encourage us for further investigations towards the synthesis of the novel potent cytotoxic compound [20,21].

New analogs are designed based on Monastrol kinesin inhibitor and Survivin inhibitor pharmacophore analysis and bio-isoester group application (Fig. 2).

Given the pharmacological importance of 2-pyridone derivatives, the investigations of their structural and electronic properties are fundamental to know the influence of different groups in the molecule to discover the relationship of these groups with their biological properties [22–26].

---

* Corresponding author.
E-mail address: vedsinghbhu@gmail.com (V.P. Singh).

https://doi.org/10.1016/j.molstruc.2021.130214

BIO-DATA

1. NAME : Lalhruaizela

2. DATE OF BIRTH : 28th December 1992

3. FATHER'S NAME : K. Lalrinthara

4. PERMANENT ADDRESS : Mamit, Mizoram, 796441

5. EMAIL ADDRESS : hruaiakhawlhring28@gmail.com

6. EDUCATIONAL QUALIFICATIONS :

Examination passed	Year of Passing	Board/University	Division	% of marks	Subjects
HSLC	2007	Mizoram Board of School Education	II	56.8	English, Mizo, Mathematics, Science, Social sciences
HSSLC	2009	Mizoram Board of School Education	II	50.04	English, Biology, Physics, Chemistry, Mathematics
B.SC (Chemistry)	2013	Mizoram University	I	62.37	Chemistry, Botany, Zoology
M.Sc (Chemistry)	2015	Mizoram University	I	71.82	Organic Chemistry (specialization), Physical Chemistry, Inorganic Chemistry, Analytical Chemistry

PARTICULARS OF THE CANDIDATE

NAME OF CANDIDATE : Lalhruaizela

DEGREE : Doctor of Philosophy (Ph.D)

DEPARTMENT : Chemistry

TITLE OF THESIS : Design, Synthesis and Study of Novel Polycyclic Aromatic Systems

DATE OF ADMISSION : 18th August, 2015

APPROVAL OF RESEARCH PROPOSAL:

1. BOS : 13th April, 2016

2. SCHOOL BOARD : 21st April, 2016

3. MZU REGN. NO. : 4459 of 2010-11

4. Ph.D REGN. NO. & DATE: MZU/Ph.D/847 of 21.04.2016

5. EXTENTION : Extension period 21.04.2021 to 20.04.2023
(No.16-2/MZU(Acad)20/15)

Head
Department of Chemistry

REFERENCES

Abdel-Hafez, Sh. H. (2008). Selenium containing heterocycles: Synthesis, anti-inflammatory, analgesic and anti-microbial activities of some new 4-cyanopyridazine-3(2H)selenone derivatives. *European Journal of Medicinal Chemistry*, *43*(9), 1971–1977. https://doi.org/10.1016/j.ejmech.2007.12.006

Adbel Aziz Hafez, E., Abdel Aziz Hafez, E., Hilmy Elnagdi, M., Ghani Ali Elagamey, A., & Mohamed Abdel Aziz El-Taweel, F. (1987). Nitriles in Heterocyclic Synthesis: Novel Synthesis of Benzo[c]coumarin and of Benzo[c]pyrano[3,2-c]quinoline Derivatives. *HETEROCYCLES*, *26*(4), 903. https://doi.org/10.3987/R-1987-04-0903

Aliev, A. E., Arendorf, J. R. T., Pavlakos, I., Moreno, R. B., Porter, M. J., Rzepa, H. S., & Motherwell, W. B. (2014). Surfing π Clouds for Noncovalent Interactions: Arenes versus Alkenes. *Angewandte Chemie International Edition*, n/a-n/a. https://doi.org/10.1002/anie.201409672

Anslyn, E. V., & Dougherty, D. A. (2006). *Modern physical organic chemistry*. University Science.

Aqui, N. A., & Vonderheide, R. H. (2008). Survivin as a universal tumor antigen for novel cancer immunotherapy: Functions of a killer clone. *Cancer Biology & Therapy*, *7*(12), 1888–1889. https://doi.org/10.4161/cbt.7.12.7219

Baig, M. H., Ahmad, K., Roy, S., Mohammad Ashraf, J., Adil, M., Haris Siddiqui, M., Khan, S., Amjad Kamal, M., Provazník, I., & Choi, I. (2016). Computer Aided Drug Design: Success and Limitations. *Current Pharmaceutical Design*, *22*(5), 572–581. https://doi.org/10.2174/1381612822666151125000550

Baim, D. S., Colucci, W. S., Monrad, E. S., Smith, H. S., Wright, R. F., Lanoue, A., Gauthier, D. F., Ransil, B. J., Grossman, W., & Braunwald, E. (1986). Survival of patients with severe congestive heart failure treated with oral milrinone. *Journal of the American College of Cardiology*, *7*(3), 661–670. https://doi.org/10.1016/S0735-1097(86)80478-8

Bandyopadhyay, D., Granados, J. C., Short, J. D., & Banik, B. K. (2012). Polycyclic aromatic compounds as anticancer agents: Evaluation of synthesis and in vitro cytotoxicity. *Oncology Letters*, *3*(1), 45–49. https://doi.org/10.3892/ol.2011.436

Barlow, W. (1883). Probable Nature of the Internal Symmetry of Crystals. *Nature*, *29*(738), 186–188. https://doi.org/10.1038/029186a0

Baron, R., Setny, P., & McCammon, J. A. (2010). Water in Cavity−Ligand Recognition. *Journal of the American Chemical Society*, *132*(34), 12091–12097. https://doi.org/10.1021/ja1050082

Beale, T. M., Chudzinski, M. G., Sarwar, M. G., & Taylor, M. S. (2013). Halogen bonding in solution: Thermodynamics and applications. *Chem. Soc. Rev.*, *42*(4), 1667–1680. https://doi.org/10.1039/C2CS35213C

Bhupathy, M., Conlon, D. A., Wells, K. M., Nelson, J. R., Reider, P. J., Rossen, K., Sager, J. W., Volante, R. P., Dorsey, B. D., Hoffman, J. M., Joseph, S. A., & Mcdaniel, S. L. (1995). A practical synthesis of 5-(chloromethyl)furo[2,3- *b*]pyridine, a key intermediate for the HIV protease inhibitor, L-754,394. *Journal of Heterocyclic Chemistry*, *32*(4), 1283–1287. https://doi.org/10.1002/jhet.5570320431

Bolton, W. (1964). The crystal structure of alloxan. *Acta Crystallographica*, *17*(2), 147–152. https://doi.org/10.1107/S0365110X6400041X

Bosshard, H. R. (2001). Molecular Recognition by Induced Fit: How Fit is the Concept? *Physiology*, *16*(4), 171–173. https://doi.org/10.1152/physiologyonline.2001.16.4.171

Bragg, S. W. H. (1921). The Structure of Organic Crystals. *Proceedings of the Physical Society of London*, *34*(1), 33–50. https://doi.org/10.1088/1478-7814/34/1/306

Bravais, A. (1850). *Mémoire sur les systèmes formés par des points distribués régulièrement sur un plan ou dans l'espace* (1850th ed.).

Breinholt, J., Ludvigsen, S., Rassing, B. R., Rosendahl, C. N., Nielsen, S. E., & Olsen, C. E. (1997). Oxysporidinone: A Novel, Antifungal N-Methyl-4-hydroxy-2-pyridone from Fusarium oxysporum. *Journal of Natural Products*, *60*(1), 33–35. https://doi.org/10.1021/np9605596

Breiten, B., Lockett, M. R., Sherman, W., Fujita, S., Al-Sayah, M., Lange, H., Bowers, C. M., Heroux, A., Krilov, G., & Whitesides, G. M. (2013). Water

Networks Contribute to Enthalpy/Entropy Compensation in Protein–Ligand Binding. *Journal of the American Chemical Society*, *135*(41), 15579–15584. https://doi.org/10.1021/ja4075776

Brejc, K., van Dijk, W. J., Klaassen, R. V., Schuurmans, M., van der Oost, J., Smit, A. B., & Sixma, T. K. (2001). Crystal structure of an ACh-binding protein reveals the ligand-binding domain of nicotinic receptors. *Nature*, *411*(6835), 269–276. https://doi.org/10.1038/35077011

Brizzolara, A., Benelli, R., Venè, R., Barboro, P., Poggi, A., Tosetti, F., & Ferrari, N. (2017). The ErbB family and androgen receptor signaling are targets of Celecoxib in prostate cancer. *Cancer Letters*, *400*, 9–17. https://doi.org/10.1016/j.canlet.2017.04.025

Bruno, I. J., Cole, J. C., Edgington, P. R., Kessler, M., Macrae, C. F., McCabe, P., Pearson, J., & Taylor, R. (2002). New software for searching the Cambridge Structural Database and visualizing crystal structures. *Acta Crystallographica Section B Structural Science*, *58*(3), 389–397. https://doi.org/10.1107/S0108768102003324

Burley, S. K., & Petsko, G. A. (1986). Dimerization energetics of benzene and aromatic amino acid side chains. *Journal of the American Chemical Society*, *108*(25), 7995–8001. https://doi.org/10.1021/ja00285a019

Caronna, T., Liantonio, R., Logothetis, T. A., Metrangolo, P., Pilati, T., & Resnati, G. (2004). Halogen Bonding and π···π Stacking Control Reactivity in the Solid State. *Journal of the American Chemical Society*, *126*(14), 4500–4501. https://doi.org/10.1021/ja039884n

Chakraborty, K., Dhara, S., & Mani, A. E. (2021). Ulvapyrone, a pyrone-linked benzochromene from sea lettuce *Ulva lactuca* Linnaeus (family Ulvaceae): Newly described anti-inflammatory agent attenuates arachidonate 5-lipoxygenase. *Natural Product Research*, 1–11. https://doi.org/10.1080/14786419.2021.1976173

Chen, X., Sood, S., Yang, C., Li, N., & Sun, Z. (2006). Five-Lipoxygenase Pathway of Arachidonic Acid Metabolism in Carcinogenesis and Cancer Chemoprevention. *Current Cancer Drug Targets*, *6*(7), 613–622. https://doi.org/10.2174/156800906778742451

Cheney, I. W., Yan, S., Appleby, T., Walker, H., Vo, T., Yao, N., Hamatake, R., Hong, Z., & Wu, J. Z. (2007). Identification and structure–activity relationships of substituted pyridones as inhibitors of Pim-1 kinase. *Bioorganic & Medicinal Chemistry Letters*, *17*(6), 1679–1683. https://doi.org/10.1016/j.bmcl.2006.12.086

Cherubim, P., Deady, L. W., Dorkos, M., Quazi, N. H., Baguley, B. C., & Denny, W. A. (1993). Synthesis and biological evaluation of phenanthrene-derived carboxamides as cytotoxic agents. *Anti-Cancer Drug Design*, *8*(6), 429–438.

Choi, W.-B., Houpis, I. N., Churchill, H. R. O., Molina, A., Lynch, J. E., Volante, R. P., Reider, P. J., & King, A. O. (1995). A practical synthesis of the 5-chloromethyl-furo[2,3-b]pyridine pharmacophore. *Tetrahedron Letters*, *36*(26), 4571–4574. https://doi.org/10.1016/0040-4039(95)00850-C

Churchill, C. D. M., Rutledge, L. R., & Wetmore, S. D. (2010). Effects of the biological backbone on stacking interactions at DNA–protein interfaces: The interplay between the backbone···π and π···π components. *Physical Chemistry Chemical Physics*, *12*(43), 14515. https://doi.org/10.1039/c0cp00550a

Clementi, E., & Roetti, C. (1974). Roothaan-Hartree-Fock atomic wavefunctions. *Atomic Data and Nuclear Data Tables*, *14*(3–4), 177–478. https://doi.org/10.1016/S0092-640X(74)80016-1

Coelho, K. R. (2012). Challenges of the Oral Cancer Burden in India. *Journal of Cancer Epidemiology*, *2012*, 1–17. https://doi.org/10.1155/2012/701932

Cosic, I. (1994). Macromolecular bioactivity: Is it resonant interaction between macromolecules?-theory and applications. *IEEE Transactions on Biomedical Engineering*, *41*(12), 1101–1114. https://doi.org/10.1109/10.335859

Cox, E. G., Cruickshank, D. W. J., & Smith, J. A. S. (1958). The crystal structure of benzene at—3°C. *Proceedings of the Royal Society of London. Series A. Mathematical and Physical Sciences*, *247*(1248), 1–21. https://doi.org/10.1098/rspa.1958.0167

Daina, A., Blatter, M.-C., Baillie Gerritsen, V., Palagi, P. M., Marek, D., Xenarios, I., Schwede, T., Michielin, O., & Zoete, V. (2017). Drug Design Workshop: A Web-Based Educational Tool To Introduce Computer-Aided Drug Design to the General Public. *Journal of Chemical Education*, *94*(3), 335–344. https://doi.org/10.1021/acs.jchemed.6b00596

Dang, L. X. (1995). Mechanism and Thermodynamics of Ion Selectivity in Aqueous Solutions of 18-Crown-6 Ether: A Molecular Dynamics Study. *Journal of the American Chemical Society*, *117*(26), 6954–6960. https://doi.org/10.1021/ja00131a018

Daze, K., & Hof, F. (2016). Molecular Interaction and Recognition. In Z. Wang (Ed.), *Encyclopedia of Physical Organic Chemistry, 5 Volume Set* (pp. 1–51). John Wiley & Sons, Inc. https://doi.org/10.1002/9781118468586.epoc3001

Decosterd, L. A., Parsons, I. C., Gustafson, K. R., Cardellina, J. H., McMahon, J. B., Cragg, G. M., Murata, Y., Pannell, L. K., & Steiner, J. R. (1993). HIV inhibitory natural products. 11. Structure, absolute stereochemistry, and synthesis of conocurvone, a potent, novel HIV-inhibitory naphthoquinone trimer from a Conospermum sp. *Journal of the American Chemical Society*, *115*(15), 6673–6679. https://doi.org/10.1021/ja00068a026

Deechongkit, S., Nguyen, H., Powers, E. T., Dawson, P. E., Gruebele, M., & Kelly, J. W. (2004). Context-dependent contributions of backbone hydrogen bonding to β-sheet folding energetics. *Nature*, *430*(6995), 101–105. https://doi.org/10.1038/nature02611

Desiraju, G. R. (1995). Supramolecular Synthons in Crystal Engineering—A New Organic Synthesis. *Angewandte Chemie International Edition in English*, *34*(21), 2311–2327. https://doi.org/10.1002/anie.199523111

Desiraju, G. R., Ho, P. S., Kloo, L., Legon, A. C., Marquardt, R., Metrangolo, P., Politzer, P., Resnati, G., & Rissanen, K. (2013). Definition of the halogen bond (IUPAC Recommendations 2013). *Pure and Applied Chemistry*, *85*(8), 1711–1713. https://doi.org/10.1351/PAC-REC-12-05-10

Dgachi, Y., Bautista-Aguilera, O., Benchekroun, M., Martin, H., Bonet, A., Knez, D., Godyń, J., Malawska, B., Gobec, S., Chioua, M., Janockova, J., Soukup, O., Chabchoub, F., Marco-Contelles, J., & Ismaili, L. (2016). Synthesis and Biological Evaluation of Benzochromenopyrimidinones as Cholinesterase Inhibitors and Potent Antioxidant, Non-Hepatotoxic Agents for Alzheimer's Disease. *Molecules*, *21*(5), 634. https://doi.org/10.3390/molecules21050634

DiMasi, J. A., Feldman, L., Seckler, A., & Wilson, A. (2010). Trends in Risks Associated With New Drug Development: Success Rates for Investigational Drugs. *Clinical Pharmacology & Therapeutics*, *87*(3), 272–277. https://doi.org/10.1038/clpt.2009.295

Ding, X.-Z., Iversen, P., Cluck, M. W., Knezetic, J. A., & Adrian, T. E. (1999). Lipoxygenase Inhibitors Abolish Proliferation of Human Pancreatic Cancer Cells. *Biochemical and Biophysical Research Communications*, *261*(1), 218–223. https://doi.org/10.1006/bbrc.1999.1012

Dixon, S. J., & Stockwell, B. R. (2009). Identifying druggable disease-modifying gene products. *Current Opinion in Chemical Biology*, *13*(5–6), 549–555. https://doi.org/10.1016/j.cbpa.2009.08.003

Dougherty, D. A. (2013). The Cation−π Interaction. *Accounts of Chemical Research*, *46*(4), 885–893. https://doi.org/10.1021/ar300265y

Dragovich, P. S., Prins, T. J., Zhou, R., Brown, E. L., Maldonado, F. C., Fuhrman, S. A., Zalman, L. S., Tuntland, T., Lee, C. A., Patick, A. K., Matthews, D. A., Hendrickson, T. F., Kosa, M. B., Liu, B., Batugo, M. R., Gleeson, J.-P. R., Sakata, S. K., Chen, L., Guzman, M. C., … Worland, S. T. (2002). Structure-Based Design, Synthesis, and Biological Evaluation of Irreversible Human Rhinovirus 3C Protease Inhibitors. 6. Structure−Activity Studies of Orally Bioavailable, 2-Pyridone-Containing Peptidomimetics. *Journal of Medicinal Chemistry*, *45*(8), 1607–1623. https://doi.org/10.1021/jm010469k

Dubey, R., Singh, P., Singh, A. K., Yadav, M. K., Swati, D., Vinayak, M., Puerta, C., Valerga, P., Ravi Kumar, K., Sridhar, B., & Tewari, A. K. (2014). Polymorphic Signature of the Anti-inflammatory Activity of 2,2′-{[1,2-Phenylenebis(methylene)]bis(sulfanediyl)}bis(4,6-dimethylnicotinonitrile). *Crystal Growth & Design*, *14*(3), 1347–1356. https://doi.org/10.1021/cg401842y

Echizen, K., Oshima, H., Nakayama, M., & Oshima, M. (2018). The inflammatory microenvironment that promotes gastrointestinal cancer development and invasion. *Advances in Biological Regulation*, *68*, 39–45. https://doi.org/10.1016/j.jbior.2018.02.001

El-Saghier, A. M. M., Naili, M. B., Rammash, B. Kh., Saleh, N. A., & Kreddan, K. M. (2007). Synthesis and antibacterial activity of some new fused chromenes. *Arkivoc*, *2007*(16), 83–91. https://doi.org/10.3998/ark.5550190.0008.g09

Exertier, P., Javerzat, S., Wang, B., Franco, M., Herbert, J., Platonova, N., Winandy, M., Pujol, N., Nivelles, O., Ormenese, S., Godard, V., Becker, J., Bicknell, R., Pineau, R., Wilting, J., Bikfalvi, A., & Hagedorn, M. (2013). Impaired angiogenesis and tumor development by inhibition of the mitotic kinesin Eg5. *Oncotarget*, *4*(12), 2302–2316. https://doi.org/10.18632/oncotarget.1490

Fischer, E. (1894). Einfluss der Configuration auf die Wirkung der Enzyme. *Berichte der deutschen chemischen Gesellschaft*, *27*(3), 2985–2993. https://doi.org/10.1002/cber.18940270364

Fleming, F. F., Yao, L., Ravikumar, P. C., Funk, L., & Shook, B. C. (2010). Nitrile-Containing Pharmaceuticals: Efficacious Roles of the Nitrile Pharmacophore. *Journal of Medicinal Chemistry*, *53*(22), 7902–7917. https://doi.org/10.1021/jm100762r

Fouda, A. M., Hassan, A. H., Eliwa, E. M., Ahmed, H. E. A., Al-Dies, A.-A. M., Omar, A. M., Nassar, H. S., Halawa, A. H., Aljuhani, N., & El-Agrody, A. M. (2020). Targeted potent antimicrobial benzochromene-based analogues: Synthesis, computational studies, and inhibitory effect against 14α-Demethylase and DNA Gyrase. *Bioorganic Chemistry*, *105*, 104387. https://doi.org/10.1016/j.bioorg.2020.104387

Fujita, Y., Oguri, H., & Oikawa, H. (2005). Biosynthetic studies on the antibiotics PF1140: A novel pathway for a 2-pyridone framework. *Tetrahedron Letters*, *46*(35), 5885–5888. https://doi.org/10.1016/j.tetlet.2005.06.115

Gilchrist, T. L. (1998). *Heterocyclic chemistry* (3. ed., reprinted). Longman.

Gomtsyan, A. (2012). Heterocycles in drugs and drug discovery. *Chemistry of Heterocyclic Compounds*, *48*(1), 7–10. https://doi.org/10.1007/s10593-012-0960-z

Goto, H., Izawa, I., Li, P., & Inagaki, M. (2012). Novel regulation of checkpoint kinase 1: Is checkpoint kinase 1 a good candidate for anti-cancer therapy? *Cancer Science*, *103*(7), 1195–1200. https://doi.org/10.1111/j.1349-7006.2012.02280.x

Guedes, I. A., de Magalhães, C. S., & Dardenne, L. E. (2014). Receptor–ligand molecular docking. *Biophysical Reviews, 6*(1), 75–87. https://doi.org/10.1007/s12551-013-0130-2

Güner, O. F. (Ed.). (2000). *Pharmacophore perception, development, and use in drug design*. International University Line.

Gungor, H., Ilhan, N., & Eroksuz, H. (2018). The effectiveness of cyclooxygenase-2 inhibitors and evaluation of angiogenesis in the model of experimental colorectal cancer. *Biomedicine & Pharmacotherapy*, *102*, 221–229. https://doi.org/10.1016/j.biopha.2018.03.066

Hardegger, L. A., Kuhn, B., Spinnler, B., Anselm, L., Ecabert, R., Stihle, M., Gsell, B., Thoma, R., Diez, J., Benz, J., Plancher, J., Hartmann, G., Banner, D. W., Haap, W., & Diederich, F. (2011). Systematic Investigation of Halogen Bonding in Protein–Ligand Interactions. *Angewandte Chemie International Edition*, *50*(1), 314–318. https://doi.org/10.1002/anie.201006781

Hashemi Goradel, N., Najafi, M., Salehi, E., Farhood, B., & Mortezaee, K. (2019). Cyclooxygenase-2 in cancer: A review. *Journal of Cellular Physiology, 234*(5), 5683–5699. https://doi.org/10.1002/jcp.27411

Hatakeyama, S., Ochi, N., Numata, H., & Takano, S. (1988). A new route to substituted 3-methoxycarbonyldihydropyrans; enantioselective synthesis of (–)-methyl elenolate. *J. Chem. Soc., Chem. Commun.*, *17*, 1202–1204. https://doi.org/10.1039/C39880001202

Hayashi, N., Koller, E., Fazli, L., & Gleave, M. E. (2008). Effects of Eg5 knockdown on human prostate cancer xenograft growth and chemosensitivity. *The Prostate*, *68*(12), 1283–1295. https://doi.org/10.1002/pros.20783

Heravi, M. M., & Zadsirjan, V. (2020). Prescribed drugs containing nitrogen heterocycles: An overview. *RSC Advances*, *10*(72), 44247–44311. https://doi.org/10.1039/D0RA09198G

Hirshfeld, F. L. (1977). Bonded-atom fragments for describing molecular charge densities. *Theoretica Chimica Acta*, *44*(2), 129–138. https://doi.org/10.1007/BF00549096

Hirshfeld, F. L. (1985). Accurate electron densities in molecules. *Journal of Molecular Structure*, *130*(1–2), 125–141. https://doi.org/10.1016/0022-2860(85)85028-6

Hirshfeld, F. L. (1991). Electron Density Distributions in Molecules. *Crystallography Reviews*, *2*(4), 169–200. https://doi.org/10.1080/08893119108032957

Hunter, C. A., & Sanders, J. K. M. (1990). The nature of .pi.-.pi. Interactions. *Journal of the American Chemical Society*, *112*(14), 5525–5534. https://doi.org/10.1021/ja00170a016

Jampilek, J. (2019). Heterocycles in Medicinal Chemistry. *Molecules*, *24*(21), 3839. https://doi.org/10.3390/molecules24213839

Jennings, W. B., Farrell, B. M., & Malone, J. F. (2001). Attractive Intramolecular Edge-to-Face Aromatic Interactions in Flexible Organic Molecules. *Accounts of Chemical Research*, *34*(11), 885–894. https://doi.org/10.1021/ar0100475

Jhoti, H., & Leach, A. R. (Eds.). (2007). *Structure-based drug discovery*. Springer.

Kaiser, A., Brembeck, F. H., Nicke, B., Wiedenmann, B., Riecken, E.-O., & Rosewicz, S. (1999). All-trans-Retinoic Acid-mediated Growth Inhibition Involves Inhibition of Human Kinesin-related Protein HsEg5. *Journal of Biological Chemistry*, *274*(27), 18925–18931. https://doi.org/10.1074/jbc.274.27.18925

Kalaria, P. N., Karad, S. C., & Raval, D. K. (2018). A review on diverse heterocyclic compounds as the privileged scaffolds in antimalarial drug discovery. *European Journal of Medicinal Chemistry*, *158*, 917–936. https://doi.org/10.1016/j.ejmech.2018.08.040

Katritzky, A. R. (2014). *Handbook of Heterocyclic Chemistry*. Elsevier Science. http://qut.eblib.com.au/patron/FullRecord.aspx?p=1838225

Kaur, N. (2020). Six-membered O-heterocycles. In *Metal and Nonmetal Assisted Synthesis of Six-Membered Heterocycles* (pp. 295–350). Elsevier. https://doi.org/10.1016/B978-0-12-820282-1.00006-3

Kearney, P. C., Mizoue, L. S., Kumpf, R. A., Forman, J. E., McCurdy, A., & Dougherty, D. A. (1993). Molecular recognition in aqueous media. New binding studies provide further insights into the cation-.pi. Interaction and related phenomena. *Journal of the American Chemical Society*, *115*(22), 9907–9919. https://doi.org/10.1021/ja00075a006

Khanna, A., Kauko, O., Böckelman, C., Laine, A., Schreck, I., Partanen, J. I., Szwajda, A., Bormann, S., Bilgen, T., Helenius, M., Pokharel, Y. R., Pimanda, J., Russel, M. R., Haglund, C., Cole, K. A., Klefström, J., Aittokallio, T., Weiss, C., Ristimäki, A., … Westermarck, J. (2013). Chk1 targeting reactivates PP2A tumor suppressor activity in cancer cells. *Cancer Research*, *73*(22), 6757–6769. https://doi.org/10.1158/0008-5472.CAN-13-1002

Klebe, G. (2000). Recent developments in structure-based drug design. *Journal of Molecular Medicine (Berlin, Germany)*, *78*(5), 269–281. https://doi.org/10.1007/s001090000084

Kumar, D., Sharma, P., Singh, H., Nepali, K., Gupta, G. K., Jain, S. K., & Ntie-Kang, F. (2017). The value of pyrans as anticancer scaffolds in medicinal chemistry. *RSC Advances*, *7*(59), 36977–36999. https://doi.org/10.1039/C7RA05441F

Lalhruaizela, Marak, B. N., Gogoi, D., Dowarah, J., Sran, B. S., Pachuau, Z., & Singh, V. P. (2021). Study of supramolecular self-assembly of pyridone and dihydropyridone co-crystal: Synthesis, crystal structure, Hirshfeld surface, DFT and molecular docking studies. *Journal of Molecular Structure*, *1235*, 130214. https://doi.org/10.1016/j.molstruc.2021.130214

Legon, A. C. (2010). The halogen bond: An interim perspective. *Physical Chemistry Chemical Physics*, *12*(28), 7736. https://doi.org/10.1039/c002129f

Li, Q., Mitscher, L. A., & Shen, L. L. (2000). The 2-pyridone antibacterial agents: Bacterial topoisomerase inhibitors. *Medicinal Research Reviews*, *20*(4), 231–293. https://doi.org/10.1002/1098-1128(200007)20:4<231::AID-MED1>3.0.CO;2-N

Liang, Y., Lin, S.-Y., Brunicardi, F. C., Goss, J., & Li, K. (2009). DNA damage response pathways in tumor suppression and cancer treatment. *World Journal of Surgery*, *33*(4), 661–666. https://doi.org/10.1007/s00268-008-9840-1

Liljefors, T., Krogsgaard-Larsen, P., & Madsen, U. (2002). *Textbook of Drug Design and Discovery* (0 ed.). CRC Press. https://doi.org/10.1201/b12381

Litvinov, V. P., Krivokolysko, S. G., & Dyachenko, V. D. (1999). Synthesis and properties of 3-cyanopyridine-2(1H)-chalcogenones. Review. *Chemistry of Heterocyclic Compounds*, *35*(5), 509–540. https://doi.org/10.1007/BF02324634

Liu, R.-S. (2001). Synthesis of oxygen heterocycles via alkynyltungsten compounds. *Pure and Applied Chemistry*, *73*(2), 265–269. https://doi.org/10.1351/pac200173020265

Lundstrom, K. (2006). Structural genomics for membrane proteins. *Cellular and Molecular Life Sciences*, *63*(22), 2597–2607. https://doi.org/10.1007/s00018-006-6252-y

Ma, J. C., & Dougherty, D. A. (1997). The Cation−π Interaction. *Chemical Reviews*, *97*(5), 1303–1324. https://doi.org/10.1021/cr9603744

Mahadevi, A. S., & Sastry, G. N. (2013). Cation−π Interaction: Its Role and Relevance in Chemistry, Biology, and Material Science. *Chemical Reviews*, *113*(3), 2100–2138. https://doi.org/10.1021/cr300222d

Mak, C. H. (2016). Unraveling Base Stacking Driving Forces in DNA. *The Journal of Physical Chemistry B*, *120*(26), 6010–6020. https://doi.org/10.1021/acs.jpcb.6b01934

March, J. (1985). *Advanced organic chemistry: Reactions, mechanisms, and structure* (3. ed). Wiley.

Marquis, L., Tran, M., Choi, W., Lee, I., Huszar, D., Siefker-Radtke, A., Dinney, C. P., & McConkey, D. J. (2012). P63 expression correlates with sensitivity to the Eg5 inhibitor AZD4877 in bladder cancer cells. *Cancer Biology & Therapy*, *13*(7), 477–486. https://doi.org/10.4161/cbt.19590

Mata, G., Rodrigues, J., Gamboa, N., Charris, K., Lobo, G., Monasterios, M., Avendano, M., Lein, M., Jung, K., Abramjuk, C., Nitzsche, B., Hopfner, M., & Charris, J. (2017). Synthesis, Antiproliferative, and Antiangiogenic Activities of Benzochromene and Benzoquinoline Derivatives on Prostate Cancer in vitro. *Letters in Drug Design & Discovery*, *14*(4), 398–413. https://doi.org/10.2174/1570180814666161118163844

Mauser, H., & Guba, W. (2008). Recent developments in de novo design and scaffold hopping. *Current Opinion in Drug Discovery & Development, 11*(3), 365–374.

Mazik, M. (2012). Recent developments in the molecular recognition of carbohydrates by artificial receptors. *RSC Advances*, *2*(7), 2630. https://doi.org/10.1039/c2ra01138g

McKinnon, J. J., Spackman, M. A., & Mitchell, A. S. (2004). Novel tools for visualizing and exploring intermolecular interactions in molecular crystals. *Acta Crystallographica Section B Structural Science*, *60*(6), 627–668. https://doi.org/10.1107/S0108768104020300

McNaught, A. D., Wilkinson, A., & International Union of Pure and Applied Chemistry (Eds.). (1997). *Compendium of chemical terminology: IUPAC recommendations* (2nd ed). Blackwell Science.

McNeely, S., Beckmann, R., & Bence Lin, A. K. (2014). CHEK again: Revisiting the development of CHK1 inhibitors for cancer therapy. *Pharmacology & Therapeutics*, *142*(1), 1–10. https://doi.org/10.1016/j.pharmthera.2013.10.005

Merz, K. M., Ringe, D., & Reynolds, C. H. (Eds.). (2010). *Drug design: Structure- and ligand-based approaches*. Cambridge University Press.

Metrangolo, P., Meyer, F., Pilati, T., Resnati, G., & Terraneo, G. (2008). Halogen Bonding in Supramolecular Chemistry. *Angewandte Chemie International Edition*, *47*(33), 6114–6127. https://doi.org/10.1002/anie.200800128

Mijin, D., Markovic, J., Brkovic, D., & Marinkovic, A. (2014). Microwave assisted synthesis of 2-pyridone and 2-pyridone based compounds. *Hemijska Industrija*, *68*(1), 1–14. https://doi.org/10.2298/HEMIND121204021M

Mirjalili, B., Kabnadideh, S., Zomorodian, K., Zamani, L., Faghih, M., Haghighijoo, Z., & Kananizadehgan, S. (2017). Synthesis, Docking Study and Antifungal Activity Evaluation of Some 1,3-benzo[d]thiazole Analogs: A Promotion in Synthetic Method with Nano-γ-Al2O3/BF3-n under Solvent Free Conditions. *Journal of Pharmaceutical Research International*, *19*(2), 1–26. https://doi.org/10.9734/JPRI/2017/35831

Moshtaghi Zonouz, A., Moghani, D., & Okhravi, S. (2014). A facile and efficient protocol for the synthesis of 2-amino-3-cyano-4H-pyran derivatives at ambient temperature. *Current Chemistry Letters*, *3*(2), 71–74. https://doi.org/10.5267/j.ccl.2014.2.001

Moss, G., & Coppens, P. (1980). Space partitioning and the effects of molecular proximity on electrostatic moments of the crystalline formamide molecule. *Chemical Physics Letters*, *75*(2), 298–302. https://doi.org/10.1016/0009-2614(80)80518-5

Muraki, M. (2002). The Importance of Ch / π Interactions to the Function of Carbohydrate Binding Proteins. *Protein & Peptide Letters*, *9*(3), 195–209. https://doi.org/10.2174/0929866023408751

Murata, T., Shimizu, K., Narita, M., Manganiello, V. C., & Tagawa, T. (2002). Characterization of phosphodiesterase 3 in human malignant melanoma cell line. *Anticancer Research*, *22*(6A), 3171–3174.

Nguyen, H. L., Horton, P. N., Hursthouse, M. B., Legon, A. C., & Bruce, D. W. (2004). Halogen Bonding: A New Interaction for Liquid Crystal Formation. *Journal of the American Chemical Society*, *126*(1), 16–17. https://doi.org/10.1021/ja036994l

Nishio, M., Umezawa, Y., Fantini, J., Weiss, M. S., & Chakrabarti, P. (2014). CH–π hydrogen bonds in biological macromolecules. *Phys. Chem. Chem. Phys.*, *16*(25), 12648–12683. https://doi.org/10.1039/C4CP00099D

Nowicki, M. O., Pawlowski, P., Fischer, T., Hess, G., Pawlowski, T., & Skorski, T. (2003). Chronic myelogenous leukemia molecular signature. *Oncogene*, *22*(25), 3952–3963. https://doi.org/10.1038/sj.onc.1206620

Okasha, R., Alblewi, F., Afifi, T., Naqvi, A., Fouda, A., Al-Dies, A.-A., & El-Agrody, A. (2017). Design of New Benzo[h]chromene Derivatives: Antitumor Activities and Structure-Activity Relationships of the 2,3-Positions and Fused Rings at the 2,3-Positions. *Molecules*, *22*(3), 479. https://doi.org/10.3390/molecules22030479

Orlando, G., Pilone, V., Vitiello, A., Gervasi, R., Lerose, M. A., Silecchia, G., & Puzziello, A. (2014). Gastric Cancer Following Bariatric Surgery: A Review. *Surgical Laparoscopy, Endoscopy & Percutaneous Techniques*, *24*(5), 400–405. https://doi.org/10.1097/SLE.0000000000000050

Oshovsky, G. V., Reinhoudt, D. N., & Verboom, W. (2007). Supramolecular Chemistry in Water. *Angewandte Chemie International Edition*, *46*(14), 2366–2393. https://doi.org/10.1002/anie.200602815

Pace, C. J., Kim, D., & Gao, J. (2012). Experimental Evaluation of CH-π Interactions in a Protein Core. *Chemistry - A European Journal*, *18*(19), 5832–5836. https://doi.org/10.1002/chem.201200334

Palmer, B. D., Rewcastle, G. W., Atwell, G. J., Baguley, B. C., & Denny, W. A. (1988). Potential antitumor agents. 54. Chromophore requirements for in vivo antitumor activity among the general class of linear tricyclic carboxamides. *Journal of Medicinal Chemistry*, *31*(4), 707–712. https://doi.org/10.1021/jm00399a003

Panda, D., Singh, J. P., & Wilson, L. (1997). Suppression of Microtubule Dynamics by LY290181. *Journal of Biological Chemistry*, *272*(12), 7681–7687. https://doi.org/10.1074/jbc.272.12.7681

Parlow, J. J., & South, M. S. (2003). Synthesis of 2-pyridones as tissue factor VIIa inhibitors. *Tetrahedron*, *59*(39), 7695–7701. https://doi.org/10.1016/S0040-4020(03)01239-0

Parreira, R. L. T., Abrahão, O., & Galembeck, S. E. (2001). Conformational preferences of non-nucleoside HIV-1 reverse transcriptase inhibitors. *Tetrahedron*, *57*(16), 3243–3253. https://doi.org/10.1016/S0040-4020(01)00193-4

Politzer, P., Lane, P., Concha, M. C., Ma, Y., & Murray, J. S. (2007). An overview of halogen bonding. *Journal of Molecular Modeling*, *13*(2), 305–311. https://doi.org/10.1007/s00894-006-0154-7

Rai, S. K., Singh, P., Khanam, S., & Tewari, A. K. (2016). Polymorphic study and anti-inflammatory activity of a 3-cyano-2-pyridone based flexible model. *New Journal of Chemistry*, *40*(6), 5577–5587. https://doi.org/10.1039/C5NJ03683F

Raimondi, M., Randazzo, O., La Franca, M., Barone, G., Vignoni, E., Rossi, D., & Collina, S. (2019). DHFR Inhibitors: Reading the Past for Discovering Novel Anticancer Agents. *Molecules*, *24*(6), 1140. https://doi.org/10.3390/molecules24061140

Raj, V., Bhadauria, A. S., Singh, A. K., Kumar, U., Rai, A., Keshari, A. K., Kumar, P., Kumar, D., Maity, B., Nath, S., Prakash, A., Ansari, K. M., Jat, J. L., & Saha, S. (2019). Novel 1,3,4-thiadiazoles inhibit colorectal cancer via blockade of IL-6/COX-2 mediated JAK2/STAT3 signals as evidenced through data-based mathematical modeling. *Cytokine*, *118*, 144–159. https://doi.org/10.1016/j.cyto.2018.03.026

Ramsay, R., & Tipton, K. (2017). Assessment of Enzyme Inhibition: A Review with Examples from the Development of Monoamine Oxidase and Cholinesterase Inhibitory Drugs. *Molecules*, *22*(7), 1192. https://doi.org/10.3390/molecules22071192

Rauf, Mohd. A., Zubair, S., & Azhar, A. (2015). Ligand docking and binding site analysis with pymol and autodock/vina. *International Journal of Basic and Applied Sciences*, *4*(2), 168. https://doi.org/10.14419/ijbas.v4i2.4123

Rees, C. W. (1992). Polysulfur-nitrogen heterocyclic chemistry. *Journal of Heterocyclic Chemistry*, *29*(3), 639–651. https://doi.org/10.1002/jhet.5570290306

René Just Haüy. (1784). *Essai d'une theorie sur la structure des crystaux*.

Rescifina, A., Chiacchio, M. A., Corsaro, A., De Clercq, E., Iannazzo, D., Mastino, A., Piperno, A., Romeo, G., Romeo, R., & Valveri, V. (2006). Synthesis and Biological Activity of Isoxazolidinyl Polycyclic Aromatic Hydrocarbons: Potential DNA Intercalators. *Journal of Medicinal Chemistry*, *49*(2), 709–715. https://doi.org/10.1021/jm050772b

Ringer, A. L., Figgs, M. S., Sinnokrot, M. O., & Sherrill, C. D. (2006). Aliphatic C−H/π Interactions: Methane−Benzene, Methane−Phenol, and Methane−Indole Complexes. *The Journal of Physical Chemistry A*, *110*(37), 10822–10828. https://doi.org/10.1021/jp062740l

Rohs, R. (2005). Molecular flexibility in ab initio drug docking to DNA: Binding-site and binding-mode transitions in all-atom Monte Carlo simulations. *Nucleic Acids Research*, *33*(22), 7048–7057. https://doi.org/10.1093/nar/gki1008

Salonen, L. M., Ellermann, M., & Diederich, F. (2011). Aromatic Rings in Chemical and Biological Recognition: Energetics and Structures. *Angewandte Chemie*

International Edition, *50*(21), 4808–4842. https://doi.org/10.1002/anie.201007560

Samir, E. M. (2016). The Uses of Cyclopentanone for the Synthesis of Biologically Active Pyran, Pyridine and Thiophene Derivatives. *OALib*, *03*(03), 1–11. https://doi.org/10.4236/oalib.1102532

Sangani, C. B., Mungra, D. C., Patel, M. P., & Patel, R. G. (2012). Synthesis and in vitro antimicrobial screening of new pyrano[4,3-b]pyrane derivatives of 1H-pyrazole. *Chinese Chemical Letters*, *23*(1), 57–60. https://doi.org/10.1016/j.cclet.2011.09.012

Sarwar, M. G., Dragisic, B., Salsberg, L. J., Gouliaras, C., & Taylor, M. S. (2010). Thermodynamics of Halogen Bonding in Solution: Substituent, Structural, and Solvent Effects. *Journal of the American Chemical Society*, *132*(5), 1646–1653. https://doi.org/10.1021/ja9086352

Scapin, G. (2006). Structural Biology and Drug Discovery. *Current Pharmaceutical Design*, *12*(17), 2087–2097. https://doi.org/10.2174/138161206777585201

Schneider, H.-J. (2009). Binding Mechanisms in Supramolecular Complexes. *Angewandte Chemie International Edition*, *48*(22), 3924–3977. https://doi.org/10.1002/anie.200802947

Scholtz, J. M., & Baldwin, R. L. (1992). The Mechanism of alpha-Helix Formation by Peptides. *Annual Review of Biophysics and Biomolecular Structure*, *21*(1), 95–118. https://doi.org/10.1146/annurev.bb.21.060192.000523

Scotti, L., & Scotti, M. (2015). Computer Aided Drug Design Studies in the Discovery of Secondary Metabolites Targeted Against Age-Related Neurodegenerative Diseases. *Current Topics in Medicinal Chemistry*, *15*(21), 2239–2252. https://doi.org/10.2174/1568026615666150610143510

Semple, G., Andersson, B.-M., Chhajlani, V., Georgsson, J., Johansson, M. J., Rosenquist, Å., & Swanson, L. (2003). Synthesis and Biological activity of kappa opioid receptor agonists. Part 2: Preparation of 3-aryl-2-pyridone analogues generated by solution- and solid-phase parallel synthesis methods. *Bioorganic & Medicinal Chemistry Letters*, *13*(6), 1141–1145. https://doi.org/10.1016/S0960-894X(03)00033-7

Sethi, A., Joshi, K., Sasikala, K., & Alvala, M. (2020). Molecular Docking in Modern Drug Discovery: Principles and Recent Applications. In V. Gaitonde, P. Karmakar, & A. Trivedi (Eds.), *Drug Discovery and Development—New Advances*. IntechOpen. https://doi.org/10.5772/intechopen.85991

Sharma, A. K., Yadav, P., Chand, K., & Sharma, S. K. (2016). ChemInform Abstract: Synthesis and Characterization of New N-Alkylated Pyridin-2(1H)-ones. *ChemInform*, *47*(40). https://doi.org/10.1002/chin.201640162

Shi, L., Xu, L., Wu, C., Xue, B., Jin, X., Yang, J., & Zhu, X. (2018). Celecoxib-Induced Self-Assembly of Smart Albumin-Doxorubicin Conjugate for Enhanced Cancer Therapy. *ACS Applied Materials & Interfaces*, *10*(10), 8555–8565. https://doi.org/10.1021/acsami.8b00875

Shinkai, S., Ikeda, M., Sugasaki, A., & Takeuchi, M. (2001). Positive Allosteric Systems Designed on Dynamic Supramolecular Scaffolds: Toward Switching and Amplification of Guest Affinity and Selectivity. *Accounts of Chemical Research*, *34*(6), 494–503. https://doi.org/10.1021/ar000177y

Singh, V. P., Dowarah, J., Lalhruaizela, & Geiger, D. K. (2020). Structural and Non-Covalent Interactions Study of 2-Pyridone Based Flexible Unsymmetrical Dimer. *Crystal Research and Technology*, *55*(1), 1900136. https://doi.org/10.1002/crat.201900136

Sinnokrot, M. O., Valeev, E. F., & Sherrill, C. D. (2002). Estimates of the Ab Initio Limit for π−π Interactions: The Benzene Dimer. *Journal of the American Chemical Society*, *124*(36), 10887–10893. https://doi.org/10.1021/ja025896h

Smith, C. W., Bailey, J. M., Billingham, M. E. J., Chandrasekhar, S., Dell, C. P., Harvey, A. K., Hicks, C. A., Kingston, A. E., & Wishart, G. N. (1995). The anti-rheumatic potential of a series of 2,4-di-substituted-4H-naphtho[1,2-b]pyran-3-carbonitriles. *Bioorganic & Medicinal Chemistry Letters*, *5*(23), 2783–2788. https://doi.org/10.1016/0960-894X(95)00487-E

Spackman, M. A., & Byrom, P. G. (1997). A novel definition of a molecule in a crystal. *Chemical Physics Letters*, *267*(3–4), 215–220. https://doi.org/10.1016/S0009-2614(97)00100-0

Spackman, M. A., & McKinnon, J. J. (2002). Fingerprinting intermolecular interactions in molecular crystals. *CrystEngComm*, *4*(66), 378–392. https://doi.org/10.1039/B203191B

Stauffer, D. A., Barrans, R. E., & Dougherty, D. A. (1990). Concerning the thermodynamics of molecular recognition in aqueous and organic media. Evidence for significant heat capacity effects. *The Journal of Organic Chemistry*, *55*(9), 2762–2767. https://doi.org/10.1021/jo00296a038

Steiner, T. (2002). The Hydrogen Bond in the Solid State. *Angewandte Chemie International Edition*, *41*(1), 48–76. https://doi.org/10.1002/1521-3773(20020104)41:1%3C48::AID-ANIE48%3E3.0.CO;2-U

Steno, N., Ferdinando, & Accademia della Crusca,. (1669). *Nicolai Stenonis De solido intra solidum naturaliter contento dissertationis prodromus, /*. Ex typographia sub signo Stellae,. https://doi.org/10.5962/bhl.title.148841

Stewart, R. F. (1979). On the mapping of electrostatic properties from bragg diffraction data. *Chemical Physics Letters*, *65*(2), 335–342. https://doi.org/10.1016/0009-2614(79)87077-3

Sveinbjörnsson, B., Rasmuson, A., Baryawno, N., Wan, M., Pettersen, I., Ponthan, F., Orrego, A., Haeggström, J. Z., Johnsen, J. I., & Kogner, P. (2008). Expression of enzymes and receptors of the leukotriene pathway in human neuroblastoma promotes tumor survival and provides a target for therapy. *The FASEB Journal*, *22*(10), 3525–3536. https://doi.org/10.1096/fj.07-103457

Talwani, R., & Temesgen, Z. (2020). Doravirine: A new non-nucleoside reverse transcriptase inhibitor for the treatment of HIV infection. *Drugs of Today*, *56*(2), 113. https://doi.org/10.1358/dot.2020.56.2.3109966

Tang, P. A., Siu, L. L., Chen, E. X., Hotte, S. J., Chia, S., Schwarz, J. K., Pond, G. R., Johnson, C., Colevas, A. D., Synold, T. W., Vasist, L. S., & Winquist, E. (2008). Phase II study of ispinesib in recurrent or metastatic squamous cell carcinoma of the head and neck. *Investigational New Drugs*, *26*(3), 257–264. https://doi.org/10.1007/s10637-007-9098-8

Tewari, A. K., & Dubey, R. (2009). Conformational tuning of molecular network stabilized via C-H….π & π-π interaction in 2-[2-(3-cyano-4, 6-dimethyl-2-

oxo-2H-pyridin-1-yl-methyl)-benzyloxy]-4, 6-dimethyl-nicotinonitrile. *Arkivoc*, *2009*(10), 283–291. https://doi.org/10.3998/ark.5550190.0010.a25

Toledo, L. I., Murga, M., & Fernandez-Capetillo, O. (2011). Targeting ATR and Chk1 kinases for cancer treatment: A new model for new (and old) drugs. *Molecular Oncology*, *5*(4), 368–373. https://doi.org/10.1016/j.molonc.2011.07.002

Tollenaere, J. P. (1996). The role of structure-based ligand design and molecular modelling in drug discovery. *Pharmacy World and Science*, *18*(2), 56–62. https://doi.org/10.1007/BF00579706

Tong, W.-G., Ding, X.-Z., Talamonti, M. S., Bell, R. H., & Adrian, T. E. (2005). LTB4 stimulates growth of human pancreatic cancer cells via MAPK and PI-3 kinase pathways. *Biochemical and Biophysical Research Communications*, *335*(3), 949–956. https://doi.org/10.1016/j.bbrc.2005.07.166

Trott, O., & Olson, A. J. (2009). AutoDock Vina: Improving the speed and accuracy of docking with a new scoring function, efficient optimization, and multithreading. *Journal of Computational Chemistry*, NA-NA. https://doi.org/10.1002/jcc.21334

Tsuzuki, S., & Fujii, A. (2008). Nature and physical origin of CH/π interaction: Significant difference from conventional hydrogen bonds. *Physical Chemistry Chemical Physics*, *10*(19), 2584. https://doi.org/10.1039/b718656h

Vasu Govardhana Reddy, P., Kiran, Y. B. R., Suresh Reddy, C., & Devendranath Reddy, C. (2004). Synthesis and Antimicrobial Activity of Novel Phosphorus Heterocycles with Exocyclic P-C Link. *Chemical and Pharmaceutical Bulletin*, *52*(3), 307–310. https://doi.org/10.1248/cpb.52.307

Wang, D.-C., Xie, Y.-M., Fan, C., Yao, S., & Song, H. (2014). Efficient and mild cyclization procedures for the synthesis of novel 2-amino-4H-pyran derivatives with potential antitumor activity. *Chinese Chemical Letters*, *25*(7), 1011–1013. https://doi.org/10.1016/j.cclet.2014.04.026

Wang, Q., Zhang, P., Hoffman, L., Tripathi, S., Homouz, D., Liu, Y., Waxham, M. N., & Cheung, M. S. (2013). Protein recognition and selection through conformational and mutually induced fit. *Proceedings of the National*

Academy of Sciences, *110*(51), 20545–20550. https://doi.org/10.1073/pnas.1312788110

Wang, R., Gao, Y., & Lai, L. (2000). LigBuilder: A Multi-Purpose Program for Structure-Based Drug Design. *Journal of Molecular Modeling*, *6*(7–8), 498–516. https://doi.org/10.1007/s0089400060498

Weichsel, A., & Montfort, W. R. (1995). Ligand-induced distortion of an active site in thymidylate synthase upon binding anticancerdrug 1843U89. *Nature Structural & Molecular Biology*, *2*(12), 1095–1101. https://doi.org/10.1038/nsb1295-1095

Wiener, C., Schroeder, C. H., West, B. D., & Link, K. P. (1962). Studies on the 4-Hydroxycoumarins. XVIII. 3-[α-(Acetamidomethyl)benzyl]-4-hydroxycoumarin and Related Products. *The Journal of Organic Chemistry*, *27*(9), 3086–3088. https://doi.org/10.1021/jo01056a024

Wilcken, R., Liu, X., Zimmermann, M. O., Rutherford, T. J., Fersht, A. R., Joerger, A. C., & Boeckler, F. M. (2012). Halogen-Enriched Fragment Libraries as Leads for Drug Rescue of Mutant p53. *Journal of the American Chemical Society*, *134*(15), 6810–6818. https://doi.org/10.1021/ja301056a

Wolff, S. K., Grimwood, D. J., McKinnon, J. J., Turner, M. J., Jayatilaka, D., & Spackman, M. A. (2012). *Crystal explorer*.

Wood, D. L., Panda, D., Wiernicki, T. R., Wilson, L., Jordan, M. A., & Singh, J. P. (1997). Inhibition of Mitosis and Microtubule Function through Direct Tubulin Binding by a Novel Antiproliferative Naphthopyran LY290181. *Molecular Pharmacology*, *52*(3), 437–444. https://doi.org/10.1124/mol.52.3.437

Xiang, M., Cao, Y., Fan, W., Chen, L., & Mo, Y. (2012). Computer-Aided Drug Design: Lead Discovery and Optimization. *Combinatorial Chemistry & High Throughput Screening*, *15*(4), 328–337. https://doi.org/10.2174/138620712799361825

Yang, A.-S., & Honig, B. (1995a). Free Energy Determinants of Secondary Structure Formation: I. α-Helices. *Journal of Molecular Biology*, *252*(3), 351–365. https://doi.org/10.1006/jmbi.1995.0502

Yang, A.-S., & Honig, B. (1995b). Free Energy Determinants of Secondary Structure Formation: II. Antiparallel β-Sheets. *Journal of Molecular Biology*, *252*(3), 366–376. https://doi.org/10.1006/jmbi.1995.0503

Yang, L., Jiang, C., Liu, F., You, Q.-D., & Wu, W.-T. (2008). Cloning, Enzyme Characterization of Recombinant Human Eg5 and the Development of a New Inhibitor. *Biological and Pharmaceutical Bulletin*, *31*(7), 1397–1402. https://doi.org/10.1248/bpb.31.1397

Zhang, Y., & Hunter, T. (2014). Roles of Chk1 in cell biology and cancer therapy. *International Journal of Cancer*, *134*(5), 1013–1023. https://doi.org/10.1002/ijc.28226

Zhang, Y., & Pike, A. (2021). Pyridones in drug discovery: Recent advances. *Bioorganic & Medicinal Chemistry Letters*, *38*, 127849. https://doi.org/10.1016/j.bmcl.2021.127849

ABSTRACT

DESIGN, SYNTHESIS AND STUDY OF NOVEL POLYCYCLIC AROMATIC SYSTEMS

A THESIS SUBMITTED IN PARTIAL FULFILLMENT OF THE REQUIREMENTS FOR THE DEGREE OF DOCTOR OF PHILOSOPHY

LALHRUAIZELA
MZU REGISTRATION NO. : 4459 of 2010-11
PH.D REGISTRATION NO. : MZU/Ph.D/847 of 21.04.2016

DEPARTMENT OF CHEMISTRY
SCHOOL OF PHYSICAL SCIENCES
MAY, 2022

ABSTRACT

DESIGN, SYNTHESIS AND STUDY OF NOVEL POLYCYCLIC AROMATIC SYSTEMS

BY

LALHRUAIZELA

Department of Chemistry

Under the supervision of

Dr. VED PRAKASH SINGH

Submitted

In partial fulfillment of the requirement of the Degree of Doctor of Philosophy in Chemistry of Mizoram University, Aizawl.

ABSTRACT

Polycyclic aromatic systems are present in most natural products and are components of our biological systems. Our DNA also contains a polycyclic aromatic purine base, i.e., Adenine and Guanine. Polycyclic aromatic compounds include all aromatic compounds with more than one aromatic ring. Many of the clinically prescribed drugs contain polycyclic aromatic rings in their structures.

Heterocyclic compounds with multiple rings, both synthetic and natural, have been found to have biological, pharmaceutical, and industrial significance. Their importance is mainly attributed to their ability to engage in a variety of intermolecular interactions such as hydrogen bond donor/acceptor capability, π...π stacking interactions, metal co-ordination bonds, and van der Waals hydrophobic forces.

Chapter 1 consists of an introduction relevant to the research work. It also contains literature survey in relation to the studies. The non-covalent interactions are a heart for supramolecular chemistry and molecular recognition, which are crucial for understanding many energetic and structural properties in complex chemical systems, from crystal packing in organic solids to base-pair stacking in DNA, protein-drug interaction, protein folding, and misfolding manner. So in nature, these interactions are the foundation of the life process itself. Life would be impossible without non-covalent interactions. For the development of supramolecular chemistry, it is necessary to have a clear understanding and exact picture of the entire compass of the non-covalent interactions. The non-covalent interactions are mainly divided into two categories such as intra and inter-molecular non-covalent interactions. Intramolecular interactions decide the confirmation of molecular structure with the minimum energy ground state. Intermolecular interactions include hydrogen bonding, σ-hole bonding (halogen bonding), π…π stacking, dipole…dipole interactions, steric repulsion, and London dispersion forces. The above interactions decide the orientation of complex structures with various chemical natures.

In Chapter 2, hetero-polycyclic aromatic systems containing pyran and 2-pyridone structural moiety were successfully synthesized. Many compounds having pyran and 2-pyridone core were found in different pharmaceutical profiles. In Scheme

1, six different 4H-pyran structural profile derivatives were synthesized by the multi-component reaction between ethyl acetoacetate, malononitrile, and aromatic aldehyde. These 4H-pyran derivatives were then further employed to synthesize 3,4-dihydropyridone and 2-pyridone derivative compounds. Conveniently, two novel synthetic routes were designed by reacting the 4H-pyrans with either iodine or formic acid as a catalyst to give 3,4-dihydropyridone derivatives, which were further oxidized with DDQ under thermal and microwave-assisted reactions. Additional techniques for the purification of products in the synthetic route of 2-pyridone derivative compounds were also reported to minimize the use of solvent and time required for the workup process, which follows the principle of green chemistry.

Benzo[h]chromenes are polycyclic aromatic systems containing pyran ring scaffolds in their structural moiety. They are an important class of heterocyclic compounds that show a wide range of potentiation antitumor activity. Traditional benzo[h]chromenes were synthesized and then reacted with formic acid, which makes alternation in the functional group converting the benzo[h]chromene derivatives into 2-oxo-3,4-dihydro-2H-benzo[h]chromenes which have both pyran and dihydrocoumarin structural framework. The participation of formic acid in the reaction is very successful in the complete conversion of benzo[h]chromenes bearing amino group.

Chapter 3 deals with the synthesis of polycyclic aromatic systems having flexible models in their structures. The 2-pyridone derivatives synthesized from 4H-pyrans and a monocyclic 2-pyridone, i.e., 4,6-dimethyl-2oxo-1,2-dihydropyridine-3carbonitrile, were used as a starting scaffold in the design for the synthesis of novel polycyclic aromatic fleximers, that were connected with aromatic ring linked by a methylene group. The synthetic method involves the alkylation of the 2-pyridones at the sides of the functional groups, i.e., O-alkylation and N-alkylation. Selectivity of O-alkylation was observed in the case of polycyclic 2-pyridone compounds. In contrast, for the monocyclic 2-pyridone, a high O-alkylation and N-alkylation ratio was observed using potassium carbonate as a catalytic base.

For both Chapter 2 and 3, X-ray crystallography was employed to study the intra and inter-molecular non-covalent interactions, which determine the conformation of the crystal structures and the modes of interactions responsible for the association of the molecules that form a supramolecular structure. The crystal analysis provided that non-covalent hydrogen bonding interactions play a significant role in forming dimmers with an unsymmetrical geometry. The aromatic ring p-orbitals also facilitate stabilizing the crystal packing by establishing π…π interaction in an eclipsed parallel displaced fashion between the aromatic rings. They also stabilize the interaction between molecules from different layers of the crystal packing. Beyond these, the aromatic ring p-orbitals were also involved in forming C-H…π, cation…π, and lone pair…π interactions.

The Hirshfeld surface analysis was conducted to support the intermolecular non-covalent interactions observed in the x-ray crystallographic studies. The d_{norm} surface determines the strength of different weak non-interactions. The 2-D fingerprint plot gave the relative percentage contribution of different weak interactions. The Hirshfeld shape-index and curvedness surface studies were carried out to explore non-covalent interactions involving π…π, C-H…π, cation…π, and lone pair…π interactions involved in the supramolecular structures. The increase in surface area by introducing other aromatic rings demonstrates the increase in the relative percentage contribution of π…π interactions.

In Chapter 4, molecular recognition properties of the synthesized compounds from chapter 2 and 3 were performed by *in silico* analysis using AutoDock Vina program software. Since some enzymes are overexpressed and activated at the inflammatory site of cancer tissue, they also promote the development of cancer cells. Chk1, Eg2, 5-LOX, and COX-2 enzymes were targeted to study the drug-receptor properties of the synthesized compounds. The docking score with the least energy provides the most stable conformation of the compounds within the pocket of the active sites. The functional groups present in the compounds play an important role in forming hydrogen bonds with the amino acid residue of the enzyme. The aromatic rings present in the structure of the synthesized compounds also facilitate the formation of non-covalent interaction with the amino acid residues of the target enzyme. The increase in surface area of the aromatic ring also facilitates the binding affinity of the molecule to the receptor enzyme, as observed in 2-pyridone, 2-oxo-3,4-dihydro-2H-benzo[h]chromenes, and 2-pyridone derivative fleximers. The docking results, which give the best scores with the target enzyme, also provide theoretical lead compounds that might inhibit the enzyme's activity.

In Chapter 5, a brief summary of the thesis and conclusion of the studies on non-covalent interactions within the supramolecular framework, by using SC-XRD and Hirshfeld surface analysis were highlighted. It also contains the conclusion on the molecular recognition properties of the synthesized compounds with the target receptor enzyme by *in silico* analysis. The current studies may provide a new platform in drug designing and crystal engineering.